8-3-2020

Interactions of Photosensitizers with Model Membranes and their Applications in Photodynamic Therapy

Poornima Kalyanram
pk2544@rit.edu

R.I.T

Interactions of Photosensitizers with Model Membranes and their Applications in Photodynamic Therapy

by

Poornima Kalyanram

A dissertation submitted in partial fulfillment of the requirements for the degree of Doctor of Philosophy in Engineering

Engineering (PhD Program)

Kate Gleason College of Engineering

Rochester Institute of Technology

Rochester, New York

August 3rd, 2020

Interactions of Photosensitizers with Model Membranes and their Applications in Photodynamic Therapy

by

Poornima Kalyanram

Committee Approval:

We, the undersigned committee members, certify that we have advised and/or supervised the candidate on the work described in this dissertation. We further certify that we have reviewed the dissertation manuscript and approve it in partial fulfillment of the requirements of the degree of Doctor of Philosophy in Engineering.

_____

Dr. Anju R. Gupta (Advisor) Date
Assistant Professor, University of Toledo, Mechanical Engineering

_____

Dr. Satish G. Kandlikar (Co-Advisor) Date
James E. Gleason Distinguished Professor, Mechanical Engineering

_____

Dr. Amlan Ganguly Date
Associate Professor, Computer Engineering

_____

Dr. Kathleen Lamkin-Kennard Date
Associate Professor, Mechanical Engineering

_____

Dr. Scott Williams Date
Professor, School of Chemistry and Materials Science, RIT

Certified by:

_____

Dr. Edward Hensel Date
Director, Engineering PhD Program

Abstract

Kate Gleason College of Engineering

Rochester Institute of Technology

Degree: Doctor of Philosophy **Program:** Engineering PhD

Author: Poornima Kalyanram **Advisor:** Dr. Anju R. Gupta

Co-Advisor: Dr. Satish G. Kandlikar

Dissertation Title: Interaction of Photosensitizers with Model Membranes and their applications in Photodynamic Therapy

Cancer is caused by the uncontrolled growth and spread of abnormal cells resulting in 1 in 6 deaths every day. The most common treatment methods include surgery, chemotherapy, and radiation. These techniques are invasive, aggressive, and non-specific to cancer cells. Therefore, alternative therapies which are both potent and does not interfere with the quality of living are on a rise. Photodynamic Therapy (PDT) is an approved alternative remedy in the treatment of cancer. The efficacy of PDT depends on the penetration power of the photosensitizer (PS) when injected into to the site of tumor. However, due to complexity involved in the structure of the PS molecules and its interaction with the cancerous cells, the potential of this therapy is not fully realized.

The PS molecules exhibit biological effect because of direct interaction with the cell membranes. Therefore, it is important to investigate this interaction and its effect on the physicochemical properties of membranes. The focus of this work is to understand the fundamental mechanism of this interaction with the cell membranes. However, due to the complexities associated on working with the human cell membrane it is appropriate to conduct experiments with model cell membranes, commonly known as liposomes. Additionally, liposomes are extremely biocompatible and are used as drug delivery vehicles or encapsulating agents.

The work reported in this dissertation is divided into two parts. In the first part, the interaction mechanism of hydrophilic riboflavin with liposomes was studied as to create a baseline. It was

found out that the hydrophilic nature of riboflavin does not penetrate the hydrophobic lipid bilayer by using a combination of laser scattering and calorimetric techniques. To further the bilayer permeation capacity of any hydrophilic PS, the idea of conjugation of hydrophobic alkyl tail chains to hydrophilic PS molecules was explored. Thereby, hydrophobicity was induced to amino methyl coumarin, a potent PS molecule, based on the setbacks of the existing hydrophilic photosensitizers. The interaction between this molecule and model cancerous cell membranes was investigated using combination of biophysical techniques and MD simulations. Our findings indicated that the addition of alkyl chains to fluorophores improves their cellular uptake and targeted delivery. It was concluded that the at longer chain coumarin fluorophore perturbs the lipid bilayer at higher concentrations by flip-flop mechanism leading to membrane thinning. Preliminary in-vitro activity reveals the photoactive potential of these amphiphilic coumarin molecules.

In the second part, alternative strategies such as encapsulation using liposomes was proposed, for FDA approved existing PS molecules (viz. HPPH and Riboflavin) to increase their efficacy during treatment. Long circulating liposome formulations of poly ethyl glycol (PEG) conjugated lipids, polymerizable lipids and cholesterol. The stability and composition of each component in the formulations was examined using biophysical methods. It was found that PEGylation increases the stability of liposomal formulation by preventing aggregation through thermal and physical stability. It was also concluded that cholesterol does not contribute to the increase in stability of PEGylated formulations. *In- vitro* and *in- vivo* studies conducted by our collaborators at NIH confirmed the efficiency of PEGylated liposome-based carriers demonstrated through longer circulation times and specificity towards tumor.

Acknowledgements

"*One fourth from the teacher, one fourth from own intelligence,*
One fourth from classmates, and one fourth only with time." – Apastamba (1.7.29)

First and foremost, I would like to express my profound gratitude to my advisor Dr. Anju Gupta. This dissertation would not be possible without her continuous mentoring, patience, and encouragement. She has always looked out for me and pushed me to realize my potential. I am grateful for her support during times of distress and her faith in my potential which kept my quest for science going.

I would like to extend my heartfelt thanks to my co-advisor, Dr. Satish Kandlikar for being a source of motivation and encouragement. His liveliness and passion for research inspired me to aim higher and do better. I would like to thank all my committee members- Dr. Amlan Ganguly, Dr. Christopher Collison, Dr. Kathleen Lamkin-Kennard, and Dr. Scott Williams for their valuble feedback and recommendations throughout my doctoral studies. I am grateful to Dr. Edward Hensel, Program Director, Engineering PhD for his constant support and mentoring.

I am thankful to all my past and present fellow lab members at Soft Nanomaterials lab, RIT, Thermal Analysis, Microfluidics and Fuel Cell Lab, RIT and Interfacial Thermal and Transport Lab, University of Toledo for their continued support. My special thanks to Shena Marshall and Andrew Layman for their efforts in experimental planning and execution during my initial stages of PhD research. I extend my sincere gratitude to my collaborators - Dr. Christina Goudreau, Dr. Istvan Stadler, Dr. Shikha Nangia and Dr. Anu Puri.

I would like to thank my aunt and uncle for being 'the home' away from home. I would also like to acknowledge the immense support system my brother, my parents-in-law and my husband have been throughout this journey of my PhD. A special shout out to all my friends

for always being my pillars of strength. Finally, I am always indebted to the Almighty for blessing me with such wonderful parents. Their sacrifices have shaped me to who I am today.

Dedication

To my Grandparents

Table of Contents:

List of Figures

List of Tables

1 Introduction

Cancer is caused by the uncontrolled growth and spread of abnormal cells. According to American Cancer Society, cancer causes 1 in 6 deaths every day in the world[1]. It is estimated that by 2035, 2.4 million new cancer cases will be diagnosed in the US annually as shown in Fig 1-1[2].

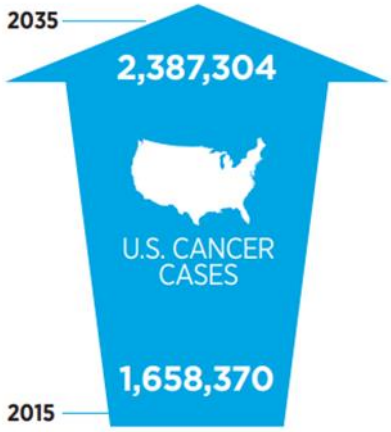

Figure 1-1: Estimated Number of rise in cancer cases by 2035. Adapted with permission from American Association for Cancer Research[2]

The most common treatment methods include surgery, chemotherapy, and radiation[3]. These techniques are invasive and non-specific to cancer cells. The aggressive nature of these treatments causes a destruction of healthy cells resulting in an immunocompromised individual[4]. Therefore, there exists a need for alternative therapies that are both potent and does not interfere with the quality of living[4]. Photodynamic Therapy (PDT) is an approved alternative remedy in the treatment of cancer. PDT is a two-step process, which are elucidated as follows and illustrated in Fig 1-2[5–7]:

i) Application of the photo-responsive drug or the photosensitizer (PS) to the affected area via injection or topical ointments;

ii) Irradiation of the affected area with light of a particular wavelength to produce singlet oxygen ($^1O_2$) from the cellular molecular oxygen (also known as Reactive Oxygen Species (ROS), which results in cell death.

This treatment is minimally invasive (for insertion of needles and tubes in certain cases) and target specific. The scarring associated with the exposure to laser light is minimum and temporary[5,6,8]. The efficacy of PDT depends on the photosensitizer and the wavelength of irradiation of the laser light[6,8]. Widespread research is on to optimize the potency of PDT and newer PS are being approved by FDA. However, due to complexity involved in the structure of the PS molecules and its interaction with the cancerous cells, the potential of this therapy is not fully realized.

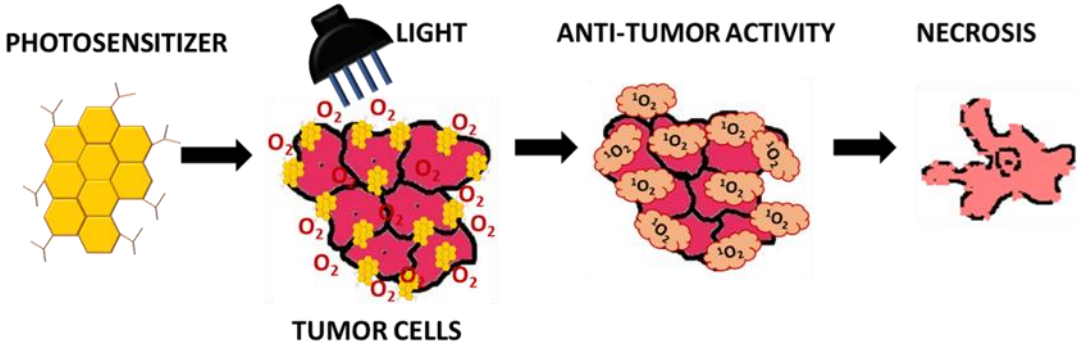

Figure 1-2: Schematic Showing steps involved in Photodynamic Therapy

The focus of this work is to understand the fundamental mechanism of the interaction of PS molecules with the cell membranes. The PS molecules exhibit biological effect because of direct interaction with the cell membranes. Therefore, it is important to investigate this interaction and its effect on the physicochemical properties of membranes. However, due to the complexities associated on working with the human cell membrane it is appropriate to conduct experiments with model cell membranes, commonly known as liposomes. Liposomes are structurally similar to human cell membranes[9,10]. They are used in lieu of human cell membranes because they are composed of phospholipids which is the same component that

constitutes 80-90% of cell membranes[9,10]. Additionally, liposomes are extremely biocompatible and are used as drug delivery vehicles or encapsulating agents[11,12].

The work reported in this dissertation is divided into two parts. In the first part, a novel design by inducing amphiphilicity to coumarin, a potent fluorescent PS molecule, was proposed, based on the setbacks of the existing photosensitizers. The interaction between this molecule and liposomes was investigated using biophysical techniques. It was concluded that the more amphiphilic the molecule is, higher its penetration power. In the second part, alternative strategies such as encapsulation using liposomes was proposed, for FDA approved existing PS molecules, to increase their efficacy during treatment. The effect of each component in the liposome was examined using biophysical methods to customize liposome-based carriers based on the nature of the PS molecule.

1.1 Liposomes: Cell Membrane Mimics

Cell membrane is a protective layer that encloses the cell organelles and cytoplasm. The cell membrane is composed of a phospholipid bilayer[13]. The lipid molecules are amphipathic in nature i.e., they have a polar phosphate hydrophilic head group and a non-polar fatty acid hydrophobic tail[13]. The phospholipids are oriented in a way such that the hydrophilic head groups point outwards with the hydrophobic tail group forms a bilayer. According to the fluid mosaic model, the lipids in the bilayer are assumed to be in motion and continuously glide from one part of the bilayer to another[13]. However, they cannot flip flop between the outer and the inner bilayer leaflets. This layer is selectively permeable to certain uncharged molecules such as CO_2, O_2 and H_2O[14]. However, it is impermeable to most of the charged ions and molecules. Therefore, it is necessary to investigate the mechanism by which pharmaceutically active components cross the lipid bilayer to design effective drug delivery systems[15]. Biological membranes are complex in nature and to study the lipid-drug mechanism *in-situ*, model cell membranes, also referred as liposomes, are preferred[16]. Liposomes are self-assemblies of

phospholipids and largely resemble a cell membrane as shown in Fig 1-3. They are prepared either by hydration of the phospholipid film or by electro formation method[17].

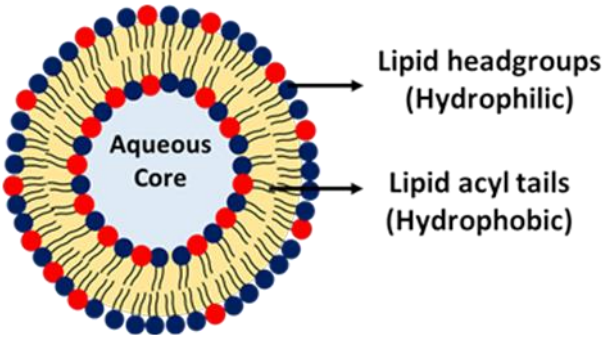

Figure 1-3: Structure of Liposome

The interaction between the liposomes and the drug molecules can be quantified by various biophysical and biochemical methods. Thus, in this study, liposomes are used as model cell membranes to understand the interactions with molecules of interest through biophysical techniques. This study is important is understanding the pharmacology of novel molecules. Though the phospholipid membrane is not the final target of the molecule, a knowledge on this initial interaction is necessary to predict the efficacy of the molecule of interest[18].

1.2 Interaction mechanisms of lipid bilayer with drug molecules:

Various mechanisms have been proposed to understand partitioning mechanism of lipid bilayer. These mechanisms depend on the nature of the molecule (whether hydrophobic, hydrophilic, and amphiphilic) and are specific to the lipids that make up the bilayer. Any foreign molecule penetrates the bilayer by two major cellular uptake process:

i. Endocytosis;
ii. Direct translocation.

Endocytosis involves two steps: phagocytosis for solid particles and pinocytosis for liquid particles. Most amphiphilic peptides follow direct translocation processes for membrane

destabilization. Since the molecules under this study have structural similarities to peptides, this review is focused on the different mechanisms of direct translocation process. The first step that precedes the destabilization mechanism is the electrostatic binding of the molecule with the lipid bilayer. Furthering which, the following mechanisms takes place. These mechanisms of destabilization are dependent on concentration, peptide and lipid charge and peptide type.

1.2.1 Pore Formation:

Pore formation was reported by Okumura et.al in 1981 in Mastoparans peptide[19,20]. This is a class of venom peptide which was studied with PC/PG vesicles. The peptide after binding electrostatically to the outer lipid leaflet, slowly translocases to the inner leaflet forming a pore. The translocation of the peptide is so rapid that it results in flip flop of the lipid molecules. The flip-flop mechanism is a secondary mechanism which results in reduced membrane elasticity and eventual pore formation and leakage of contents[19,20]

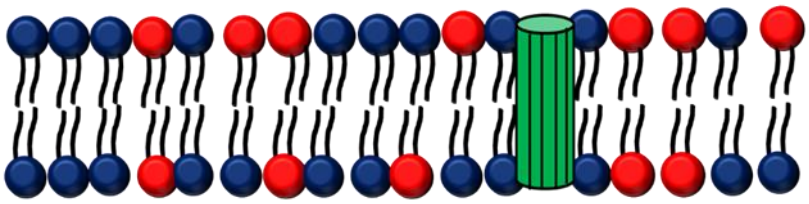

Figure 1-4: Schematic of Pore Formation

1.2.2 Carpet Mechanism:

Carpet mechanism was observed first in Dermaseptin peptide by Pouny et al., in 1991[21,22]. In this mechanism the peptides do not penetrate deep into the membrane. They bind preferentially like carpets on the surface resulting in orientation with the hydrophilic and hydrophobic parts of the peptide with the bilayer and results in thinning of the bilayer and eventual destabilization. Membrane thinning is a secondary mechanism that accompanies carpet mechanism[21,22].

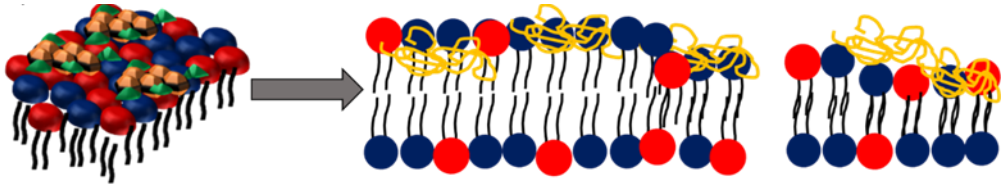

Figure 1-5: Schematic of Carpet Mechanism

1.2.3 Inverse Micelle Formation:

Inverse micelle formation is observed in homeodomain proteins of Drosophila[23,24]. These proteins are attracted to the hydrophilic groups on the lipid bilayer and creates membrane destabilization. This membrane destabilization results in formation of a micelle that travels across the membrane and releases the protein on the cytoplasmic side. This mechanism in non-invasive and recommended for gene therapies[25,26].

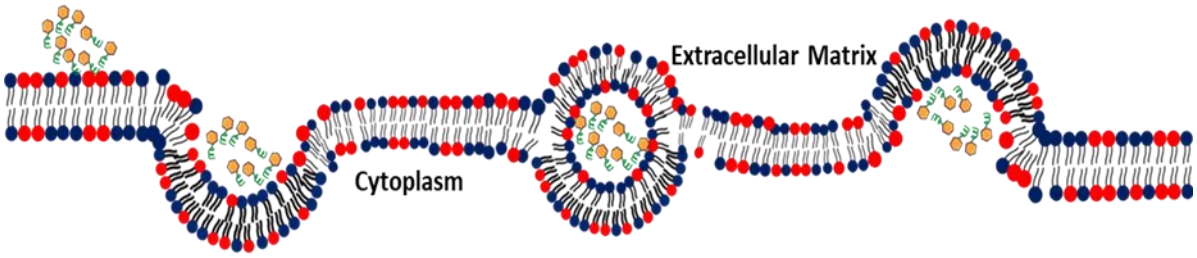

Figure 1-6: Schematic of Inverse Micelle Mechanism

Table 1-1 summarizes the selected bilayer interaction studies that have used molecules of nature and their bilayer partition mechanism. The different techniques used in the each of the study are also listed. These methods are elucidated in Chapter 2.

Table 1-1: Summary of different lipid-molecule interaction

Lipids used in forming the bilayer	Type of molecules/Name of molecules used in interaction Study	Techniques used	Mechanism of Interaction	Comments/Remarks
EPC [27]	Antitumoral drug Daunorubicin - Amphiphilic	Derivative Spectrometry and Zeta Potential	Electrostatic interactions and hydrophobic forces stabilize the drug in the lipid bilayer	This work establishes the use of spectroscopy and zeta potential measurements to locate the position of the drug in the bilayer
PC [28]	2′-hydroxy derivatives of 2,5-diaryl-1,3-oxazole Fluorophore - Hydrophobic	Molecular Dynamics and Fluorescence Spectroscopy	Hydrophobicity drives internalization of molecules into the bilayer	Molecular dynamics study establishes the location of the probe in the bilayer
POPC, POPG and Cholesterol [29]	2,6-bis(1H-benzimidazol-2-yl) pyridine Fluorophore-Hydrophobic	Molecular Dynamics and Fluorescence Spectroscopy	Hydrophobic nature of the probe drives binding and internalization	This study establishes the switchable nature of fluorescence of this probe in different environments
POPC/ Cholesterol [30]	Pyrene- Hydrophobic	Molecular Dynamics	Mechanism of partition is not elucidated	Lays out the effects of acyl chains of the lipids in the presence of pyrene
DPPC [31]	DiL-Hydrophobic	Molecular Dynamics	Charge induced perturbation of membrane bilayer	This study is important in determining the conditions for DiL perturbation
DPPC [32]	DPH-Hydrophobic	DSC, NMR, Molecular Dynamics	No significant perturbation. Probe lies in the hydrophobic region of bilayer	Complete study on the effects of DPH on the DPPC membrane perturbation
PC/PG [33]	Fluorescent AMP-PMAP-23-Amphiphilic	Fluorescence Spectroscopy and Molecular Dynamics	Carpet mechanism of disruption induced by charge and hydrophobicity	The location of the peptide in the bilayer is not determined. However, the

				mechanism of perturbation is complete
DPPC/ Cholesterol [34]	Paclitaxel-Hydrophobic Drug	DSC, Spin labelled Electro Paramagnetic Resonance (EPR)	Paclitaxel penetrates the hydrophobic region of DPPC rendering instability. Cholesterol alleviates the instability	Wholesome study on the location as well as the release kinetics of the drug
DPPC/ Cholesterol/ DSPC [18]	Ofloxacin and rifampicin	DSC, Zeta Potential, NMR	No significant change in the liposomal structure	Study on the design of liposomal formulation foe delivery of these two drugs
DPPC [35]	Codeine-Hydrophobic	DSC and EPR Spectroscopy	Interaction only with the polar headgroup and does not internalize much	Investigates the effect of morphine derived drugs on the bilayer to design effective carriers
DMPC [36]	Dequalinium chloride-Amphiphilic	Zeta, DSC, TEM, SAXS/WAXS, NMR	Strong interaction with polar groups and insertion	Establishes the complete activity of DQ on accumulation in positively charged lipid membranes
DPPC & DPPG [37]	Simvastatin	FTIR, DSC	Charge based insertion and lipid phase separation	Findings suggests that certain molecules exert activity based on charge on lipids
DPPC [38]	Bedaquiline-Hydrophobic	DLS, ZETA, DSC General Polarization	Causes fusion of membrane resulting in destabilization of membrane	Complete study on the mechanism using various techniques and mice studies
DMPC/DMPG [39]	Carvedilol-Hydrophobic	Fluorescence Spectroscopy and DSC	Drug is in the hydrophobic region of bilayer and	Study focuses on the antioxidant damage on lipid bilayer

			causes membrane destabilization	
DPhPC [40]	Alamethicin-Amphiphilic Molecule	XRD and Circular Dichroism	Phase separation of lipids bilayer thinning	Establishes the partitioning mechanism of amphiphilic peptide
POPC [41]	βAP (1-40)-Amphiphilic Molecule	NMR and CD	Intramolecular hydrogen bonding and peptide folding due to charge-based interaction	First of few biophysical studies focusing on amyloid peptide-membrane interactions
DPPC/DPPS [42]	Fluorescent-LPA Amphiphilic Peptide	DSC, Cryo-TEM	Charge based binding and hydrophobicity driven partitioning	Hydrophobicity in amphiphiles results in permeation of bilayer
POPC/POPS [43]	Synthetic β-Hairpin Peptides	CD and Molecular Simulation	Barrel mechanism of pore formation	Complete experimental and theoretical study on β-hairpin peptide association and permeation of lipid bilayer
DPPC/DPPG [44]	SVS-1 peptides	CD, Molecular Simulation and Fluorescence Spectroscopy	Charge based preferential binding and transient flip-dip mechanism of folding	Novel mechanism of flip dip explained through modelling
DMPC/ Cholesterol/ SM [45]	Doxorubicin	Molecular Dynamics	Preferentially partitions and inserts due to hydrophobicity in the presence of cholesterol	In-dept investigation on the influence of cholesterol in partitioning
DPPC [46]	NSAID	DSC, Raman, MD	Bind to the hydrophobic region	Pharmacological activity of NSAID is studied

DPPC(dipalmitoylphosphatidylcholine);POPC(palmitoyloleoylphosphatidylcholine);POPG(1-palmitoyl-2-oleoyl-sn-glycero-3-phospho-(1'-rac-glycerol));EPC(egg-phosphatidylcholine);DPPG(dipalmitoylphosphatidylglycerol);DMPC(dimyristoyl phosphatidylcholine);DMPG(dimyristoylphosphatidylglycerol);DPhPC(Diphytanoylphosphatidylcholine);DPPS (dipalmitoylphosphatidylserine);POPS(palmitoyloleoylphosphatidylserine)

Matos and coworkers[12] used derivative spectroscopy and zeta potential measurements to determine the partial coefficient of daunorubicin when interacted with zwitterionic (presence of both positive and negative charges on the headgroup) DPPC. The shift in fluorescence spectra of daunorubicin is due to the penetration of the molecule in the hydrophobic zone of the bilayer. The authors also reported that at lower concentrations electrostatic attraction caused the penetration into the bilayer and at higher concentrations, hydrophobicity induced penetration.

Budai et al[35], studied the effect of hydrophobic morphine derivatives on DPPC lipid bilayer using DSC. It has been reported that the presence of these molecules decreased the main transition temperature of DPPC. This is attributed to the fact that these molecules reduce the fluidity of the headgroups of the bilayer which results in reduction in transition temperature. This work gives an insight on the different thermodynamic parameters and their significance to the bilayer-drug interaction studies using DSC. However, this study does not investigate the concentration effects of the drug on the bilayer.

A recent study by Sarilisk et al[37]., has investigated the effect of partitioning by Simvastatin on zwitterionic DPPC vesicles and anionic DPPG vesicles. This study presents an in-depth analysis on the thermodynamic parameters calculated from the DSC thermogram suggesting that permeation of lipid bilayer was charge dependent. Though this study gives a complete mechanism of permeation, it does not describe the effects of the drug on the membrane after incorporation into the bilayer.

Many of the studies involving existing fluorescent probes and drugs listed in the table above use MD simulations[28–33] to investigate the effect on the drug on the bilayer post the incorporation. A variety of mechanisms of destabilization such as carpet mechanism, flip-dip mechanism, pore formation mechanism has been proposed when the concentrations of the drug

is increased or when the relaxation time conditions of the simulations are varied[28–33]. However, these studies have not been validated experimentally. Experimental validation is required for MD simulations as simulations occur at perfect microenvironmental conditions.

It is also been established from the above studies that amphiphilic molecules[40–44] penetrate bilayers better due to their ability to align with the different regions of the bilayer as compared to pure hydrophobic or hydrophilic molecules.

1.3 Liposomes as carriers:

Cancerous cells have a different vasculature as compared to healthy cells. This imparts a different pH to the cancerous cells[47,48]. Drug and fluorophore molecules lack the sensitivity to adhere on to these cells and have low bioavailability. These molecules, however, localize themselves on healthy cells causing damage to them and have a reduced specificity towards tumors[49]. Most of the fluorescent molecules used are hydrophobic in nature and have aromatic rings present in them. The presence of aromatic rings makes them aggregate in solution due to $\boldsymbol{\pi}$-$\boldsymbol{\pi}$ stacking[50,51]. To lessen the aggregation in the fluorophores as well as to improve the specificity and constant delivery, it is imperative to encapsulate the molecule in nano-carriers. Nano-carriers, owing to their smaller size, escape the body's immune system and circulate longer in the body[52–54].

The smaller size of nano-carriers also provides a high surface-volume ratio which helps in effective uptake of the particles by the cells and increased bioavailability of the drug. In addition to this, they adhere to the site of the tumor due to its leaky vasculature by enhanced permeation retention (EPR) effect and provide sustained release[52–54]. To escape the immune system of the body, the size of the nano-carriers should be between 100-150 nm[52].

Nano-carriers are further classified as organic and inorganic carriers[55–57]. Table 1-2 lists the types and most reported carriers in literature for PDT. However, most of the organic polymeric

nanocarriers get accumulated in the liver and spleen, which in-turn are destroyed by immune cells, thus failing to reach the target organ[58,59]. Inorganic carriers, on the other hand, pose a problem of *in-vitro* toxicity[58,59]. Quantum dots usually have a coating of organic layer to make them biocompatible. However, the complexity associated with the Quantum dots is the exposure of the inorganic core by etching away of the organic layer which makes them cytotoxic[58,59]. Carbon and metallic nanoparticles also pose a threat of subacute cytotoxicity[58,59].

Table 1-2: Commonly used Nano-carriers

ORGANIC CARRIERS	
Type of Carrier	**Commonly used Carrier examples**
Liposomes	Phosphatidyl inositol, phosphatidyl serine, and phosphatidyl choline
Natural Polymeric Nanocarriers	Albumin, hyaluronic acid, and chitosan
Synthetic Polymeric Nanocarriers	Poly acrylamide (PAA), Poly lactic acid (PLA), Poly glycolic acid (PGA), Poly(lactide-*co*-glycolide) (PLGA), dendrimers, and hyperbranched polymers
INORGANIC CARRIERS	
Quantum Dots	CdSe/CdS/ZnS nanocrystals
Ceramic Nanoparticles	Silica based Nanoparticles
Metallic Nanoparticles	Gold Nanoparticles
Carbon Nanoparticles	Functionalized Fullerenes, Single walled Carbon Nanotubes and Graphene Oxide

Liposomes, on the other hand, are composed of phospholipids making them biocompatible. In addition, their biophysical characteristics can be tuned to enhance their biological properties[60]. They are inactive pharmacologically and negligibly toxic[60].

Liposomes are self-assemblies of lipid molecules. The lipids that make up the bilayer have both a hydrophilic head group and a hydrophobic tail, which self-assemble to give rise to an aqueous core[42,61]. Liposomes are preferred as carriers in drug delivery systems over metallic, polymeric,

or dendritic carries because of their biodegradability, biocompatibility and their versatility to encapsulate micro and macro molecules[58,62,63]. Besides, liposomes can be customized according to size, charge and number of lamellae depending on the applications[64,65]. The classification of liposomal drug delivery is broadly divided into conventional and long circulation liposomes.

1.3.1 Conventional and Long Circulating Liposomes:

Conventional or the first-generation liposomes were developed commercially in the beginning of 1980s for the delivery of hydrophobic doxorubicin and amphotericin[11,66]. These liposomes comprised of a combination of cationic, anionic and zwitterionic phospholipids in conjunction with cholesterol. However, conventional liposomes were found to attract plasma proteins, also called as opsonin proteins, from the blood stream. The opsonins serve as identification markers for macrophages [67,68]. Opsonins attach themselves electrostatically to the surface of the lipids. The presence of opsonins on the liposomal surface makes them susceptible to macrophage attack and eventually, their removal through the reticuloendothelial system (RES). This phenomenon is also known as liposomal opsonization[69–71]. A comprehensive review on opsonization mechanisms of conventional liposomes is previously presented[68]. Therefore, various strategies have been exploited to induce stealth-ness in liposomes to prevent their opsonization and impart longer circulation in the bloodstream[66,72,73]. One of the commonly used techniques is introduction of steric stabilization by augmenting the liposomal surface with hydrophilic polymers as shown in Fig 1-7[69,74,75]. Fig 1-7 represents the effects of steric stabilization on RES clearance; opsonins (shown in green) adhere only to conventional liposomes and not to the sterically stabilized liposomes (polymer chains shown in pink). This results in attack of conventional liposomes by the macrophage cells and subsequent clearance by RES. However, sterically stabilized liposomes have longer circulation times and successfully reach the tumor sites. Stealth nature of the liposomes is responsible for longer

circulation times. This stealth nature is affected by the polymer's hydrophilicity, spatial conformation, density and molecular weight[76–78].

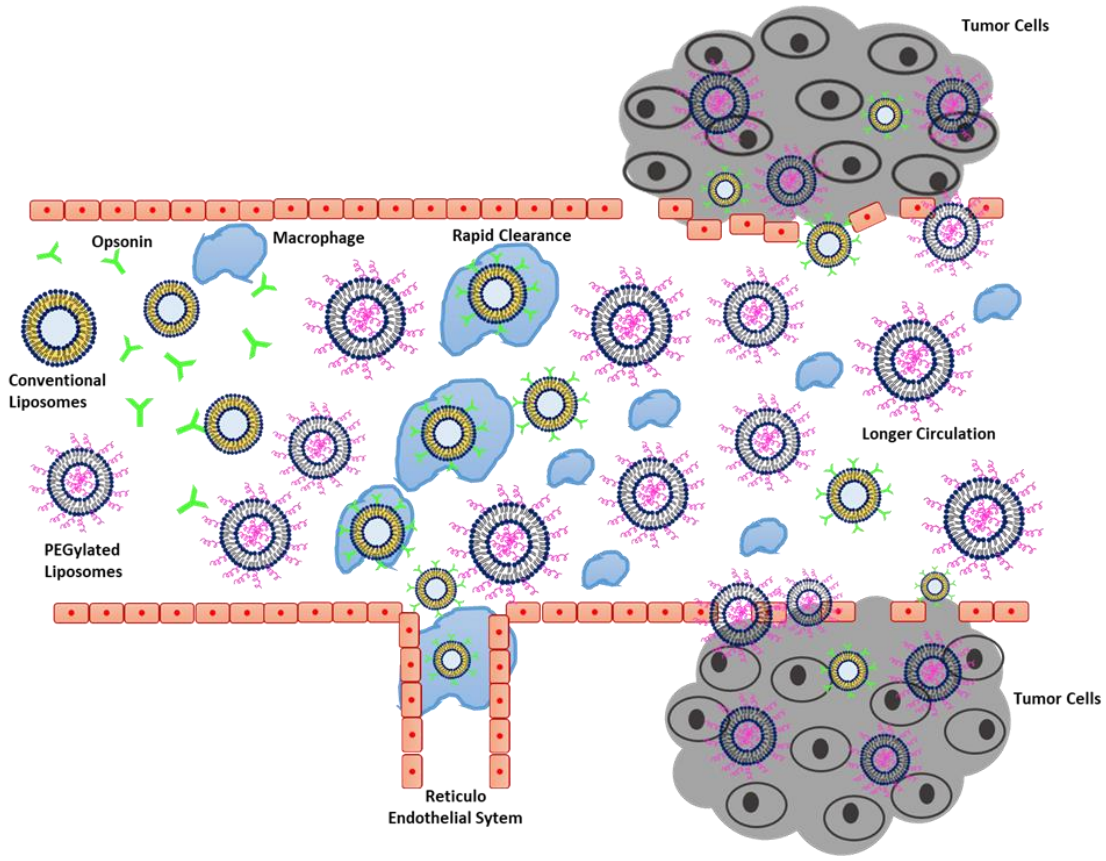

Figure 1-7: Conventional vs Long Circulating Liposomes and its effect on Macrophage clearance

Some commonly reported polymers include PLA (poly lactic acid)[79], polystyrene (PSt)[80,81], polyvinyl alcohol (PVA), polyacrylamide[80], polysaccharides[76,80,82], and Polyethylene glycol (PEG). However, PLA and PSt are highly anionic with zeta potentials ranging between −20 and −76 mV and these coatings easily attacked by macrophages[83–87], polysaccharide coatings on the other hand activate the immune system, due to the presence of hydroxyl groups, resulting in elimination[78,88]. Liposomes coated with PVA and polyacrylamide copolymers have shown to suffer mechanical degradation and subsequent leaking of contents[89].

Amongst the various polymers researched, PEG being hydrophilic, biocompatible, non-immunogenic and non-ionic[70,77,90–93] has demonstrated potential in steric stabilization. Doxil™

is the benchmark formulation demonstrating the stealth nature of PEG[94,95]. The stealth nature of PEG is attribute to its hydrophilicity and uncharged surface. The inclusion of PEG increases the hydrophilicity and reduces the overall charge or the zeta potential on the liposomes preventing opsonization[96–98]. This has been demonstrated in various research studies, where the coating of PEG on anionic liposome reduced the zeta potential to a near-neutral value, thereby increasing the circulation[99–101].

1.3.2 PEG (Polyethylene Glycol) linked lipids:

PEG (Poly-ethylene glycol) is non-ionic[102], bio-compatible[103], hydrophilic[97], and easy to synthesize[104] which makes it more favourable. PEGylated lipids consist of PEG chains, a linker, and a hydrophobic anchor [104]. One of the ends of the PEG chain in PEGylated lipids is attached to the hydrophobic anchor through the linker.

The molecular weight of the PEG chains is usually in the range of 50kDa to 400 Da and can be functionalized by covalent conjugation with folate, biotin, amine, azide, carboxylic acid [105,106]. The functionalization of PEG lipids which is vital to increase its target specificity has been reported extensively [107] and is beyond the focus of this review.

1.3.3 Conformation of PEG Chains:

The molecular weight and grafting density affect the conformation of PEG chains on the lipid bilayer surface. At lower grafting density, the PEG molecules assume a lesser interacting mushroom regime with conformed chains, and increasing grafting density, the PEG chains extend and branch out to interact with neighbouring molecules. [108,109]. Brush regime is preferred to improve the stealth properties of a liposome as in this regime the interaction of the particle is less and diffuses faster through the tissues than the mushroom regime[94]. Moreover, opsonins bind predominantly through hydrophobic and electrostatic interactions. Non-ionic

PEG chains in brush conformation render the surface of the liposome hydrophilic, reducing the interactions. Furthermore, some adsorbed opsonins tend to compress the brush like chains to mushroom like configuration. This change in energy impedes the attractive nature of opsonins from reaching the surface of the liposomes[71,110].

According to Alexander-deGennes theoretical model of polymer regimes, the transition from mushroom to brush regime depends on the distance (D) between the grafting sites and the length of the random PEG coils (R_f). R_f or Flory dimension is mathematically represented as $aN^{3/5}$, where N is the degree of polymerization and *a* is the monomer size[111]. The conditions for each of the configuration depicted in Fig 1-8 is as follows: (i) $D > R_f$, the PEG chains have very little interaction and follow interdigitated mushroom configuration (ii) $R_f < D < 2R_f$, a mushroom packing is observed (iii) $D \ll 2R_f$, chains are closer and a brush like extended conformation is observed[70,74,111]. In all conformations, PEG chains form a fixed aqueous layer thickness (FALT) around the liposomes. This FALT value controls the regime type and circulation time of liposomes. It is reported that a combination of shorter and long PEG chain lengths help in lengthening the circulation time[104].

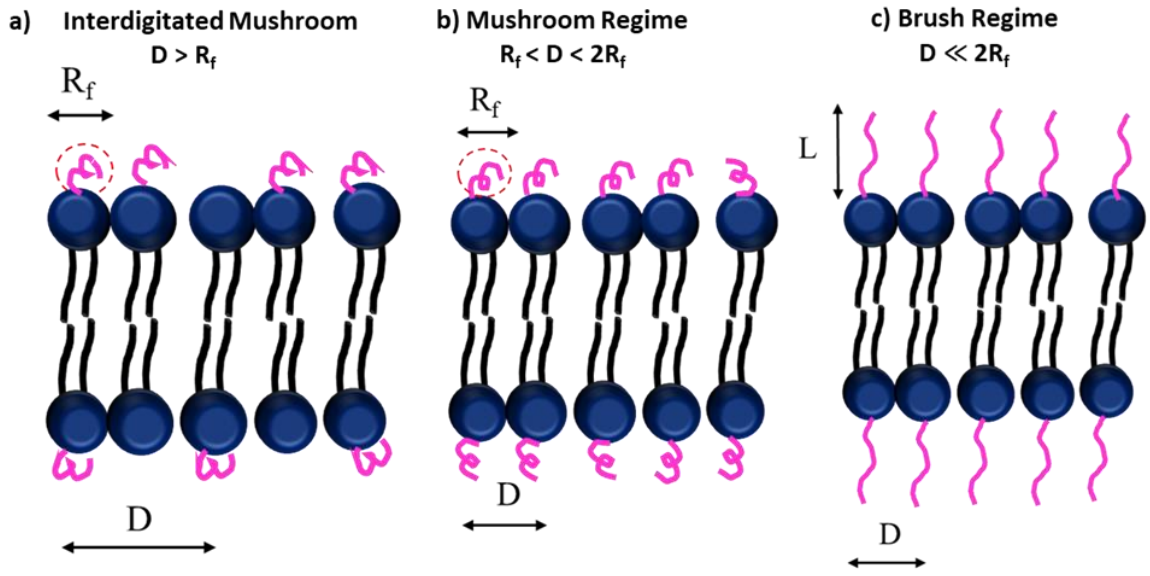

Figure 1-8: Regimes in a PEG coated liposome a) Interdigitated Mushroom; b) Mushroom Regime; c) Brush Regime

The PEG chains are further attached to the hydrophobic acyl anchor through linker moieties. Common linker moieties include phosphate ester, ether, disulfide, carboxyl ester, amide, and peptide linkages[112–116]. The linker moieties affect the surface charge and binding properties of the liposomes. The conventional linker has been the phosphate linker, based on its presence or absence the PEGylated lipids are categorized as PEG-phospholipids and PEG-non-phospholipids[104]. The third component of PEG lipids is the hydrophobic anchor comprising of acyl groups that associate into the lipid bilayer with PEG chains branching into the aqueous region. The acyl groups determine the lamellar or micellar morphology of the lipid assemblies[117] and the extent of inclusion of PEGylated lipid in the liposome[118,119]. In case of PEG-phospholipids, the acyl group is usually a fatty acid chain such as distearoyl, dipalmitoyl or dimyristoyl that is covalently bonded to the polar phospholipid head group[104]. These heads groups are then attached to a linear chain methoxy-PEG (mPEG) as shown in Fig 1-9a. It is found that the length of the mPEG chains which is directly related to the molecular weight influences the FALT values, thereby determining the circulation time. Shorter m-PEG chains (350-750 Da) have shown relatively limited effects to avoid macrophage clearance due to their inherent mushroom configuration. Increasing the mPEG chain length has shown to increase the circulation time[120–125]. Additionally, mPEG phospholipids having a mixture of PEG chain lengths in the same molecule (1,2-distearoyl-*sn*-glycero-3-phosphoethanolamine-PEG^2) elongates the circulation time and has increased tumor contact time because of its differing hydrophilic and hydrophobic properties[123]. It is also been found that concentration of mPEG-phospholipids in a liposome influence the rate of release of drugs. The higher molecular weight mPEG-phospholipids transform a diffusion-controlled drug release to an interfacial-controlled drug release[126].

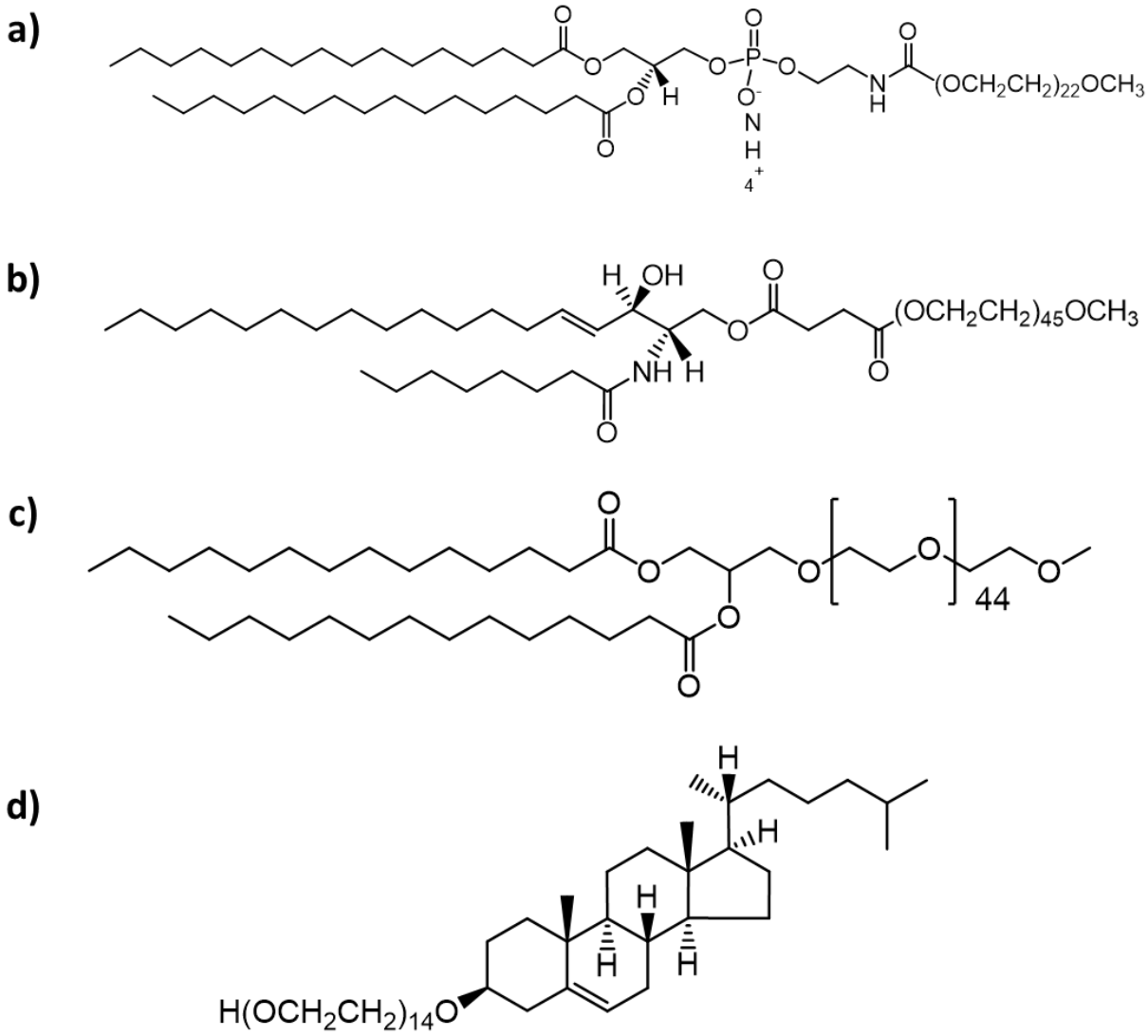

Figure 1-9: Structure of Phospholipid PEG a) DSPE-PEG2000 1,2-distearoyl-sn-glycero-3-phosphoethanolamine-N-[methoxy(polyethylene glycol)-2000]; Non-Phospholipid PEG b) C8 PEG2000 Ceramide N-octanoyl-sphingosine-1-{succinyl[methoxy(polyethylene glycol)2000]}; c) DMG-PEG 2000 1,2-dimyristoyl-rac-glycero-3-methoxypolyethylene glycol-2000; d) Chol-PEG600 Cholesterol-(polyethylene glycol-600)

Conventional phosphate linkers are anionic in nature that can activate the complement system, which is responsible for innate immunity, leading to hypersensitivity reactions, however neutralizing these anionic charges, with cationic groups or methylation has shown to thwart this activation[127]. The costs associated with production of phospholipids is not justified due to proneness to enzymatic degradation by lipases and phospholipases[128–132] that results in their rapid clearance. Consequently, PEG chains conjugated to glycerolipids, sphingolipids and cholesterol shown in Figs 1-9 b-d have been explored as alternatives to PEG-phospholipids. A

study investigating the different lengths of PEGylated ceramides on the circulation times of liposomes concluded that longer acyl chained ceramides (C_{24}) compared to shorter chain ceramides (C_8), had stronger anchoring properties that resulted in longer circulation time and higher drug release rates[133,134].

Cholesterol linked PEG or Cholesteryl-PEG (Chol-PEG) includes cholesterol as the hydrophobic anchor. Due to the lipophilicity, compatibility with other lipids and stabilizing properties, cholesterol is a favourable choice for anchoring PEG chains through ester bonds[128,135,136]. Chol-PEG is found to regulate the membrane fluidity, which helps in adding stability to the bilayer and prevents the leakage of drugs[104]. Additionally, the drug loading efficiency of Chol-PEG is found to be dependent on the percentage of Chol-PEG. Lower Chol-PEG ratios in the formulation could encapsulate more amount of drugs[137–139]. Studies have reported the synthesis of pH cleavable PEG chains by linking Cholesterol through succinate and carbamate linkers[140,141]. Despite its advantages, Chol-PEG demonstrated shorter circulation time than PEG phospholipids. This is because cholesterol anchors deep into the hydrophobic zone of the lipids, counteracting the advantages offered by PEG chains. The addition of extra linkers is proposed to overcome this limitation, however complicates the synthesis process.[104,142].

Furthermore, it is necessary to cleave the PEG chains after the circulation time is achieved to increase the absorption of drugs[141,142]. This is accomplished by attaching linker moieties that either cleave the PEG chains upon the reaching the target site or when exposed to a suitable stimulus such as change in pH, temperature, or in the presence of an enzyme in the cellular microenvironment[143,144]. Some prominent moieties that are used as cleavers include vinyl ether bond, hydrazine bond, disulphide, peptide and ester bonds[145]. Vinyl ether bonds are non-reactive in near neutral and basic conditions that makes them labile in acidic conditions especially under pH < 5[146]. Vinyl ether linked PEG to dioleoyl phosphatidyl ethanolamine

(DOPE) liposomes have demonstrated efficacious release of therapeutic contents post the cleavage of PEG moiety under varying pH conditions [146]. It is also observed these PEG conjugated vinyl ether bonds are cleavable by reactive singlet oxygen generated encapsulated by photosensitizers[141]. Peptide bonds, are cleaved only in the presence of tumor specific enzymes such as matrix metalloproteinases (MMPs)[147–149]. *In-vitro* studies have shown that peptide conjugated PEG lipids have longer circulations times and prefer to accumulate on tumor sites due to the enhanced permeability and retention effect (EPR), which arise from lack of draining in the tumor tissue[147]. For intracellular delivery specific, PEGylated liposomes conjugated with disulfide bonds are desirable[150–152]because the disulfide linkage in nanocarriers gets cleaved in the presence of glutathione, an antioxidant overexpressed in the cytoplasm of cancerous cells. Furthermore, many studies indicate that antibody delivery by cleavable PEG linked by disulfide bond can potentially be used in cancer diagnosis and treatment[150,153,154].

1.3.4 Benefits of PEGylated Liposomes in the clinics:

Based on previous discussions on the composition, properties, and advantages offered by PEGylated it is proven that PEGylated formulations provide shielding effect from macrophages, longer circulation time, preferential accumulation to sites of interests. Due to the substantial research in stealth technology, several PEGylated liposomes have been tested for clinical trials and approved by the FDA for treatment on humans. PEGylated lipids in combination with regular phospholipids and cholesterol have been used in various formulations. The very first PEGylated liposomal formulation to be approved was Doxil®. Doxil®, is an intravenous formulation developed by Sequus Pharmaceuticals, USA in 1995 for the delivery of DOX (doxorubicin) hydrochloride for the treatment of ovarian and breast cancer. This formulation has 5 mol% of phospholipid DSPE-PEG 2000, 39 mol% cholesterol and 59 mol % hydrogenated soy phosphatidylcholine (HSPC) [155–157]. Subsequently, Onivyde™,

which has irinotecan, as the active ingredient, was approved by the FDA for the treatment of metastatic adenocarcinoma. Onivyde™ contains distearoyl-sn-glycero-phosphoethanolamine (DSPC), cholesterol and distearoylphosphatidyl ethanolamine (MPEG-2000-DSPE) in the ratio of 3:2:0.015[158,159].

Several other formulations which contain PEG-Phospholipids and Chol-PEG are currently in different phases of clinical trials. The active ingredient and composition of the formulations has been tabulated below in Table 1-3[160].

Thus, the stealth nature of PEGylated liposomes makes it suitable for encapsulation of a variety of therapeutics. A very interesting recent application of PEGylated lipids is to use it in combination with photopolymerizable lipids. The potential of this work is still not completely explored. The review of several recently published work on the use of PEGylated lipids in conjunction with photopolymerizable lipids are reviewed as follows. Our previous work describes utilization of the PEGylated phospholipid DSPE-PEG2000 to fabricate vesicular morphology to photopolymerizable lipid, $DC_{8,9}PC$ (1,2 bis (tricosa-10, 12-diynoyl)-*sn*-glycero-3-phosphocholine)[161]. $DC_{8,9}PC$ is a polymeric lipid having a tubular morphology. Previously, $DC_{8,9}PC$ has been successively used in combination with DPPC for delivery of HPPH photosensitizer and this technology is patented[162] and promoted by Nano-Red™[163]. It has been recently discovered that the presence of hydrophilic PEG chains is can induce formation of lamellar structure, thus resulting in eliminating the need for the presence of DPPC. The liposomal formulation containing $DC_{8,9}PC$ and DSPE-PEG-2000 in the molar ratio of 90:10 and could encapsulate hydrophobic photosensitizer HPPH [161]. Similarly, another study has investigated the encapsulation of dexamethasone, a potent rheumatoid arthritis drug[164] in this formulation. Both these researches have concluded longer circulation, stealth nature, and preferential accumulation of these formulations in the respective sites of interest in animals.

Table 1-3: FDA approved Formulations involving PEGylated Liposomes

Formulation	Active Ingredient	Composition	Stage	Application	Company
Doxil [155–157]	Doxorubicin	HSPC: Cholesterol: PEG 2000-DSPE (56:39:5 molar ratio	Approved	Ovarian/Breast Cancer	Sequus Pharmaceuticals (1995)
Onivyde [158,159]	Irinotecan	DSPC:MPEG-2000: DSPE (3:2:0.015 molar ratio	Approved	Metastatic adenocarcinoma of the pancreas	Merrimack Pharmaceuticals Inc. (2015)
Thermodox [165]	Doxorubicin	DPPC, Myristoyl stearyl phosphatidylcholine and DSPE-N- [amino (polyethylene glycol)-2000]	Phase 3	Hepatocellular carcinoma	Celsion Corporation
Lipoplatin [166,167]	Cisplatin	DPPG, soy phosphatidyl choline, mPEG-distearoyl phosphatidylethanolamine lipid conjugate and cholesterol	Phase 3	Non-small cell Lung Cancer	Regulon Inc.
S-CKD602 [168,169]	Potent topoisomerase I inhibitor	Phospholipids covalently bound to mPEG	Phase 2	Cancer	Alza Corporation
2B3-101 [164]	Doxorubicin	Glutathione PEGylated liposomes	Phase 1	Solid Tumors	2-BBB therapeutic
MCC-465 [170]	Doxorubicin	DPPC, cholesterol and maleimidated palmitoyl phosphatidyl ethanolamine; immunoliposomes tagged with PEG and the F(ab0)2 fragment of human monoclonal antibody GAH	Phase 1	Metastatic Stomach Cancer	Mitsubishi Tanabe Pharma Corporation

1.4 Photosensitizers and Photodynamic Therapy (PDT)

1.4.1 Conventional Porphyrin based Photosensitizers:

This class of PS molecules have backbone structures made of four pyrroles linked by methine bonds as shown in Fig 1-10. Porphyrinoid molecules absorb strongly at 400 nm (Soret Band) and weakly from 600-800 nm (Q-Band). However, the Q-Band wavelength is preferred for deep-set tumors. Based on the efficacy of these PS, they are divided as first, second and third generation porphyrins[5,6,8]. However, most of the approved porphyrinoid PS makes the skin highly photo sensitive. The evolving research in this field is focused on naturally occurring or synthesizing new PS molecules that have low skin photosensitivity, high target specificity, greater singlet oxygen yield, molecules absorbing in the near-infra red spectrum[5,6,8].

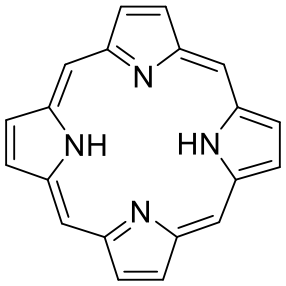

Figure 1-10: Structure of Porphyrin

Table 1-4 lists the commercially available porphyrin compounds[5,6,8] and their absorption wavelengths

Table 1-4: List of Porphyrinoid PS

Compound Name	Commercial Trademark	Absorption Wavelength (nm)
Porfimer Sodium	Photofrin	632
5-Aminoluvenic Acid	Levulan	632
Methyl aminolevulinate	Metvixia	N/A
Hexaminolevulinate	Cysview	N/A
Benzoporphyrin derivative monoacid ring A	Visudine	689
Meta-tetra(hydroxyphenyl)chlorin	Foscan	652
Tin ethyl etiopurpurin	Purlytin	664
N-aspartyl chlorin e6	Laserphyrin, Litx	664
2-(1-Hexyloxyethyl)-2-devinyl pyropheophorbide	Photochlor	665
Palladium bacteriopheophorbide	Tookad	763
Motexafin lutetium (Lu-Tex)	Lutrin, Optrin	732
Aluminum phthalocyanine tetrasulfonate (AlPcS4)	Photosens	676

1.4.2 Alternative Non-Porphyrin based Photosensitizers:

Apart from the porphyrinoid PS, several chromophores have also been found to have phototoxic properties and their potential applications in PDT have been researched upon. Most of these fluorophores are hydrophilic in nature. Table 1-5 lists the various non-porphyrinoid PS which are yet to be approved by the FDA for commercial use. It is interesting to note that most of these PS can be operated in the UV - Visible region[5,6,8].

Table 1-5: Non-porphyrinoid PS and their wavelength

Compound Name	Absorption Wavelength (nm)
Hypericin	590
Methylene blue	666
Toluidine blue	630
Rose bengal	549
Merocyanine 540	556
Curcumin	420

1.5 Hypothesis and Research Needs:

The understanding of the mechanism of binding and internalization of amphiphilic fluorophore probes to cell membranes are very limited. To this end, the use of liposomes as model cell membranes will be useful in predicting the mechanism. It has been demonstrated that, amphiphilic molecules (linked with hydrophobic tail chains[171–173]), have better cellular uptake. Molecules with longer hydrophobic tail chains showed better uptake, due to their ability to penetrate deeper into the cell membrane due to electrostatic[174,175], hydrophobic[42,176,177]and hydrogen bonding mechanisms[178,179]. We hypothesize that the mechanism of binding and internalization of the amphiphilic fluorophores to the surface of negatively charged cancerous cell membrane[180,181] is similar to that of cell penetrating cationic peptides. The peptide hydrophobicity drives the perturbation of the cell membrane. The insertion of the amphiphilic molecule in the phospholipid bilayer results in formation of domains and phase separation of lipids[182]. This is used to predict the degree of internalization of the amphiphilic fluorophores[182,183].

In addition to this, there are not many studies that focuses on the concentration effects of therapeutic molecules on the bilayer. There exists a need to study the effects of concentration

variation and penetration effects of these molecules on the bilayer through a combination of experimental methods. This would provide a validation for the MD simulation and better explanations to predict the mechanistic aspects of permeation and membrane destabilization. The MD simulations can only serve as a supportive data to experimental analysis as it is difficult to predict the changes in *in-vitro* conditions on a computational platform.

Besides, all the major successful liposomal formulations of the previous decade have been presented. Despite the enormous body of work done, formulations for the delivery of photosensitizers remain very marginal. Lipids in combination with sterols and polymers have been employed for increasing the longevity of liposomal formulations. However, the role of concentration and polymer density in the stability of the formulations have not been investigated for the delivery of photosensitizers.

1.6 Objectives of this work:

This dissertation harnesses the versatility of liposomes to act as a model cell membrane and as a carrier for drug delivery to enhance the efficacy of photodynamic therapy using biophysical techniques. The main objectives of this research are as follows:

i. To examine the role of amphiphilicity on novel non-porphyrinoid fluorophore interactions with model cell membranes;
ii. Based on this information, propose mechanisms of cellular penetration and destabilization;
iii. To propose a suitable stable liposomal formulation by optimizing the lipid and polymer composition biophysically for encapsulation of existing hydrophilic and hydrophobic photosensitizers.

In this chapter, a basic introduction to liposomes and the various mechanisms involving liposomes and drug interaction has been addressed. In addition, a review on their role as drug

delivery carriers and the importance of PEGylated liposomes is discussed. Finally, an introduction to photodynamic therapy has been introduced to provide the necessary background for the following chapters.

Chapter 2 provides the discussion on the biophysical techniques used in this dissertation. The parameters, experimental details for the specific instruments at RIT and the other collaborating institutes have been provided.

Chapter 3 focuses on the interactions between amphiphilic amino methyl coumarin with mixed liposomes comprising of zwitterionic dipalmitoyl phosphatidylcholine (DPPC) and anionic dipalmitoyl phosphoserine (DPPS). DPPC/DPPS liposome mixture is used as model cancer membranes. The amphiphilic coumarins (C_n) were designed synthesized with varying alkyl linkage length (n= 5 to 12) represented by C_n. The effect of alkyl chain length on the model cell membrane was investigated using a combination of biophysical techniques. The efficacy of amphiphilic coumarins in liposomal lipid bilayers demonstrates the promise of these molecules as a tool in the treatment of cancer.

In Chapter 4 and chapter 5, the premise of encapsulation of riboflavin to improve its bioavailability and stability while making the clinical applications more efficient has been evaluated. This detailed study on cellular inhibition of liposome encapsulated riboflavin-5-phosphate investigation and the effect of unencapsulated riboflavin on liposome bilayers aims to improve the efficiency of cellular delivery of riboflavin. Cell studies demonstrate high inhibition rates for the liposome encapsulated riboflavin formulations in the presence of blue light, despite the lower encapsulation loading.

Chapter 6 investigates the effects of chain length and molecular weight of polyethylene glycol in liposomal formulations for the delivery of photosensitizer for potential photodynamic therapy applications. Differential Scanning Calorimetry (DSC) studies were performed to

demonstrate the stability of the formulations. The effects of varying ratios of the PEGylated lipids in the phase separation of the bilayer is indicated by the changes in the melting transition profile of the lipids. The effect of encapsulation of hydrophobic photosensitizer HPPH and the impact on the stability of the Lipid Nanoparticles (LNPs) is correlated through the enthalpy and thermotropic transition temperature.

Finally, chapter 7 summarizes and concludes this dissertation with future directions, respectively. In the appendices (Chapter 8), additional supplemental information for chapter 3 and 4 has been provided. Appendix 8.1 includes the characterization data of amphiphilic coumarin derivatives, type-A Isothermal titration calorimetry (ITC) data conducted to study the interaction of amphiphilic coumarin with liposomes and the results of apoptosis assay of amphiphilic coumarin. Appendix 8.2 contains the NMR characterization of riboflavin liposome interaction. Appendix 8.3 lists the journal publications and conference disseminations associated with this dissertation.

2 Methods and Biophysical Techniques

In this chapter, the principles and theory behind various biophysical techniques employed in this dissertation are introduced. The techniques and experimental parameters for each of these are specific to the materials used and the aim of the study and will be explicitly stated in the corresponding chapters.

Biophysical techniques are important to quantify the physicochemical effect on cell membranes in the presence of the foreign molecule. However, there is no one possible technique that can give a complete information on the mechanistic view. A variety of analytical and optical methods are being used to characterize the physicochemical properties and assess the stability of PEGylated liposomes for in vivo studies and clinical trials are summarized. The techniques can be classified according to the information they provide. A variety of biophysical techniques are used in quantification of the interactions which are described as follows.

2.1 Morphological Information:

The influence of drug on the orientation of the lipids in the membrane can be obtained by electron microscopy (EM), Phase contrast microscopy (PCM), atomic force microscopy (AFM) and fluorescence microscopy (FM). Sample preparation in the case of EM and AFM and presence of other dyes in FM can generate spatial and resolution artefacts[184,185].

2.2 Structural Studies:

X-Ray Diffraction (XRD, SAXS, WAXS), Neutron Reflectivity (NR), Nuclear Magnetic Resonance (NMR), Electron Paramagnetic Resonance (EPR), Atomic Force Microscopy (AFM), Fluorescence, Differential Scanning Calorimetry (DSC), Circular Dichroism (CD) are

the techniques that give information on the location of the drug and the changes in the orientation of the lipid molecules in the membrane[184,185].

The use of X-Ray to obtain information on the structural properties is constrained because of the difficulty arising in crystallizing the samples resulting in lack of long-range order[186,187].

NR is preferred for its accurate measurements at the solid water interfaces that is due to the penetration power of neutrons[188,189]. NMR is a powerful technique that gives a complete picture on the orientation, dynamics, and membrane topologies in the presence of a foreign molecules. NMR exploits the protons, C^{13}, N^{15} and P^{31} nuclei to predict the drug-membrane interaction[190–192]. EPR is relatively simple as compared to NMR as it monitors the activity of the drug (such as folding in the case of peptides) in the presence of membranes. However, EPR requires chemical tagging of the peptides which might interfere with the measurements[193,194].

AFM provides in-depth structural characteristics in systems where peptides interactions are considered but does not give any information on the chemical properties of the system. AFM is usually combined with FM to get a complete picture of the membrane-peptide interaction[195,196].

Calorimetric techniques include DSC and ITC (Isothermal Calorimetry). These techniques are extremely sensitive to the changes in the phase transition of the bilayer in the presence of a foreign moiety. The thermographs obtained can give information on the changes in the lipid acyl chain and membrane destabilization due to drug aggregations[197,198].

Circular Dichroism is another technique that predicts the behavior of peptides, proteins, and amino acids in the presence of lipid bilayer. This technique gives information that is useful to predict mechanism of insertions in the bilayer and membrane destabilization[199]. Of the different techniques mentioned above, this research uses Dynamic light Scattering, Fluorescence spectroscopy, UV-Visible spectroscopy, DSC, ITC, NMR, and MD techniques for

understanding the mechanism of interaction between bilayer and molecules. The underlying physics beneath these techniques are elaborated as follows:

2.2.1 Dynamic Light Scattering (DLS):

DLS provides hydrodynamic diameter, polydispersity index, and zeta potential of the liposomal solution as shown in Fig 2-1. A monochromatic light reflected in the liposomal solution gets scattered due to the Brownian motion of the liposomes in the solution[136,200–202]. The motion is related to the diffusion coefficient of the liposomes. Temperature and viscosity of the liposomal solution also influences the size measurement. The diffusion coefficient (D_τ) is related to the hydrodynamic radius (R_H) is given by the stokes-Einstein equation[203]:

$$D\tau = \frac{k_B T}{6\pi\eta R_H} \qquad (1)$$

Where k_B is Boltzmann coefficient (1.380×10^{-23} kg.m^2. s^{-2}.K^{-1}), T is an absolute temperature, and η is the viscosity of the aqueous medium. In addition to the hydrodynamic radius measurements, this technique also generates the poly dispersity index (PDI) of the liposomes which determines the size uniformity of the liposomes.

When an electric field is applied to a liposomal suspension, the liposomes move towards the oppositely charged electrodes of zeta potential measurement cell. The ratio between the velocity of motion of the particles and the electric field is called the electrophoretic mobility (μ_e) which is related to zeta potential (z) by the Henry equation,

$$\mu_e = \frac{2\,\varepsilon z f(k.\alpha)}{3\eta} \qquad (2)$$

Where ε and η are the dielectric constant and the absolute zero-shear viscosity of the aqueous medium. $f(k.\alpha)$is known as "the Henry function", where α is the radius of the particle and k is known as the Debye-Huckel parameter, which represent the thickness of the electrical double layer[201,204].

The zeta potential can be calculated from the electrophoretic velocity of the particles using Helmholtz-Smoluchowski equation-

$$\mu_e = V_p E = \zeta \varepsilon \eta \quad (3)$$

where V_p is the electrophoretic velocity, ζ is the zeta potential, ε is the permittivity, and η is the viscosity of the medium.

Another important parameter that determines the circulation ability of the PEG liposomes is the FALT, which is derived from the zeta potential or surface charge of the liposomes [205–207]. The Zeta potential is measured using the Laser Doppler electrophoresis technique. When PEGylated liposomes are dispersed in water and when voltage is applied, a layer of ions from the solution strongly bind to the liposome surface forming a stern layer. This charged layer induces loose adhesion of ions of opposite charge called the diffuse layer. The two layers combined is called the electrical double layer. The electrical potential measured at the surface of the electrical double layer is called the zeta potential. The FALT measurement is calculated from the slope of the graph of the zeta potential vs Debye-Huckel parameter.

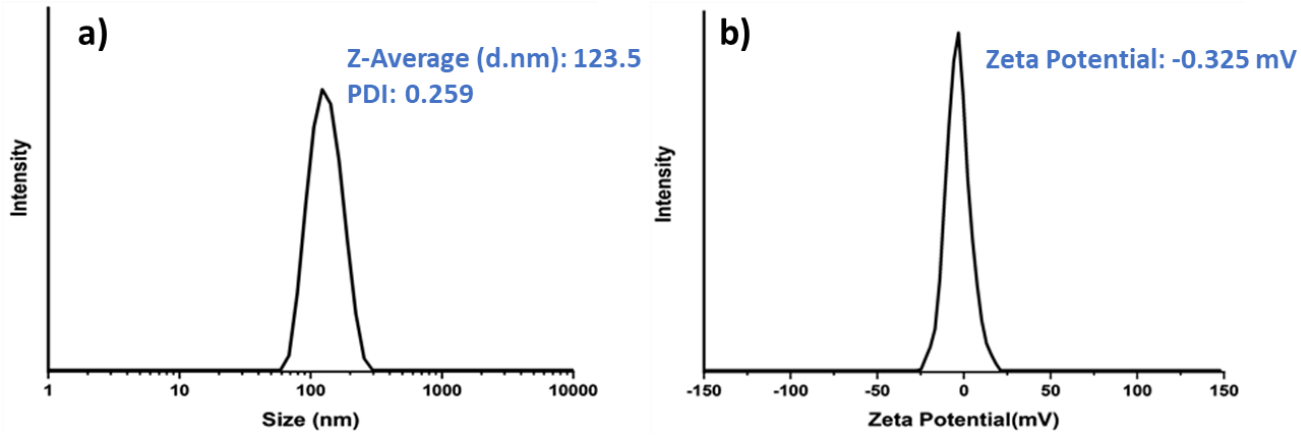

Figure 2-1: Dynamic Light Scattering graphs a) Particle size and distribution b) Zeta Potential

2.2.2 Differential Scanning Calorimetry (DSC):

Differential scanning calorimetry (DSC) is used to gain an insight on the thermal stability and stressed induced in the lipid bilayer due to annealing and presence of peptides, and porphyrin,

non-porphyrin amphiphilic fluorophores[42,136,202,208]. DSC is a thermo-analytic technique that measures the differential heat flow from the reference pan to the sample pan. DSC measures change in c heat capacity (C_p)as a function of temperature. Lipid molecules have characteristic pretransition and melting temperature that is accompanied during their thermal transition from gel to fluid crystalline transition which is endothermic in nature as shown in Fig 2-2. The nature of the thermal transition is affected in the presence of foreign molecules in the lipid bilayer. Change in enthalpy of transition is measured from the area under the melting transition and mathematically represented by the following equation [42,136,201,202,208–210]:

$$\textit{Calorimetric Enthalpy: } \Delta H_C = \int C_P \, dT \qquad (4)$$

The change in shape of the melting peak of the lipids imply the presence of surface bound or encapsulated therapeutic molecules. Additional information on the cooperativity of these molecules can be obtained by computing thermodynamic parameters of the lipid-molecule system[197,198].

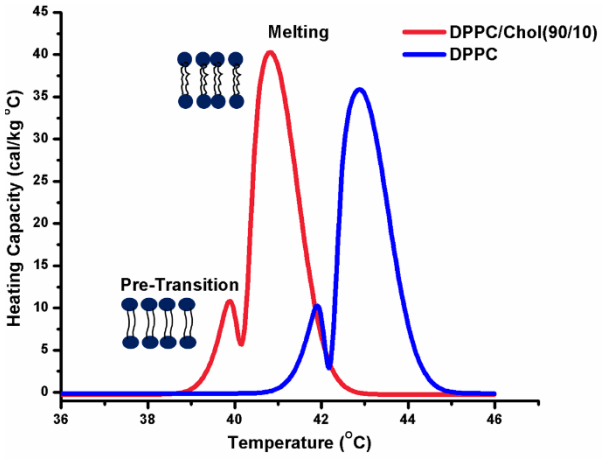

Figure 2-2: DSC thermograph of lipid melting

2.2.3 Isothermal Titration Calorimetry (ITC):

Isothermal Titration Calorimetry (ITC) is a useful technique to study interactions between two molecules in a solution i.e., between a photosensitizer and a liposome. It provides information

on the binding kinetics and the thermodynamic process associated with the interaction[211,212]. Like the DSC, the ITC consists of a sample cell and a reference cell, in addition to the syringe. Typically, two kinds of titrations are performed using an ITC- Type A and Type B. In type A, liposome is in the cell and the photosensitizer (PS) in the syringe. In type B, the PS molecule is in the cell and liposome is in the syringe. The refence cell contains the DI water. As the titrant from the syringe is injected into the cell, heat is released. This heat released in the sample cell is measured and compared with the reference DI water at isothermal conditions. The ITC thermogram shown in Fig 2-3a, is a plot of injection rate vs time. Each spike represents one injection. In the first few injections, the titrant is very less and gets bound to the titrate releasing high heats. As the number of injections increase, the system gets saturated resulting in a sigmoid curve (Fig 2-3 b). The slope of the curve gives the association constant.

The Gibbs Free energy (ΔG) is related to the association constant by,

$$\Delta G = -RT\ lnK_a \qquad (5)$$

$$\Delta G = \Delta H - T\Delta S \qquad (6)$$

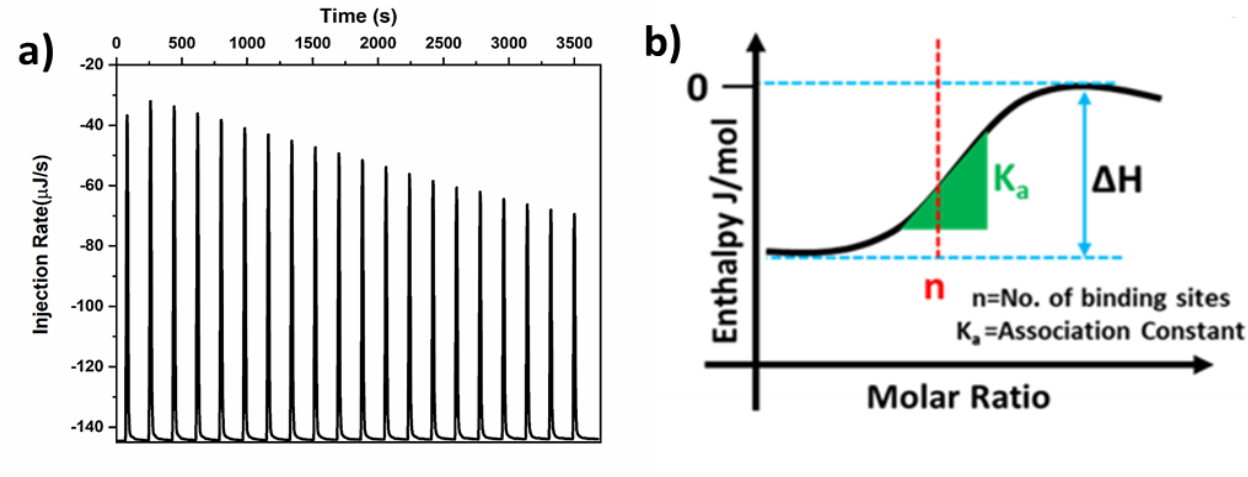

Figure 2-3: Regimes in a PEG coated liposome a) Interdigitated Mushroom; b) Mushroom Regime; c) Brush Regime

Where R and T are the ideal gas constant and temperature, respectively. Since binding is driven by enthalpy and entropy, it is possible to infer the entropy of binding from equation 5 and 6[213–215].

2.2.4 Fluorescence and UV-Visible Spectroscopy:

The two different kinds of spectroscopic characterization are Fluorescence and UV-Visible spectroscopy. Both these techniques operate in the same wavelength range of 200-800nm[216]. Fluorescence spectroscopy is the measure of intensity of emission when the sample is excited at a select wavelength. When a fluorescent molecule is excited, the electron on excitation fall to the ground state with emission of light. This phenomenon is called fluorescence and is exploited in many biomedical applications[217,218]. The property of fluorescence of a molecule changes in the presence of other molecules, with pH and temperature. Change in fluorescence is used to detect lipid bilayer-drug molecule interactions[219]. The absorption and emission spectrum indicate the spatial position of the fluorescent molecule's dipole in the microenvironment, when excited by a polarized light. The subset of the fluorescent molecules that are vertical to the direction of the polarized light absorbs the light and gets excited[220,221]. The resulting emission gives information about the relative position of the fluorescent molecule in the vertical and horizontal planes. Fluorescence anisotropy *(r)* is related to the intensity of emitted light from the horizontal (I_{VH}) and vertical planes (I_{VV}) by[220,221]

$$r = \frac{I_{VV} - I_{VH}}{I_{VV} + 2I_{VH}} \qquad (7)$$

This technique is called fluorescent anisotropy and is used extensively to understand bilayer fluidity and bilayer interactions[221,222].

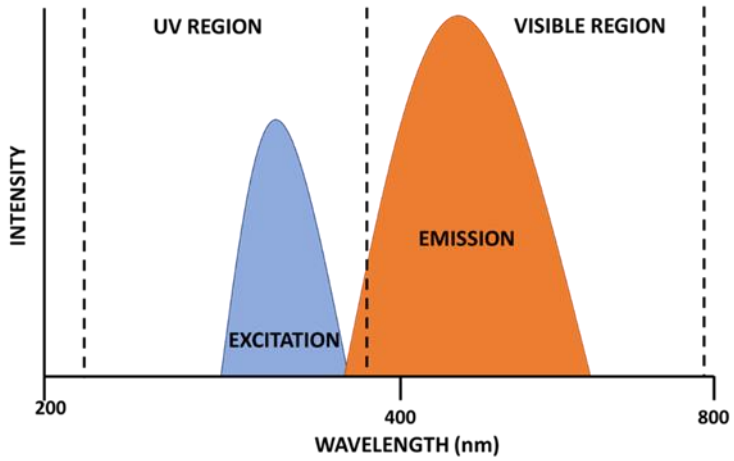

Figure 2-4: Graphical representation of excitation and emission spectra

In the case of UV-Visible spectroscopy, the sample under study, absorbs a photon in the UV-Vis range and gets excited from the ground state to the excited state. This absorbed light is measured as a function of wavelength in the UV-Vis range (200-800 nm)[216]. UV-Vis spectroscopy is used to measure the efficiency of drug encapsulated in the liposomes[223–225].Spectrometers usually have a sample holder a detector and a source of light which provides the light of a wavelength to excite the molecule[201,226].

2.2.5 Nuclear Magnetic Resonance:

NMR relies on the fact that subatomic particles, such as protons and electrons, have a quantum property called nuclear spin, which gives two distinct energy levels when brought into a magnetic field. This nuclear spin causes a small magnetic dipole moment, and the relationship between this magnetic dipole moment and the nuclear spin is characterized by the gyromagnetic ratio. The four most common nuclei to study using an NMR are ^{1}H, ^{13}C, ^{19}F, and ^{31}P. These four nuclei are also classified as having a spin of ½, meaning that the magnitude of their magnetic moments in any given direction has only two equal, but opposite, observable values that correspond to spin quantum numbers equal to +½ and –½ [227,228]. The different kinds of NMR are solvent suppression, One-dimensional NMR, Two-dimensional NMR and Diffusion Ordered Spectroscopy NMR (DOSY-NMR). In this work, proton NMR and DOSY-

NMR were used to understand the interaction between lipids and PS molecules. Proton NMR is the one of the most common types of 1D NMR that can be run. This is because the proton is the most sensitive NMR nuclei, so samples do not need to be very concentrated to produce spectra that have a large signal to noise ratio. As stated before, chemical shifts are a result of the different chemical groups that surround the nuclei in being studied. Proton chemical shifts typically lie within the range of 0-10 ppm and because the shift is dependent on the chemical environment of the proton, they can be used to determine the chemical structure of a sample [229]. Another common type of 1D NMR is ^{31}P NMR. Phosphorous, like proton has a spin of ½ and the ^{31}P nuclei has 100% abundance. While this is promising, the transverse relaxation is accelerated considerably by chemical shift anisotropy meaning that 400 MHz is the best compromise between sensitivity and line broadening caused by chemical shift anisotropy. ^{31}P NMR can be used to identify the presence of Z-DNA or changes in the torsion angles involving phosphate, and can also be used to report on the phosphate backbone [230]. Diffusion ordered spectroscopy (DOSY) is a pseudo 2D experiment and has been developed from earlier 1D pulsed gradient spin echo diffusion NMR as a means to measure the diffusion coefficients of molecules in solution [231]. It is called a pseudo 2D experiment because while the spectrum contains axis like other 2D experiments, the other axis is not another nucleus, but it represents the diffusion axis. Diffusion spectra can be obtained by incrementing the areas of the gradient pulses (q) in PFG-NMR and transforming the NMR signals amplitudes with respect to q2. The result is diffusion ordered NMR spectroscopy (DOSY) [232].

2.3 Computational Study- Molecular Dynamics Simulation:

Molecular Dynamics (MD) is an exhaustive research tool to study the drug induced changes, position, orientation, and effect on surrounding lipids at a molecular level[233,234]. It is a N-body simulations atoms and molecules considering the macroscopic properties such as pressure, temperature, volume, and microscopic properties such as velocities and positions of the system.

These simulations depend on a force field for calculations. The force field is the energy field depicting the motion of atoms and molecules. The total energy involved in the calculation of the force field is the sum of potential and kinetic energies[235,236].

$$E_{total} = E_{Kinetic} + U_{potential} \quad (8)$$

The kinetic energy is calculated from the velocities of the atoms/molecules in a 3-dimensional topology. The potential energy arises from bending, vibrational and columbic interactions in an atom. One such force field used in simulating the interaction of particles is coarse grained (CG) model. The common model used for lipids and proteins is MARTINI. The particle is categorized under one of the four types based on the chemical groups present: Q-Charged, P-Polar, N-Nonpolar and C-Apolar. The subtypes in each of the main type are divided based on the hydrogen bonds and polarities (acceptor, donor, both, none). The MARTINI model is based on a four-to-one mapping scheme, where four heavy atoms and their associated hydrogen atoms are combined into a single CG site[233–235,237]. The output of the MD simulations comes in the form of ensemble of frame. Time dependent ensemble is called trajectory, which is further divided into canonical, micro-canonical and isothermal-isobaric ensemble. In a canonical ensemble, number of atoms (N), volume(V), and temperature are fixed. In microcanonical ensemble no exchange of mass, volume and temperature is allowed and isolated. In an isothermal and isobaric ensemble, both temperature and pressure are fixed[234]. However, MD does not give accurate results due to the assumptions made in the force field methodology and smaller relaxation times in the simulations[184] and hence is used as a validation tool only.

2.4 *In-Vitro* Studies:

Any biophysical study requires a practical validation. This is accomplished by *in-vitro* studies. *In-vitro* studies is the study on isolated cells and tissues from an organism.

2.4.1 Cell culture:

Cancer cells of known origin in a cell culture flask with Dulbecco's modified Eagle's medium (DMEM) supplemented with 10% Fetal Bovine Serum (FBS), Streptomycin/Penicillin/Fungizone (SPF), Glutamine, Pyruvate) for 24 hr. After 24 hr., the cells were removed and washed with 0.25% (w/v) solution of Trypsin- 0.53 EDTA to remove residual traces of the medium. This was followed by addition of the cell culture serum to 24 well cell culture plates and 200 µl of molecules of interest. The cells were incubated for 4, 24 and 48 hr. at 37 °C at 5% CO_2.

2.4.2 MTT Assay:

To evaluate the toxic nature of molecules of interest, at the mentioned time intervals, 50 µl of 5 mg/ml MTT reagent without phenol red was added to the wells. On incubation for 6 hr, crystals were formed due to the metabolism of the living cells. The residual media was removed, and the formed crystals were dissolved in Isopropanol/10% Triton/0.1 N HCl mixture. The samples were placed in an EL 340 Bio Kinetics microplate reader spectrophotometer (Bio-Tek Instruments, Winooski, VT) and the absorbance of the samples were measured at 540 nm from which the inhibition percent was calculated. This procedure for cell culture and MTT assay has also been reported elsewhere[238–240]. No phenol red was used in the cell culture preparation consistent to our previous works[238–240].

2.4.3 Apoptosis Assay:

e-Bioscience™ Annexin V Apoptosis Detection PE and 7-AAD Kits for flow cytometry were used to measure early and late-stage apoptosis in cancer cells of known origin. The treated cells were collected and washed with ice-cold phosphate buffered saline (PBS) followed by cells resuspension in 100 µl of 1X Annexin V binding buffer on an ice-cold bath. 5 µl of Annexin V was added to the 100 µl of cell suspension and incubated for 10-15 mins at room temperature. Next, the cells were washed with ice-cold PBS and resuspended in 200 µl of 1X binding buffer.

Then, 5 µl of 7-AAD viability staining solution was added to the cell suspension. Finally, flow cytometry was used to detect the fluorescence of stained cells at excitation/emission maxima: Annexin V PE® : 499/521 nm; 7-AAD® : 535/617 nm with *BD FACSAria IIu High-Speed Cell Sorter* flow cytometer from BD Biosciences (Becton-Dickinson, San Jose, CA, USA).The data were viewed and analyzed using FlowJo v10.2 software from FlowJo LLC (Ashland, OR, *USA).*

3 Interaction of Amphiphilic Coumarin with DPPC/DPPS Lipid Bilayer: Effects of Concentration and Alkyl Tail Length

---

This chapter was originally published in ***Phys. Chem. Chem. Phys.***, 2020,**22**, 15197-15207 by Poornima Kalyanram, Huilin Ma, Shena Marshall, Christina Goudreau, Ana Cartaya, Tyler Zimmermann, Istvan Stadler, Shikha Nangia, Anju Gupta. In addition to the published work, this chapter also contains ITC modelling. In this work, interactions between amphiphilic amino methyl coumarin with dipalmitoyl-sn-glycero-3-phospho*choline*/dipalmitoyl-sn-glycero-3-phospho*serine* (DPPC/DPPS) lipid bilayer were investigated. A combination of experimental techniques (zeta potential, fluorescence spectroscopy, differential scanning calorimetry) along with molecular dynamics simulations was employed to examine the influence of alkyl tail length and concentration of the amphiphilic coumarin on the lipid bilayer. Alkyl tails comprising of 5(C_5), 9(C_9), and 12(C_{12}) carbon atoms were conjugated to amino methyl coumarin via a single-step process. The binding and insertion mechanisms of the amphiphilic coumarins were studied in increasing concentrations for short-tailed (C_5) and long-tailed (C_{12}) coumarins. The simulation results show that C_5 coumarin molecules penetrate the lipid bilayer, but owing to the short alkyl tail, they interact primarily with the lipid head groups resulting in lipid bilayer thinning; however, at high concentrations, the C_5 coumarins undergo continuous insertion-ejection from the outer leaflet of the lipid bilayer. On the contrary, C_{12} coumarins interact favorably with the hydrophobic lipid tails and lack the ejection-reinsertion behavior. Instead, the C_{12} coumarin molecules undergo flip-flops between the outer and inner leaflets of the lipid bilayer. At high concentrations, the high-frequency flip-flops lead to lipid destabilization, causing the lipid bilayer to rupture. The simulation results are in excellent agreement with the toxicity of amphiphilic coumarin activity in cancer cells. The efficacy of

amphiphilic coumarins in liposomal lipid bilayers demonstrates the promise of these molecules as a tool in the treatment of cancer.

3.1 Introduction

Coumarin is a well-known, naturally occurring fluorescent compound belonging to the benzopyrone class.[241] It is well-studied for its anti-tumor and anti-inflammatory activities.[242–244] Besides, derivatives of coumarin are of interest due to the high quantum yield, intense fluorescence bandwidth and sensitivity, resistance to photochemical degradation and bio-compatibility.[245–248] They find applications in bio-imaging as fluorescent dyes and probes and as chemical sensors.[249–252] There have been numerous coumarin derivatives namely 7-hydroxycoumarin, linear and angular pyranocoumarins, 6-7-dihydroxycoumarin, 7-methoxycoumarin, aminocoumarins that have been investigated for both their diagnosing and curative properties.[253–257] Out of these derivatives, 7-amino-4-methylcoumarin (AMC) is of importance because of the presence of electron donating amino group in the 7th position, [253,258] which can donate electrons and acts as fluorescence enhancers for probing applications with longer wavelengths and improved intensity.[259,260] The ability of 7-amino-4-methylcoumarin to function as a therapeutic and diagnostic fluorophore probe in the treatment of cancer is of paramount interest in this study.

It has been demonstrated that amphiphilic fluorophore probes (linked with hydrophobic tails[171–173]) have better cellular uptake. Probes with longer hydrophobic tails showed better uptake, due to their ability to penetrate deeper into the cell membrane due to electrostatic,[174,175] hydrophobic,[42,176,177] and hydrogen bonding interactions.[178,179] Most common hydrophobic groups include alkyl,[42,208,261] acyl,[262,263] or prenyl chain.[264–266] We hypothesize that the mechanism of binding and internalization of these amphiphilic fluorophores to the surface of negatively charged cancerous cell membrane[180,181] is like that of cell penetrating cationic

peptides. Most amphiphilic cationic peptides have reported to disrupt the cell membrane offering a therapeutic promise.[42,267–269] The cationic peptide binds to the anionic phospholipid head group of the cell membrane through electrostatic interaction.[42,208,270] Further, the peptide hydrophobicity drives the perturbation of the cell membrane. The insertion of the amphiphilic molecule in the phospholipid bilayer results in formation of domains and phase separation of lipids.[182] This is used to predict the degree of internalization of the amphiphilic fluorophores.[182,183]

In this study, 7-amino-4-methyl-coumarin was conjugated with hydrophobic alkyl tails of lengths 5, 9 and 12 are represented as C_5, C_9, C_{12}, respectively. A mixture of 1,2-dipalmitoyl-sn-glycero-3-phosphocholine(DPPC))/1,2-dipalmitoyl-sn-glycero-3-phosphoserine (DPPS) in 85:15 ratio was used to model the liposomal lipid bilayer to study the binding and internalization of the newly designed amphiphilic coumarin fluorophores. To understand the interaction of these fluorophores with liposomal lipid bilayer, the fluorophores were added to the preformed liposome. This approach is in alignment with our previous works.[42,136,208] The encapsulation of these probes are being investigated for future dissemination, however it is beyond the scope of this work.

The binding of the fluorophores to the lipid head groups was investigated using Zetasizer and Spectro fluorometer and Isothermal Titration Calorimetry (ITC). Differential scanning calorimeter (DSC) was used to observe the temperature induced phase transitions in the lipid bilayer. Preliminary cytotoxicity assays were conducted using human bladder carcinoma cell lines to test the efficacy of the amphiphilic coumarin for potential cancer applications. In addition, coarse grained molecular dynamics (CGMD) simulations were performed to determine the mechanism of perturbation in the lipid bilayer in the presence of fluorescent probes with respect to the alkyl tail lengths at varying concentrations. It is observed that the

(i) fluorophores bind to the lipid bilayer through electrostatic attraction and insert into the bilayer by means of their alkyl tails and (ii) the degree of insertion of the fluorophore is dependent on the alkyl tail length and its movement across the bilayer is concentration dependent.

3.2 Experimental Methods

3.2.1 Materials and Methods

3.2.1.1 Synthesis and Characterization of Amphiphilic Coumarin

All reagents were purchased from Sigma Aldrich without further purification. Dichloromethane solvent purification was conducted according to Purification of Laboratory Chemicals 2nd ed. (Perrin, D. D., Armarego, W. L. F. and Perrin, D. R., Pergamon Press: Oxford, 1980). Reactions were monitored by thin layer chromatography (TLC) supplied by EMD Millipore Corporation, Merck (Germany). Visualization was accomplished with UV light.

3.2.1.1.1 Synthesis:

An oven-dried round bottom flask equipped with a stir bar was charged with 7-amino-4-methylcoumarin (1.0 equiv), 10 mL of dichloromethane, and the anhydride (2.2 equiv). The solution was stirred at room temperature for 48 hours and monitored by TLC. The solution was diluted in 15 mL of dichloromethane and washed with 3x 10 mL aliquots of 1M NaOH. The organic layer was dried with $MgSO_4$, filtered, and concentrated *in vacuo* to give the product as summarized in Figure 3-1. The resulting C_5 product was compared with previously reported characterization data[271] and the chemical structure of C_9 and C_{12} products were fully characterized.

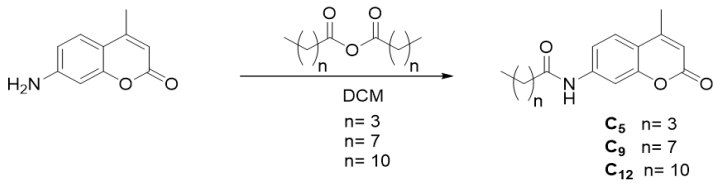

Figure 3-1: Synthesis of alkyl tail conjugated coumarin molecules of lengths: C_5, C_9 and C_{12}

3.2.1.1.2 Characterization of Amphiphilic Coumarin:

The resultant white solid at 90% yield substance was characterized using ^{1}H NMR and ^{13}C NMR in d-DMSO at room temperature on Bruker 300 and 500 instruments. The chemical shifts (δ) were recorded in parts per million (ppm). The infra-red (IR) spectra were recorded on Shimadzu FT-IR Prestige-21 spectrometer using attenuated total reflectance (ATR) method. High-resolution mass spectra (HRMS), shown in Figure 8-5, was obtained from University at Buffalo Mass Spectrometry Facility.

3.2.2 Preparation and Characterization of liposomes:

The DPPC and DPPS lipids were purchased from Avanti Polar Lipids (Alabaster, AL). The DPPC/DPPS (85/15 mol%) liposomes of 10 mM concentration were prepared using the steps reported by Gupta et al.[42] *Invivogen* endotoxin free water maintained at 45°C (average weighted melting temperature of DPPC and DPPS lipids that constituted the lipid bilayer) used to the thin dry film of lipids to form liposomes. The liposomes were extruded through 100 nm polycarbonate membranes to obtain unilamellar liposomes. The extruder was kept on a hotplate and maintained at 45°C during the extrusion process. Amphiphilic coumarin fluorophores were suspended in DMSO (99.9%, Fisher chemicals) at 5- and 25- mM concentrations. The amphiphilic coumarins were added to the preformed liposomes at 25°C and the ratio of liposomes to fluorophores were maintained at a ratio of 2:1 by volume.

3.2.3 DLS and Zeta Potential measurements:

The DLS and zeta potential experiments were recorded using Zetasizer nano-series (Malvern Nano-ZS). The size distribution of the liposomes was obtained by placing 1 ml of sample in SARSTEDT polystyrene cuvettes at 25°C and at a 173° backscatter angle with 120 s equilibration time. The size of the DPPC/DPPS liposomes was measured to be 118±2 nm. The zeta potential measurements were made using DTS1070 folded capillary cells. The fluorophores were added to the liposomes and the zeta potential was measured at 37°C (physiological temperature), 43°C (melting transition of DPPC) and 55°C (melting transition of DPPS). The zeta potential of the liposomes in the absence of the fluorophores was also measured under the same conditions.

3.2.4 Fluorescence Spectroscopy:

The fluorescence experiments were carried out in a Shimadzu spectrofluorometer (RF-5301 PC) equipped with a xenon lamp as the light source. The intensities were measured at excitation wavelength of coumarin at 350 nm over the range of melting temperatures (37°C, 43°C, and 55°C). The temperatures were controlled using Fisher Scientific Isotemp® water bath.

3.2.5 Differential Scanning Calorimetry:

DSC studies were performed on a Q-2000 TA instrument DSC in T-zero Hermetic pan. The phase behavior of the lipid bilayer in the presence of these fluorophore was studied at 5 mM and 25 mM. About 20 mg of sample was sealed using a sample press and were subjected to five continuous cycles of annealing in the range of 25 to 75 °C at the rate of 5 °C /min, under ultra-pure nitrogen environment at 40ml/min.

3.2.6 Isothermal Titration Calorimetry:

ITC studies were performed in a TA instrument Affinity-ITC. The temperature of the cells was maintained at 25°C. Both the liposome solution and C_9 solution was degassed. The period

between two successive titrations was typically 200 sec. The experiments were performed, and the resulting curves and thermodynamic parameters were calculated with the Nanoanalyze™ software (TA instruments inc.,). The two different types of titration and the concentrations of the solutions are as follows:

i. Type A: C_9 solution in the syringe (0.5 mM), liposome suspension in the cell (0.05 mM and 0.025 mM);
ii. Type B: Liposome suspension in the syringe (5 mM), C_9 solution in the cell (0.50 mM and 2.5 mM).

3.2.7 Molecular Dynamics Simulations

A four-to-one Martini coarse grain (CG) mapping approach[272] was adopted for C_5 and C_{12} coumarin fluorophores. Based on the atomistic structure, CG beads were assigned (Figure 2) PyCGTOOL was used to generate the CG models and the force field parameters for C_5 (Table S1) and C_{12} (Table S2) as well as their related topology files. The PyCGTOOL automates the process of generating the CG equilibrium parameters and force constants from atomistic molecular simulations, which significantly improves the reliability and quality of CG models,[273] The CGMD simulations of C_5 and C_{12} molecules in contact with 85:15 DPPC/DPPS lipid bilayer was performed using GROMACS MD package (version 2018.1).[274,275] A 10×10 nm^2 patch of lipid bilayer was built with 166 DPPC/29 DPPS (MARTINI_v2.0) in both leaflets of the bilayer.[276] A total of eight systems were generated, including a control (no coumarin) and seven other concentrations of C_5 and C_{12} (Table 3-1) coumarins. We have used the naming convention C_i-*j*, where *i* = 5 for 12 for coumarin chain length and *j* is the number of coumarin

molecules in the system. The remainder of the simulation box was solvated with explicit standard MARTINI water. Periodic boundary conditions were applied in the three dimensions.

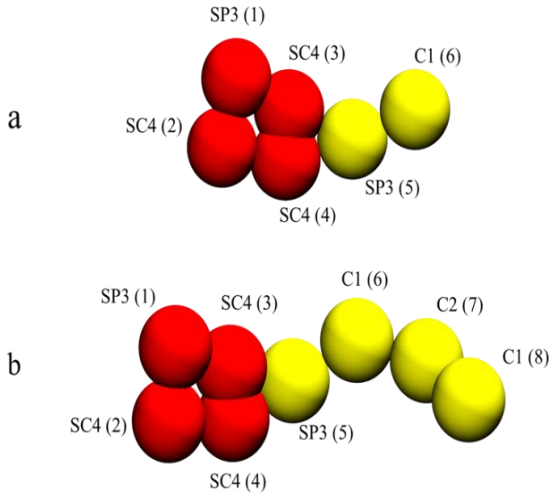

Figure 3-2: MARTINI CG mapping and bead types for (a) C_5 and (b) C_{12} coumarin. Color scheme: Head groups (red) and alkyl tails (yellow). Numbers in the bracket indicates the index of the beads used in Tables 8-1 and 8-2

A flat-bottomed position restraint was applied in the *z*-direction to prevent coumarin molecules from crossing periodic boundary and interacting with the inner leaflet.

Energy minimization was performed using the steepest-decent algorithm[276] until the maximum force on any bead was below the tolerance parameter of 10 $kJmol^{-1}nm^{-1}$. The isothermal-isochoric *NVT* and isothermal-isobaric *NPT* equilibration runs were performed for 20 ns. A semi-isotropic pressure coupling was used, and the systems were maintained at 1 bar using the Berendsen barostat[276] with time constant, τ_p = 4.0 ps. The temperature was maintained at 323 K by independently coupling the coumarin, DPPC/DPPS lipids and the solvent to an external thermostat with τ_T = 1.0 ps.[276] The neighbor list was updated every 25 steps using 1.4 and 1.2 nm for short-range van der Waals and electrostatic cutoffs, respectively. The production *NPT* simulations were performed for 8 μs using a 20-fs time step. Molecular visualization and graphics were generated using visual molecular dynamics (VMD) software.[277]

Table 3-1: System details of Coumarin simulations

Systems	Number of molecules in the system			
	Coumarin (C_5 or C_{12})	DPPC	DPPS	Water
Control	-	332	58	8376
C_i-42	42	332	58	8376
C_i-74	74	332	58	10140
C_i-106	106	332	58	10140
C_i-138	138	332	58	10140
C_i-166	166	332	58	10140
C_i-184	184	332	58	10140
C_i-209	209	332	58	10140

3.2.8 Cytotoxicity Studies: MTT Assay

Human bladder carcinoma cells HT-1376 (American Type Culture Collection (ATCC) no. CRL1472) were grown in a cell culture flask with Dulbecco's modified Eagle's medium (DMEM) supplemented with 10% Fetal Bovine Serum (FBS), Streptomycin/Penicillin/Fungizone (SPF), Glutamine, Pyruvate) for 24 hr. After 24 hr, the cells were removed and washed with 0.25% (w/v) solution of Trypsin- 0.53 EDTA to remove residual traces of the medium. This was followed by addition of the cell culture serum to 24 well cell culture plates and 200 µl of amphiphilic coumarin molecules dispersed in DMSO. Pure DMSO was used as negative control. The cells were incubated for 4, 24 and 48 hr. at 37 °C at 5% CO_2. To evaluate the toxic nature of these probes, at the mentioned time intervals, 50 µl of 5 mg/ml MTT reagent without phenol red was added to the wells. On incubation for 6 hr., crystals were formed due to the metabolism of the living cells. The residual media was removed, and the formed crystals were dissolved in Isopropanol/10% Triton/0.1 N HCl mixture. The samples were placed in an EL 340 Bio Kinetics microplate reader

spectrophotometer (Bio-Tek Instruments, Winooski, VT) and the absorbance of the samples were measured at 540 nm from which the inhibition percent was calculated. This procedure for cell culture and MTT assay has also been reported elsewhere.[238–240] No phenol red was used in the cell culture preparation consistent to our previous works.[238–240]

3.3 Results and Discussion

3.3.1 Characterization of amphiphilic coumarin

C_9 amphiphile: The C_9 molecule was fully characterized using ^{1}H NMR and ^{13}C NMR techniques. The results of these techniques are reported in the appendix section (Figures 8-1 and 8-2).

C_{12} amphiphile: The FTIR spectra of the C_{12} amphiphile (Figure 3-3) showed two prominent peaks at 2916 cm^{-1} and 1681 cm^{-1}, respectively. The peak at 2916 cm^{-1} corresponds to C-H stretch[278] which confirmed the presence of alkyl tails, and the peak at 1681 cm^{-1} represents carbonyl group (C=O) inferring the linkage of the alkyl tail to coumarin.[279] This was further confirmed by ^{1}H NMR and ^{13}C NMR studies (Figures 8-3 and 8-4). The ^{1}H NMR and ^{13}C NMR showed characteristic peaks and the suitable chemical shifts (δ) are tabulated in Table 3-2. This confirmed the conjugation of the alkyl tails by carbonyl linkage (atom number (12) =179.8) to the aminocoumarin molecule. The following abbreviations were used to explain the multiplicities: s = singlet, d = doublet, t = triplet, q = quartet, br = broad, m = multiplet, and coupling constants (J) are reported in Hertz (Hz).

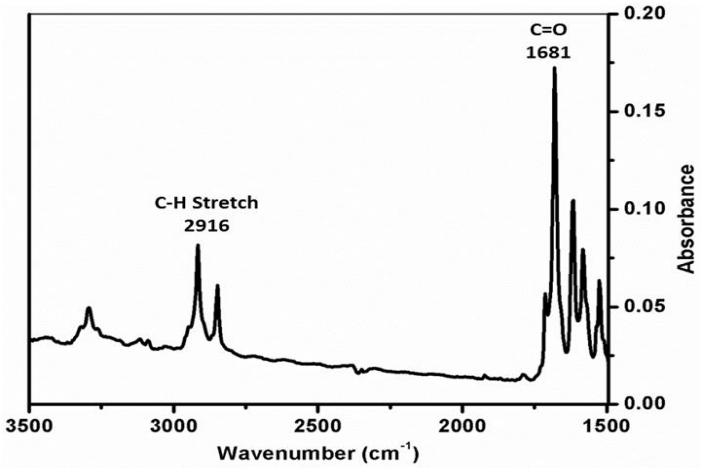

Figure 3-3: FTIR spectra of the C_{12} coumarin amphiphiles

Table 3-2: NMR data for C12 amphiphile

Atom Number	^{13}C (δ)	^{1}H (δ)
1	160.8	-
2	112.5	6.25 (s, 1H)
3	19.4	2.39 (s, 3H)
4	152.7	-
5	115.2	-
6	124.3	7.88 (d, J = 1.8 Hz, 1H)
7	118.3	7.77 (m, 2H)
8	138.1	-
9	111.9	7.45 (m, 2H)
10	154.8	-
11	-	10.31 (s, 1H)
12	179.8	-
13	38.3	2.34 (t, J = 8 Hz, 2H)
14	25.6	1.63 (m, 2H)
15	28.6	1.23 (m, 16H)
16	28.9	1.23 (m, 16H)
17	29.6	1.23 (m, 16H)
18	29.3	1.23 (m, 16H)
19	29.3	1.23 (m, 16H)
20	29.3	1.23 (m, 16H)
21	31.9	1.23 (m, 16H)
22	22.7	1.23 (m, 16H)
23	14.1	0.85 (t, J = 6.5 Hz 3H)
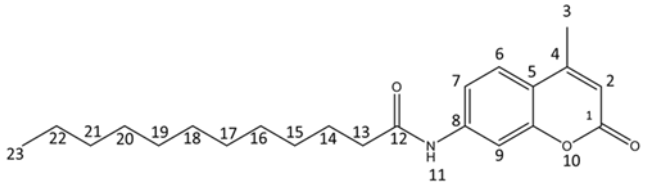		

3.3.2 Electrostatic binding and aggregation of amphiphilic coumarin on DPPC/DPPS liposomes

The zeta potential of the various sample was recorded at 37°C (the physiological temperature) and 43°C and 55 °C (the melting temperatures of DPPC and DPPS lipids respectively). The control studies of pure zwitterionic DPPC liposomes reported a zeta potential values as 0.022±0.03 mV and 0.015±0.009 mV for DPPC at 37°C and 43°C, respectively. DPPC lipid has both negative and positive charges in the headgroup, rendering the surface charge of the liposome neutral. Hence, DPPC liposome was taken as a negative control.

The zeta potential of Pure DMSO and all the amphiphilic coumarin compounds suspended in DMSO were recorded to be -8.89 mV and 7.79±1.4 mV at all the above-mentioned temperatures.

At 43°C, the zeta potential of the neutral DPPC liposomes, in the presence of C_5 increased to 6.93±0.02mV, with C_9 increased to 6.78±0.10 mV and with C_{12} increased to 7.45±0.30mV. Since there was no significant change in the zeta potential of the DPPC liposomes (negative control), an absence of electrostatic binding was concluded with the neutral liposome.

The zeta potential of DPPC/DPPS liposomes were recorded as -7.20 mV at 37°C, −8.3 mV at 43°C and −28.1 mV and 55°C. The apparent change in zeta potential from 43° to 55 °C is attributed to the negative PS (phosphoserine) group of DPPS lipid. At 55 °C, the DPPC lipids headgroups tilt owing to the tail fluidity which further exposed the negatively charged moiety on the phosphate groups of DPPC lipids thereby altering the surface charge density.[280–282]

The change in zeta potential of liposomes in presence of C_5, C_9 and C_{12} at 37 °C (yellow) 43 °C (blue) and 55 °C (red) is shown in Figure 3-4. The measured zeta potential of DPPC/DPPS increased with addition of lower concentration (5mM) of amphiphilic coumarin and temperature of measurement. In the presence of C_5, the zeta potential yielded, 0.095 mV at

37°C, 0.14 mV at 43°C and increased to 0.22 mV at 55°C. Similarly, with C_9, the zeta potential of the liposomes was observed to be 0.242 mV at 37 °C and 0.247 mV at 43°C, which increased marginally to 0.257 mV at 55°C. On addition of C_{12} at 5 mM, a slight increase in zeta potential was recorded at 0.268 mV, 0.272 mV and 0.28 mV at 37 °C, 43°C and 55°C, respectively. The change in the negative zeta potential of DPPC/DPPS liposomes to a positive potential in the presence of amphiphilic amino coumarin fluorophores confirms the electrostatic binding between the amino coumarin derivatives and the lipid headgroups. The amphiphilic coumarin molecules were suspended in DMSO before being added to the preformed liposomes. The pKa of the amide moiety of the coumarin DMSO was approximated to 21.6.[283] Upon addition, this amide proton bonded with the negative groups on the lipids through hydrogen bonding that altered the pKa environment of the amide proton to 15.6,[283] because the liposomes were prepared in DI water. It is postulated that this deviation from a less acidic environment of DMSO to proton rich DI water resulted in the stabilization of the amide proton and aided in the binding of the amino coumarin probes to the lipid headgroups.

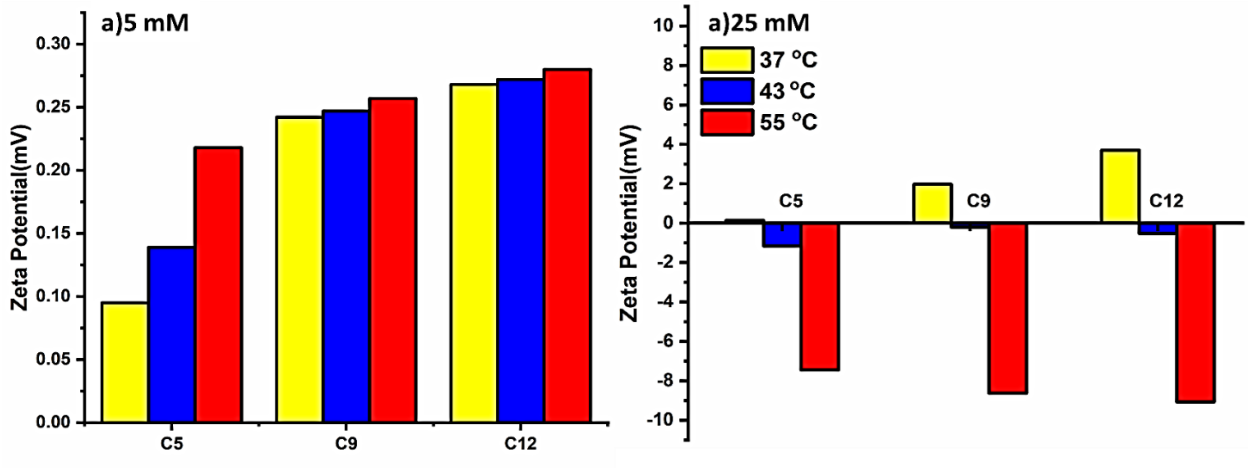

Figure 3-4: Zeta Potential plots representing the interaction of fluorometric probes of a) 5 mM concentration and b) 25 mM concentration with DPPC/DPPS liposomes at different temperatures. Y-axis represent the change in the zeta potential of DPPC/DPPS liposomes in the presence of C_5, C_9 & C_{12} fluorophores (x-axis)

This trend was also observed at 37°C for 25mM (Figure 3-4b) amphiphilic coumarin added to DPPC/DPPS liposomes (C_5=0.15Mv, C_9=1.98mV & C_{12}=3.75mV). However, when measured at 43°C and 55°C, the increased zeta potential was on the negative scale. The zeta potential of the liposomes with C_5 was measured to be −1.16 mV at 43 °C which decreased to −7.45 mV at 55°C. Similarly, with C_9, the zeta potential of the liposomes was observed to be 0.206 mV at 43°C which decreased to −8.63 mV at 55°C. With C_{12}, the zeta potential values again decreased with temperature and were found to be -0.524 mV and -9.08mV at 43 °C and 55 °C, respectively. This was mainly because at increased concentration of amphiphilic coumarin, molecules exceed the critical aggregation concentration and began to aggregate.[284,285] This aggregation behavior of amphiphilic coumarin molecules is attributed to the electrostatic attractions between aromatic rings and overlapping of the benzopyran rings.[286,287] In case of C_5, formation of strong intermolecular hydrogen-amide bonding results in parallel displaced structures that tend to form C_5 clusters due to their the shorter alkyl tail,[50,51] causing lesser individual molecules to bind on the liposomes. With respect to C_{12}, the aggregation is lower due to the longer tails that may hinder the stacking of the rings.[288,289] Furthermore, the C_{12} may be inserting themselves into the bilayer as opposed to being bound on the surface, due to increased lipid fluidity at melting temperature of lipids.[290] Thus, as the lipid bilayer permeability increases, the agglomerated fluorophore molecules enter the hydrophobic tail region. This reduced the surface charge on the liposomes, lead to a negative zeta potential.

The aggregation effects of electrostatic binding were further confirmed by fluorescence spectroscopy shown in Figure 3-5. For unconjugated coumarin the excitation and absorption wavelength were noted as 350 nm and 420 nm in DMSO at 55°C, and 389.5 nm for C_5 and C_{12} at 5 mM concentration in DMSO. The emission spectra of 5 mM C_5, C_9 and C_{12} in DMSO (shown in black, red, and blue dotted lines in Figure 3-5a.) had an absorption wavelength (λ_{max}) of 386.5 nm. When added to pre-formed liposomes, absorption spectrum of C_5 showed a shift

towards higher wavelength (red shift) to 391.3 nm, C_9 to 395nm and C_{12} (black, red and blue line resp. in Figure 3-5a.) showed a red shift to 424.6 nm. The red shift in fluorescence of the C_5, C_9 and C_{12} in the presence of liposomes, which is the characteristic of amino coumarins, indicated the electrostatic binding and insertion of the C_5, C_9, and C_{12} in the lipid bilayer.[219]

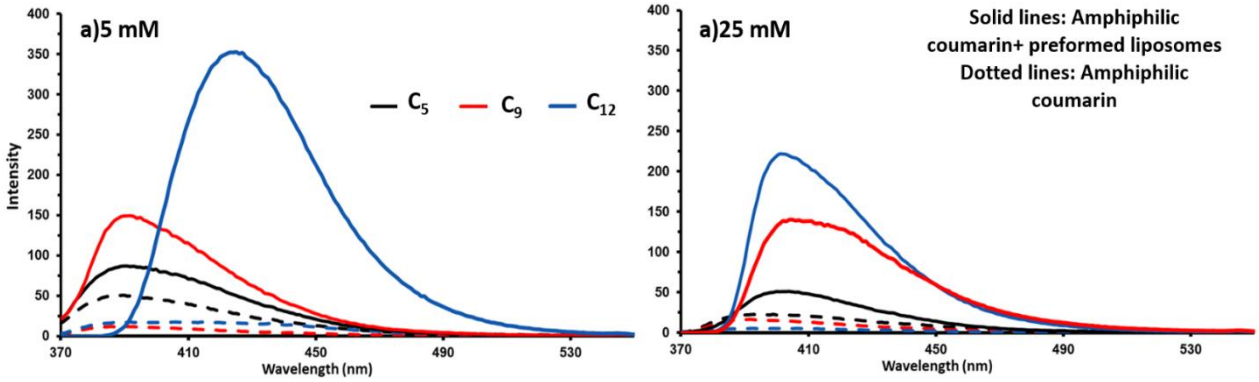

Figure 3-5: Fluorescence spectroscopy of amphiphilic fluorometric probes at 55 ^{O}C

Shift in fluorescence occurred when the coumarin moieties experience a change from polar to non-polar environment, indicating the insertion of the coumarin molecules in the bilayer.[219] The magnitude of shift in fluorescence was more in C_{12} as compared to C_5 and C_9 because of the longer alkyl tails that forms intermolecular hydrogen bonds with the lipid alkyl tail regions.[178,179] At 25mM concentration of amphiphilic coumarin (Figure 3-5b.), the intensity of fluorescence was halved due to fluorescence quenching as a result of aggregation[291–294] . The inner filler effects have not been considered in this work and being investigated for future dissemination.

3.3.3 The Effect of amphiphilic coumarin on DPPC/DPPS lipid bilayer Phase Transition

The melting temperatures of pure DPPC and DPPS were reported as 41 °C and 53 °C respectively[42] . Amphiphilic coumarin showed a melting temperature between 150-175 °C as opposed to unconjugated coumarin (melting ~ 230 °C). This is because the presence of alkyl

tails in the coumarin molecules resulted in a shift in the melting transition. The range of melting of amphiphilic coumarin was beyond the lipid transition temperature.

The thermogram of DPPC/DPPS (85/15 mol%) showed 3 transition peaks - a DPPC rich peak at 42.5°C, a mixed peak at 49.35 °C and a DPPS rich peak at 57.4 °C [201] (refer to Figure 8-8 in the supporting information for DSC thermogram).

To understand the effect of DMSO on the phase transition of the DPPC/DPPS (85/15 mol%), pure DMSO (1 mol%) was added to the preformed liposomes prior to DSC. In the presence of DMSO, a single broad peak was recorded (refer to Figure 8-8 in supporting information for DSC thermogram). This is because, at lower concentrations, DMSO helps in better mixing of the lipids. It has also been demonstrated that DMSO does not disturb the bilayer conformation at lower concentrations.[295,296]

Figure 3-6 represent the DSC thermograms of DPPC/DPPS liposomes in the presence of 5 and 25 mM of C_5, C_9, C_{12} at heating scans 1 and 5. In heating scan 1 (Figure 3-6a), it was observed that on addition of 5 mM of C_5 to the liposomes, a the DPPC-rich transition disappeared and a peak was observed at the mixed domain regions 52.7 °C as compared to the thermogram devoid of fluorophores. The peak associated with the DPPC-rich melting disappeared, this is possibly due to better mixing of lipid domains in the presence of C_5. In the fifth heating scan, the peak that corresponded to the mixed domain transition broadened, indicating a reduction in calorimetric enthalpy (from 46.5E-3 to 44E-3cal/g °C) as the heating scans increase. The calorimetric enthalpy is measured as the area under the DSC peak. A decrease in enthalpy in the mixed domain is indicative of the reduction in van der Waals force that exists between the lipid head groups and acyl chains.[297] This occurs when a molecule is present in the hydrophobic tail region of the outer bilayer leaflet, indicating the perturbation of C_5 in the tail region.[297] This was consistent with the intermediate heating scans (not shown here), inferring that the C_5

doesn't internalize further on annealing. As the concentration of C_5 is further increased to 25 mM (Figure 3-6b), there was initially formation of multiple domains in the first heating cycle, which was assumed to be the result of probe-induced uneven thinning of the lipid bilayer at higher concentrations.[298,299] Further, with continuous annealing in heating scan 5, a clear phase separation in the DPPC and DPPS regions was indicated by presence of two prominent DPPC and DPPS domains and their higher enthalpy of transition (51E-3 cal/g °C). This occurs at higher concentrations of the probe where the molecules interact with the lipid head groups and induce disordering causing phase separation.[298,299] This was also confirmed by the MD simulation results shown in the following section.

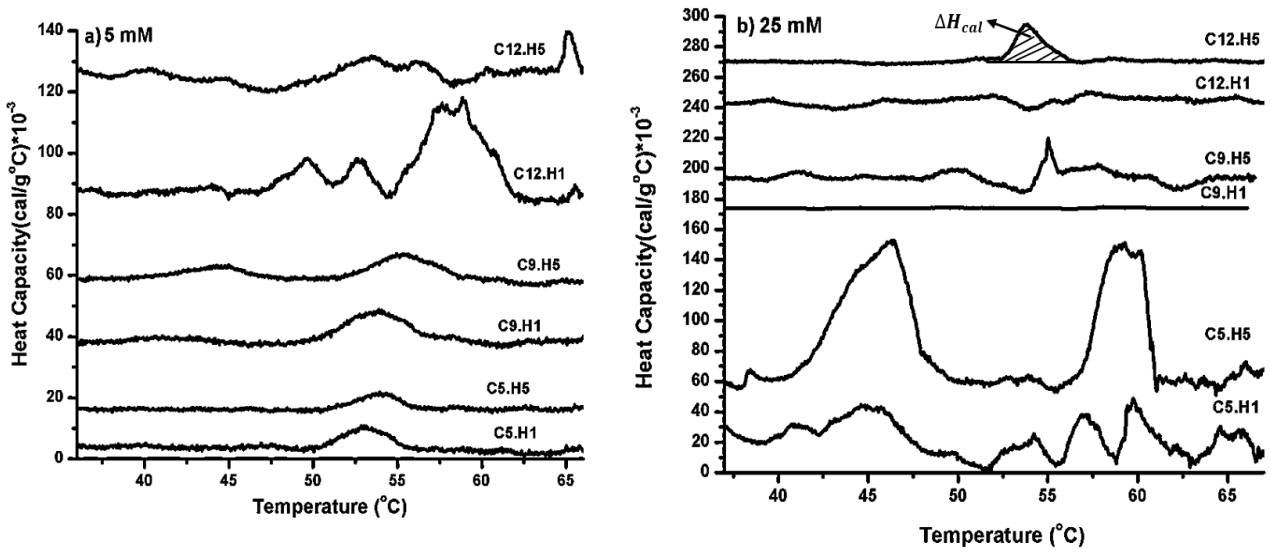

Figure 3-6:DSC thermogram showing interaction of a) 5mM concentration of fluorophore probes with PC/PS b) 25mM concentration of fluorophore probes with PC/PS. H.1 & H.5 indicates heating scans 1&5 respectively

C_9 probe exhibited a similar behavior to C_5 probe with the enthalpies of transition reducing from 40.17E-3 cal/g °C to 38.15E-3 cal/g °C in the first and the fifth heating cycles respectively at 5mM concentration (Figure 3-6a). At 25mM concentration (Figure 3-6b), initially there were no lipid domains peaks observed in the presence of C_9 probes which might be a result of forming of carpet like aggregates of C_9 probes on the lipid bilayer resulting in thinning of the

bilayer. On annealing, these probes try to insert themselves by displacing the lipid molecules and flip-flop between the bilayer leaflets and the outer surface, which was indicated by the presence of a prominent peak at 55 °C in the fifth heating cycle in the thermogram.

On addition of 5mM concentration of C_{12} to liposomes (Figure 3-6a), three peaks appeared in the mixed domain region at 48 °C, 54.2°C and 58.6°C in the heating scan 1. These peaks disappeared on annealing and only one single broad peak around 53 °C is seen in the mixed domain region, in heating scan 5. This indicates that the order in the lipid acyl chains are reduced initially due to the insertion of C_{12} in the bilayer in heating scan 1 and the insertion of C_{12} leads to a well-mixed system of lipids in the bilayer. The transition of DPPC-rich region, which was absent in the heating scan 1, appears on annealing with a broad transition at 39°C, showing an increased melting cooperativity. Measurement of cooperativity or cooperativity unit (CU) is calculated from calorimetric enthalpy[300] (ΔH_{cal}) which is the area under the melting curve ,

$$CU = \frac{6.9}{\Delta H_{cal}} \frac{T_m^2}{T_{\frac{1}{2}}} \qquad (1)$$

where, T_m is the temperature of melting transition, and $T_{1/2}$ is the peak half width.

Similarly, in the presence of 25mM concentration of C_{12} (Figure 3-6b), DPPC-rich domain did not show any peaks and three broad peaks appeared in the mixed domain region at 47.2 °C and 52 °C and 57.5 °C (for 25 mM) in heating cycle 1. The mixed domains in the DSC of heating scan 1, disappeared on annealing. A prominent narrow peak appears, in the heating scan 5, which is accompanied with an increase in enthalpy. This is assumed to occur because C_{12}, owing to its longer alkyl tail length, traverses to the inner leaflet of the lipid bilayer. This insertion of fluorophore probes caused a cavity in the arrangement of the lipid molecules, which resulted in the narrow transition[301]. This cavity formation is probable consequence of the flip-

flopping of the amphiphilic coumarin molecules between the bilayer leaflets which was confirmed by MD simulations.

3.3.4 Cytotoxicity Studies:

MTT assay was performed to assess the toxicity of these amphiphilic coumarin on cancer cells. All the probes (C_5, C_9 and C_{12}) showed a minimum inhibition (damage to cancer cells) between 15-25% at the end of 4hr. The inhibition rate increased with time and reached a maximum of 70% at the end of 48 hr. as shown in Figure 3-7.

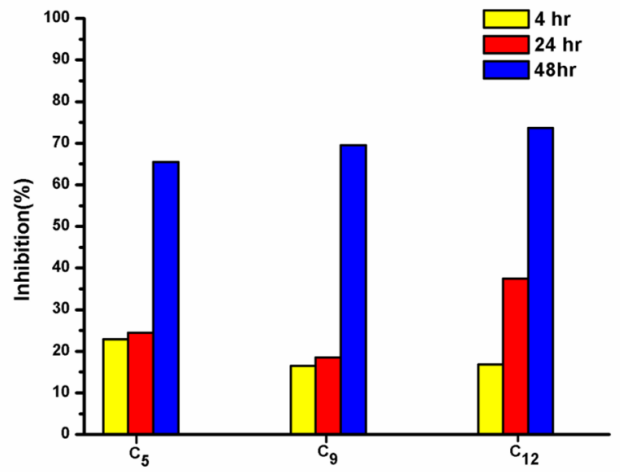

Figure 3-7: MTT Cytotoxicity Assay in human bladder cancer cells

The cytotoxicity studies substantiate that C_9 shows intermediate activity between C_5 and C_{12}. To obtain further insight into the concentration mechanisms of these probes, MD simulations were undertaken. We have considered to examine the activity of C_5 and C_{12} probes only for the MD simulations that are explained below. The binding studies to validate the driving force behind these molecules was examined using ITC experiments and modelling, with C_9 as the reference molecule and is presented in the last section of this chapter.

3.3.5 Simulation results:

The CGMD simulations were performed to compare the lipid bilayer penetration and partitioning behaviors of C_5 and C_{12} in the DPPC/DPPS lipids as a function of amphiphilic

coumarin concentration (Figure 3-8). The C_5 and C_{12} head groups interact with the headgroups of the DPPC and DPPS lipids, while the hydrophobic alkyl tails insert in the bilayer's hydrophobic core. These results are consistent with the zeta potential and fluorescence spectroscopy studies (Figures 3-4 and 3-5). Although, both C_5 and C_{12} insert into the lipid bilayer, they have different effect on the lipid bilayer stability, also evidenced experimentally in the DSC thermographs (Figure 3-6). The C_5 amphiphilic coumarin insertion spans a wide range of concentrations without bilayer disruption, however, higher C_{12} coumarin concentrations (system C_{12}-166 and higher), disrupt the lipid bilayer as observed in Figure 7d.

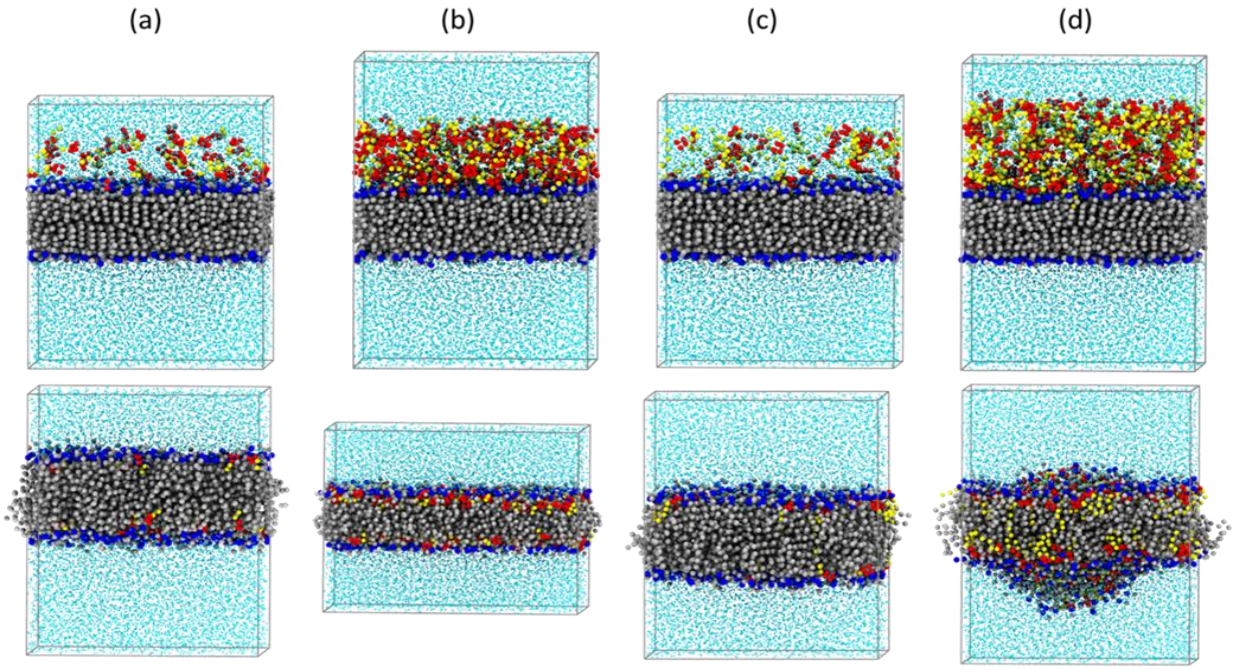

Figure 3-8: Side-view snapshots of the initial (upper panel) and final (lower panel) system configurations: (a) C_5-42, (b) C_5-209, (c) system C_{12}-42 , and (d) C_{12}-209. Color scheme: DPPC/DPPC lipid head groups (blue beads), acyl chains (grey beads); C_5 and C_{12} head groups (red beads), and alkyl tails (yellow beads); water (cyan dots)

To capture the effects of coumarin insertion, area per lipid (A_L) and bilayer thickness (D_M) of the lipid bilayer were computed for each system.

3.3.6 Insertion into the Lipid Bilayer:

Even though the C_5 amphiphilic coumarin molecules insert in the bilayer they were seen primarily interacting with the lipid head groups because their short alkyl tails prevented their effective interaction with the lipid chains. The insertion of C_5 coumarin molecules, however, disrupted the lipid head-head interactions and modified the bilayer properties resulting in the increase in A_L and decrease in D_M. This change in the A_L and the D_M is clear in C_5-42 and C_6-166 system profiles (Figure 3-9). On the contrary, in C_{12}-42 and C_{12}-166 systems, longer C_{12} alkyl tails resulted in stable interactions with 16-carbon DPPC/DPPS acyl chains due to their insertion in the lipid bilayer leaflet without changing the area per lipid and lipid bilayer thickness substantially shown in Figure 8. It is worth noting that in system C_{12}-209, the lipid bilayer was disrupted by high concentration of C_{12} in this system, leading to the formation of an aggregate C_{12} coumarin with lipids removed from the membrane. System C_{12}-184 also showed similar phenomena (data not shown for C_{12}-184); due to disruption, the lipid bilayer thickness failed to be a good marker for comparing the bilayer properties.

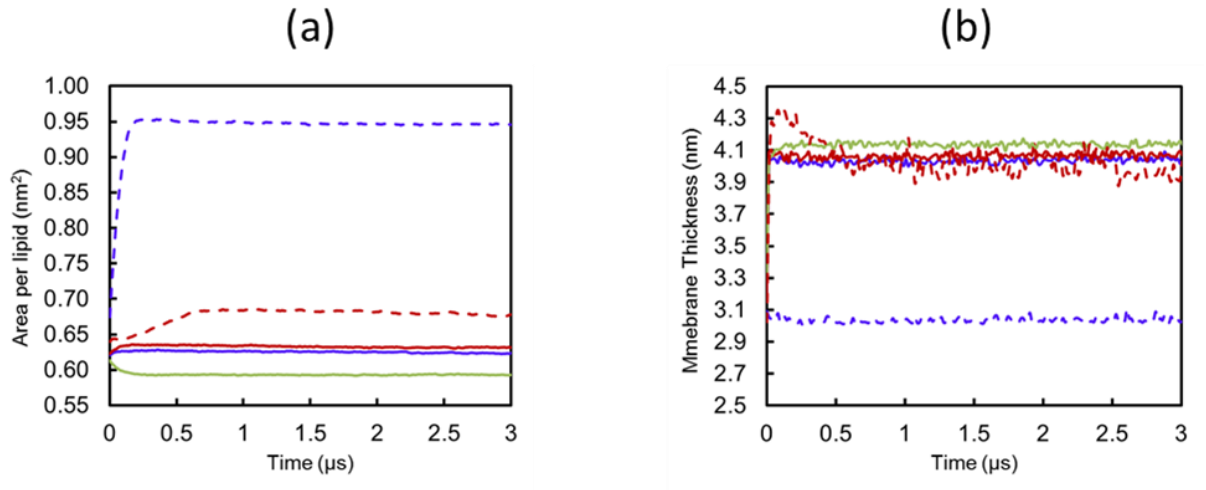

Figure 3-9: Membrane properties. Panel (a) A_L and (b) D_M of DPPC/DPPS versus simulation time plots for C_5-42 (solid blue) C_{12}-42 (solid red), C_5-166 (dashed blue), C_{12}-166 (dashed red), and control (green).

Flip-flop mechanism: Both amphiphilic coumarin C_5 and C_{12} molecules showed dynamic interleaflet transport or flip-flop behavior in the lipid bilayer, similar to cholesterol in the physiological membranes.[302–304] The coordinates of the each amphiphilic coumarin molecule were recorded as it traversed between the upper and lower leaflet of the lipid bilayer during a simulation; position of amphiphilic coumarin head group is shown for a subset of 20 randomly selected C_5 (Figure 8-7) and C_{12} (Figure 8-9) molecules. The C_5 coumarin molecules demonstrated three modes of interleaflet transport: one-flip to the inner leaflet (no return or flop back to the outer leaflet), regular flip-flop (back and forth transport between the two leaflets with short stays on each leaflet), and no-flip (remains on outer leaflet). Remarkably, C_5 coumarin molecules also showed regular ejection into the solution and rapid reinsertion into the lipid bilayer in the flip-flop plots shown in Figure S8, indicating an unstable insertion of C_5 molecules. Although C_{12} coumarin molecules show the same three flip-flop modes (Figure 8-

7), they lack ejection-reinsertion behavior that is prominent in C_5 molecules. Thus, MD simulations concur with the DSC studies that confirm C_{12} coumarin molecules stabilizes in the lipid bilayer owing to their longer carbon tails that aid in hydrophobic interactions with the lipids in the bilayer.

Table 3-3: Flip-flop percentages of C_5 and C_{12}

System (i = 5 or 12)	**C_5**		**C_{12}**	
	≥1 flip	≥ 2 flip-flops	≥ 1 flip	≥ 2 flip-flops
C_i-42	31%	0%	36%	5%
C_i-74	39%	7%	54%	16%
C_i-106	54%	11%	56%	22%
C_i-138	59%	20%	65%	30%
C_i-166	46%	7%	54%	21%
C_i-184	42%	5%	-	-
C_i-209	33%	1%	-	-

The percentage of flip-flops in both C_5 and C_{12} systems were computed and are summarized in Table 3-3 (except in lipid bilayer disrupted C_{12} systems). It is observed that for the same concentration, C_{12} systems had higher flip-flop than C_5. This phenomenon is due to the instability of C_5's in the lipid bilayer, which causes them to jump back to water or flip to the inner leaflet, thereby reducing the probability of flip-flop within the lipid bilayer. We observed that the flip-flop percentage is sensitive to the concentration and the highest percentage of flip-flop for both C_5 and C_{12} occurs for an optimal concentration (Figure 8-10). The plots demonstrate that the number of flip-flops increase with the concentration of the amphiphilic coumarin molecules, however, at very high concentrations the bilayer is saturated with amphiphilic coumarin molecules, consequently, it either disrupts the bilayer as seen in C_{12} systems or causes C_5 coumarin molecules to eject and reinsert at a higher frequency. This occurs because, amphiphilic coumarin molecules insert themselves into the outer leaflet of the lipid bilayer and then undergo a flip to the inner leaflet. This flip-flop phenomena is observed for other amphiphilic molecules such as cholesterol[305]. There are examples, where fluorophores flip-flop between the outer and inner leaflets to achieve an equal distribution across the bilayer.[306–308]

Highest flip-flop is observed with mid-range concentrations; supporting the findings from the binding and DSC studies to concur that concentration is critical parameter for amphiphilic coumarin insertion into the lipid bilayer.

3.3.7 ITC Modelling and Data Analysis:

The thermodynamic parameters of C_9 binding to DPPC/DPPS liposomes by applying the sequential three site model. This model is applicable because the binding and insertion of the

C_9 molecule is sequential and follows these three steps as elucidated by the previous studies[309,310]

i. C_9 has an electrostatic attraction to the lipid headgroups
ii. The alkyl tails of C_9 inserts itself partially into hydrophobic zone of the bilayer
iii. The entire C_9 molecule flip-flops between the bilayer leaflets

Each of these steps have a binding constant (dissociation constant- K_d, association constant- K_a), enthalpy and entropy change associated with it. Our preliminary results of type-A (refer to plot in appendix B) titration are tabulated in Table 3-4 as follows. When the DPPC/DPPS liposomes (0.5 mM) was titrated with two concentrations of C_9 0.025 mM and 0.05 mM, the resulting binding parameters are as follows:

Table 3-4: K_d and ΔH estimated for Type-A titration:

List of Variables	Concentration of C_9 in the syringe	
	0.025 mM	**0.05 mM**
K_{d_1} (M)	7.38E-05	1.89E-04
K_{d_2} (M)	1.00E-01	8.36E-02
K_{d_3} (M)	1.00E-10	7.11E-06
ΔH_1 (kJ/mol)	-1274	-1030
ΔH_2 (kJ/mol)	2547	-4998
ΔH_3 (kJ/mol)	-2052	-2343
K_{a_1} (M^{-1})	1.36E+04	5.30E+03
K_{a_2} (M^{-1})	1.00E+01	1.20E+01
K_{a_3} (M^{-1})	1.00E+10	1.41E+05
ΔS_1 (J/mol·K)	-4.20E+03	-3.39E+03
ΔS_2 (J/mol·K)	8.56E+03	-1.67E+04
ΔS_3 (J/mol·K)	-6.69E+03	-7.76E+03

However, type-A titration has an inherent drawback to it. Towards the end point of the titration, the saturation of the C_9 molecules bound to the liposomes is achieved resulting in more molecules binding to the same liposomes. Hence destabilizing the bilayer[309,311,312]. However, for type-B titration, more liposomes are present for the C_9 molecules, thus the

saturation point is not reached, and the accuracy of the results is valid. The plot (Fig 3-10) and the binding parameters for type B titration, with liposome concentration of 5 mM in the syringe (table 3-5) are as follows:

Table 3-5: K_d and ΔH estimated for Type-B titration:

List of Variables	Concentration of C_9 in the cell	
	0.025 mM	**0.05 mM**
K_{d_1} (M)	6.70E-03	3.79E-03
K_{d_2} (M)	6.73E-03	4.71E-03
K_{d_3} (M)	1.09E-02	5.00E-03
ΔH_1 (kJ/mol)	-7945	-9999
ΔH_2 (kJ/mol)	-2198	-4914
ΔH_3 (kJ/mol)	-73.1	-2482
K_{a_1} (M^{-1})	1.49E+02	2.64E+02
K_{a_2} (M^{-1})	1.49E+02	2.12E+02
K_{a_3} (M^{-1})	9.20E+01	2.00E+02
ΔS_1 (J/mol·K)	-2.66E+04	-3.35E+04
ΔS_2 (J/mol·K)	-7.33E+03	-1.64E+04
ΔS_3 (J/mol·K)	-2.08E+02	-8.28E+03

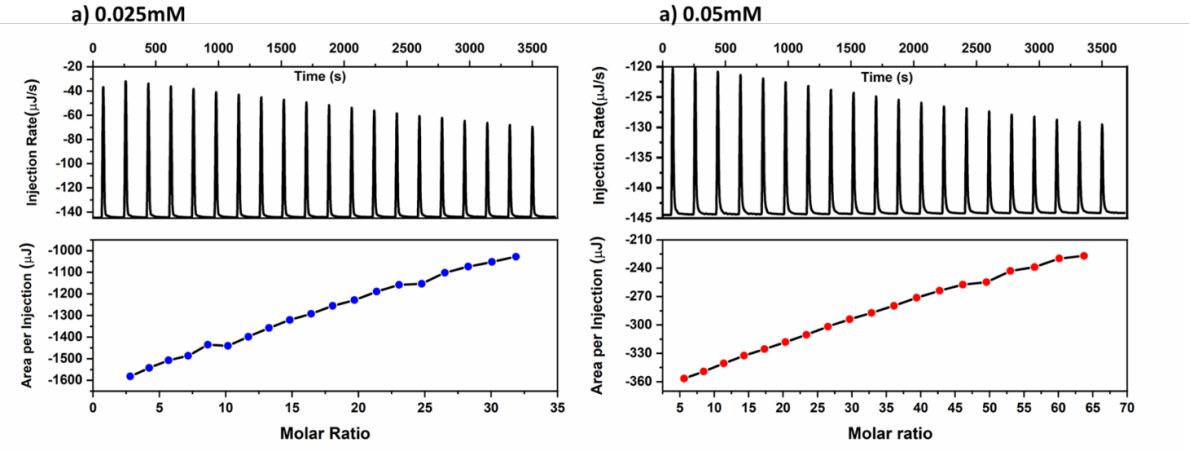

Figure 3-10: ITC data chart and corresponding modelling fit for Type-B titration with differing C_9 concentrations in the cells and 5 mM liposome concentration in the syringe

3.3.8 Thermodynamic Parameters of C_9 molecules binding to Liposomes:

The total association constant, enthalpy, entropy, and Gibbs Free energy associated for type-B titration are calculated as follows and tabulated in table 3-6:

$$K_{a-total} = K_{a1} + K_{a2} + K_{a3} \quad (2)$$

$$\Delta H_{total} = \Delta H_1 + \Delta H_2 + \Delta H_3 \quad (3)$$

$$\Delta S_{total} = \Delta S_1 + \Delta S_2 + \Delta S_3 \quad (4)$$

$$\Delta G = -RT \ln (K_a) \quad (5)$$

Table 3-6: Thermodynamic Parameters of C_9 molecules binding to Liposomes

Concentration of C_9	$K_{a-total}$ **(M^{-1})**	ΔH_{total} **(kJ/mol)**	ΔS_{total} **(J/mol·K)**	ΔG **(kJ/mol)**	**-TΔS/ΔG**
0.025 mM	3.90E02	-10,216	-3.4E04	-14.78E03	-0.0006
0.05 mM	6.76E02	-17,395	-5.81E04	-16.15E03	-1.07

The binding of molecules to liposomes is predominantly driven by entropy, predominantly driven by the lipophilicity of the molecules. This is called the classical hydrophobic effect[313,314]. However, in this case the driving force is enthalpy change. The non-classical hydrophobic effect occurs because of differences in the water surrounding the bulk and hydrophobic lipid bilayer[315,316]. The **-TΔS/ΔG** value, which signifies the dependence of entropy on free energy change, is negative[311,314]. This implies that enthalpy is the significant driving factor behind the binding and insertion of these amphiphilic coumarin molecules. This enthalpy driven binding is called non-classical hydrophobic effect.

3.4 Conclusions

In this study, we presented the synthesis, and mechanisms of interaction with lipid bilayers of novel amphiphilic fluorophores consisting of amino methyl coumarin headgroup with C_5, C_9 and C_{12} alkyl tails. A detailed binding, bilayer phase transition, and MD simulation studies reveal:

1. The amphiphilic coumarin molecules interact with the lipid bilayer and insert themselves into the bilayer by virtue of their alkyl tails and their driving force behind binding is enthalpy;

2. At smaller concentrations, C_{12} coumarin molecules insert into the bilayer, which causes phase separation in the lipid bilayer, however, with subsequent annealing, the insertion of C_{12} results in a well-mixed system of lipids in the bilayer. This is evident by the presence of a broader transition peak that correlates to an increased melting cooperativity represents greater number of lipid molecules undergoing transitions. On the contrary, C_5 molecules, due to their shorter tail lengths remain on the outer leaflet of the bilayer. Insertion behavior of C_9 is concentration dependent and has a transitional activity pattern that conforms to both C_5 and C_{12};

3. The MD simulations confirm coumarin's lipid bilayer penetration dependency on the coumarin concertation. The C_5 coumarin molecules penetrate the lipid bilayer, but due to the short alkyl tail, they interact primarily with the lipid head groups resulting in lipid bilayer thinning. At high concentrations, however, the C_5 coumarins undergo continuous insertion-ejection from the outer leaflet of the lipid bilayer. In contrast, C_{12} coumarins interact favorably with the hydrophobic lipid tails and undergo flip-flops between the outer and inner leaflets of the lipid bilayer. At high concentrations, the high-frequency flip-flops lead to lipid destabilization, causing the lipid bilayer to rupture.

The preliminary MTT studies in conjunction with the interaction studies with the lipid bilayer indicate the potency of these amphiphilic coumarin molecules in cancer inhibition.

4 Interaction of Riboflavin-5-Phosphate with Liposome Bilayers

---

This chapter was originally published in *Journal of Nanotoxicology and Nanomedicine (JNN) 3.1 (2018): 49-59* by Poornima Kalyanram, Istvan Stadler and Anju Gupta. This work was conducted in collaboration with Rochester General Hospital.

Riboflavin presents tremendous potential as a photosensitizing agent for photodynamic therapy (PDT) for treating microbial infection and cancer therapy. Encapsulation of riboflavin can improve its bioavailability and stability while making the clinical applications more efficient. Our detailed study on cellular inhibition of liposome encapsulated riboflavin-5-phosphateinvestigation, and the effect of unencapsulated riboflavin on liposome bilayers aims to improve the efficiency of cellular delivery of riboflavin. Liposomes composed of 1,2-dipalmitoyl-sn-glycero-3-phosphocholine (DPPC) and cholesterol were used in this study. Cell studies demonstrate high inhibition rates for the liposome-encapsulated high concentration riboflavin formulations in the presence of blue light, despite the lower encapsulation lading. Our Differential Scanning Calorimetry (DSC) confirm the incorporation of riboflavin in the outer leaflet of the bilayer with moderate phase separation of the lipids and cholesterol which further provides the mechanism of photoactivation and triggered release confirmed by in-vitro studies. DSC studies also confirmed that high concentration of riboflavin that may be encapsulated in the liposomes do not disrupt the lipid bilayer integrity.

4.1 Introduction

A beam light at a visible or near infrared (NIR) wavelength to destroy the target cells bases photodynamic therapy (PDT) or a photodynamic reaction involving a light-sensitive substance (a photosensitizer) combined with the irradiation. It is emerging as a highly effective, non-invasive therapeutic approach in the struggle against cancer and other infectious diseases [317]. Despite the significant progress and scientific reports, PDT is yet to be established as an effective and safe technique to eradicate microbes and tumors [318]. Riboflavin-5-phosphate, also referred as vitamin B_2, is a potent antioxidant and is used as a supplement in chemotherapy due to its anti-carcinogenic properties [319,320]. In addition to the anti-carcinogenic properties, riboflavin has also reported as a potential photosensitizer for PDT. The photosensitive property of riboflavin has been investigated in eliminating tumor, ocular and skin and bacterial infections [321–327]. However, the hydrophilic nature of riboflavin causes rapid clearance of the drug in the blood stream and lowers the intracellular absorption, thereby, reducing its therapeutic efficacy [328]. Liposome based carriers have been exploited to encapsulating hydrophilic drugs to prevent their rapid clearance and increase their circulation time upon administration [328–331].

Liposomes are self-assemblies of lipids, which are amphipathic in nature consisting of a hydrophilic head and a hydrophobic tail. Liposomes are characterized by a lipid bilayer surrounding aqueous core which self-assemble to give rise to an aqueous core [42,61]. Due to this unique structure, they are capable of entrapping both hydrophobic and hydrophilic molecules [58]. A variety of simple and economic methods such as dry film hydration, solvent exchange, electro formation methods have been investigated to form liposomes with variable size, surface charge, and number of bilayers[17]. Addition of cholesterol improves the circulation of liposomes in the blood stream while providing the steric stabilization through increasing the rigidity of the bilayer[60]. Although the efficacy of liposome encapsulated riboflavin-5-phosphate

formulations has been reported[332,333]however, the effects of interaction between the free-floating riboflavin-5-phosphate, a potent riboflavin derivative on the stability of liposome carriers remain unaddressed.

The objective of the current work is two folds, first to test the efficacy of liposome encapsulated riboflavin riboflavin-5-phosphate in the presence and absence of blue light for their potential application in photodynamic therapy against cancer and infectious diseases. Secondly, to gain insight on the interaction of unencapsulated riboflavin-5-phosphate at higher concentrations on the liposomal bilayers. Accordingly, a combination of analytical studies such as zeta potential, DSC (Differential Scanning Calorimetry) were used to examine the electrostatic binding between the riboflavin and lipid headgroups. DSC was used to obtain information on the perturbations and disordering of the lipid bilayer due to the presence of riboflavin. A detailed quantification of thermodynamic properties associated with incorporation of riboflavin within the lipid bilayer was also conducted.

4.2 Materials and methods:

4.2.1 Materials:

DPPC (1,2-Dipalmitoyl-sn-glycero-3-phosphocholine) dissolved in chloroform was purchased from Avanti Polar Lipids. Sigma Aldrich supplied cholesterol in powdered form. Riboflavin-5-monophosphate sodium salt (98% purity) was purchased from VWR. Invitrogen Ultra-pure distilled water was used in the preparation of Liposomes and riboflavin-5-phosphate solutions. Table 4-1 enlists the molecules used in this study along with their chemical structure and the properties.

Table 4-1: Chemical Structure of molecules investigated in this study

Component	Structure	Property
1,2-Dipalmitoyl-sn-glycero-3-phosphocholine (DPPC) (MW = **734.039 g/mol**)	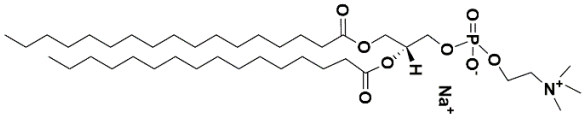	Zwitterionic Membrane Lipid
Cholesterol (MW = **386.65 g/mol**)	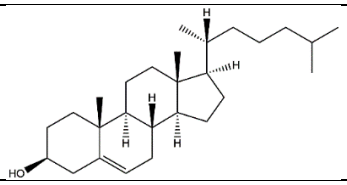	Membrane Component
Riboflavin-5-phosphate (MW = **456.344 g/mol**)	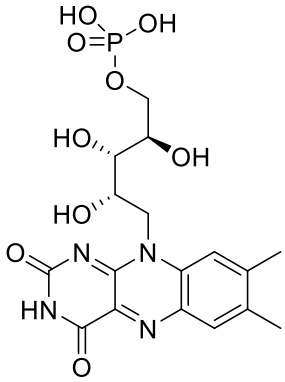	Negatively Charged Fluorophore

4.2.2 Preparation of Liposomes:

1,2-Dipalmitoyl-sn-glycero-3-phosphocholine (DPPC), cholesterol and polycarbonate membranes were purchased from Avanti Polar Lipids (Alabaster, AL). DPPC/Cholesterol (90/10, 10mM) liposomes were prepared by mixing the DPPC and Cholesterol in known volumes. The mixture was left to dry under a stream of nitrogen followed by vacuum drying for 20 minutes. The dried lipid film was re-hydrated with *Invivogen* endotoxin free and the liposomes were extruded through 100 nm polycarbonate membranes to obtain unilamellar liposomes. To prepare the riboflavin-encapsulated liposomes, the dried lipid film was hydrated with 0.5 mM and 10 mM riboflavin-5-phosphate.

4.2.3 DLS and Zeta Potential Measurements:

DLS (Dynamic Light Scattering) and Zeta potential experiments were recorded using Zetasizer nano-series (Malvern Nano-ZS). The size distribution of the liposomes was obtained by placing

1 ml of sample in SARSTEDT polystyrene cuvettes at a 173° backscatter angle with 120 s equilibration time. Zeta potential measurements were made using DTS1070 folded capillary cells. Size and zeta potential measurements were conducted at 25 and 43°C.

4.2.4 Differential Scanning Calorimetry:

DSC studies were performed on a Q-2000 TA instrument DSC in Tzero Hermetic pan. About 20 mg of sample was sealed using a sample press and were subjected to three continuous cycles of annealing in the range of 25 to 65 ºC at the rate of 10 ºC/min, under nitrogen environment at 40ml/min.

4.2.5 Fluorescence Spectroscopy:

The fluorescence experiments were carried out on a Shimadzu spectrofluorometer (RF-5301 PC) equipped with a xenon lamp as the light source. The intensities were measured at excitation wavelength of riboflavin-5-phosphate was 450 nm at 43 ºC. The temperature was controlled using Fisher Scientific Isotemp® water bath.

4.2.6 Cell Studies and Imaging:

Human bladder carcinoma cells HT-1376 (American Type Culture Collection (ATCC) no. CRL1472) were grown in a 1.7 cm^2 cell culture well with Dulbecco's modified eagle's medium (DMEM) supplemented with 10% fetal bovine serum (FBS), Streptomycin/Penicillin/Fungizone (SPF), glutamine, pyruvate at 37 ºC and 5% CO_2. After the growing cells formed a monolayer on the wells in approximately 24 -36 hours, the cell culture media was removed. The wells were rinsed with PBS (phosphate buffered saline) and new media along with liposome-encapsulated riboflavin-5-monophosphate was added. The cells were incubated for 4 hours to ensure absorption of the encapsulated riboflavin. After the absorption, the photo-activation of liposome-encapsulated riboflavin-5-monophosphate, blue light at 450 nm was irradiated to some of the wells. This was followed by the addition of 50µl

of 5mg/ml MTT (2h-Tetrazolium, 2-(4,5-dimethyl-2-thiazolyl)-3,5-diphenyl-bromide) reagent to evaluate the toxicity induced by riboflavin 5-monophosphate.

On incubation for 6 hr., the metabolism of the living cells resulted in the formation of crystals. The residual media was removed, and the crystals were dissolved in isopropanol/10% triton/0.1 N HCl mixture. The samples were placed in an EL 340-bio kinetics microplate reader spectrophotometer (Bio-Tek instruments, Winooski, VT) and the absorbance of the samples were measured at 570 nm from which the inhibition percent was calculated.

To evaluate the photodynamic therapy effectiveness of the encapsulated riboflavin the following control groups were created.

1. Absolute control: did not received any encapsulated riboflavin, light irradiation
2. Control 1: Irradiation by blue light irradiation for 10min without encapsulated RBP
3. Control 2: Received only encapsulated riboflavin (no light irradiation)
4. Control 3: Received only encapsulated riboflavin with blue light irradiation

4.2.7 UV-Vis Spectroscopy:

Encapsulation was quantified using Shimadzu UV-2501PC – High Resolution UV-Vis Spectroscope. A calibration curve was prepared by dissolving Riboflavin-5-phosphate in DI water. Absorbance of riboflavin-5-phosphate was recorded at 445 nm.

4.3 Results and discussion

4.3.1 Cell inhibition studies of Liposome encapsulated Riboflavin-4-phosphate

The DPPC/Chol encapsulating liposomes used for cell studies were tailored to be in the size range of 100-200 nm based on the guidelines provided by FDA to design effective nanocarriers[160]. The resultant liposomes were sized using 100 nm membranes; however, the hydrodynamic diameter of riboflavin-5-phosphate encapsulated liposomes were measured to

be 173 nm with a Polydispersity Index (PDI) of 0.230. This increased size and moderate PDI arises due to the presence of unencapsulated molecules on the liposome surface that may result in minimal aggregation. These effects of unencapsulated molecules on liposomes are investigated in the following section.

The cell inhibition studies were conducted using 0.25, 1, 2.5 and 5 mg/ml riboflavin encapsulated in DPPC/Chol liposomes (denoted as RBNP) in the absence (control 2) and presence (control 3) of blue light. The encapsulation relied on the self-assembling of the lipids, and additional encapsulation techniques such as freeze thawing were not used to prevent the degradation of riboflavin 5-monophosphate The drug loading and entrapment efficiency of Riboflavin-5-phosphate encapsulated liposomes were calculated by

$$\text{Drug Loading}(\%) := \frac{\text{Final Concentration of Fluorophores}}{\text{Initial Concentration of Liposomes}} \times 100 \quad (1)$$

$$\text{Encapsulation Efficiency}\ (\%): \frac{\text{Conc. of drug added} - \text{Conc. of unentrapped drug}}{\text{Conc. of drug added}} \times 100 \quad (2)$$

Figure 4-1 shows around 20% or less cell inhibition rates with lower and higher concentration Riboflavin encapsulated in liposomes (RBNP) in the absence blue light. However, the cell inhibition rate increases to 78% with 5 mg/ml Riboflavin encapsulated liposomes in the presence of blue light almost three times greater than the same concentration of encapsulated riboflavin-5-phosphate treated without the blue light. The absolute control without riboflavin and blue light showed no inhibition while control 1 showed a minimum inhibition of 0.25%. Overall, it was observed that the inhibition rate of cancer cells increased linearly with increasing the concentration of Riboflavin-5-phosphate in the liposomes. It is inferred that; a combination of the higher concentration of riboflavin and blue light is necessary for a

successful inhibition of cancer cells. Another noteworthy observation is the inhibition rate of 78% at a low encapsulation efficiency of 24%.

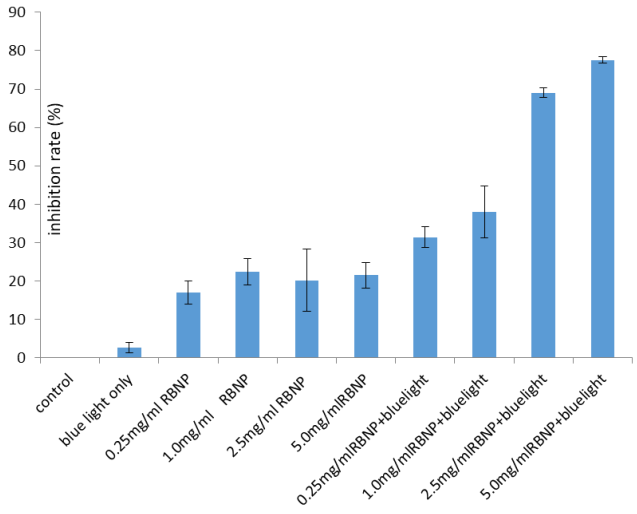

Figure 4-1: Inhibition of cancer cells in the presence and absence of blue light by DPPC/Chol liposomes encapsulating Riboflavin-5-phosphate

4.3.2 Effect of unencapsulated Riboflavin-5-phosphate on Liposome Bilayers

The DPPC/Chol liposomes used to study the effects of unencapsulated riboflavin were prepared using the same technique and were measured to be 118±2 nm in diameter with a low PDI of 0.186. The zeta potential of the unencapsulated DPPC/Cholesterol was found to be 0.828 ±0. 50 mV congruous to the zwitterionic nature of the DPPC lipids. The measured zeta potential of Riboflavin-5-phosphate dispersed in endotoxin free water was -2.44± 0.40 mV. When riboflavin-5-phosphate was added to the preformed DPPC/Cholesterol liposomes, the resultant zeta potential decreased to -6.20±3.00 mV at 43^{o}C. This is attributed to the electrostatic binding between the positively charged choline moieties of DPPC headgroup and monophosphate groups of riboflavin-5-phosphate (as shown schematically in Figure 4-2). At

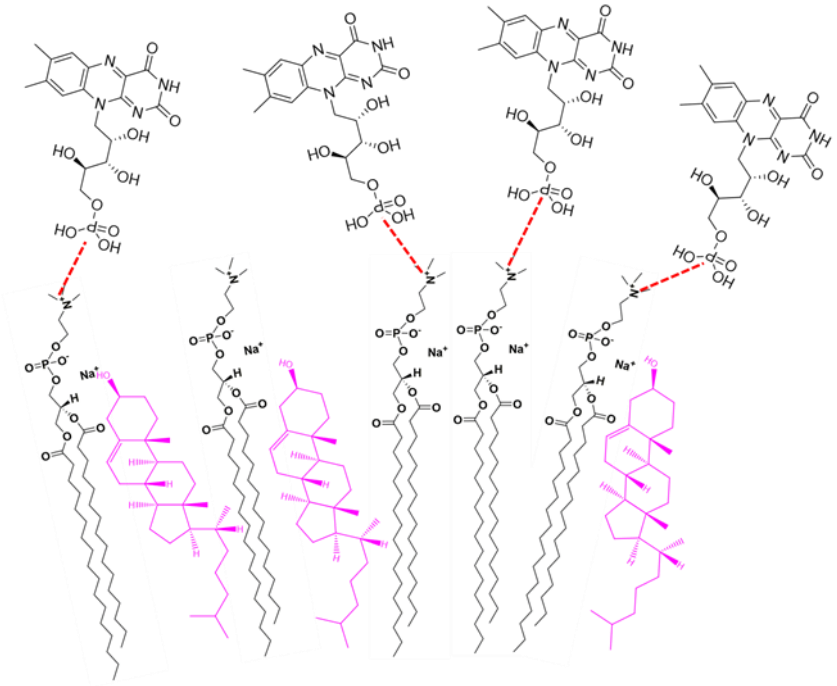

Figure 4-2: Electrostatic Binding of Riboflavin-5-phosphate onto the choline head group of the DPPC lipids

the transition temperature of the lipids (43°C for DPPC), the lipid headgroups tend to get titled and the negatively charged surface is exposed, which further decreases the surface charge [280–282]. This explains the decrease in zeta potential value on addition of riboflavin to the liposomes.

The thermodynamic behavior specifically, the phase transitions, subsequent enthalpy change and resultant domain formations in the lipid bilayer in the presence of encapsulated and/or un-encapsulated therapeutics is studied using Differential Scanning Calorimetry[334,335]. Figure 3 represents the thermographs of DPPC and DPPC/Chol (90/10) liposomes in the presence of varying concentrations of riboflavin. When lipids are heated, they undergo a pre-transition and a transition phase. During the pre-transition phase, the gel like lipid undergoes a rippling effect in the tail region. On further heating, the rigid tail region of the bilayer becomes fluid in nature, with an expansion of molecules in the head group. This happens during the melting phase and is exhibited by a sharp peak[201,336]. The transition temperature (T_m) of the DPPC liposomes occurs at 43 °C as seen by single melting peak (Fig 4-3a). In the presence of cholesterol, the

melting peak of DPPC liposomes (T_m) broadened and shifted to a lower temperature of 40.8 °C as seen on Fig 4-3b. This is attributed to the presence of cholesterol between the alkyl chains of the lipids that restricts the mobility of the lipid tails [337,338].

To observe the additional effects of riboflavin on the phase transition of DPPC/Cholesterol liposomes, the samples were also subjected to annealing. Exposure to laser during photodynamic therapy causes localized heating at the affected area to approximately 42°C and the annealing studies conducted on DSC compares to this intermittent exposure of the light[339]. The thermograph in Fig 4-3c shows the first heating cycle when 0.5 mM riboflavin was added to DPPC/Cholesterol. Although the addition of riboflavin did not cause a significant shift in the transition temperature, the melting peak was broadened significantly, due to the of binding of the cationic riboflavin to the negative moiety of the DPPC lipid headgroups, which causes perturbation in the organization of the DPPC molecules [340]. We hypothesize that the broadening of the peak is partially due to the interdigitation effect that causes the tail group of lipids to overlap in the presence of small hydrophilic molecules[236,341]. Fig 4-3d line representing the heating cycle 3, with 0.5 mM riboflavin shows a modest peak or a shoulder of the main transition peak along with the narrowing of the main peak. The formation of such shoulder is attributed is the characteristic to the phase separation of the lipids that arises from the insertion of the riboflavin molecules in the outer leaflet of the lipid bilayer [342]. The narrowing of the main phase transition peak suggests the cooperative nature of the transition which is reported as increase in the motional freedom and collective movement of the lipid molecules[343].

Effects of excessive riboflavin on the lipid bilayer was also studied by adding 10 mM of riboflavin (corresponding to 5 mg/ml riboflavin used in the cell inhibition studies) to the preformed liposomes. The first heating cycle (Fig 4-3e) shows broadening and a right-hand side shift of the main transition peak of DPPC/Chol compared to Fig 4-3b. This increase in temperature could possibly be due to the change in the surface hydration behavior of the lipid

headgroups by larger number of round riboflavin [340]. In the third heating cycle with 10 mM riboflavin, however, a left shoulder appears on the main transition similar to the one observed with 0.5 mM in Fig 4-3d representing phase separation and the narrowing of the peak is also the indication of increased cooperativity. Thus, annealing studies confirm the absence of pore formation and destabilization of the lipid bilayer that poses detrimental effects to the cell membrane integrity [344]. These studies substantiate the moderate disordering of the lipid bilayer in the presence of low and high concentration of riboflavin-5-phosphate, thus, indicating the safety of normal cells when subjected to PDT with hydrophilic fluorophores such as riboflavin.

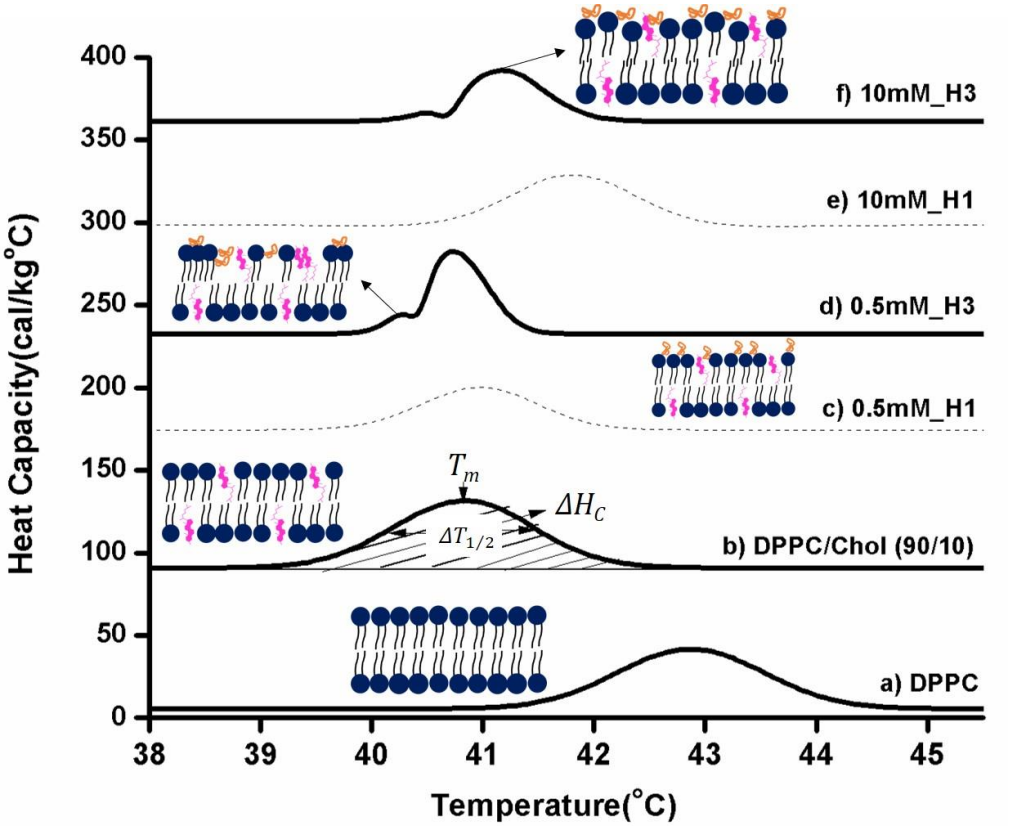

Figure 4-3: DSC thermograph of DPPC/Cholesterol with Riboflavin-5-phosphate

A detailed quantification of the thermodynamic properties associated with cooperativity of DPPC/Chol lipid bilayer in the presence of riboflavin is presented. Table 4-2 summarizes the calculated calorimetric enthalpy and vant Hoff enthalpy values for DPPC/Chol in the presence and absence of riboflavin. Calorimetric enthalpy, H_C is the area under the transition peak, and

vant Hoff enthalpy (ΔH_{vH}) is the function of melting or the transition temperature, T_m and half width of transition peak, $\Delta T_{1/2}$[297] .

$$\Delta H_{vH} = {}^{4RT_m^2}\Big/_{\Delta T_{1/2}} \qquad (3)$$

Table 4-2:Calculated Thermodynamic Properties

Sample Name	Calorimetric Enthalpy(cal/kg) ΔH_C	Melting Temperature T_m (°C)	Cooperativity Units *10^3 (C.U)	
Pure DPPC/Cholesterol	49.02	40.80	8.59	
0.5mM_H1_DPPC/Chol	34.11	40.99	10.76	Increased Cooperativity compared to DPPC/Cholesterol
0.5mM_H3_DPPC/Chol	30.37	40.74	28.17	
10mM_H1_DPPC/Chol	41.01	41.64	8.8	Increased Cooperativity on annealing
10mM_H3_DPPC/Chol	24.19	42	21.44	

The broadening of the transition peak due to the moderate lipid disordering in the presence of riboflavin as seen in Fig 4-3c-f is accompanied by a decrease in calorimetric enthalpy of the DPPC/Chol. With subsequent heating, the transition enthalpy further dips validating the insertion of riboflavin in the outer leaflet of the bilayer. Cooperativity or the number of DPPC molecules undergoing phase is the function of calorimetric and vant Hoff enthalpies. In a unilamellar DPPC liposome of 100 nm diameter the total number of DPPC lipids is approximately 80047, and 90/10 DPPC /Cholesterol solution consists of nearly 6.8E12 liposomes are present per ml of solution. Accordingly, 0.5 mM riboflavin corresponds to 551 molecules of riboflavin with respect to one DPPC lipid molecule and 10 mM riboflavin represents 11153 molecules to one DPPC lipid molecule. The calculated cooperativity units on Table 4-2 demonstrate a surge in cooperativity of DPPC/Chol liposomes with the increasing concentration of riboflavin-5-phosphate. At 0.5 mM, riboflavin-5-phosphate molecules occupy

a small number of binding sites as compared to 10 mM riboflavin-5-phosphate, and the unoccupied binding sites on the lipid decreases causing an increase in vant Hoff enthalpy.

In summary, the riboflavin-5-phosphate molecules bind electrostatically with the DPPC lipid headgroup via weak hydrogen bond with the positively charged choline head group of the DPPC lipids. Furthermore, DSC studies demonstrated the insertion of riboflavin molecules in the outer leaflet of the lipid bilayer causing minimal perturbation of the lipid bilayer. Consequently, confirming no detrimental effects of unbound and free-floating high concentration of riboflavin on the liposome bilayers. Cancer cell inhibition studies confirmed the PDT activity in the presence of the blue light despite lower encapsulation efficiencies of the liposomes.

4.4 Conclusion

In this study, DPPC/Cholesterol based liposomal formulation for the encapsulation of riboflavin-5-phosphate derivative for potential photodynamic therapy are presented. The encapsulation resulted from the self-assembling properties of the lipids posing no detrimental effects on the functionality of the riboflavin molecule. Despite, the lower encapsulation efficiently of 24%, a cell inhibition of 78% was observed in the presence of blue light for high concentration riboflavin. Cell studies also showed very low inhibition in the absence of blue light acknowledging, the safety of non-targeted healthy cells. The effects of unencapsulated on liposome bilayers were also studied using differential scanning calorimetry that further confirmed the bilayer integrity and inferring the safety of unbound riboflavin on the stability of the liposome carriers. A detailed quantification of thermodynamic properties associated with the lipid bilayer and the presence of therapeutics was conducted.

5 Insights on the Thermal and Physical Stability of the Modified Polymerizable Liposomes for Improved Photoactivity

---

This chapter by Poornima Kalyanram, Noor Hussein, Amit Tiwari and Anju Gupta has been accepted for publication in *International Journal of Lipids, Special Issue.* This work is a continuation of Chapter 4. In this work, we have improvised the liposomal formulation detailed in chapter 4, thereby provide increased stability for the delivery of Riboflavin.

We investigated physical steric and thermal stability effects induced by cholesterol and polyethylene glycol (PEG) in liposomes encapsulated with riboflavin. The composition of liposome was varied systematically to decipher the individual and combined effects of cholesterol and PEG on the stabilization of liposomes, specially the photopolymerizable liposomes for their potential applications in photo-treatments. Our results indicate that inclusion of PEG in the lipids enhances the steric stabilization by adopting a brush-like regime that prevents the agglomeration of encapsulated liposomes. A mechanistic differential scanning calorimetry studies reveal the phase transitions and enthalpy changes in the lipid bilayer due to the presence of cholesterol suggesting its role in regulating membrane fluidity. Supporting *in-vitro* studies confirm the efficacy of PEGylated formulations encapsulating riboflavin.

5.1 Introduction:

Liposomes or phospholipid vesicles offer several advantages in theragnostic due to their biocompatibility[345,346], ease of surface functionalization[347,348], and their ability to entrap both hydrophilic[62,349] and hydrophobic drugs and targets [350,351]. However, the stability and leakiness of the phospholipid-based vesicles pose limitations for their applications in targeted delivery that require longer circulation periods in human bodies [352,353]. Several strategies such as

inclusion of cholesterol, photopolymerizable lipids, polymeric lipids through conjugation of polyethylene glycol (PEG) have been exploited to overcome the poor stability of the liposomes[65,354,355]. Photopolymerizable lipids consist of conjugated diynes in their alkyl tails, that can be stimulated by UV (ultra-violet) light[356,357], this aids in prevention of leakage and sustained release of contents[358–360].

The PEG molecules are known to cause steric stabilization in the liposomes. The hydrophilic PEG chains cover the surface of the lipid bilayer and extend and stay associated with the aqueous bulk instead of interacting with other molecules on the nearby liposomes[361,362]. Additionally, as the concentration of the PEG molecules increases in the bulk, the water molecules balance out by diluting the bulk concentration of PEG by keeping the PEG molecules apart, thereby preventing the agglomeration of PEGylated liposomes[224,362,363]. In addition to PEG, cholesterol is also used in liposomal formulations to induce rigidity to the bilayer to further control the inherent leakiness of the liposomes[364,365]. Cholesterol is also known to regulate the fluidity, permeability and packing of the bilayer[211,366]. Both cholesterol and PEG enriched liposomes have been approved by FDA for delivery of the potent drugs including doxorubicin as (Doxil®) and irinotecan (Onivyde™)[160]. However, cholesterol has shown to undergo oxidization in the presence of reactive oxygen species (ROS) resulting in the production of cholesterol oxidation products (COPs) or derivatives of oxysterols such as 7-ketocholesterol, 20α-hydroxycholesterol, 25-hydroxycholesterol, α,β-epoxycholesterol, and 7α, 7β-hydroxycholesterol, that cause atherogensis in humans[364,367–372]. Additionally, the majority of the cholesterol used in commercially available and FDA approved liposomal formulations in drug delivery and vaccine are derived from animal sources such as egg or wool grease that poses a threat of contamination and allergies [373].

In this work, we have investigated the stability of a Riboflavin encapsulated liposomes comprising of photopolymerizable lipid $DC_{8,9}PC$ lipids along with DSPE-PEG2000 and

cholesterol. Riboflavin was used as a model photosensitizer to test the efficacy of liposomal formulations in vitro for potential applications in Photo Dynamic Therapy (PDT) [320,322,374]. The work primarily focused on:

(i) thermal stability of the liposomal formulations through phase transition thermodynamics studies using Differential Scanning Calorimetry (DSC);

(ii) assessing the contributions of PEG and cholesterol in the physical stability of liposomal formulation.

Our findings indicate that the thermal and physical stability of the liposomal formulations can be achieved by exploiting the PEG ratio, and the choice of the lipid, thereby, eliminating the need of cholesterol. Such cholesterol-limiting liposomal formulations can address the safety concerns associated with the use of animal-derived cholesterol and further investigations are warranted to determine the optimum lipid type and PEG ratio for enhanced stability for the liposomes.

5.2 Materials and Methods:

5.2.1 Materials:

23:2 Diyne PC [$DC_{8,9}PC$] (1,2-bis(10,12-tricosadiynoyl)-sn-glycero-3-phosphocholine) and DSPE-PEG-2000(1,2-distearoyl-sn-glycero-3-phosphoethanolamine-N[methoxy(polyethylene glycol)-2000] (ammonium salt)) suspended in chloroform were purchased from Avanti Polar Lipids (Alabaster, AL). Cholesterol and Riboflavin-5-phosphate sodium salt dihydrate were procured from Sigma Aldrich. Invitrogen™ RNase-free PBS - Phosphate-Buffered Saline (PBS) pH 7.4 was purchased from Fisher Scientific. Invitrogen™ e-Bioscience™ Annexin V Apoptosis Detection Kit PE and 7-amino-actinomycin D (7-AAD) components were purchased from Fisher Scientific.

5.2.2 Preparation of Liposomes:

Lipids and cholesterol were suspended in chloroform. The lipid mixtures were dried under ultra-pure nitrogen environment to obtain a thin film in the bottom of the tubes that were hydrated with PBS buffer (10X) of pH 7.4. For the encapsulated liposomes, riboflavin was suspended the PBS buffer prior to hydration of dried films. On re-hydration, liposomes were uniformly sized by extruding through polycarbonate membrane of pore size 100 nm. Liposomes were prepared using thin film hydration technique and sized as described in prior literature[42,136,200,202,208]. Details of the formulations are given in Table 5-1. The unencapsulated riboflavin was removed by ultracentrifugation followed by rinsing with fresh batch of PBS buffer. The total liposome to riboflavin ratio was maintained at 20:1 by weight ratio in this study.

Table 5-1: Details of the formulations used in the study

$DC_{8,9}PC$ (L1) /DSPE-PEG-2000 (L2) / Cholesterol mole ratio (mol%)	**Formulation Name**	**Riboflavin (RB) added at lipid: RB (20:1) w/w ratio**
90/ 10	L1/L2 (90/10)	NO
80/ 20	L1/L2 (80/20)	NO
87.5/ 7.5/ 5	L1/L2 (90/10) + Chol (5)	NO
77.5/ 17.5/ 5	L1/L2 (80/20) + Chol (5)	NO
90/ 10/ 0	L1/L2 (90/10) + RB	YES
87.5/ 7.5/ 5	L1/L2 (87.5/7.5) + Chol (5) + RB	YES

5.2.3 Dynamic Light Scattering (DLS):

The size, polydispersity index (PDI) and surface charge of both encapsulated and unencapsulated liposomes were analyzed using a Malvern Instruments Zetasizer by dynamic light scattering method at 25 °C and at 173° backscatter angle with 120 s equilibration time.

5.2.4 Differential Scanning Calorimetry:

10 µl of the liposome samples were placed in T-zero Hermetic pan. The pans were sealed with a sample press prior to placing them on a TA Instruments Q-2000 DSC. The DSC scans were performed in an inert nitrogen environment maintained at 40 mL/min in the temperature range of 25 to 65ºC at a heating rate of10 ºC/min. The stability study for these formulations was conducted using a Differential Scanning Calorimetry (DSC) for a four-week time frame. DSC measures the specific heat capacity as a function of temperature. In this case lipids, on heating undergo a gel to fluid crystalline endothermic transition. These transitions are detected by the DSC and the main transition is a sharp intense peak that occurs at the melting point. The nature of the transition is affected in the presence of other molecules[338,375]. Any changes in the enthalpy of transition is measured from the area under the peak given by:

$$\textit{Calorimetric Enthalpy: } \Delta H_C = \int C_p dT \qquad (1)$$

Where C_p is the heating capacity. The changes in enthalpy is an indicator of stability.

5.2.5 Apoptotic Studies:

e-Bioscience™ Annexin V Apoptosis Detection PE and 7-AAD Kits for flow cytometry were used to measure early and late-stage apoptosis in human prostate cancer cells (DU-145).Briefly, the cells were grown in cell culture media (DMEM) supplemented with 4.5 g of glucose, 10% fetal bovine serum (FBS) and 1% penicillin/streptomycin). The cells were grown in cell culture flasks to form adherent monolayers and were stored in a humidified incubator at 37 °C and 5% CO_2.. , The cells were washed with PBS, seeded at a density of 5000 cells/well in 24 well plates, and allowed to grow overnight. Next day, riboflavin encapsulated liposomes at 200 µl volume were added to the cells. The cells were incubated overnight to ensure uptake of the liposomes. After 24 hr, the cells were treated with UV-light to cause photo-polymerization of $DC_{8,9}PC$ lipids and subsequent activation of the riboflavin-encapsulated

liposomes. The cells were then collected and washed with ice-cold phosphate buffered saline (PBS) followed by cells resuspension in 100 µl of 1X Annexin V binding buffer on an ice-cold bath. 5 µl of Annexin V was added to the 100 µl of cell suspension and incubated for 10-15 mins at room temperature. Next, the cells were washed with ice-cold PBS and resuspended in 200 µl of 1X binding buffer. Then, 5 µl of 7-AAD viability staining solution was added to the cell suspension. Finally, flow cytometry was used to detect the fluorescence of stained cells at excitation/emission maxima: Annexin V PE® : 499/521 nm; 7-AAD® : 535/617 nm with BD FACSAria IIu High-Speed Cell Sorter flow cytometer from BD Biosciences (Becton-Dickinson, San Jose, CA, USA).The data were viewed and analyzed using FlowJo v10.2 software from FlowJo LLC (Ashland, OR, USA).

5.3 Results:

5.3.1 Characterization of liposomal formulation: hydrodynamic diameter and surface charge

The size and surface charge of the liposomal formulations were recorded for four weeks. It was observed that the measured zeta potential of the formulations were in the range of -0.347±0.0075 mV or near neutral consistent to the zwitterionic nature of the DSPE lipids[376]. The near constant zeta potential also confirms the absence of un-associated and excess riboflavin in the liposomal solution. The average hydrodynamic diameters and polydispersity indices (PDI) of the formulations measured over a period of weeks are summarized in Fig 5-1. The size measurements studies conducted in Week 1 indicated that all the formulations were within the acceptable size range of 70-140±5 nm at a PDI of less than 0.25±0.0005 mV indicating the uniformity of the extruded liposomes. However, after week 4, most of the formulations agglomerated with a significant increase in the measured average diameters. The presence of cholesterol did not affect the size or PDI of the formulations. It is also observed that with an increase in DSPE-PEG 2000 by 10 mol% the aggregation and dispersity of the

particles also increased with time. It is implied that the presence of cholesterol has minimal influence on the physical stability of the liposomes with regards to the controlling the size and possibly their aggregation.

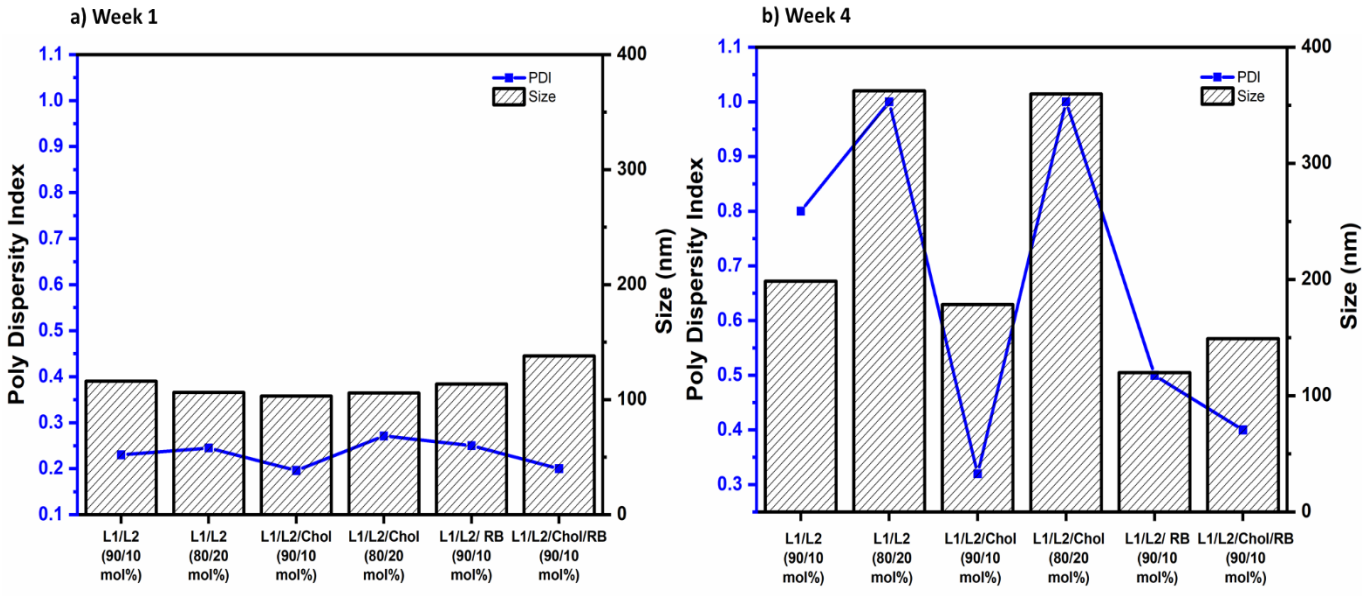

Figure 5-1: Size and PDI of the formulations for a) Week 1 b) Week 4

5.3.2 Differential Scanning Calorimetry-Thermal Stability Studies:

In this work, we have focussed on the stability study through thermal characterization (DSC) technique. DSC was used to study the phase behaviour and changes in $DC_{8,9}PC$ and DSPE lipid in the presence of PEG and cholesterol. The resultant changes in the melting temperature and shape of the melting peak as summarized on Fig 5-2. The melting temperature represents the transition from gel to fluid phase of the lipid molecules represented on the x-axis, whereas the area under the melting peak corresponds to the calculated change in enthalpy, $\Delta H_C = \int C_p \, dT$ of the lipid formulations summarized on Table 5-2. C_p is the specific heat capacity of the lipids plotted on the y-axis. In a lipid bilayer, the fluidity and the movement of the lipid molecules constitute the internal energy of the system. The fluidity of the bilayer is more as we get closer to the transition temperatures of the liposomes. This is demonstrated by the change in enthalpy. The change in enthalpy (ΔH) is represented as follows [377],

$$\Delta H\ (Change\ in\ Enthalpy) = \Delta U\ (Change\ in\ Internal\ Energy) +$$

$$\Delta(PV)\ (Change\ in\ Pressure\ x\ Volume) \quad (2)$$

The internal energy represents various molecular interactions occurring within the system. Since the liposomal formulations were sealed in T-zero hermetic pan during the DSC studies, the change in pressure (P) and volume (V) is considered negligible. Therefore, the change in enthalpy depends mostly on the inter-molecular interactions such as van der Waals forces occurring between the lipid, PEG and encapsulated riboflavin and intramolecular polar bonds.

The melting temperatures of pure $DC_{8,9}PC$, DSPE-PEG , and cholesterol are reported as 45°C, 52°C and 150°C respectively. [161,378,379]. Fig 5-3a) represents the thermograms of the formulations $DC_{8,9}PC$ liposomes containing 10 and 20 mol% of DSPE-PEG-2000 labelled as L1/L2 (90/10) and L1/L2 (80/20) by mol% respectively and measured at weeks 1 and 4. A slight decrease in the melting transition temperature of 0.43°C was observed for the formulation L1/L2 (90/10 mol%) over the four-week period. The associated enthalpy with the melting transition, which is also the indicator of the stability of the liposomal formulations was computed from the area under the melting peak and tabulated in Table 5-2. Despite the negligible shift in the melting temperature, the enthalpy of transition was found to be nearly doubled. With increased PEG from 10 to 20 mol% in the formulation L1/L2 (80/20 mol%), a significant shift towards a lower temperature from 43.16 °C to 41.81 °C denoted by blue lines on Fig 2a was observed. The temperature shift was accompanied a dramatic increase in the enthalpy by 178%. A discrepant observation in Fig 5-2b) thermograms was made in the presence cholesterol. 5 mol% of cholesterol was added to both L1/L2 at 90/10 and 80/20 formulations to study the effects of cholesterol on the stability of the formulations. L1/L2 (90/10) + 5 mol% cholesterol had imperceptible increase in transition temperature of 0.14°C and a decrease in enthalpy of 14.5% from week one to week four as observed in Fig 5-2b. However, L1/L2 (80/20) + 5 mol% showed a more prominent change in the temperature from

42. 48 °C to 43.58 °C and a significant decrease in enthalpy of 68.18% from week one to week 4. From Figs 5-2 a) and b), the L1/L2 (90/10) formulation demonstrated more consistent thermal behaviour with regards to change in enthalpy and melting temperature in the presence and absence of cholesterol observed in a period of four weeks. Fig 5-2c) compares the thermal stability of L1/L2 (90/10) formulations encapsulated with riboflavin in the presence and absence of cholesterol. A dramatic decrease in the enthalpy by 89% was noted by week 4 with L1/L2 (90/10) encapsulated formulations. However, the same formulations impregnated with 5 mol% cholesterol demonstrated a slight change in the enthalpy and melting temperature. DSC studies imply the role of cholesterol in acquiring thermal stability of the liposomal formulations.

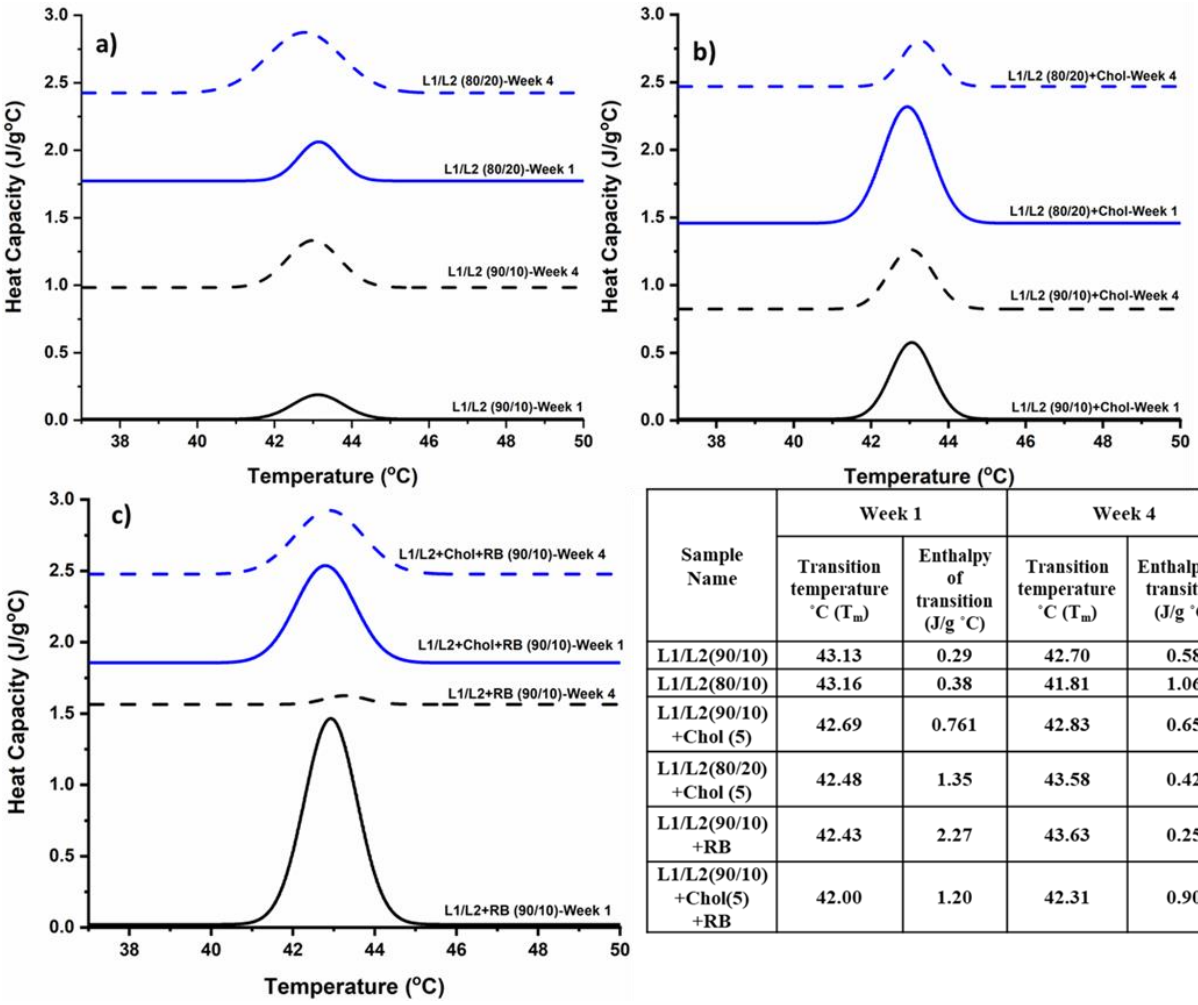

Sample Name	Week 1		Week 4	
	Transition temperature °C (T_m)	Enthalpy of transition (J/g °C)	Transition temperature °C (T_m)	Enthalpy of transition (J/g °C)
L1/L2(90/10)	43.13	0.29	42.70	0.58
L1/L2(80/10)	43.16	0.38	41.81	1.06
L1/L2(90/10) +Chol (5)	42.69	0.761	42.83	0.65
L1/L2(80/20) +Chol (5)	42.48	1.35	43.58	0.42
L1/L2(90/10) +RB	42.43	2.27	43.63	0.25
L1/L2(90/10) +Chol(5) +RB	42.00	1.20	42.31	0.90

Figure 5-2: DSC thermograms of liposomal formulations measured in weeks 1 and 4 a) DC8,9PC:DSPE-PEG-2000 (L1/L2) at (90/10) and (80/20) mole ratios b) L1/L2 (90/10) and (80/20) + 5 mol% cholesterol c) L1/L2 (90/10) only + 5 mol % cholesterol, encapsulated with riboflavin

5.3.3 Apoptotic Studies:

Previous studies have extensively reported the toxicity of encapsulated riboflavin in cancerous cells[136,380–382] and the non-toxic behaviour of the lipid formulations [161,225]. This *in vitro* work further delved into investigating the nature of apoptosis of encapsulated riboflavin under UV radiation. The apoptosis was assessed using Annexin V PE and 7-AAD quadrants in DU145 cells as shown in Fig 5-3. Apoptosis is indicated by the increased intensity of Annexin V as it bind to the phosphatidylserine in the cancerous cells[383].Q1 represents dead cells by necrosis (Annexin V PE^-/7-AAD^+),Q2 demonstrates dead cells by late apoptosis (Annexin V PE^+/7-

AAD$^+$), Q3 represents early apoptosis (Annexin V PE$^+$/7-AAD$^-$) and Q4 represents live cells devoid of apoptosis or necrosis (Annexin V PE$^-$/7-AAD$^-$)[384].

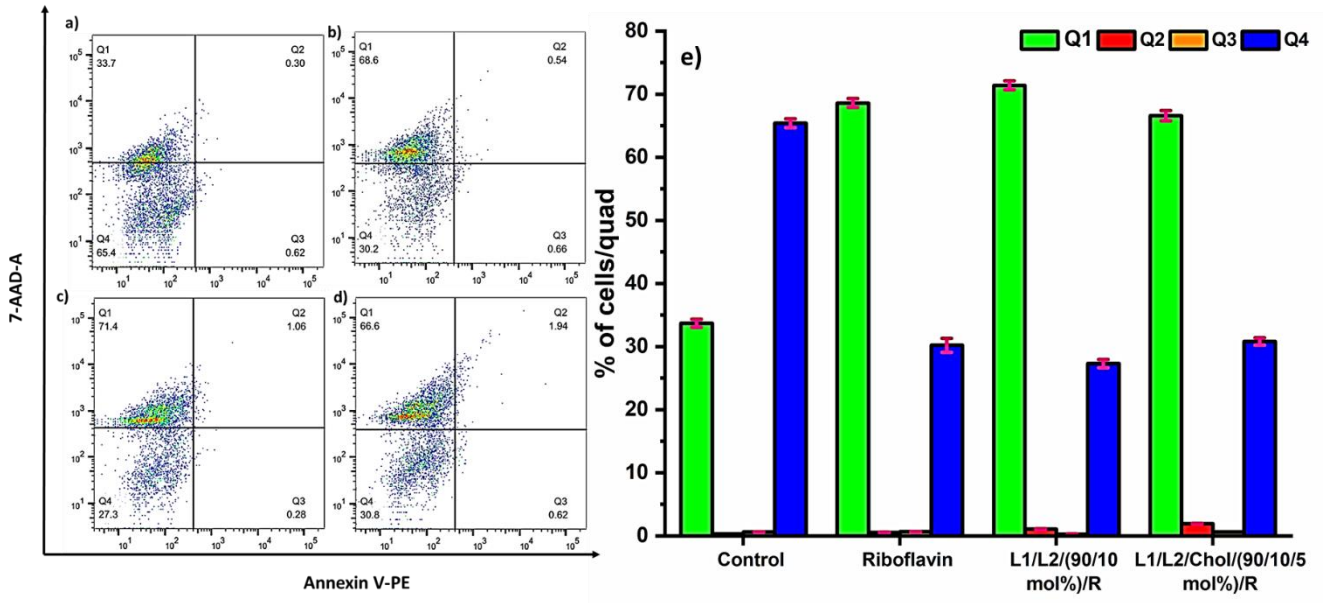

Figure 5-3: Apoptosis assay using Annexin V PE/7-AAD a) Control-Cells treated with UV b) Cells seeded with Unencapsulated Riboflavin and UV treated c) Cells seeded with Formulation L1/L2 (90/10 mol%)/RB and treated with UV d) Cells seeded with Formulation L1/L2/Chol (90/10/5 mol%)/RB and treated with UV e) Graphical representation of cell apoptosis in the four quadrants

Control UV treated cells (Fig 5-3a) were 65.4% viable. The addition of riboflavin and photoactivation resulted in increase in necrotic cells at 68.6% as seen in Figs 5-3b and e. Similarly, cells treated with photoactivated formulations L1/L2 (90/10 mol%) with encapsulated RB, and L1/L2 (90/10) + 5 mol% cholesterol with encapsulated RB showed an increase in necrotic cells by 71.4% and 66.6% respectively as depicted in Figs 5-3c-e. Riboflavin is known to produce reactive oxygen species (ROS) upon activation by UV radiation which are lethal to cancerous cells[7,374]. The cancerous cell lines in the presence of unencapsulated riboflavin showed a maximum necrotic rate of 68.6%. Riboflavin encapsulated photopolymerizable formulations, showed an equal to higher necrotic rate in the same cell lines. Our previous studies have shown that riboflavin encapsulated riboflavin formulations have >50% encapsulation efficiency [136]. This is noteworthy as encapsulated formulations shown similar

rate of effectiveness as free riboflavin. The necrotic rate of cholesterol based formulation L1/L2 (90/10) with 5 mol% cholesterol was found to be lower than L1/L2 (90/10) alone, which probably attributes to the lower drug loading capacity by the liposomes in the presence of cholesterol. This could be due to the lower reduced fluidity caused by the cholesterol molecules in the lipid bilayer during the encapsulation process [385,386]. This was also supported by our DSC studies that demonstrated insignificant change in melting behaviour of the liposomal formulations impregnated with cholesterol. It should also be noted that riboflavin in the absence of photoactivation does not induce apoptotic pathways and in fact, exhibits anti-proliferative/anti-migratory effects [384]. The mechanism of apoptosis/necrosis by ROS produced by encapsulated riboflavin is subject to further research.

5.4 Discussion:

5.4.1 Physical steric stability:

Agglomeration of liposomes is a key issue in drug delivery and vaccine design that can be addressed through electrostatic and steric stabilization shown schematically in Figs 5-4a and b. Another key requirement is their longer circulation times which can be achieved by rendering electrostatic stabilization that may be achieved by employing zwitterionic or uncharged surfaces to prevent their adherence to charged plasma proteins *in vivo* [71]. This work focused on using zwitterionic lipids to create liposome formulations, and to address the agglomeration issues, PEGylated lipids were incorporated. The incorporation of conjugated PEG or PEGylated lipids in liposomal formulations prevented the overall agglomeration as seen from the size measurements. PEG chains are grafted to the surface of the liposomes on one end and based on their concentration and density they result in mushroom or brush-type configuration as depicted in Fig 5-4.

At lower concentrations, the PEG chains do not interact with each other and assume a mushroom-like random coiled configuration shown in Fig 5-4c. With an increasing

concentration, the mushroom regime transitions to brush regime in which the PEG chains begin to uncoil or branch out and interact with each other as shown in Fig 5-4d. The transition from mushroom to brush regime happens when the following condition is fulfilled[74].

$$X_p^{m\to b} > [\frac{A_1}{\pi a_m{}^2}]n_p^{-1.2} \quad (3)$$

Where $X_p^{m\to b}$ is the mole fraction of PEG; for PEG lipids with chains of molecular weights 2000 (n_p=*45*) is presumed to occur at 0.014.

A_1 is the membrane surface area per lipid molecule[74].

Brush regime is preferred for drug delivery application for steric stabilization and longer circulation time[387–389]. However, when the concentration of PEG chains in the brush regime increases the surrounding aqueous layer dehydrates resulting in aggregation[390]. This is

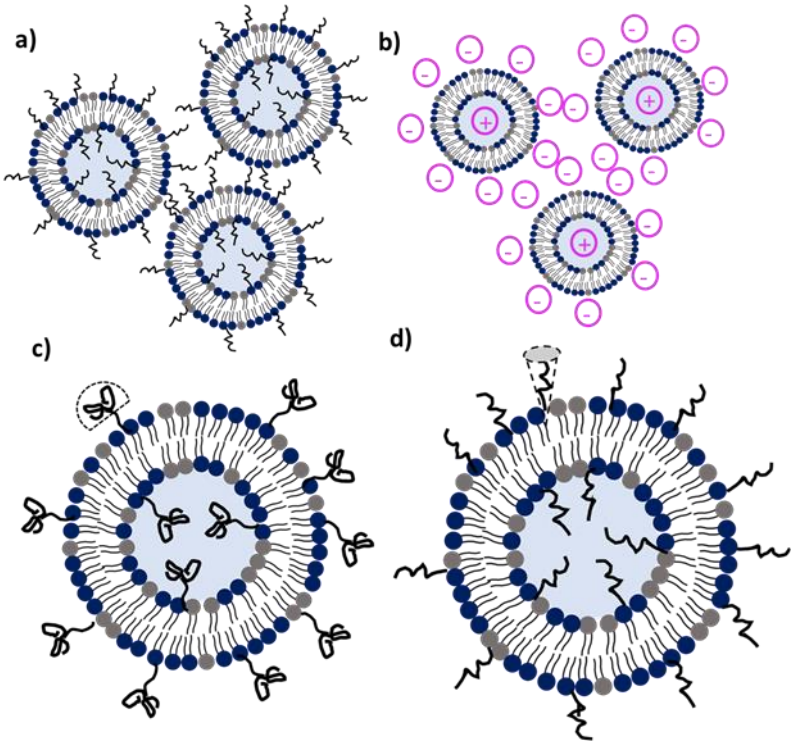

Figure 5-4: Schematic representation of a) steric stabilization of liposomes, b) electrostatic stabilization via opposite charges , c) mushroom regime with coiled PEG chains , and d) brush regime with extended PEG chains

observed in when the concentration of PEG lipids is increased from 10 to 20 mol% in LI/L2 (80/20 mol%) formulation, which aggregates after four weeks.

The hydrophilic nature of the elongated PEG chains in the brush regime tends to interact more with aqueous bulk than with the other grafted PEG chains of neighbouring liposomes, thereby preventing the agglomeration of the liposomes. The steric stabilization, $W(h)_{steric}$ between two liposomes of rendered PEG chains in brush regime of thickness L_b is quantified by

$$W(h)_{steric} = \frac{100RL_b^2}{\pi s^3} k_B T exp(\frac{-\pi h}{L_b}) \quad \ldots(4)$$

where k_B is the Boltzmann constant, $L_b = (N_{EO} \times l^{5/3} / s^{2/3})$. N_{EO} is the number of monomers in the PEG chain, l is the effective segment length and s is the distance between the grafting points[391].

5.4.2 Thermal stability*:*

The presence of DSPE-PEG2000 at 10 mol% in L1/L2 (90/10) formulation enabled the steric stabilization of $DC_{8,9}PC$ vesicles as evidenced by the size and zeta potential measurements in Fig 1, which is further supported by previous studies [161].

The enthalpy of transitions which quantifies the inter and molecular interactions, was found to increase in L1/L2 (90/10) and L1/L2 (80/20) formulations from week 1 to 4 with an accompanying decrease in the melting transition temperature as shown in Fig 5-2a. This is attributed primarily to the interaction and subsequent entangling of PEG chains which further increases the van der Waals forces. The energy required to overcome this van der Waals forces which is represented by an increase in enthalpy. Based on the DSC studies, it is noteworthy that increased concentration of PEGylated lipids from 10 to 20 mol% in the liposomal formulation, the resultant enthalpy of transition increases due to intermolecular interactions between the various lipid bilayer components.

Fig 5-2b) summarizes the combined effects of cholesterol and PEG on the thermal stability of the liposomal formulations. In L1/L2 (90/10) mol%, for every DSPE-PEG lipid there are 114 $DC_{8,9}PC$ lipid molecules. When 5 mol% cholesterol is added, there are 2 cholesterol molecules per one PEG molecule. It is implied that the addition of cholesterol to PEGylated lipids render thermal stability to the lipid bilayer owing to their known stabilizing properties of the liposomes. This is could possibly due to the lowered molecular interactions between the lipid components in presence of cholesterol in the lipid bilayer. Cholesterol, being hydrophobic gets incorporated in the bilayer region of the liposomes that results in an reorganized packing and respacing of lipids in the bilayer[386,392] limiting the interaction among the PEG chains which in turn lowers the van der Waals force [393].This results in a slight increase in melting transition temperature is accompanied by a decrease in the enthalpy. Additionally, the presence of PEG and cholesterol also induce heterogenicity to the bilayer, resulting in a lateral phase separation[338,394] which is supported by the broadening of melting peaks mostly seen during week 4 measurements indicated by blue lines on Fig 5-2b.

DSC and size analysis indicated the stability of $DC_{8,9}PC$/DSPE-PEG2000 (90/10) with and without 5 mol% cholesterol, which were further encapsulated with riboflavin. The riboflavin encapsulated formulations in absence of cholesterol showed an enormous change in enthalpy suggesting major intermolecular events in the lipid bilayer as seen on Fig 5-2c. This is attributed to the hydrophilicity of riboflavin that results in their encapsulation in the aqueous core and bound on the hydrophilic headgroup region of the bilayer that further increases the spacing and packing between the lipids[136]. The presence of cholesterol, however, counterbalances this lipid disorganization due to riboflavin binding consequently reducing the molecular forces responsible for the enthalpy change. Additionally, it is proposed that the presence of riboflavin in the aqueous core also prevents the entanglement of PEG chains in the

formulation further reducing the interactions between the PEG groups thereby concurrently reducing the enthalpy change in encapsulated formulations.

5.5 Conclusion:

The present study elucidated the distinct roles played by cholesterol and PEG in liposomal formulations by investigating varying concentration of each of the components in photo-polymerizable liposomes in the presence and absence of encapsulated riboflavin over a duration of four weeks. Following conclusions can be drawn based on the combined experimental and mechanistic studies:

a) PEG chains extend outward creating a layer around the liposomes that creates a steric layer that prevents liposomal agglomeration as supported by the lower polydispersity index, small hydrodynamic diameters, and surface charge measurements

b) Inclusion of cholesterol with PEGylated lipids at lower ratios lowers the overall enthalpy change arising from intermolecular interactions indicating the role of cholesterol in minimizing the molecular interactions and probably the bilayer fluidity

c) Encapsulated riboflavin further stabilized the formulations as confirmed by changes in the specific heat capacity and transition temperatures of the formulations

6 Thermotropic study of polyethylene glycol-based lipids on the stability of HPPH-encapsulated photoactive Lipid Nanoparticles (LNP)

This chapter is prepared by Poornima Kalyanram, Anu Puri and Anju Gupta for submission to an internationally recognized journal. This work is in collaboration with National Institutes of Health. In this work, we present the effects of size and ratio of polyethylene glycol (PEG) in photo-polymerizable lipids based liposomal formulations for the delivery of photosensitizer for potential photodynamic therapy applications. We also demonstrate a remarkable reduction in liposomal size and improved monodispersity due to the presence of hydrophobic HPPH photosensitizer in the lipid bilayer. Differential Scanning Calorimetry (DSC) studies were performed to demonstrate the stability of the formulations. The effects of varying ratios of the PEGylated lipids in the phase separation of the bilayer is indicated by the changes in the melting transition profile of the lipids. The effect of encapsulation of hydrophobic drug and the impact on the stability of the Lipid Nanoparticles (LNPs) is correlated through the enthalpy and thermotropic transition temperature.

6.1 Introduction

Liposomes or lipid nanoparticles are the self-assemblies of lipids in aqueous environment. Due to the presence of hydrophobic and hydrophilic regions, they can be used to encapsulate a variety of molecules. However, liposomes are susceptible to leakage and aggregation[64] hence stability of liposome is an important consideration for their applications in drug delivery[346,395] and vaccine design[63,396,397]. The headgroup and the chain length of the constituent lipids influences the overall packing , surface charge of the lipid bilayer and the stability of the liposomes or lipid nanoparticles (LNP's)[398,399]. An approach to overcome the leakage is to crosslink the acyl tail chains of lipids. Partial polymerization of lipid tails prevents the leakage of liposomal contents. The lipid tails are activated in the presence of light of a suitable wavelength to release the contents in the organ of interest[400,401]. Further, steric stabilization to prevent aggregation can be achieved by coating the surface of LNP's by polyethylene glycol (PEG), polyvinyl alcohol (PVA)[402,403], polylactic acid (PLA)[404,405], and polyglycolic acid (PGA) polymers[406,407] and block co-polymers[408,409]. Amongst these, only PEG polymer has shown an efficient and lasting steric stabilization[407,409].

$DC_{8,9}PC$ (1,2-bis(10,12-tricosadiynoyl)-sn-glycero-3-phosphocholine) is phospholipid which contains polymerizable diacetylene linked to the tail chains[410]. $DC_{8,9}PC$ is a photopolymerizable lipid that assembles into tubule-like structures in aqueous environment[411,412]. It is observed that $DC_{8,9}PC$ forms vesicle-like structures in the presence of matrix phospholipids like DPPC and other polymeric lipids like DSPE-PEG. The photo-activation of these liposomes results in release of the encapsulated molecules[225,357,413,414]. Our recent work demonstrated the inclusion of only PEGylated-DSPE lipids along with $DC_{8,9}PC$, in the absence of any matrix or helper lipids, resulted in formation of LNPs resulted in the formation stable vesicular lipid nanoparticles (LNP's) structures in the nanometer size range[161]. This unique lipid packing was found to be dependent on the included mole ratios of the

pegylated lipids (DSPE-PEG), with optimal concentrations of up to 20 mol%. Furthermore, these LNP's composed of this polymeric, $DC_{8,9}PC$ along with DSPE-PEG2000 successfully encapsulated of the photodynamic therapy (PDT) drug, 2-[1-hexyloxyethyl]-2-devinyl pyropheophorbide-a (HPPH) at relatively high concentrations. HPPH is a well-known hydrophobic photosensitizer, which has demonstrated faster skin clearance and deeper tumor penetration at lower dosage rates as opposed to various other FDA approved photosensitizers[415–417].

These LNP formulations were found to be stable at room temperatures and in the presence of serum components. The HPPH-loaded LNPs exhibited remarkable PDT efficiency and animal survival compared to the current formulations being tested in the clinical trials[161]. (Patent application, NIH E-154-2018; PCT/US2019/041464).These LNP have been demonstrated to have biomedical applications for enhanced drug delivery[161,418] .

Inclusion of hydrophilicity of the PEGylated lipids in LNP's induces stealth protection and stabilization preventing the attachment of macromolecules from the blood stream thereby resisting phagocytosis[104,110,419–421]. PEGylation also increases the packing order in the headgroup and the bilayer region[108,422–424]. It is also assumed that PEG molecules attract water and as a result form a steric barrier to the adherence of other macromolecules[425–427]. The PEGylated lipids usually assume mainly two conformations namely mushroom and brushes within the lipid bilayer based on their density. At lower PEG concentrations, the lipid head groups do not interact and follow random configurations, described as mushroom configurations. In contrast at high concentrations of PEG lipids, the surface associated mushrooms begin to overlap and transitions to brush conformations which results in expansion of membrane area due to the lateral pressure exerted by the brush conformations[109,393,428].

The thermal transitions in a lipid bilayer indicates the fluidity of the bilayer which has been widely studied using Differential Scanning Calorimetry (DSC)[341,375,429]. DSC has also been

used to study the encapsulation, stability, and thermal stresses of the liposomes. DSC is a sensitive technique which detects the changes to the pre-transition and the transition peak exhibited by the melting of lipids in the bilayer[345,430]. The composition of the constituent lipids in the LNP changes the thermal stresses of the system and affects the nature of the transition peaks. In addition, presence of encapsulated foreign molecules such as drug and protein in the bilayer has an impact on the thermogram[42,136,200,202]. These factors influence the shape of the thermogram and thereby the thermodynamic parameters of the liposomal formulations are calculated.

In this study, we investigated the steric stabilization and effects on lipid packing exerted by the DSPE-PEG lipid when mixed with $DC_{8,9}PC$ lipids at various ratios between a 1 and 50 mol%. The effects of varying molecular weights of PEG, MW= 1000, 2000 and 5000 is also reported. An extensive thermal analysis of the liposomal formulation encapsulating HPPH was conducted to study the phase changes and segregation of the lipid bilayer, quantify the thermotropic properties such as enthalpy (ΔH) and transition temperature (T_m) to test the stability of the formulations. This work provides a mechanistic understanding of the increased stability of the liposomal formulations in the presence of PEG. The novelty of the work lies in providing an insight on the effect of molecular weight and molar ratios of PEGylated lipid DSPE-PEG in a lipid bilayer comprising of a photopolymerizable lipid $DC_{8,9}PC$. The experimental investigation on the effect of stability by varying the molecular weights of DSPE-PEG in a photo-polymerizable liposome formulation has not been reported elsewhere.

6.2 Experimental Methods

6.2.1 LNP Formulations

(a) Materials Used:

The lipids used in this study were purchased from Avanti Polar Lipids- $DC_{8,9}PC$ (1,2-bis(10,12-tricosadiynoyl))-sn-glycero-3-phosphocholine (cat# 870016); DSPE-PEG1000 (1,2-distearoyl-sn-glycero-3-phosphoethanolamine-N-[methoxy(polyethylene glycol)-1000] (ammonium salt), cat# 880720); DSPE-PEG2000 (1,2-distearoyl-sn-glycero-3-phosphoethanolamine-N-[methoxy(polyethylene glycol)-2000] (ammonium salt), cat # DSPE-PEG2000)); DSPE-PEG5000 (1,2-distearoyl-sn-glycero-3-phosphoethanolamine-N-[methoxy(polyethylene glycol)-5000] (ammonium salt), cat # 880220). HPPH (2-[1-hexyloxyethyl]-2-devinyl pyropheophorbide-*a*) was synthesized by Dr. Gary Pauly (Chemistry Core, Chemical Biology laboratory, CCR). HBS buffer of pH 7.4 of reagent grade was used.

(b) Preparation and Characterization of LNP's:

Lipids suspended in chloroform were mixed in glass tubes. Details of various formulations are provided in Table 6-1. To prepare HPPH containing LNP's, known volumes HPPH solution (in DMSO) were added to the lipid mixtures prior to making the films. LNP's were prepared at 5 mg total lipid/ml in HBS, pH 7.4. Lipid suspensions were subjected to at least 5 freeze-thaw cycles and sonicated using a Probe sonicator (Branson Sonifier, Microtip probe, Fisher Scientific; 5-10 cycles, 1 minute per cycle followed by 1 minute of rest) using an ice bath. Unincorporated HPPH was removed by low speed centrifugation and LNP's in the supernatant were analyzed by dynamic light scattering (DLS).

Table 6-1: LNP's Formulations used in this study

$DC_{8,9}PC$: PEGylated lipid mole ratio	Liposomal (LNP) Formulation*	PEGylated lipid Type	HPPH Added (20:1 lipid: drug w/w)
100:00	$DC_{8,9}PC$ only	None	NO
90:10	$DC_{8,9}PC$ /1K (10)	DSPE-PEG1000	NO
99:1	$DC_{8,9}PC$ /2K (1)	DSPE-PEG2000	NO
95:5	$DC_{8,9}PC$ /2K (5)	"	NO
90:10	$DC_{8,9}PC$ /2K (10)	"	NO
80:20	$DC_{8,9}PC$ /2K (20)	"	NO
50:50	$DC_{8,9}PC$ /2K (50)	"	NO
99:1	$DC_{8,9}PC$ /5K (1)	DSPE-PEG5000	NO
90:10	$DC_{8,9}PC$ /5K (10)	"	NO
80:20	$DC_{8,9}PC$ /5K (20)	"	NO
90:10	$DC_{8,9}PC$ /1K (10)	DSPE-PEG1000	YES
90:10	$DC_{8,9}PC$ /2K (10)/HPPH	DSPE-PEG2000	YES
80:20	$DC_{8,9}PC$ /2K (20)/HPPH	DSPE-PEG2000	YES
90:10	$DC_{8,9}PC$ /5K (10)/HPPH	DSPE-PEG5000	YES

**The numbers in parentheses indicate the mol% of PEGylated lipid in the liposomal formulations added*

6.2.2 Dynamic Light Scattering

Liposomal formulations containing PEGylated lipids and $DC_{8,9}PC$ were suspended by probe sonication and diluted in HBS at either 1:20 or 1:40 (v/v) ratios. The size and dispersity index of the liposomes in the sample was measured using a Malvern Zetasizer (NANO ZS, Malvern Instruments, CA, USA).

6.2.3 Differential Scanning Calorimetry

DSC studies were performed on a TA Instruments Q-2000 DSC. 10 microliters of the sample were placed in T-zero Hermetic pan and sealed using DSC sample press. The samples were scanned from 25 to 75ºC at a heating rate of 10ºC/min in an inert nitrogen environment maintained at a flowrate of 40 mL/min.

6.3 Results and Discussion:

6.3.1 Size and surface charge of the LNPs:

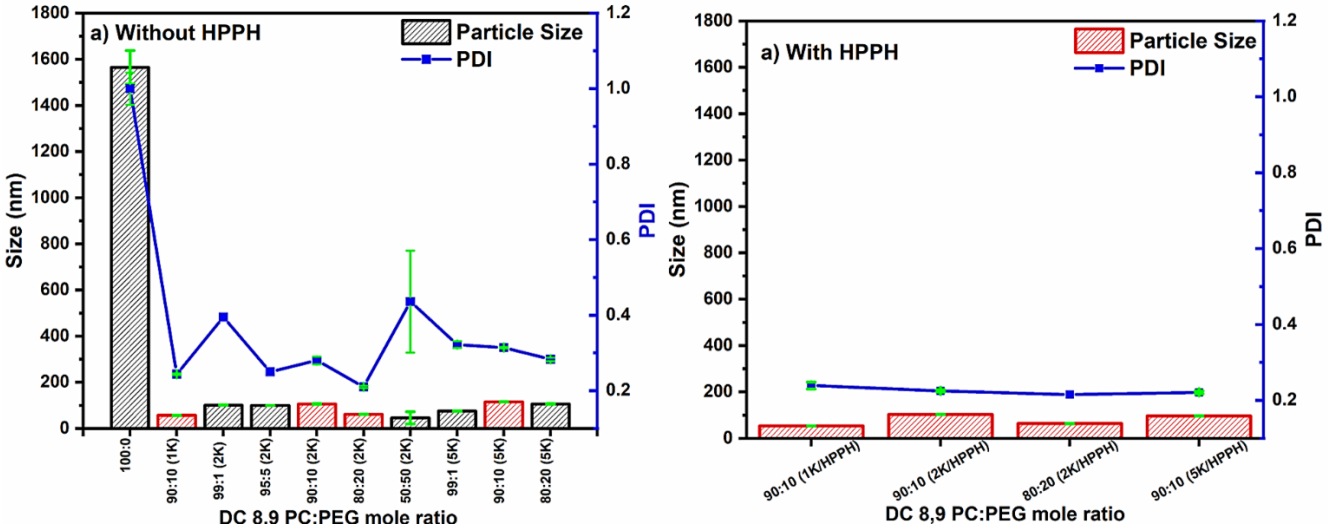

Figure 6-1: Size and PDI of a) LNP formulations prepared without HPPH; b) LNP's formulations prepared in the presence of HPPH (20:1 w/w, lipid: drug ratios, ref. Table 1)

Fig 6-1 indicates the average particle hydrodynamic diameter and polydispersity indices (PDI) of the liposomal formulations with (a) and without (b) encapsulated HPPH corresponding to the ones enlisted on Table 6-1. The results were reproducible from at least three independent experiments.

$DC_{8,9}PC$ lipids have reported to form larger tubular structures in aqueous solutions which is consistent with the large particle size of 1580 nm with a PDI >1[161,367]. Upon the addition of PEGylated DSPE to $DC_{8,9}PC$ lipids, the measured diameter of the resultant LNPs sizes reduced

from 1580 nm to the range of 50 to 110 nm with lower PDIs between 0.2 and 0.45. This 93-96 % reduction is size and induced uniformity in the particle diameters is attributed to the inclusion of DSPE-PEG in the tubular $DC_{8,9}PC$ bilayer. Owing to the large hydrophilic head group, DSPE-PEG, induces curvature in the tubular morphology at smaller concentrations. With an increase in concentration of DSPE-PEG, the outer layer of the tubular bilayer is increased resulting in a favorable shape transformation i.e., the formation of vesicles.(Fig 6-1a)[425,431–433]. It is also observed that the formulations with 10 mol% DSPE-PEG in the case of 1K and 5K DSPE- PEG and 10 mol% and 20 mol% DSPE-PEG2000 are found to be uniformly monodisperse. Since these formulations were found to be monodisperse and within the acceptable nano-carrier size range of 70-200nm[434,435], they were used to encapsulate hydrophobic drug HPPH. Fig 1b represents the change in hydrodynamic diameter and PDI of the selected formulations. The encapsulation of hydrophobic HPPH is seen to further reduce the average diameter of the LNPs representing an overall 5-15 % in size reduction at lower PDIs of 0.2. This is attributed to the tighter packing of the lipids induced by the presence of HPPH. The presence of donor hydrogen electrons in the porphyrin ring of HPPH molecules forms intermolecular bonds with acceptor oxygen atoms on the glycerol moiety in the lipids. An in-depth mechanistic study of the influence of varying concentration of HPPH in the lipid bilayer is under investigation. Preliminary studies indicate that higher concentrations of HPPH molecules in the bilayer leads to stronger bilayer packing and thus increases the stability of the lipid bilayer [425,431,436,437]

6.3.2 Thermal analysis of the LNPs

The scope of the current work it to investigate the changes in thermotropic phase behavior of $DC_{8,9}PC$ liposomes in the presence of DSPE-PEGylated lipids. The influence of varying concentration, molecular weights of PEG, and the presence of hydrophobic HPPH on the lipid segregation that leads to phase separation and domain formation in the lipid bilayer was

observed by DSC. Further quantification was performed by analyzing melting peak and calculation of associated enthalpy. The melting temperatures of pure $DC_{8,9}PC$ is 45 ˚C, pure DSPE-PEG dispersions (irrespective of molecular weight) was 52 ˚C and porphyrin photosensitizers degrade around 200-300 ˚C[378,438,439].

6.3.3 Effect of lower molecular weight DSPE-PEG (1000 & 2000) on Phase Transitions of DC $_{8,9}$ PC/PEG- DSPE LNPs without HPPH:

Fig 6-2 shows the DSC thermogram of $DC_{8,9}PC$/DSPE PEG 2000 with varying DSPE PEG 2000 concentrations.

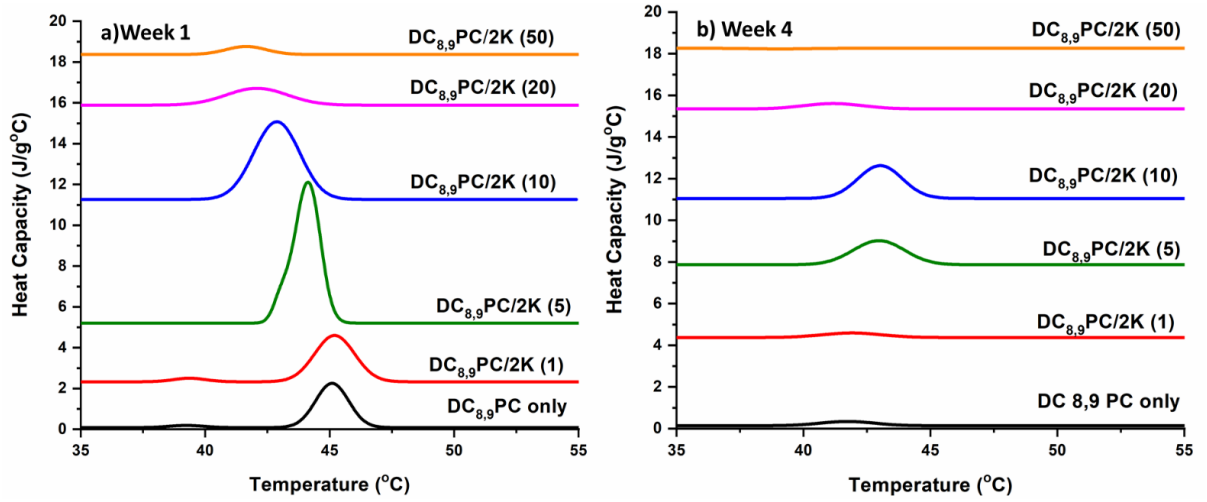

Figure 6-2: The DSC thermograms of $DC_{8,9}PC$/DSPE-PEG 2000 LNPs varying in PEG lipid concentrations

Fig 6-2a. shows the thermograms of the formulation measured at the end of week 1 that shows a clear shift of the main melting transiting peak towards lower temperature with increased in mole ratio of PEG-2000 associated DSPE lipids. Pure $DC_{8,9}PC$ liposomes show a melting peak (T_m) at 45˚ C with a small pretransition peak around 38˚C (shown in black) which is reported to occur due to the melting of the characteristic tubular microstructures of $DC_{8,9}PC$ that are formed at lower temperatures[440]. These microtubular structure were observed during the size

analysis as shown earlier in Fig 6-1a. In the presence of 1 mol% of DSPE-PEG2000 lipid (red), no significant change was observed except a slight broadening of the melting peak compared to pure $DC_{8,9}$ PC. However, at 5 mol% DSPE-PEG2000, a very sharp melting peak at a slightly lower temperature of 43.97˚ C with larger heat capacity was observed in addition to the disappearance of the small peak at 38 ˚C. On further increasing the DSPE-PEG2000 concentration to 10 mol%, the main transition peak broadened and shifted to 42.87 ˚C. With subsequent addition of DSPE-PEG2000 at 20 and 50 mol%, the main transition peak began to diminish while shifting towards lower temperature. The thermographs for the corresponding formulations in the week 4 on Fig 6-2b showed similar trends however, with reduced prominence of the melting peak. We also observed that at the end of 4 weeks (Fig 6-2b.), except for formulations (2K (5) & 2K (10)), all the other formulations were devoid of significant enthalpies of transition. Further quantification of the melting behavior was performed by calculating the area under the peak or the enthalpy of transition and the half width of transition that reflects the nature of the transition. The nature of the transition is affected by the constituent lipids molecules (DSPE-PEG and $DC_{8,9}$PC) in the bilayer. The presence of foreign molecules (HPPH) and their effect on the cooperativity of the bilayer in undergoing a transition is also indicated by the enthalpy and the half-width of transition[202,341,429].

In week four, formulation 2K (5) has a 66% decrease in enthalpy with broadening of the T_m peak and a transition shift to 42.96 ˚C. Similarly, 2K (10) exhibited a 61% decrease in enthalpy with negligible change in $T_{m.}$ This decrease in enthalpy after four week is possibly due to the steric exclusion experienced by the overlapping of the grafted PEG on the head groups leading to the dehydration of the lipid bilayer[441,442]. This results in disrupting the bilayer surface, which is represented by the widening of the peak.

The addition of DSPE-PEG2000 lipid to $DC_{8,9}$PC in the examined range (1 mol% to 50 mol %), during the formation of LNP's, decreased the transition temperature and altered the

associated enthalpy of transition of DC8,9PC bilayers as reported in Table 6-2. Table 6-2 enlists the thermodynamic properties associated with the melting peak observed in Figs 6-1a and b.

Table 6-2: Calculated Thermodynamic Parameters

Sample Name	Week 1			Week 4		
	Transition temperature ˚C (T_m)	**Enthalpy of transition (J/g ˚C)**	**Half Width of Transition ($\Delta T_{1/2}$)**	**Transition temperature ˚C (T_m)**	**Enthalpy of transition (J/g ˚C)**	**Half Width of Transition ($\Delta T_{1/2}$)**
$DC_{8,9}PC$	45.09	3.6	1.67	41.67	2.05	2.4
1K (10)	42.42	1.18	2.8	42.66	0.81	2.1
2K (1)	45.19	4.55	4.02	41.9	0.626	2.89
2K (5)	43.97	8.54	1.37	42.96	2.9	2.28
2K (10)	42.87	8.66	2.03	43.02	3.4	2.02
2K (20)	42.04	2.5	2.5	41.17	0.74	2.94
2K (50)	41.66	0.8	1.65	No peak Observed		
5K (1)	42.06	3.33	1.92	44.11	1.69	1.3
5K (10)	42.06	6.08	1.99	42.92	1.24	1.93
5K (20)	43.17	0.49	4.76	42.79	0.627	2.18

According to the first law of thermodynamics, ΔH(Enthalpy) = ΔU (Internal energy) + Δ(PV); since pressure and volume remains constant in a DSC cell, enthalpy then becomes equal to internal energy. Internal energy corresponds to the energies including translational kinetic energy, vibrational and rotational kinetic energy and potential energy arising from intermolecular forces at microscopic level[377].The motion of lipids is affected by temperature which results in change in the internal energy and thus impacting the enthalpy.

The change in enthalpy observed in Table 6-2 occurs due to lateral separation of lipids induced by the presence of DSPE-PEG lipids[394,443] in the $DC_{8,9}$ PC bilayer. Lateral separation is brought by the heterogeneity of lipids present in the bilayer. Besides, the presence of three different head groups- zwitterionic PC and PE and PEG chain; the intermolecular acyl tails in the different lipids as well as the presence of dienes in the tail chain increases the heterogeneity of the LNP carriers[444,445]. These groups result in lateral phase separation which is indicated by the broadening of the transition peaks.

Furthermore, the main phase transition temperature of $DC_{8,9}PC$ bilayer membranes was shifted to a lower temperature by the addition of DSPE-PEG. The shift became significant as the mole fraction of DSPE-PEG increased. This may be attributed to several reasons. The presence of intercalated PEG is their amorphous state in the LNP's maybe disrupting the hydrogen bonding between the adjacent PC head groups thereby destroying the structural arrangement of the head groups. Since the transition temperature is affected by the head group species, the meting point is decreased as the concentration of DSPE-PEG increases[300,446]. The presence of salt in the HBS buffer might have induced an osmotic stress resulting in decrease in size of the LNP's. To maintain the shape of the bilayer, some lipid molecules adopt a $P_{\beta'}$ ripple phase from the crystalline L_β phase. This presence of rippled tails results in lowering of phase transition temperature[447,448].

Since the 10mol % DSPE-PEG2000 exhibited greater stability for a period of 4 weeks, we tested the stability of LNP's formulation of 10 mol % DSPE-PEG1000 when added to the $DC_{8,9}PC$ lipids (1K (10)) (Fig 2a). Over the four-week period, there is no change in the T_m (T_m for this formulation = 42.5 ˚C) and enthalpy increases by 45% (Table 6-2). The increase in enthalpy in the case of smaller lipid chain (DSPE-PEG1000) might be because of the van der Waals forces governing the intercalation of PEG chains weakens over time resulting in an undisrupted bilayer[136].

6.3.4 Effect of higher molecular weight DSPE-PEG (5000) on Phase Transitions of DC $_{8,9}$ PC/PEG- DSPE LNPs without HPPH:

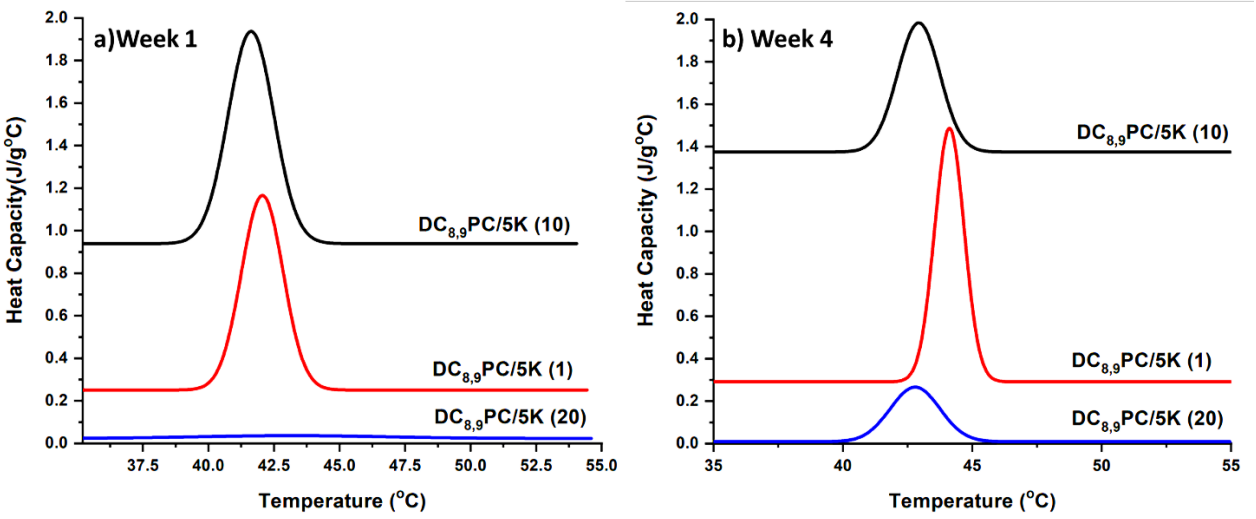

Figure 6-3: The DSC thermograms of binary mixtures of DC$_{8,9}$PC/DSPE-PEG 5000 LNP's varying in PEG concentrations

Effect of presence of high molecular weight PEG associated with DSPE lipid in mixed liposomes with DC$_{8,9}$PC lipids were studied at varying ratios of PEG5000 after weeks 1 and 4. Fig 6-3 represents the DSC thermographs of DC$_{8,9}$PC/DSPE-PEG5000 at 1, 10 and 20 mol% ratios of PEG5000. This study focused on primarily 1 and 10 mol % ratios, since concentrations higher concentrations > 20 mol% resulted in the disappearance of the melting peak due to lateral phase separation[161].

In the presence of 1 mol% of DSPE-PEG5000 lipids, the T_m was found to be 42.06 ˚C at the end of week 1, which increased to 44.11 °C demonstrating a 23% decrease in enthalpy due to the narrowed peak. Compared to DSPE-PEG2000, where the 1 mol % formulations showed a 31.5% decrease in enthalpy.

With formulation 5K (10), T_m remains the same as 5K (1) at the end of week 1. At the end of week 4, there is a slight shift in T_m to 42.92 ˚C, with a reduction in peak height and enthalpy by 79%. At 20 mol% of DSPE-PEG5000, a very broad peak at 43.17˚C with an enthalpy of

0.49 J/g˚C and $\Delta T_{1/2}$ = 4.8 ˚C, at the end of week 1 was observed. Subsequently, at week 4, there was a shift of T_m to 42.79 ˚C, with an increase in 28% enthalpy. The reduction in enthalpy in the DSPE-PEG5000 formulations is congruent with formulations containing 10 and 20 mol% DSPE-PEG2000. The increase in transition temperature and decrease in enthalpy at the end of four weeks in samples containing DSPE-PEG5000 is caused by the increased length of PEG chain on the lipid head group as tabulated in Table 6-2. The longer PEG chains in the DSPE-PEG5000 has an increased mobility resulting in more inter and intra molecular interactions, thus adding to the internal energy of the system. This increased chain length results in additional van der Waals forces the between the PEG moieties in the lipid head group, leading to higher transition temperatures[69,449]. However, the presence of $P_{\beta'}$ ripple phase reduces the enthalpy involved in transition[447,448].

Thermal analysis studies, LNP sizes and their PDIs, indicated that the formulations containing 10 and 20 mol% PEG 2000 and 10 mol% of DSPE-PEG 1000 and DSPE-PEG 5000 remain stable over a period of four weeks. Additionally, the size distribution of these LNP formulations remain monodisperse. Based on the stability data, HPPH encapsulated LNPs were synthesized comprising of 10 mol% DSPE-PEG (1000, 2000 &5000) lipids & 20 mol% DSPE-PEG2000.

6.3.5 Effect of incorporation of HPPH on the DC $_{8,9}$ PC/DSPE-PEG LNPs:

The HPPH encapsulated LNPs were monodisperse in nature with a PDI $\leq$ 0.2 like the unencapsulated LNPs of the same formulation. However, the presence of HPPH systemized the bilayer packing and there was a 5-15% reduction in size depending on the mol % and molecular weight of the DSPE-PEG used in the bilayer. Further, the effects of presence of HPPH on the DSPE-PEG molecular weight and mol%, can be inferred from the results of the thermal analysis shown in Fig 6-4.

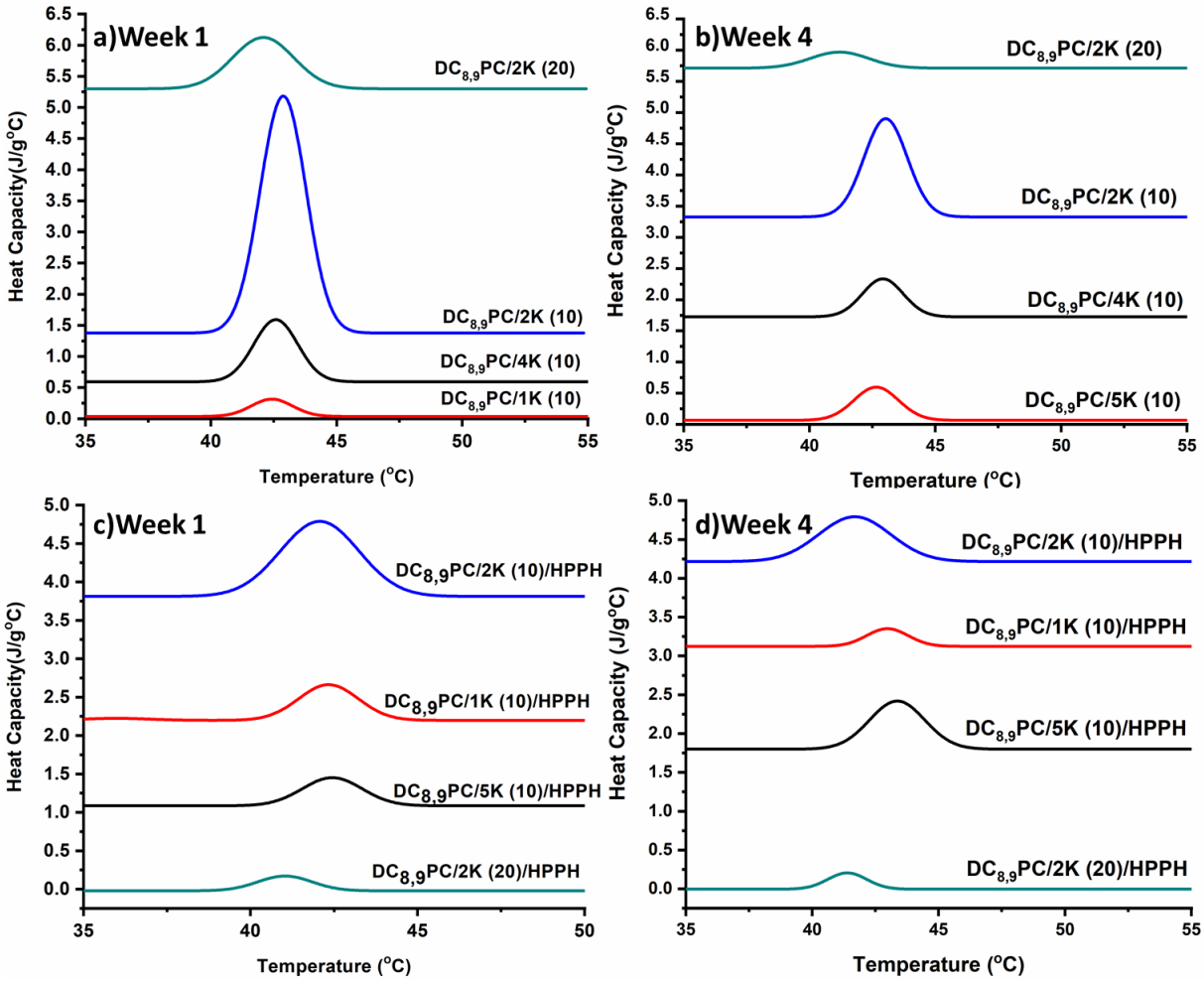

Figure 6-4: 90:10 $DC_{8,9}PC$/DSPE-PEG formulation in the absence of HPPH (a,b); DC 8, 9 PC/DSPE-PEG formulation in the presence of HPPH (c, d)

Fig. 6-4 a, b represents the stability of formulations containing 10 mol% of DSPE-PEG LNP's of varying PEG chain length (i.e. 1000,2000,5000). When compared to unencapsulated LNPs 2K (10), during week 1, on incorporating HPPH (Fig 6-4c), there is no significant change in the enthalpy of transition and the T_m is shifted to a slightly lower temperature (T_m = 42.06 ˚C). In the week 4, 2K (10)/HPPH, had further shifter to a lower T_m of 41.67 ˚C with an enthalpy of transition of 2.05 J/g˚C, which was 40% decrease in enthalpy as compared to the plain sample in Fig 6-4b.

Similar trends of lower T_m & enthalpy have been observed in formulations with HPPH has been observed with 1K (10), 2K (20) and 5K (10) as tabulated in Table 6-3. However, all the

formulations with HPPH have their enthalpies lesser than the plain samples at the end of week four except with 5K (10). This is because HPPH being hydrophobic gets accumulated in the tail region of the bilayer. HPPH has donor hydrogen electrons in the porphyrin ring which interact with the acceptor oxygen electrons in the glycerol moieties and form hydrogen bonds[436,437]. The presence of HPPH in the hydrophobic alkyl tails also results in van der Waals forces and results in increased tightness of packing and the membrane curvature. The formation of these bonds results in lesser mobility of the lipid molecules and thereby reducing the internal energy of the HPPH loaded liposomes. This is indicated by the decrease of enthalpy in congruence with the size data [450,451].

Table 6-3: Change in transition temperature and enthalpy of transition on addition of HPPH

Formulation Name	Week 1		Week 4	
	Transition temperature ˚C (T_m)	Enthalpy of transition (J/g ˚C)	Transition temperature ˚C (T_m)	Enthalpy of transition (J/g ˚C)
1K (10)	42.42	0.81	42.66	1.18
1K (10)/HPPH	42.32	6.79	42.97	0.468
2K (10)	42.87	8.66	43.04	3.4
2K (10)/HPPH	42.06	8.08	41.67	2.05
2K (20)	42.04	2.5	41.17	0.74
2K (10)/HPPH	41.06	0.38	41.37	0.21
5K (10)	42.02	6.08	44.11	1.69
5K (10)/HPPH	42.45	0.89	42.92	1.24

In samples 1K (10)/HPPH and 2K (10)/HPPH &2K (20)/HPPH, the enthalpy reduces from week 1 to week 4. With 1K (10)/HPPH, 2K (10)/HPPH and 2K(20)/HPPH, the enthalpy reduction at the end of week 4 is very significant because van der Waals force between the shorter PEG chains are disrupted by the presence of HPPH in the hydrophobic zone. However, in 5K (10)/HPPH, there is a significant increase in enthalpy at the end of week 4. This is assumed due to the strong van der Waals force arising from the intercalation of longer DSPE-5000 PEG chains, which counteracts the presence of HPPH. This results in an increased curvature of the LNP rendering them unsuitable for drug delivery applications.

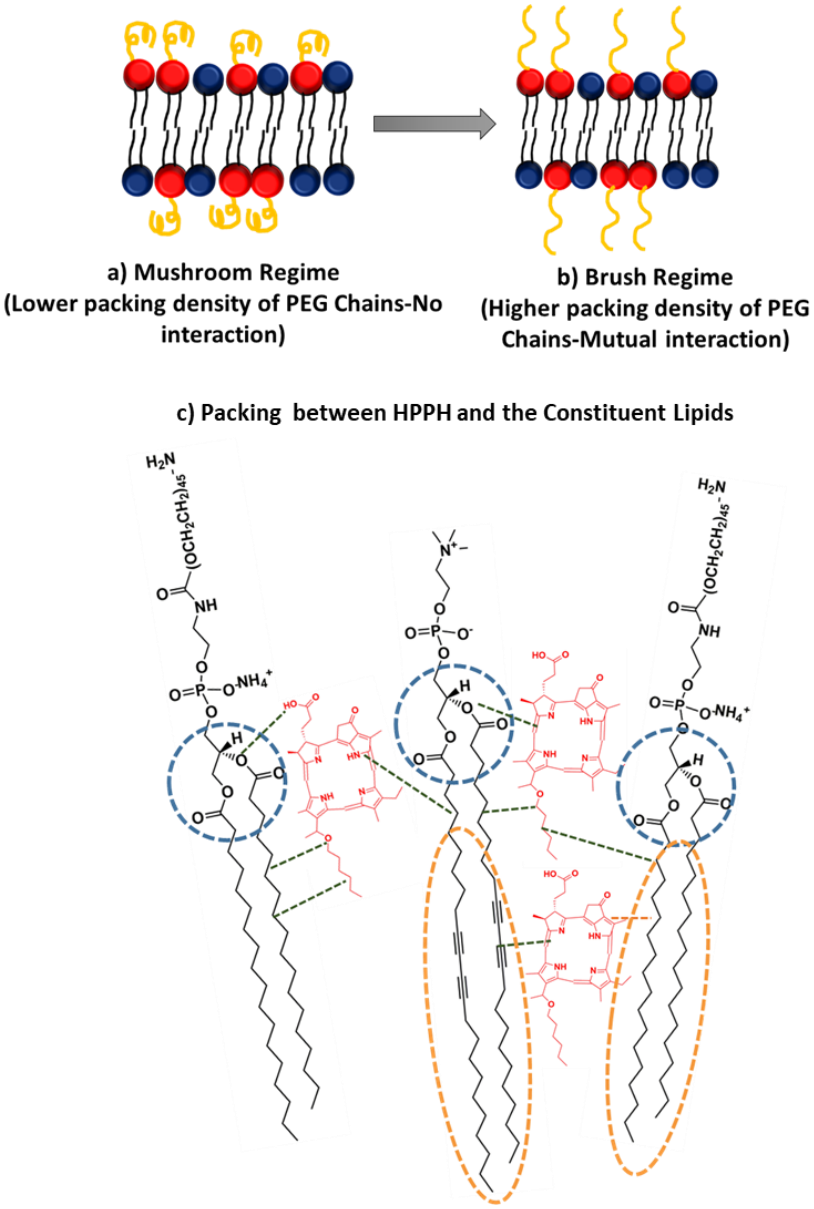

Figure 6-5: Schematic representation of a) Mushroom regime b) Brush Regime, due to shorter chain length; loss of curvature c) packing forces between HPPH and the constituent lipids in LNPs

Thus, we can infer from the size and DSC results that, out of four of the formulations that encapsulated HPPH, 2K (10)/HPPH is the optimum formulation because size of the carrier (104 nm) is well within the standard size range of the nano-carriers (70-200nm) used in drug delivery.

The reduction of enthalpy in the presence of HPPH, which corresponds to phase separation of formulation, at the end of week 4 is not significant compared to 2K (10)/Week 4. This is

presumed due to the optimum van der Waals force that counteracts the presence of HPPH in the hydrophobic zone and is responsible for the stability of the formulation as shown in Fig 6-5.

6.4 Conclusions

In this work, we have investigated the effect of various chain lengths and molar ratios of DSPE-PEG lipids when included with $DC_{8,9}PC$ lipids. The size, dispersity and DSC study reveal that:

1. Inclusion of DSPE-PEG at lower molar ratios (1-20 mol%) induce uniform dispersity to $DC_{8,9}PC$ vesicles. However, at higher molar concentrations, heterogeneity of lipid molecules causes lateral phase separation.
2. DSC studies confirm that formulations with 10 and 20 mol % of DSPE-PEG 2000 and 10 mol% of DSPE-PEG 1000 & 5000 form stable LNPs with uniform dispersity.
3. Hydrophobic HPPH forms hydrogen bonds and van der Waals forces with the lipid moieties resulting in organized packing of the bilayer.
4. The four week DSC stability study also confirm that DSPE-PEG of chain length 2000 has optimum van der Waals force and offers a four-week stability when a hydrophobic drug is encapsulated as compared to short chain DSPE-PEG1000 and long chain DSPE-PEG5000.

7 Conclusions and Future Recommendations

7.1 Summary:

In this dissertation, amino methyl coumarin was conjugated with hydrophobic alkyl tail chains to increase the amphiphilicity of the molecule. The interactions studies revealed that binding to the lipid bilayer was through charge difference. The mechanism of the bilayer destabilization was alkyl chain length and concentration dependent. Besides, FDA approved photosensitizers (PS) were encapsulated in PEGylated liposomes. The addition of PEGylated lipids to the liposomal formulation increased the steric stability and reduced aggregation. The above goals were achieved by utilizing the versatility of liposomes to function as model cell membrane and as carriers for drug delivery. This fundamental work is aimed at understanding and improving the chemical structure and pharmacological properties of photosensitizers, to achieve therapeutic success in Photo Dynamic Therapy (PDT) for cancer applications.

To realize the goal of understanding the interaction mechanisms of photosensitizers using biophysical techniques, riboflavin was used as a baseline. The initial studies involved studying the interactions of zwitterionic DPPC and DPPC/Cholesterol liposomes with riboflavin, a well-known photosensitizer. One- and two-dimensional NMR was used to understand the interactions with the phospholipid membrane. However, NMR was insensitive to the liposome concentrations under study and labor-intensive nature of NMR resulted in an inconclusive study. The results of the NMR are elucidated in the appendix section. Subsequently, the interactions between riboflavin with DPPC and DPPC/Cholesterol liposomes was investigated using Dynamic Light Scattering (DLS) and differential scanning calorimetry (DSC). The results of this study are elaborated in chapter 4 of this dissertation. DLS studies concluded that riboflavin bound to the DPPC liposomes predominantly through electrostatic interactions. The

riboflavin molecules inserted itself in the outer leaflet of the lipid bilayer causing minimal perturbation of the lipid bilayer. Further insertion was not possible due to the hydrophilic nature of riboflavin, resulting in its lower bioavailability and efficacy. Encapsulation of riboflavin in liposomal formulations of DPPC and cholesterol increased the bioavailability. However, cholesterol caused aggregation of liposomes thus lowering stability and the loading capacity as well. Thus, we investigated ways to maintain the stability of formulations which is detailed in our work in Chapter 5 of this dissertation. Aggregation of liposomes is prevented by inducing steric stabilizations in formulations; this is done by adding PEGylated lipids to the liposomes. Riboflavin was encapsulated in a formulation containing 90 mol% photo-polymerizable lipid $DC_{8,9}PC$ and 10 ml% DSPE-PEG 2000. It was found that this formulation had a shelf-life of four weeks without aggregating and the photo-polymerizable lipid $DC_{8,9}PC$ reduced the leakage, thus eliminating the need for cholesterol. This solved the bioavailability issue associated with riboflavin.

However, the efficacy of PDT relies on the penetration power of the PS molecule. Hydrophilic molecules such as riboflavin, fail to penetrate deeper into the tissues. It has been demonstrated that amphiphilic fluorophore probes (linked with hydrophobic tails[171–173]) have better cellular uptake. Probes with longer hydrophobic tails showed better uptake, due to their ability to penetrate deeper into the cell membrane due to electrostatic,[174,175] hydrophobic,[42,176,177] and hydrogen bonding interactions[178,179]. However, amphiphilic riboflavin probes have already been researched upon as components for liposomal formulation for drug delivery applications[452]. Another well-known fluorophore is 7-amino-methy coumarin. 7-amino-4-methylcoumarin (AMC) is of importance because of the presence of electron donating amino group in the 7^{th} position, [253,258] which can donate electrons and acts as fluorescence enhancers for probing applications with longer wavelengths and improved intensity.[259,260] We designed a novel class of amphiphilic amino-coumarin fluorophores C_n, by attaching linear alkyl tail

chains to amino-coumarin molecules, where n = 5 to 12. These fluorophores were synthesized by one-step synthesis and demonstrated a higher cellular uptake in cancerous cells. The mechanism of uptake and cellular destabilization were investigated using liposomes as described in Chapter 3 of this dissertation.

The model cancerous cell membrane (DPPC/DPPS) was prepared by thin film hydration technique. The coumarin fluorophores were added to the preformed liposomes and the binding and interactions were studied using dynamic light scattering (DLS), differential scanning calorimetry (DSC), fluorescence spectroscopy, isothermal titration calorimetry (ITC) and molecular dynamics (MD) simulations. Our studies indicated that the amphiphilic coumarin molecules were first attracted to the bilayer through electrostatic interactions. The penetration to the bilayer was controlled by the concentration of the molecules and the alkyl chain length $C_{n.}$ It is important to note that at smaller concentrations of amphiphilic coumarin, the membrane remained stable, and the membrane thinning was a consequence of flip-flop of coumarin molecules in the inner and outer leaflets. The nature of binding and uptake of these molecules was quantified by ITC studies. It was concluded that enthalpy is the major driving force in the uptake of coumarin fluorophores. Besides, our preliminary cell studies reveal that these fluorophores can be used as potential photosensitizers (PS) in Photodynamic Therapy (PDT). Our work thus clarifies that the efficacy issue surrounding hydrophilic PS molecules can be overcome by inducing amphiphilicity.

Chapter 6 of this work investigates encapsulation of hydrophobic photosensitizers. HPPH (also known as Photochlor) well-known hydrophobic photosensitizer, which has demonstrated faster skin clearance and deeper tumor penetration at lower dosage rates as opposed to various other FDA approved photosensitizers[415–417]. To further enhance the penetration power and selectivity of HPPH, encapsulation with photopolymerizable $DC_{8,9}PC$ and DSPE-PEG. In this work, the effect of molecular weight of PEG chains and composition on the encapsulation of HPPH was

studied extensively using DSC and DLS. Dynamic light scattering and differential scanning calorimetry was used to optimize the composition of lipids and PEG chain length (DSPE-PEG 1000, DSPE-PEG 2000 and DSPE-PEG 5000) and understand the effect of each of the components on stability. It was concluded that the optimum PEG chain length of 2000 and 10 mol% of PEGylated lipid has optimum van der Waals force and offers a four-week stability when HPPH is encapsulated as compared to short chain DSPE-PEG1000 and long chain DSPE-PEG5000.

7.2 Key Contributions:

The key contributions of this work are as follows

i. Hydrophilic Photosensitizers such as riboflavin and coumarin interdigitate with the lipid headgroup and do not penetrate further into the hydrophobic zone. Their efficacy can be enhanced in two ways a) by conjugating hydrophobic alkyl chains thereby inducing amphiphilicity b) by encapsulating them in liposomal formulations

ii. Liposomal formulations containing zwitterionic lipids and cholesterol aggregate quickly due to the absence of steric stability. Steric stability is induced by coating liposomes with PEGylated lipids. The addition of PEGylated lipids eliminates the need for cholesterol in formulations. The molecular weight and composition of PEGylated lipids determine the stability of the formulations. Short chain PEG lipids (DSPE-PEG 1000) have low intermolecular force of attraction resulting in lesser steric stabilization Very long chain PEG lipids (DSPE-PEG5000) have very high intermolecular forces of attraction, resulting in entanglement of polymeric chains. Intermediate chains (DSPE-PEG2000) have optimum van der Waals force that helps in sustaining hydrophobic HPPH and hydrophilic riboflavin photosensitizers in liposomal formulations.

iii. The conjugation of alkyl chains to hydrophilic coumarin resulted in deeper penetration into the lipid bilayer. Short chain C_5 had more hydrophilic properties and did not reach

the lipid tails at lower concentrations. At higher concentrations, C_5 demonstrated ejection-reinsertion mechanism at the surface resulting in membrane thinning. Longer chain C_{12} is more hydrophobic and penetrates to the lipid bilayer zone. At higher concentrations, flip-flopping of C_{12} between inner and outer leaflets results in membrane destabilization. Enthalpy is the major driving force behind the binding and insertion process.

iv. Mechanistic examination of these interactions is established by a combination of calorimetric and dynamic light scattering techniques in this dissertation. DSC elaborated on the thermodynamic parameters involved in the interaction and stability studies, while DLS and ITC provided congruent information on nature and kinetics of binding. These combinations of these techniques eliminated the need for heavy spectroscopic and electron microscopic measurements in this dissertation.

v. The findings from the work are summarized in 7 journal articles and disseminated in 10 conference proceedings (refer section 8.3).

7.3 Future Recommendations:

This work focused on enhancing PDT by developing amphiphilic photosensitizers and designing liposomal formulations for PS delivery. However, in some cases, PDT-induced oxygen can trigger newer angiogenesis activators comprising the efficacy of the treatment[453,454]. Small interfering RNA (siRNA) is specific to these angiogenesis activators and is found to overcome these drawbacks of PDT[453–455]. Some relevant suggestions to future work are discussed here:

7.3.1 Amphiphilic Coumarin- siRNAs Complexes:

Small RNA (ribonucleic acids) moieties with two nucleotide 3'-overhangs. Amphiphilic coumarin investigated in this work can be complexed to siRNA by electrostatically conjugating positively charged amino groups to the and negatively charged phosphate moieties of siRNA. The obtained complex is further added to preformed DPPC/DPPS liposomes. The subsequent binding and insertion of the complex in the bilayer can studied using DSC, ITC, Circular dichroism and DLS techniques and the mechanism of interaction can be deduced. This can be challenging because of the presence of RNA subunits. This will aid in understanding the synergistic effect of siRNA and photosensitizer on the site of the tumor.

7.3.2 Formation and Characterization of Lipoplex for co-delivery of HPPH:

The aim of this work is to enable the delivery of HPPH and siRNA to the site of the tumor, thereby damaging the cancer cells using HPPH and preventing the recurrence by siRNA. In this proposed work, PEG-oxime ether complexes are synthesized initially. Further, this complex is conjugated to lipids. The conjugation of PEG to oxime and PEG-oxime ether to lipids is outlined in previous literature[456,457]. Liposomes comprising of PEGylated-Oxime ether

lipids and helper lipid DOPE (1,2-Dioleoyl phosphatidylethanolamine) can be formed by thin layer hydration technique.

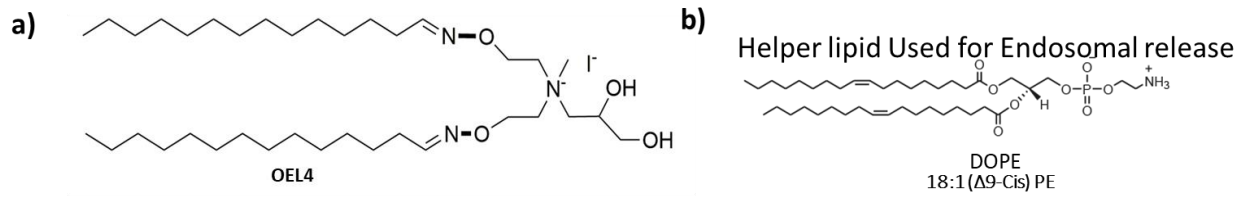

Figure 7-1: Structure of a) Oxime Ether lipids b) Helper Lipid DOPE

Further, lipoplexes can prepared by introducing the preformed PEGylated-Oxime ether/DOPE liposome to DS RNA by incubation and serum washing. The obtained liposomes are then subjected to dynamic light scattering (DLS) studies, fluorescence anisotropy and ITC to confirm the attachment of nucleic acids, binding affinities, and morphological characterization. Further, cell viability assay on cancerous cells using flow cytometer and uptake studies using fluorescent microscopy is performed to understand the toxicity of these lipoplexes. Further, these lipoplexes can be encapsulated with HPPH. The drug loading efficiency of HPPH can be calculated using UV-Vis spectroscopy and Thermogravimetric Analysis.

7.3.3 Stealth Liposomes with conjugated coumarin for co-delivery of siRNA in PDT:

The amphiphilic coumarin examined in this work can be conjugated to the PEG-Oxime-ether lipids. The conjugation procedure and synthesis routes can be found in prior literature[202,456–458]. The obtained PEG-coumarin-oxime ether lipids is self-assembled with helper DOPE lipids. The resulting liposomes are characterized for size, charge, morphology, and stability using DLS, Cryo-TEM and DSC. In-vitro cytotoxicity on cancer cells is assessed using MTT assay, prior to the MTT-assay the cell culture is treated with light of a particular wavelength to understand the preliminary photoactivity of these self-assemblies. These proposed liposomes will not only increase the efficacy of PDT by reducing the drawback but also prevent early macrophage clearance due to stealth nature.

8 Appendix

In this section, all the supporting information pertaining to Chapter 3 - The interaction of amphiphilic coumarin with DPPC/DPPS lipid bilayer are available. The description of each of the figure is mentioned throughout chapter 3. ^{1}H NMR and ^{13}C NMR analyses of C_9, ^{1}H NMR, ^{13}C NMR, FTIR and HRMS analyses of C_{12}, flip-flop profiles of C_5 and C_{12} amphiphiles in the lipid bilayer, and the coarse-grained force field parameters for C_5 and C_{12} amphiphiles.

8.1 Supporting information for interaction studies of Amphiphilic Coumarin

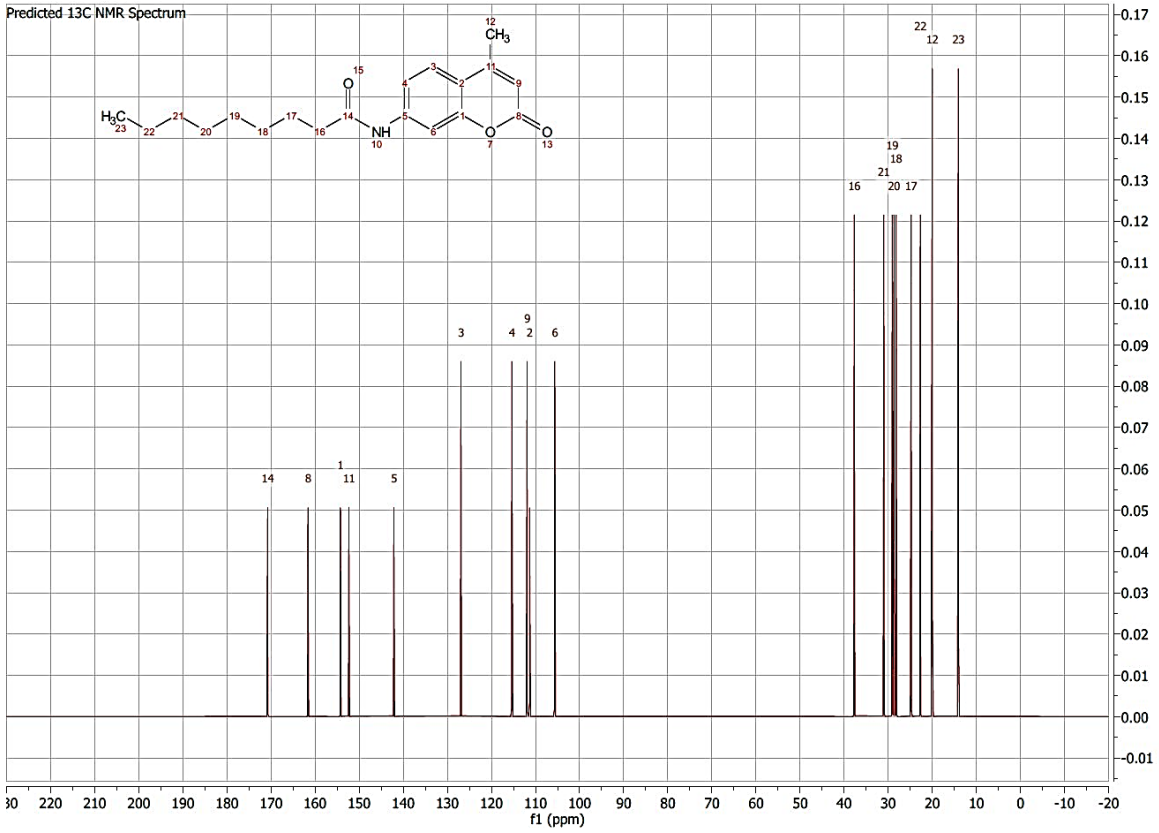

Figure 8-1: ^{13}C-NMR spectra of C_9 amphiphile

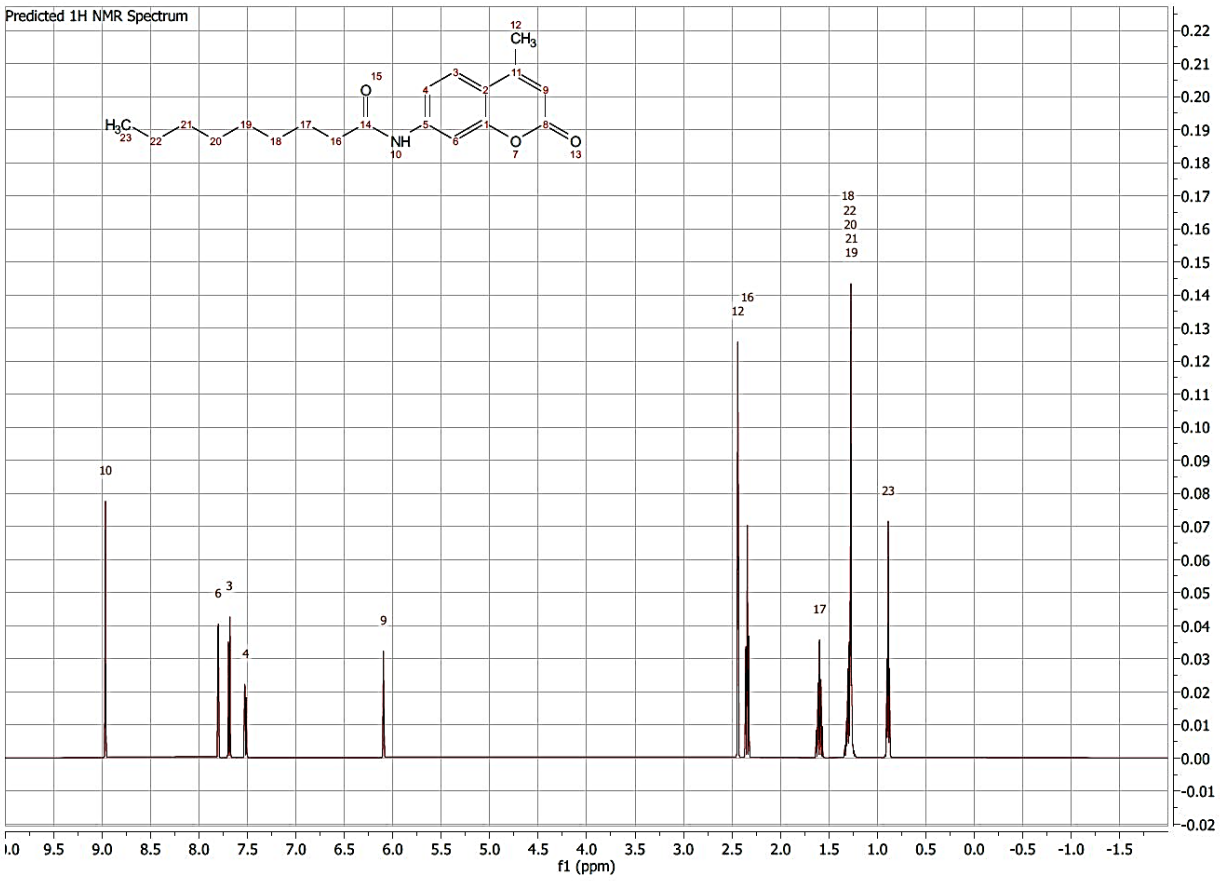

Figure 8-2: ^{1}H-NMR spectra of C_9 amphiphile

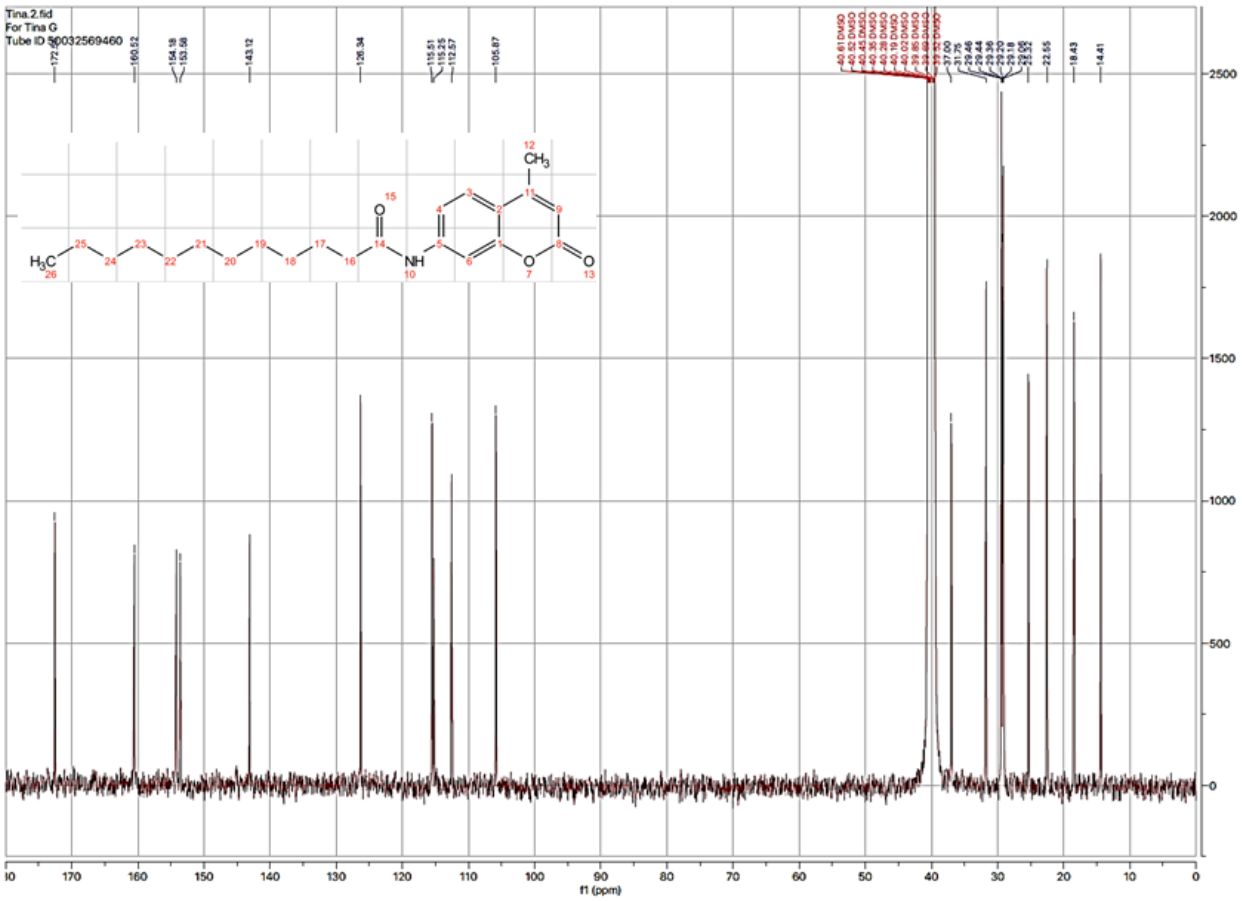

Figure 8-3: ^{13}C-NMR spectra of C_{12} amphiphile

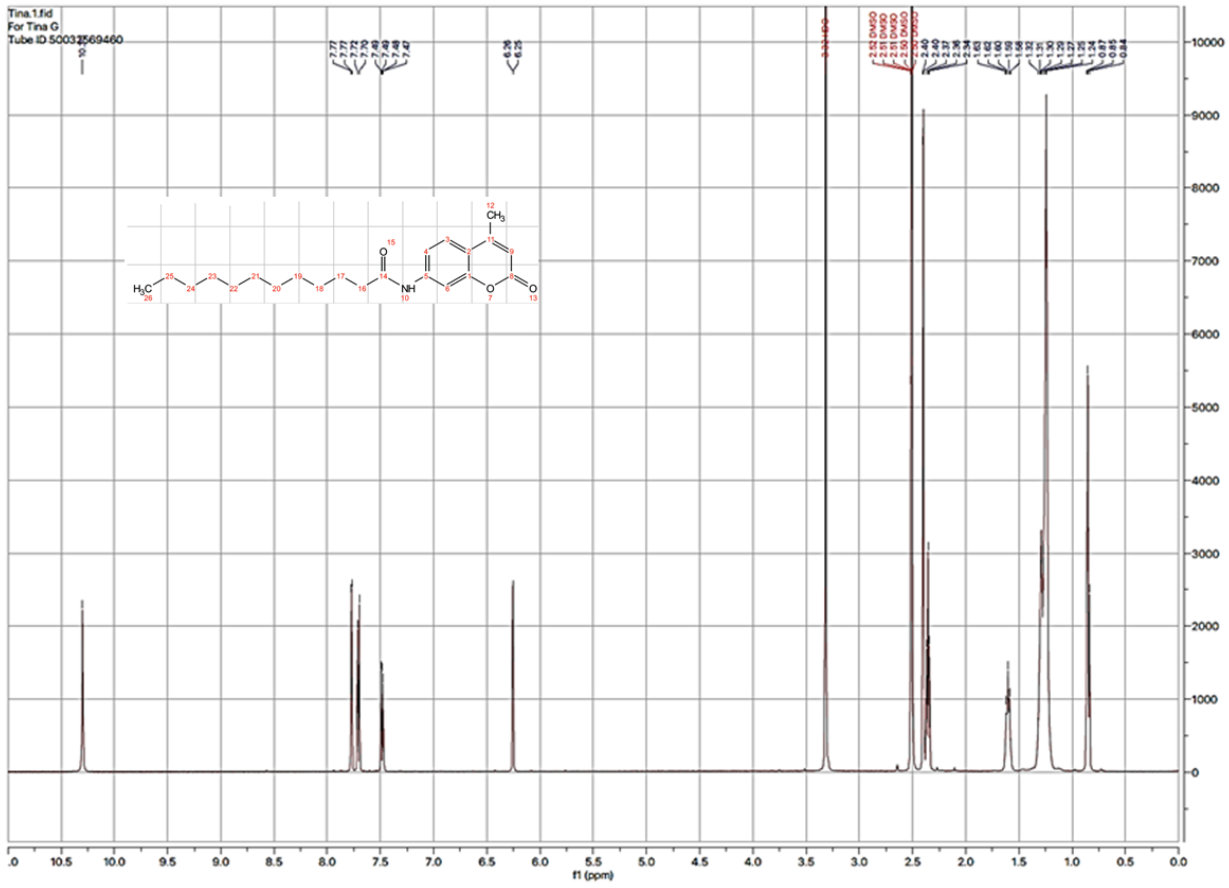

Figure 8-4: ^{1}H-NMR spectra of C_{12} amphiphile

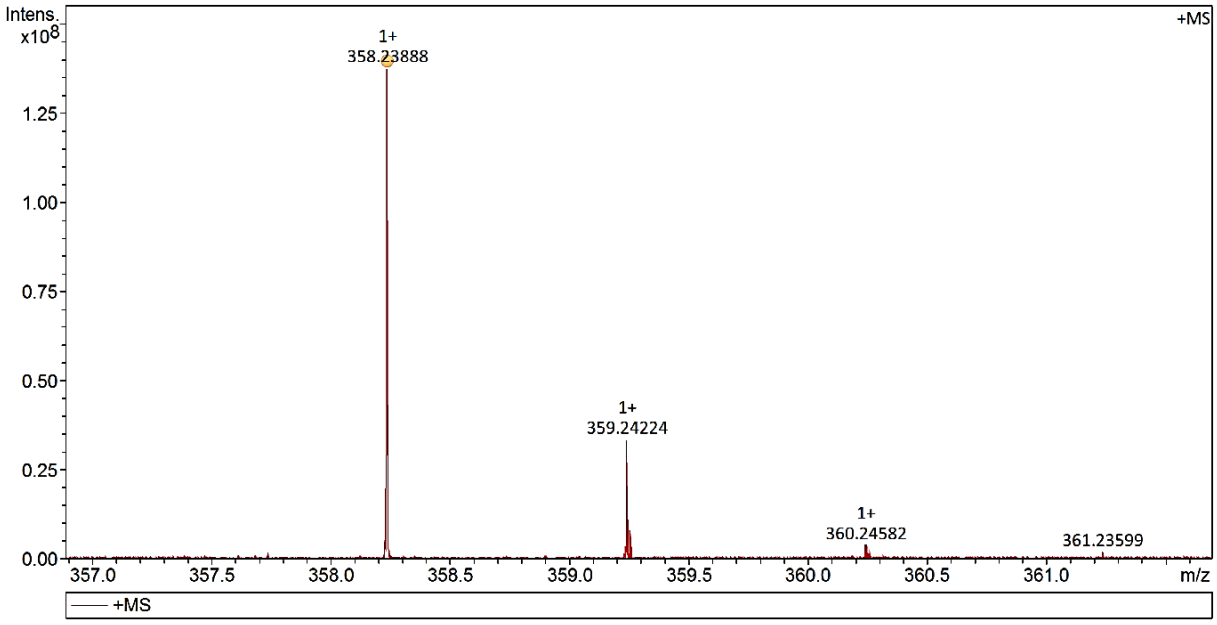

Meas. m/z	#	Ion Formula	Score	m/z	err [ppm]	Mean err [ppm]	mSigma	rdb	e¯ Conf	N-Rule
358.238880	1	C22H32NO3	100.00	358.237670	-3.4	-3.7	4.1	7.5	even	ok

Figure 8-5: HR-MS spectra of C_{12} amphiphile

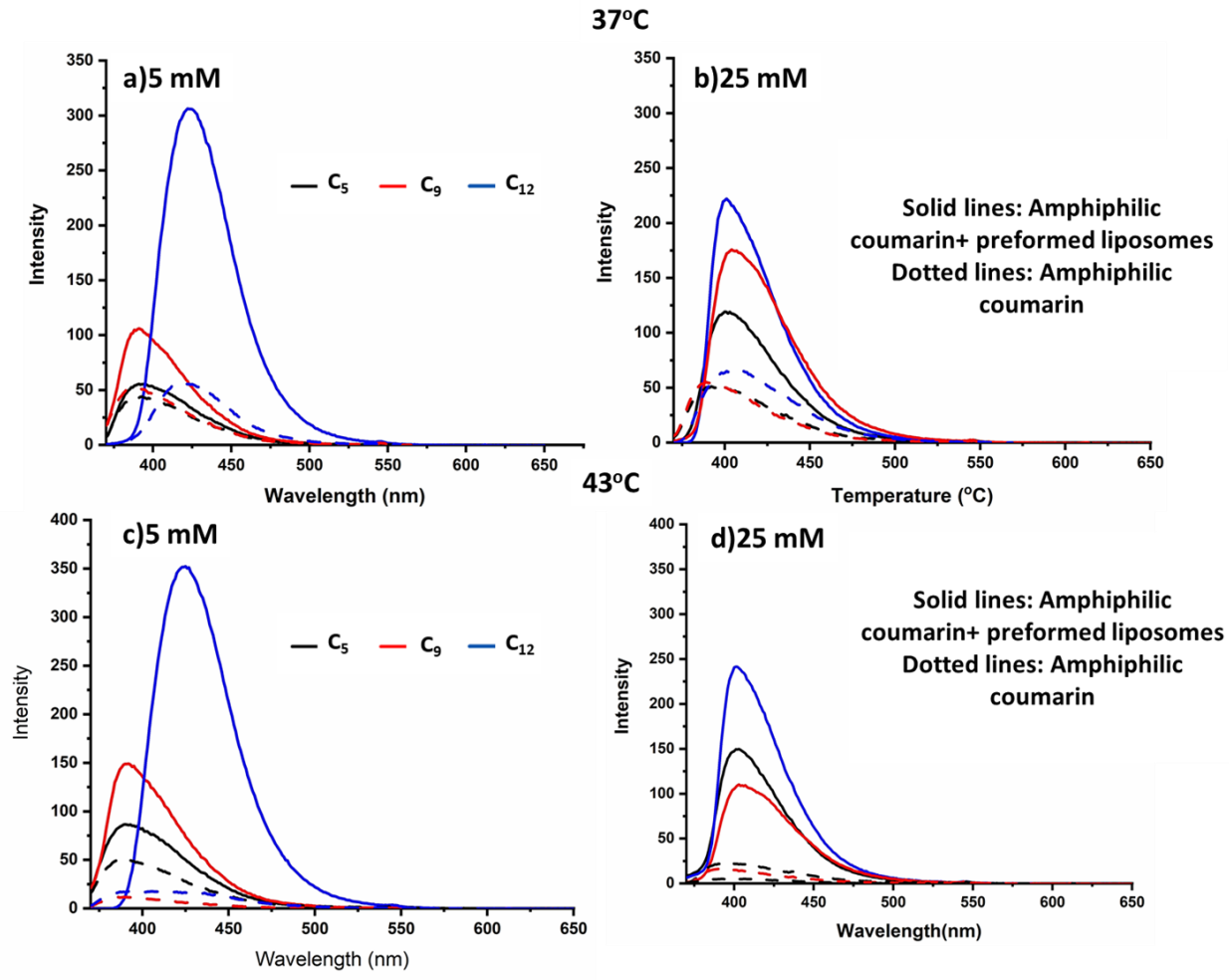

Figure 8-6: Fluorescence spectroscopy of amphiphilic fluorometric probes at 37°C & 43°C

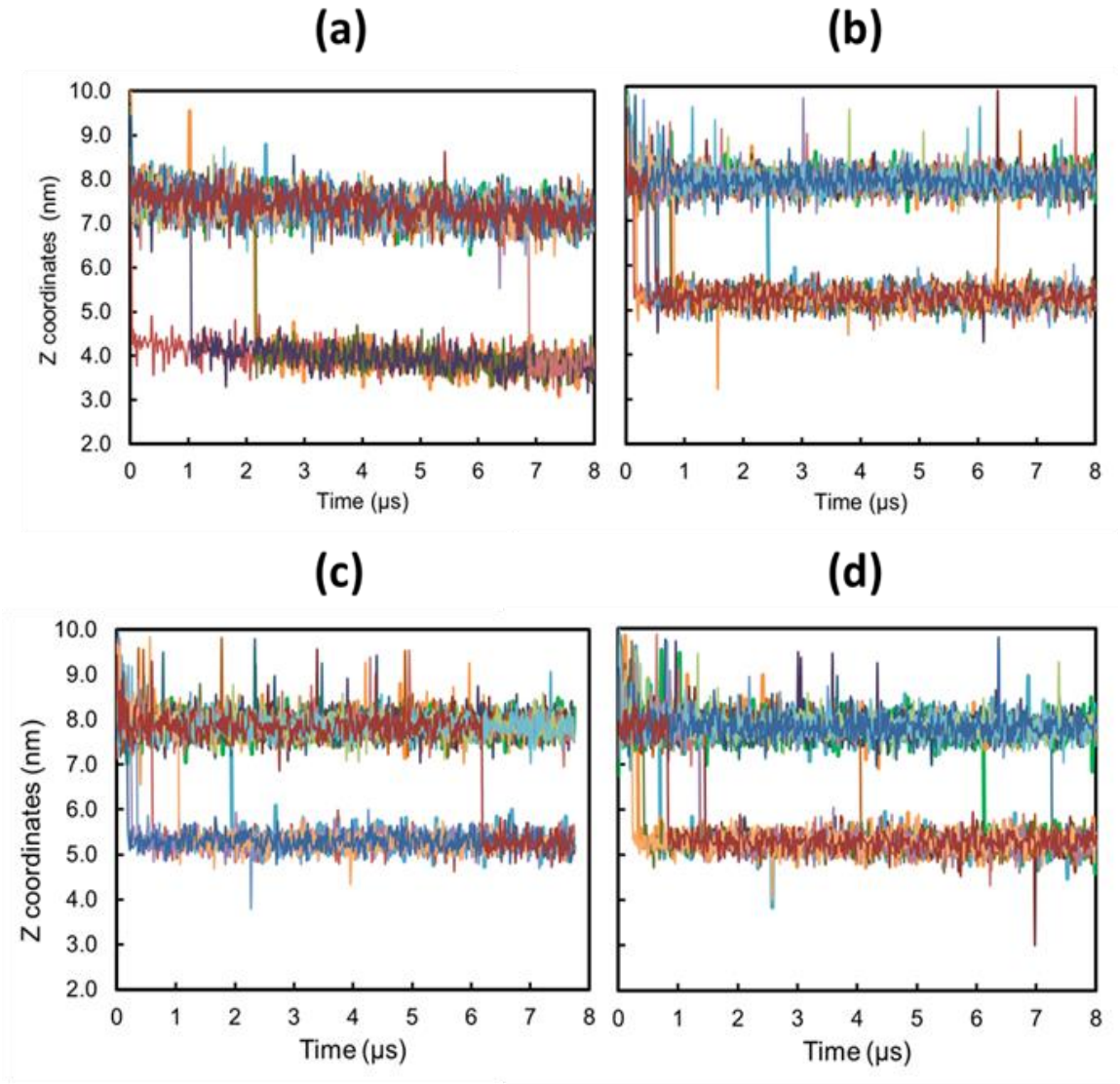

Figure 8-7: Flip-flop modes for 20 randomly selected molecules (each in a unique color) in system (a) C_5-42, (b) C_5-166, (c) C_5-166, and (d) C_5-209. Trajectory of the coumarin ring for each molecule is shown in a unique color.

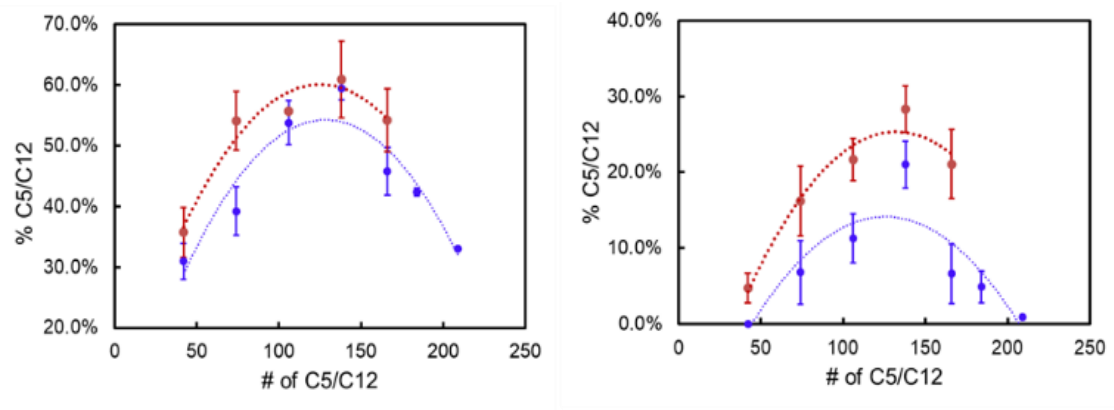

Figure 8-8: Comparison of flip-flop (%) for C_5 (blue) and C_{12} (red) molecules over a range of concentrations. with (a) ≥1 flip-flop (b) ≥2 flip-flops

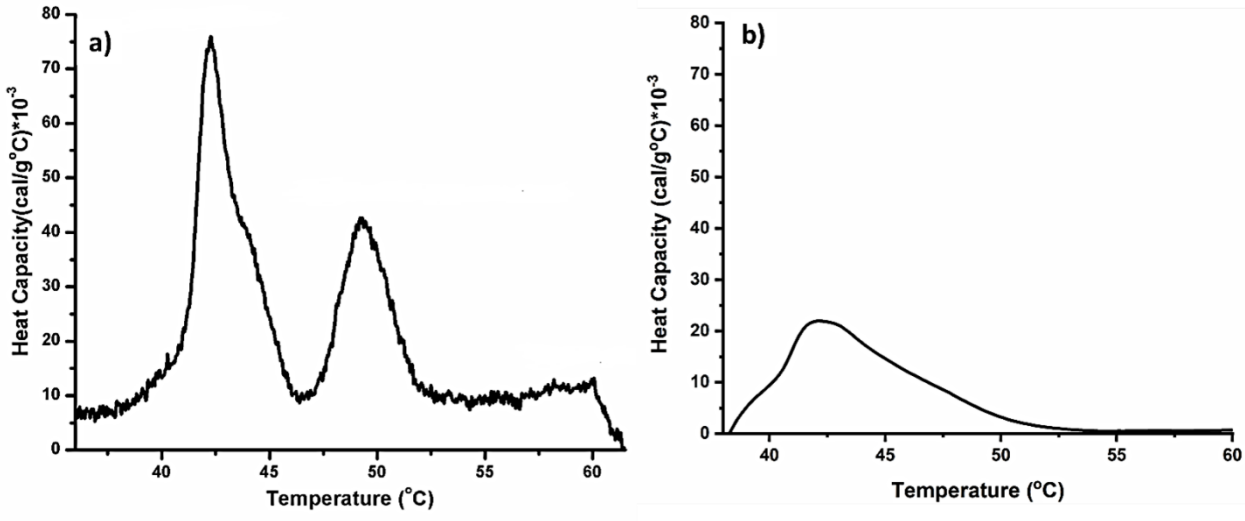

Figure 8-9: DSC Thermogram of a) pure DPPC/DPPS(85/15mol%) b) effect of DMSO on DPPC/DPPS (85/15 mol%)

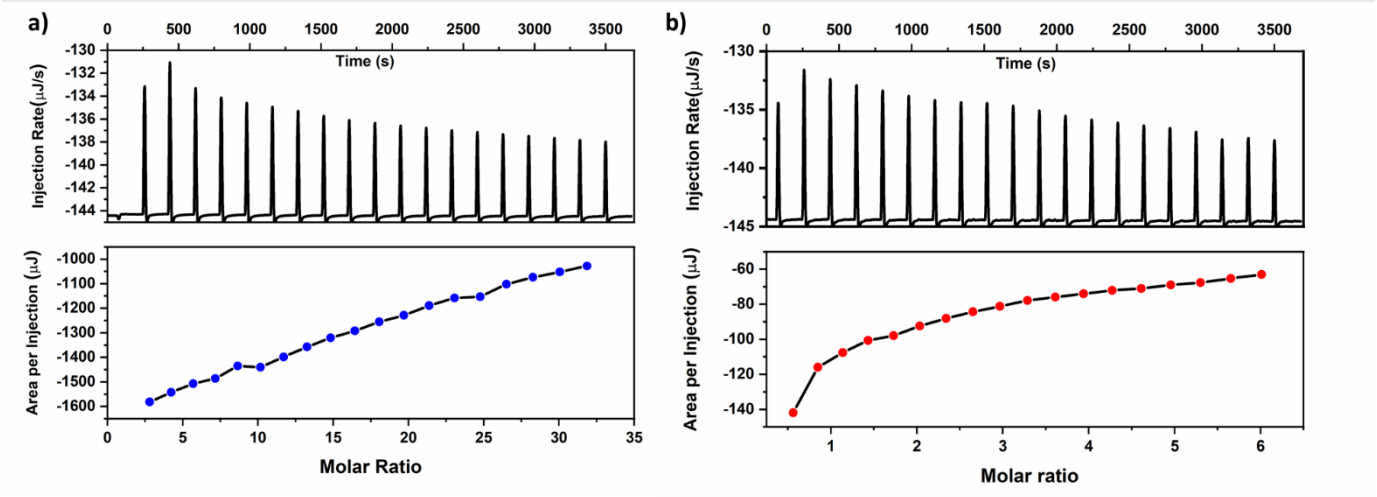

Figure 8-10: ITC thermogram of C_9 interaction (Type-A Titration-0.5 mM) with DPPC/DPPS liposomes of concentration a) 2.5 mM b) 5 mM

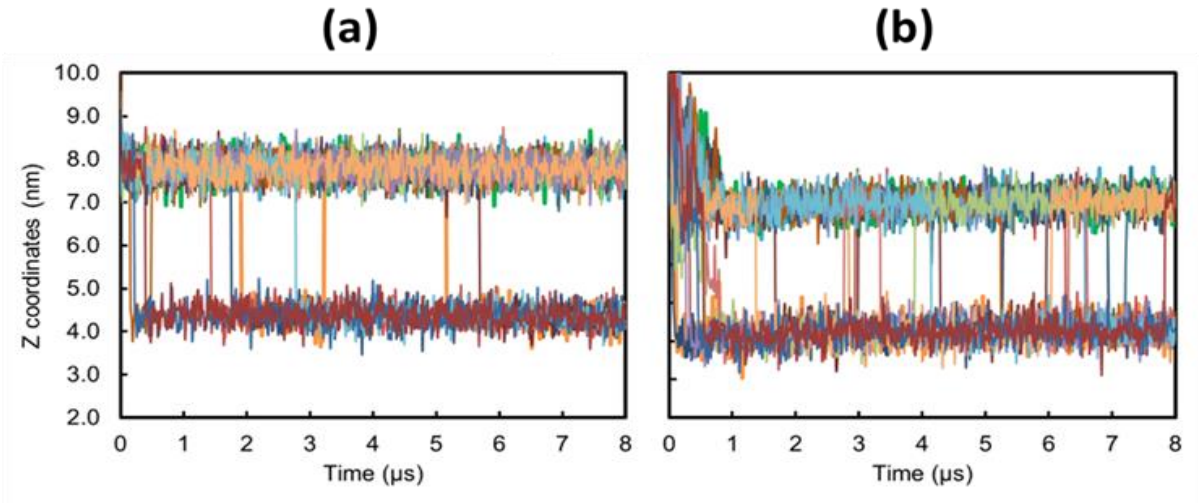

Figure 8-11: Flip-flop modes for 20 randomly selected molecules (each in a unique color) in system (a) C_{12}-42 and (b) C_{12}-166. Trajectory of the coumarin ring for each molecule is shown in a unique color.

Table 8-1: Equilibrium bond length (req), angle (θeq), and respective force constant for C_5 model.

Bond	r_{eq}(nm)	k_{bond} (kJ mol^{-1} nm^{-2})	Angle	θ_{eq}(deg)	k_{angle} (kJ mol^{-1})
1-2	0.295	Constrained	1-2-4	87	50
1-3	0.288	Constrained	2-1-3	75	50
2-4	0.303	Constrained	1-3-4	112	50
3-4	0.206	Constrained	1-3-5	155	50
3-5	0.330	5000	2-4-3	86	50
4-5	0.393	5000	2-4-5	142	50
5-6	0.347	5000	3-5-6	92	50
			4-5-6	108	50

Table 8-2: Equilibrium bond length (req), angle (θeq), and respective force constant for C_{12} model.

Bond	r_{eq}(nm)	k_{bond} (kJ mol^{-1} nm^{-2})	Angle	θ_{eq}(deg)	k_{angle} (kJ mol^{-1})
1-2	0.295	Constrained	1-2-4	87	50
1-3	0.288	Constrained	2-1-3	75	50
2-4	0.303	20000	1-3-4	112	50
3-4	0.206	Constrained	1-3-5	171	50
3-5	0.348	5000	2-4-3	86	50
4-5	0.341	5000	2-4-5	158	50
5-6	0.339	5000	3-5-6	122	50
6-7	0.398	5000	4-5-6	144	50
7-8	0.413	5000	5-6-7	120	50
			6-7-8	143	50

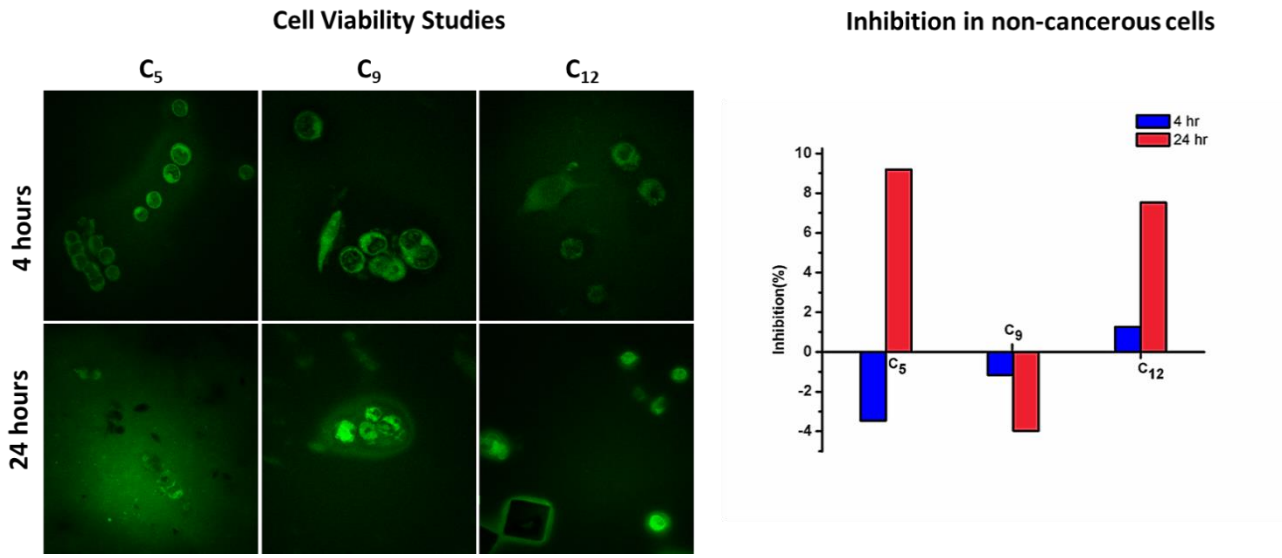

Figure 8-12: Fluorescence Microscopy Images of uptake of coumarin fluorophores in cancerous cells and specificity of coumarin fluorophores to cancerous cells

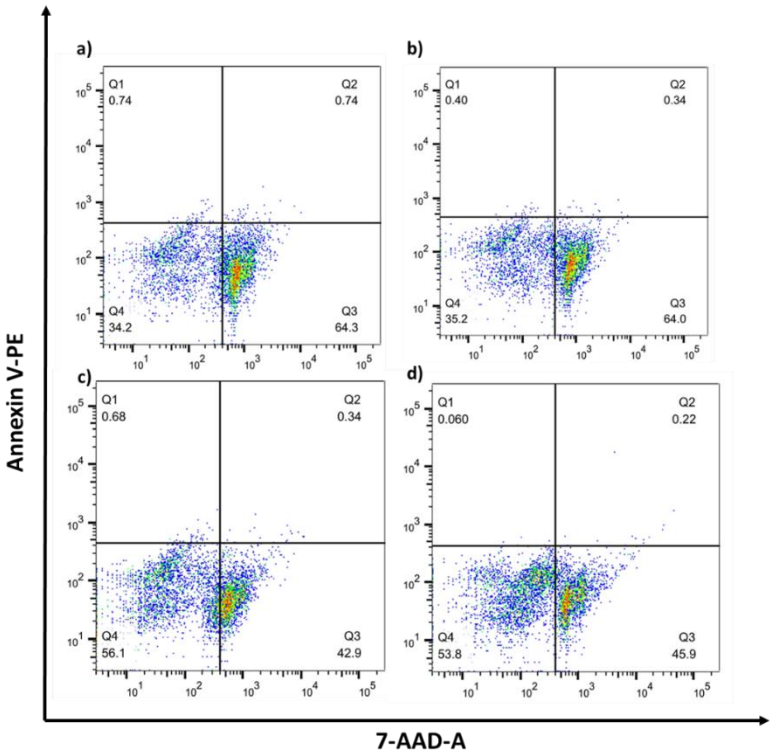

Figure 8-13: Apoptotic Studies with C_9

8.2 NMR studies- Interaction of Riboflavin

8.2.1 ^{1}H-NMR Studies:

In this section, all data pertaining to the NMR analysis (1&2-dimensional NMR) of interaction of Riboflavin with DPPC & DPPC/Cholesterol are presented as a part of the studies undertaken in Chapter 4. Additionally, circular dichroism data pertaining to the interactions are also presented.

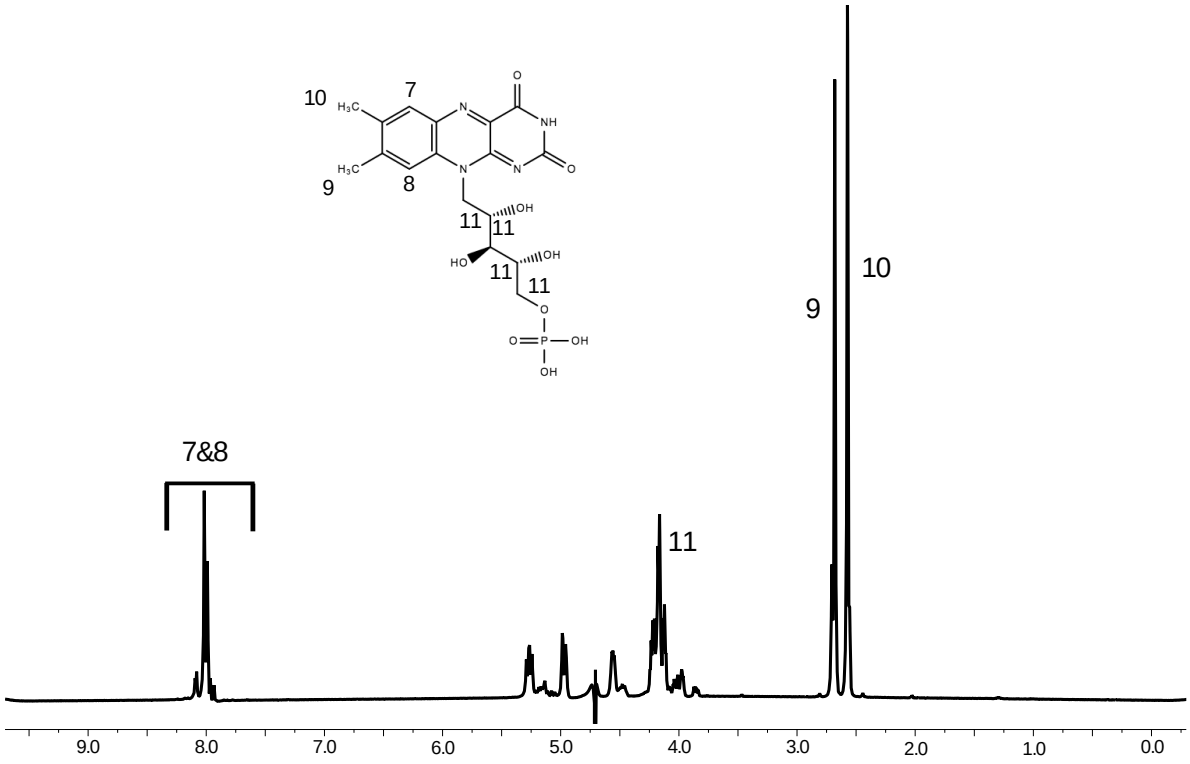

Figure 8-14: ^{1}H NMR spectrum of riboflavin 5' monophosphate

Figure 8-14 shows the ^{1}H NMR spectrum of riboflavin 5' monophosphate. The methine hydrogens that are on the ring structure are correspond to the signals labeled 7 and 8. The methyl hydrogens of the CH_3 groups attached to the ring correspond to the signals that are labeled 9 and 10. Finally signal 11 corresponds to the methylene and methine hydrogens of the branch.

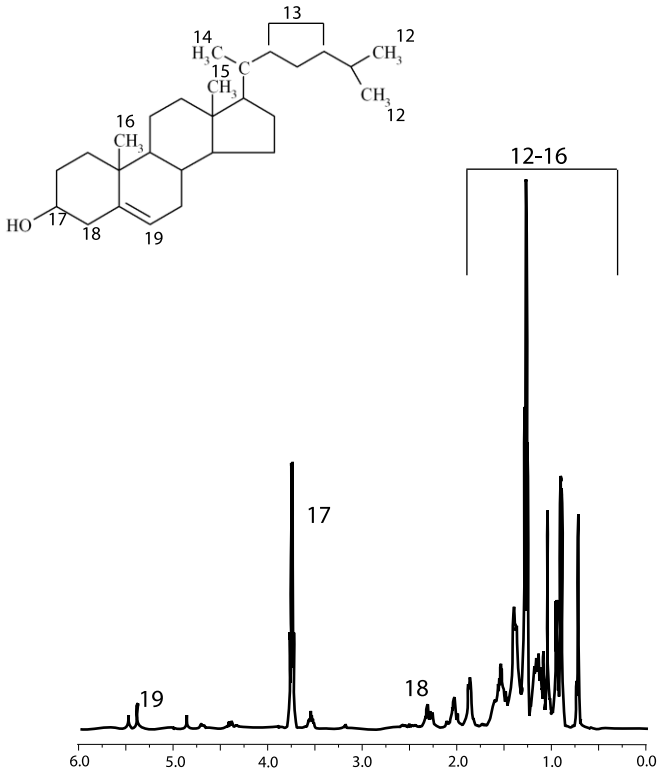

Figure 8-15: ^{1}H NMR spectrum of cholesterol

Figure 8-15 shows the ^{1}H NMR of cholesterol. Signals 12 through 16 correspond to the methyl and methylene hydrogens that make up the branch attached to the pentane ring and the two methyl hydrogen groups connected to the cyclic rings. Signal 17 corresponds to the methine hydrogen of the alcohol carbon. Signal 18 corresponds to the methylene hydrogen of the cyclic ring with the alcohol. Finally signal 19 corresponds to the methine hydrogen of the double bond carbon in the second 6 membered ring.

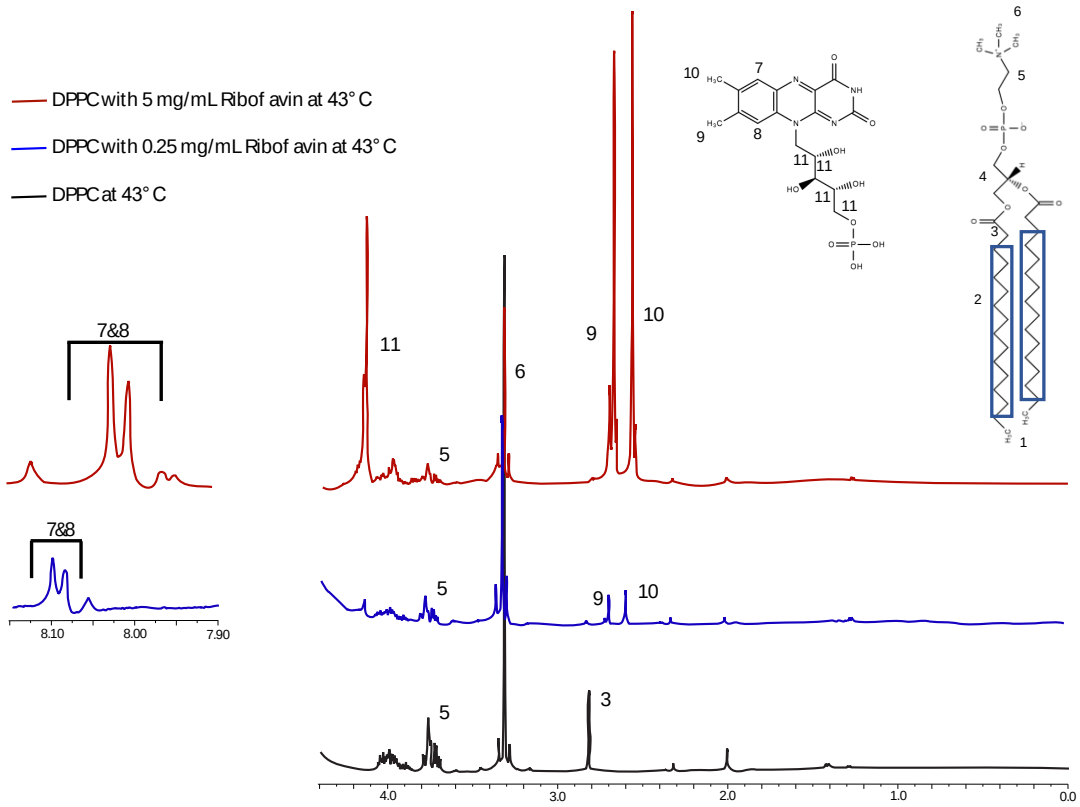

Figure 8-16: Overlay ^{1}HNMR spectrum of DPPC, DPPC with 0.25 mg/mL riboflavin, and DPPC with 5 mg/mL riboflavin at 43° C

Figure 8-16 shows the ^{1}H NMR data of the DPPC liposomes by itself, with 0.25 mg/mL riboflavin 'monophosphate and with 5 mg/mL riboflavin 5' monophosphate at 43° C. The signals 9 and 10 correspond to the methyl hydrogens of the CH_3 groups attached to the ring. Signal 3 corresponds to the methylene protons on the non-polar tail just before the glycerol moiety. Signal 6 corresponds to the methyl hydrogens on the nitrogen group of the polar head group. Signal 5 corresponds to the methylene hydrogens on the polar head group. Signal 11 corresponds to the methylene and methine hydrogens of the branch and signals 7 and 8 correspond to the hydrogens of the aromatic ring.

Comparing the three spectra, the signal given by the methylene protons right before the glycerol moiety is lost with the addition of riboflavin 5' monophosphate. Even at the lower concentration of riboflavin the signal is diminished completely. Also, there is a change in intensity, and slight chemical shift change in the signal given by the methylene protons on the polar head group. The signals given by the aromatic protons of riboflavin also become shifted at the higher concentration of riboflavin when compared to the lower concentration.

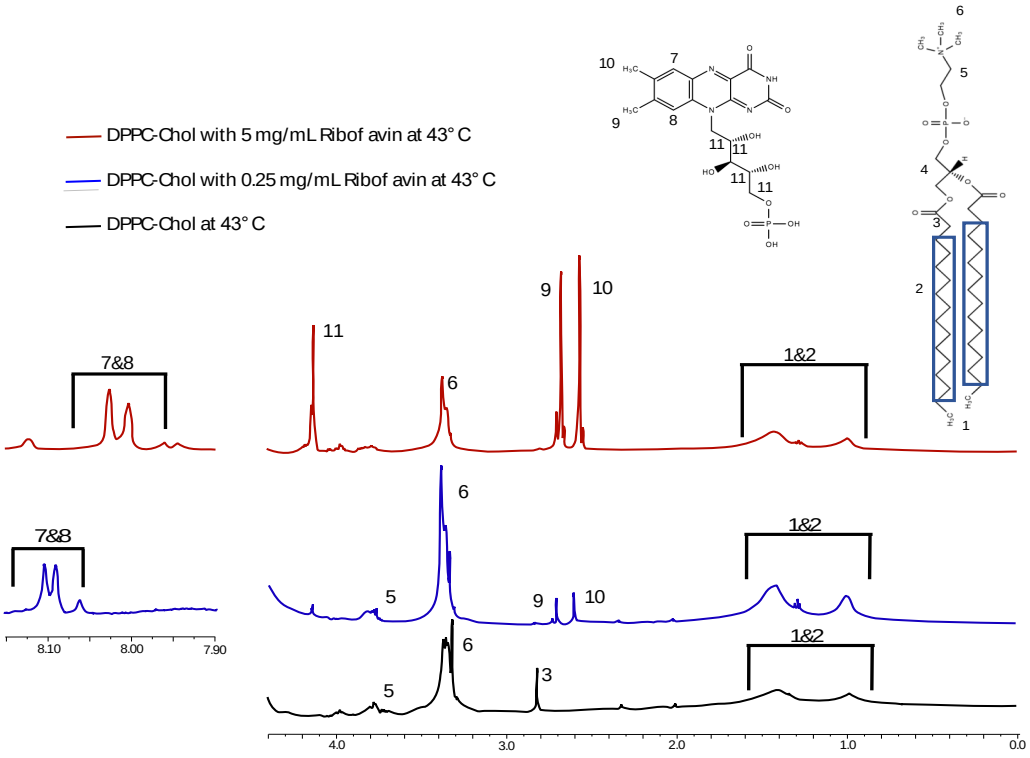

Figure 8-17:Overlay of 1H NMR spectra of DPPC-Chol, DPPC-Chol with 0.25 mg/mL riboflavin, and DPPC-Chol with 5 mg/mL riboflavin at 43° C

Figure 8-17 shows the ^{1}H NMR data of the DPPC-Chol liposomes by itself, with 0.25 mg/mL riboflavin 'monophosphate and with 5 m/mL riboflavin 5' monophosphate at 43° C. The signals 1 and 2 correspond to the methyl and methylene protons that make up the non-polar tail. The signals 9 and 10 correspond to the methyl hydrogens of the CH_3 groups attached to the ring. Signal 3 corresponds to the methylene protons on the non-polar tail just before the glycerol moiety. Signal 6 corresponds to the methyl hydrogens on the nitrogen group of the

polar head group. Signal 5 corresponds to the methylene hydrogens on the polar head group. Signal 11 corresponds to the methylene and methine hydrogens of the branch and signals 7 and 8 correspond to the hydrogens of the aromatic ring.

Comparing the three spectra, the signal given by the methylene protons right before the glycerol moiety is lost with the addition of riboflavin 5' monophosphate. Even at the lower concentration of riboflavin the signal is diminished completely. Also, there is a change in intensity, and a slight chemical shift change in the signal given by the methylene protons on the polar head group. The signals given by the aromatic protons of riboflavin also become shifted at the higher concentration of riboflavin when compared to the lower concentration and get slightly shifted away from each other.

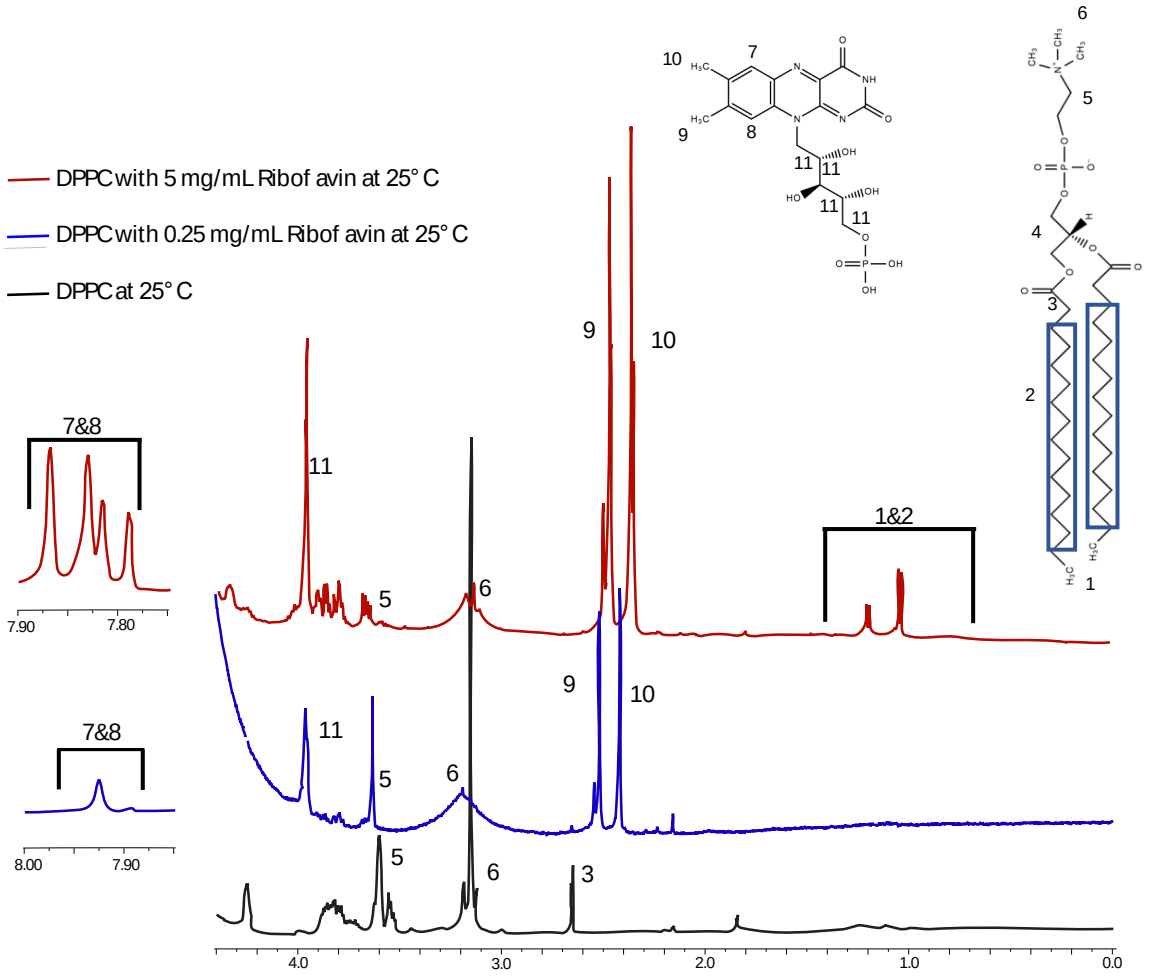

Figure 8-18:Overlay of 1H NMR spectra of DPPC, DPPC with 0.25 mg/mL riboflavin, and DPPC with 5 mg/mL riboflavin at 25° C

In all cases, the DPPC and DPPC-Chol liposomes completely lost the signal of the methylene protons that are right before the glycerol moiety and all spectra also saw a shifting of the signal of the methylene protons in the head group with the addition of riboflavin. The hydrogen peaks on the aromatic rings of riboflavin 5' monophosphate shift away from each other at the higher concentrations of riboflavin. It is hypothesized that this may be caused by the insertion of riboflavin into the lipid bilayer. The shift of the aromatic protons at the higher concentration could indicate that the interaction is concentration dependent.

Figure 8-18 shows the ^{1}H NMR data of the DPPC liposomes by itself, with 0.25 mg/mL riboflavin 'monophosphate, and with 5 m/mL riboflavin 5' monophosphate at 25° C. The signals 1 and 2 correspond to the methyl and methylene protons that make up the non-polar tail. The signals 9 and 10 correspond to the methyl hydrogens of the CH_3 groups attached to the ring. Signal 3 corresponds to the methylene protons on the non-polar tail just before the glycerol moiety. Signal 6 corresponds to the methyl hydrogens on the nitrogen group of the polar head group. Signal 5 corresponds to the methylene hydrogens on the polar head group. Signal 11 corresponds to the methylene and methine hydrogens of the branch and signals 7 and 8 correspond to the hydrogens of the aromatic ring.

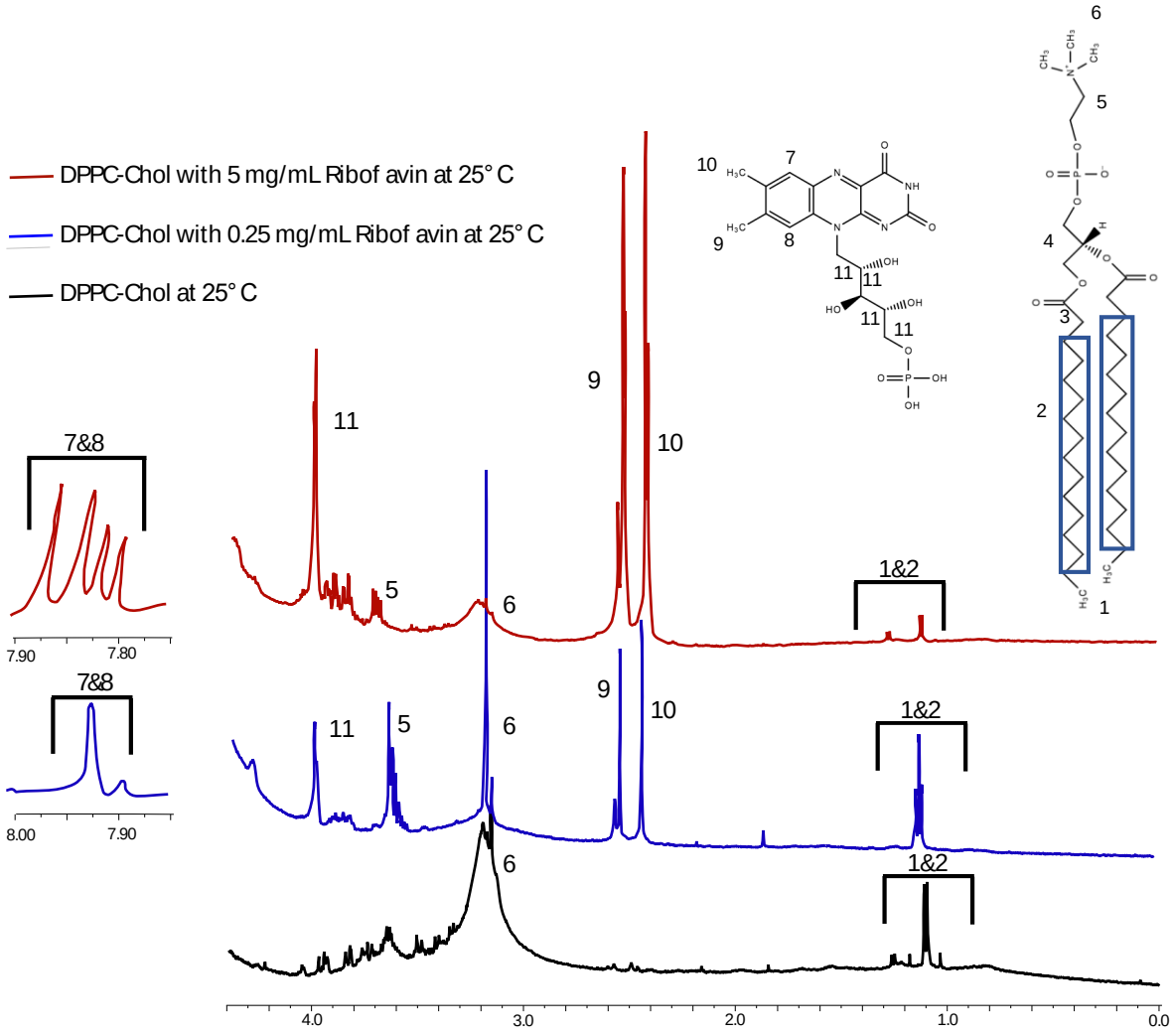

Figure 8-19:Overlay of 1H NMR spectra of DPPC-Chol, DPPC-Chol with 0.25 mg/mL riboflavin, and 5 mg/mL riboflavin at 25° C

Comparing the three spectra, the signal given by the methylene protons right before the glycerol moiety is lost with the addition of riboflavin 5' monophosphate. Even at the lower concentration of riboflavin the signal is diminished completely. Also, the signal given by the methylene protons on the polar head group is almost completely diminished at the highest concentration of riboflavin. The signal given by the methyl protons on the non-polar head group is greatly diminished at the higher concentration of riboflavin. The signals given by the aromatic protons of riboflavin also become shifted at the higher concentration of riboflavin when compared to the lower concentration and get slightly shifted away from each other. Also, when looking at the signals given by the aromatic protons in riboflavin, four peaks are seen at

the higher concentration while only one is seen at the lower concentration. Figure 8-19 shows the ^{1}H NMR data of the DPPC-Chol liposomes by itself, with 0.25 mg/mL riboflavin 'monophosphate and with 5 m/mL riboflavin 5' monophosphate at 25° C. The signals 1 and 2 correspond to the methyl and methylene protons that make up the non-polar tail. The signals 9 and 10 correspond to the methyl hydrogens of the CH_3 groups attached to the ring. Signal 6 corresponds to the methyl hydrogens on the nitrogen group of the polar head group. Signal 5 corresponds to the methylene hydrogens on the polar head group. Signal 11 corresponds to the methylene and methine hydrogens of the branch and signals 7 and 8 correspond to the hydrogens of the aromatic ring.

Comparing the three spectra, the signal given by the methylene protons on the polar head group is shifted when comparing the higher concentration of riboflavin to the lower concentration. The signal given by the methyl protons on the non-polar head group is greatly diminished at the higher concentration of riboflavin. The signals given by the aromatic protons of riboflavin also become shifted at the higher concentration of riboflavin when compared to the lower concentration and get slightly shifted away from each other. Also, when looking at the signals given by the aromatic protons in riboflavin, four peaks are seen at the higher concentration while only one is seen at the lower concentration.

In all cases, both 25° C and 43° C the DPPC and DPPC-Chol liposomes saw a shifting of the signal of the methylene protons in the head group with the addition of riboflavin. In the case of the DPPC liposomes, the loss of signal from the methylene hydrogens that were connected to the glycerol moiety and the non-polar tail is shown. The signals given by the aromatic protons of riboflavin also become shifted at the higher concentration of riboflavin when compared to the lower concentration. It is hypothesized that riboflavin is becoming inserted into the lipid bilayer, which causes a slight conformational change in the head group as well as a restriction of mobility in the non-polar tail. The shift of the aromatic protons at the higher

concentration could indicate that the interaction is concentration dependent. When comparing the data at the two different temperatures, it is shown that in the 25° C spectra that the peaks of the non-polar tails, are less defined and much sharper. This is a result of the liposome being in the gel phase, which means that the tails are much more rigid resulting in a loss of signal. For this reason, it was decided that 43° C would be the temperature to run the ^{31}P NMR and DOSY experiments at.

8.2.2 ^{31}P-NMR Studies:

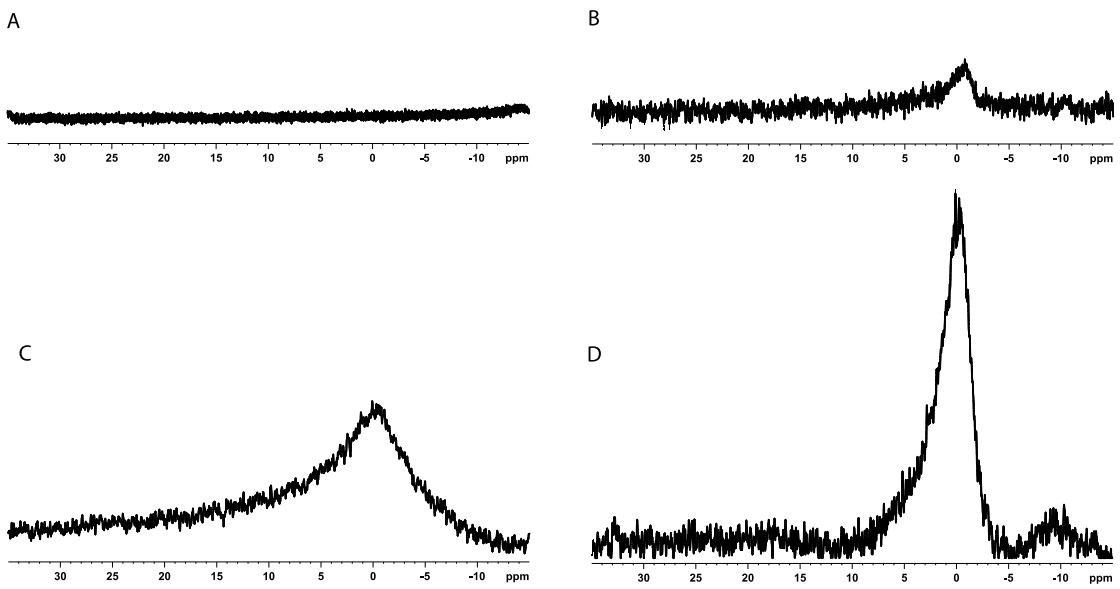

Figure 8-20: ^{31}P NMR of extruded vs non-extruded liposomes

Figure 8-20 shows four different attempts at running ^{31}P NMR on liposomes samples. Figure A shows no signal, which is due to the sample aggregating outside the coil window. This meant that the instrument saw no sample, so no signal was obtained. This led to the extrusion of the samples, so that the chances of aggregation were limited. Figures b, c, and d in D-7 show an increase in peak height as the length of the run increased. To get the desired spectrum, a 48-hour run is necessary.

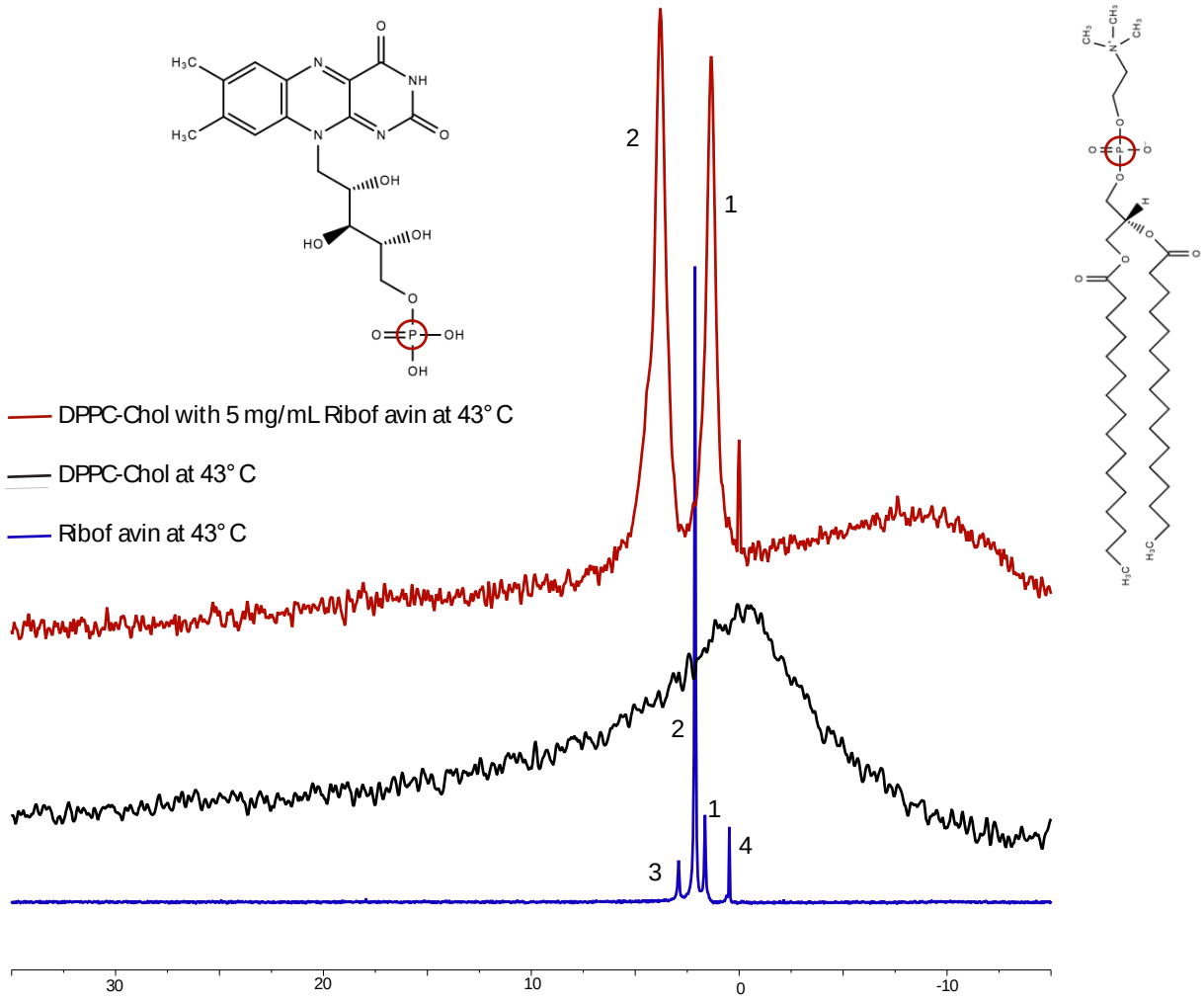

Figure 8-21:^{31}P NMR spectra of riboflavin, DPPC-Chol, and DPPC-Chol with 5 mg/mL riboflavin

Figure D-21 shows the ^{31}P NMR spectra of plain riboflavin as well as the DPPC liposomes both with and without 5 mg/mL riboflavin. Comparing the DPPC with and without riboflavin, the liposome peak shifts up-field slightly, and two of the peaks from riboflavin appear in the spectrum. When comparing the DPPC 5 mg/mL riboflavin spectrum to the spectrum of plain riboflavin, the liposome peak overlaps the peak of isomer that gave rise to signal 4. The riboflavin 5' monophosphate peak and the isomer peak labeled 1 are shifted down field slightly which causes the signal of the isomer that gave rise to peak 3 to also be overlapped and hidden. When comparing the riboflavin 5' monophosphate peak and the peak of the isomer next to it in the liposome spectrum to those in the plain riboflavin spectrum, it can be seen that the peaks

in the liposome spectrum have better resolution. These changes are hypothesized to be caused by an electrostatic surface between the liposomes and riboflavin.

8.2.3 DOSY-NMR Studies:

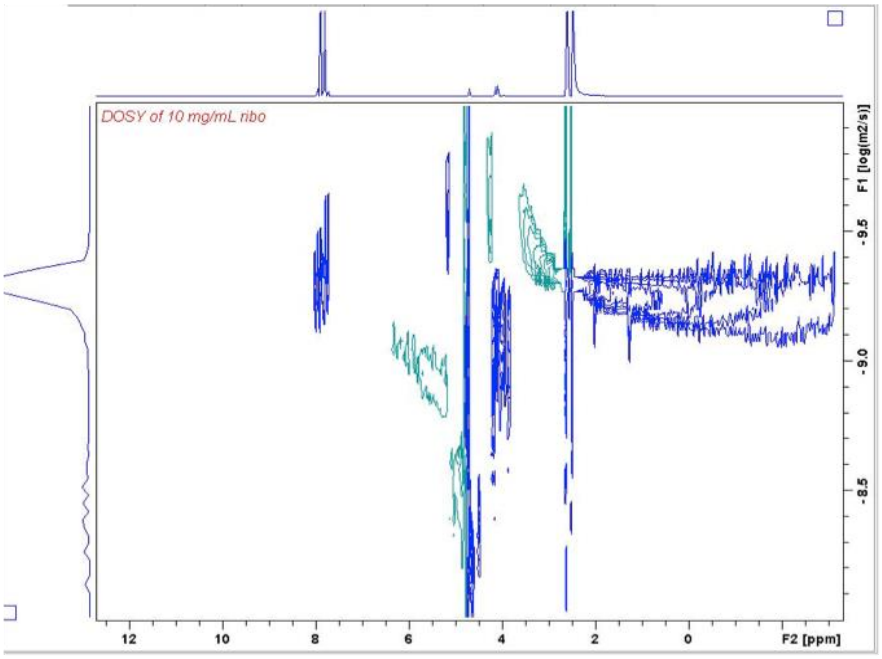

Figure 8-22:DOSY spectrum of riboflavin 5' monophosphate

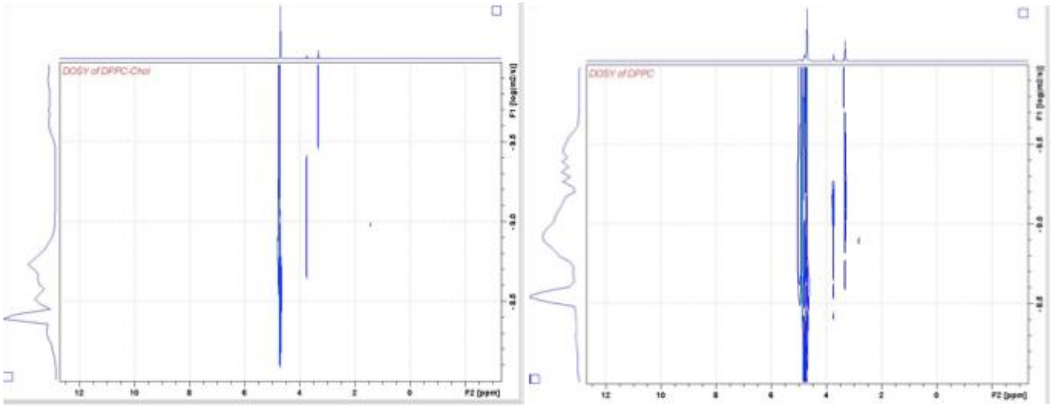

Figure 8-23: DOSY spectra of DPPC and DPPC-Chol liposomes

Figure D-22 shows the repeat DOSY data for riboflavin 5’ monophosphate. The spectrum shows that riboflavin has a diffusion coefficient of -9.32 log (m^2/s).

Figure 8-23 shows the repeat DOSY data for the DPPC and DPPC-Chol liposomes. The spectrum shows that both sets of liposomes have a diffusion coefficient of -9.02 log (m2/s) and -8.88 log (m2/s).

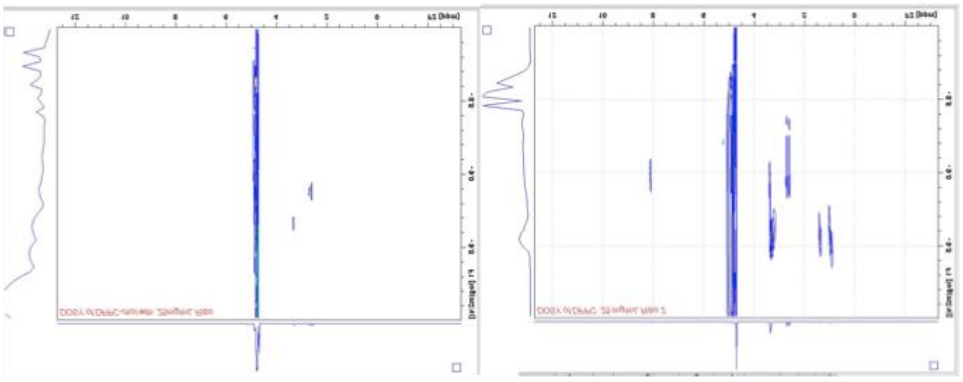

Figure 8-24: DOSY spectra of DPPC and DPPC-Chol liposomes with 0.25 mg/mL riboflavin

Figure 8-24 shows the DOSY data for both DPPC and DPPC-Chol liposomes with the addition of 0.25 mg/mL riboflavin 5’ monophosphate. In both spectra, the values of the diffusion coefficients remained the same, -9.20 log (m2/s) for riboflavin and -8.96 log (m2/s) for both liposomes. This means that no interaction between riboflavin 5’ monophosphate and the liposomes was seen during the experiment.

For both the DPPC and DPPC-Chol liposomes at the two different concentrations, the diffusion coefficients for riboflavin and DPPC remain the same, which means that no interaction between riboflavin 5’ monophosphate and the liposomes was seen during the experiment. This, however, does not necessarily mean that there was no interaction between the riboflavin and liposomes. The DOSY experiment was set up so that the diffusion delay was 200 milliseconds.

If the interaction between riboflavin and the liposomes was not permanent, and lasted less than 200 milliseconds, it would be undetectable.

8.2.4 Circular Dichroism Studies:

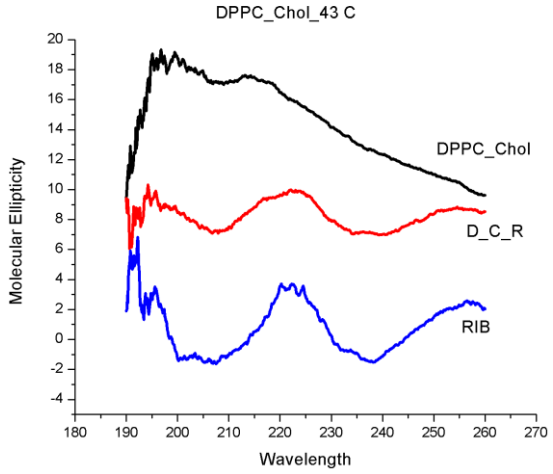

Figure 8-25: Circular dichroism data of riboflavin, DPPC, and DPPC with 5 mg/mL riboflavin at 43° C

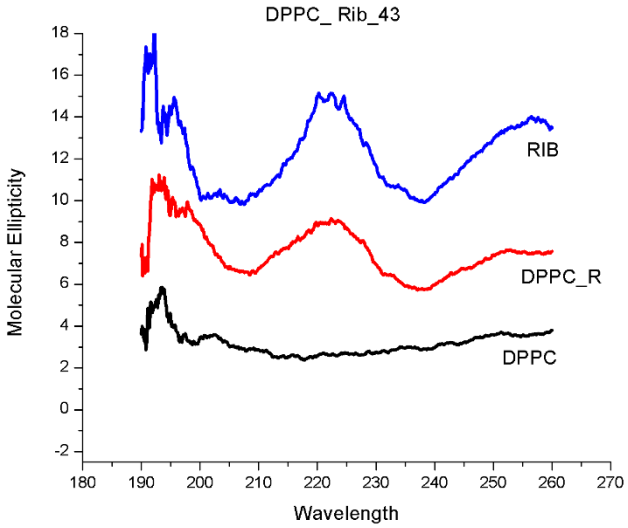

Figure 8-26: Circular dichroism data for riboflavin, DPPC-Chol, and DPPC-Chol with 5 mg/mL riboflavin at 43° C

Figures 8-26 and 8-27 show the Circular dichroism data for riboflavin, the liposomes, either DPPC or DPPC-Chol, and the liposomes with 5 mg/mL riboflavin. The data shows that the addition of cholesterol does not affect the electrostatic interaction and supports the conclusion from the zeta potential data that there is an electrostatic interaction between the riboflavin and liposomes.

8.3 Publication List

8.3.1 Journal Papers

1. **Kalyanram P**, Ma H, Marshall S, Goudreau C, Cartya A, Zimmermann T, Stadler I, Nangia S, Gupta A, Interaction of Amphiphilic Coumarin with DPPC/DPPS Lipid Bilayer: Effects of Concentration and Alkyl Tail Length, *Physical Chemistry Chemical Physics, https://doi.org/10.1039/D0CP00696C.*
2. **Kalyanram P**, Stadler I, Gupta A, Interaction of Riboflavin-5-Phosphate with Liposome Bilayers, *Journal of Nanotoxicology and Nanomedicine (JNN), 3(1), pp.49-59.*
3. **Kalyanram P**, Puri A, Gupta A, Understanding the Stealth Properties of PEGylated lipids: A Mini-Review (Accepted for Publication- International Journal of Lipids: Special Issue)
4. **Kalyanram P**, Hussein N, Tiwari A, Gupta A, Insights on the Thermal and Physical Stability of the Modified Polymerizable Liposomes for Improved Photoactivity (Accepted for Publication- International Journal of Lipids: Special Issue)
5. **Kalyanram P**, Puri A, Gupta A, Investigation of Lateral Association, Domain Formation and Segregation of a Polymeric PEGlyted Lipid by Differential Scanning Calorimetry, 2020 (Under Submission to ACS Omega)
6. **Kalyanram P**, Gupta A, Interaction of Delocalized Lipophilic Cation with Lipid Bilayer: A Thermodynamic Study,2020 (Under Submission)
7. **Kalyanram P**, Gupta A, Binding of Amino coumarin Derivative studied with Isothermal Titration Calorimetry,2020 (Under Submission)

8.3.2 Conference Proceedings

1. **Kalyanram P**, Gupta A, Biothermal Analysis of Interactions between Delocalized Lipophilic Cation (DLC) and Composite Lipid Bilayer, 2020 AIChE Annual Meeting, San Francisco, CA
2. **Kalyanram P**, Gupta A, Binding and Kinetics of Coumarin Amphiphiles with Composite Lipid Bilayer, 2020 AIChE Annual Meeting, San Francisco, CA
3. **Kalyanram P**, Gupta A, Thermodynamic and kinetics study of the effects of amphiphilicity of photosensitizers in photodynamic therapy (PDT), ACS Fall 2020 National Meeting & Exposition in San Francisco, CA
4. **Kalyanram P**, Gupta A, Effects of amphiphilicity on uptake and penetration of Photosensitizers, International Conference on Porphyrins and Phthalocyanines (ICPP), Buffalo, NY
5. **Kalyanram P**, Stadler I, Gupta A, Lipid Membrane Bilayer Destabilization by Amphiphilic Coumarin: A Biophysical Study for Cancer Applications, 2019 AIChE Annual Meeting, Orlando, FL
6. **Kalyanram P**, Stadler I, Nangia S, Gupta A, Interaction of Amphiphilic Coumarin with DPPC/DPPS Using DSC and MD Simulations: Effects of Concentration and Chain Length, 2019 AIChE Annual Meeting, Orlando, FL

7. **Kalyanram P**, Stadler I, Gupta A, Non-Porphyrin Photosensitizers for Photodynamic Therapy: Biophysical and Preliminary Cell Studies, 2019 AIChE Annual Meeting, Orlando, FL
8. **Kalyanram P**, Stadler I, Gupta A, Biophysical, Cytotoxicity and Cellular Uptake Studies of Novel Amphiphilic Fluorophores for Photodynamic Therapy (PDT), 2018 AIChE Annual Meeting, Pittsburgh, PA
9. **Kalyanram P**, Gupta A, Phase Transition Study of Lipid Bilayer with Flavin Mononucleotide using Differential Scanning Calorimetry, North American Thermal Analysis Society, Aug 6-9,2018
10. **Kalyanram P,** Gupta A, Phase Inversion, Creaming and Multiple Emulsions in Food Grade Surfactants, Colloidal, Macromolecular and Polyelectrolyte Solutions (GRS) Gordon Research Seminar, February 3 - 4, 2018, Ventura, CA

9 References:

1 M. Plummer, C. de Martel, J. Vignat, J. Ferlay, F. Bray and S. Franceschi, *Lancet Glob. Heal.*, 2016, **4**, e609–e616.

2 American Association for Cancer Research, *Clin Cancer Res*, 2015, **21**, S1-128.

3 Cancer - Our World in Data, https://ourworldindata.org/cancer, (accessed 26 November 2018).

4 M. Chidambaram, R. Manavalan and K. Kathiresan, *J. Pharm. Pharm. Sci.*, 2011, **14**, 67–77.

5 I. Stamati, Imperial College, London, 2010.

6 S. Brown, E. Brown and I. Walker, *Lancet Oncol.*, 2004, **5**, 497–508.

7 D. E. J. G. J. Dolmans, D. Fukumura and R. K. Jain, *Nat. Rev. Cancer*, 2003, **3**, 380–387.

8 S. Mitra, University of Rochester, 2004.

9 G. Bozzuto and A. Molinari, *Int. J. Nanomedicine*, 2015, 10, 975–999.

10 N. Monteiro, A. Martins, R. L. Reis and N. M. Neves, *J. R. Soc. Interface*, 2014, 11.

11 G. Bozzuto and A. Molinari, *Int. J. Nanomedicine*, 2015, 10, 975–999.

12 C. Matos, C. Moutinho and P. Lobão, *J. Membr. Biol.*, 2012, **245**, 69–75.

13 H. F. Lodish, A. Berk, C. Kaiser, M. Krieger, M. P. Scott, A. Bretscher, H. L. Ploegh and P. T. Matsudaira, *Molecular cell biology*, W.H. Freeman, 2008.

14 A. A. Gurtovenko, O. I. Onike and J. Anwar, *Langmuir*, 2008, **24**, 9656–9660.

15 C. Matos, C. Moutinho, P. L.-T. J. of membrane Biology and U. 2012, *Springer*, 2012,

254, 69–75.

16 T. G. Pomorski, T. Nylander and M. Cárdenas, *Adv. Colloid Interface Sci.*, 2014, **205**, 207–220.

17 Y. P. Patil and S. Jadhav, *Chem. Phys. Lipids*, 2014, **177**, 8–18.

18 M. Bermúdez, E. Martinez, M. Mora, M. L. Sagristá and M. A. de Madariaga, *Colloids Surfaces A Physicochem. Eng. Asp.*, 1999, **158**, 59–66.

19 K. OKUMURA, K. INUI, … Y. H.-B. and undefined 1981, *jstage.jst.go.jp*.

20 K. Matsuzaki, S. Yoneyama, O. Murase and K. Miyajima, *Biochemistry*, 1996, **35**, 8450–8456.

21 Y. Shai, *Biochim. Biophys. Acta - Biomembr.*, 1999, **1462**, 55–70.

22 Y. Pouny, D. Rapaport, A. Mor, P. Nicolas and Y. Shai, *Biochemistry*, 1992, **31**, 12416–12423.

23 A. Prochiantz, in *Annals of the New York Academy of Sciences*, New York Academy of Sciences, 1999, vol. 886, pp. 172–179.

24 S. Kawamoto, M. Takasu, T. Miyakawa, R. Morikawa, T. Oda, S. Futaki and H. Nagao, *J. Chem. Phys.*, 2011, **134**, 095103.

25 D. Derossi, S. Calvet, A. Trembleau, A. Brunissen, G. Chassaing and A. Prochiantz, *J. Biol. Chem.*, 1996, **271**, 18188–93.

26 D. Derossi, G. Chassaing and A. Prochiantz, *Trends Cell Biol.*, 1998, **8**, 84–87.

27 C. Matos, C. Moutinho and P. Lobão, *J. Membr. Biol.*, 2012, **245**, 69–75.

28 Y. Posokhov and A. Kyrychenko, *Biophys. Chem.*, 2018, **235**, 9–18.

29 A. Kyrychenko, I. Y. Sevriukov, Z. A. Syzova, A. S. Ladokhin and A. O. Doroshenko, *Biophys. Chem.*, 2011, **154**, 8–17.

30 L. M. S. Loura, A. M. T. M. do Canto and J. Martins, *Biochim. Biophys. Acta - Biomembr.*, 2013, **1828**, 1094–1101.

31 R. R. Gullapalli, M. C. Demirel and P. J. Butler, *Phys. Chem. Chem. Phys.*, 2008, **10**, 3548.

32 J. Repáková, J. M. Holopainen, M. R. Morrow, M. C. McDonald, P. Čapková and I. Vattulainen, *Biophys. J.*, 2005, **88**, 3398–3410.

33 B. Orioni, G. Bocchinfuso, J. Y. Kim, A. Palleschi, G. Grande, S. Bobone, Y. Park, J. Il Kim, K. Hahm and L. Stella, *Biochim. Biophys. Acta - Biomembr.*, 2009, **1788**, 1523–1533.

34 L. Zhao, S.-S. Feng, N. Kocherginsky and I. Kostetski, *Int. J. Pharm.*, 2007, **338**, 258–266.

35 M. Budai, Z. Szabó, M. Szőgyi and P. Gróf, *Int. J. Pharm.*, 2003, **250**, 239–250.

36 F. Sauvage, F.-X. Legrand, M. Roux, I. Rajkovic, T. M. Weiss, Z. Varga, L. Augis, G. Nugue, J.-C. Debouzy, J. Vergnaud-Gauduchon and G. Barratt, *J. Colloid Interface Sci.*, 2019, **537**, 704–715.

37 E. Sariisik, M. Koçak, F. Kucuk Baloglu and F. Severcan, *Biochim. Biophys. Acta - Biomembr.*, 2019, **1861**, 810–818.

38 K. N. Belosludtsev, N. V. Penkov, K. S. Tenkov, E. Y. Talanov, N. V. Belosludtseva, A. V. Agafonov, A. E. Stepanova, V. S. Starinets, O. V. Vashchenko, S. V. Gudkov and M. V. Dubinin, *Chem. Biol. Interact.*, 2019, **299**, 8–14.

39 H.-Y. Cheng, C. S. Randall, W. W. Holl, P. P. Constantinides, T.-L. Yue and G. Z. Feuerstein, *Biochim. Biophys. Acta - Biomembr.*, 1996, **1284**, 20–28.

40 Y. Wu, K. He, S. J. Ludtke and H. W. Huang, *Biophys. J.*, 1995, **68**, 2361–2369.

41 ‡ Evelyne Terzi, § and Günter Hölzemann and ‡ Joachim Seelig*, *Biochemistry*, 1997, **36**, 14845–14852.

42 A. Gupta, D. Mandal, Y. Ahmadibeni, K. Parang and G. Bothun, *Eur. Biophys. J.*, 2011, **40**, 727–736.

43 K. Gupta, H. Jang, K. Harlen, A. Puri, R. Nussinov, J. P. Schneider and R. Blumenthal, *Biophys. J.*, 2013, **105**, 2093–103.

44 K. A. Reid, C. M. Davis, R. B. Dyer and J. T. Kindt, *Biochim. Biophys. Acta - Biomembr.*, 2018, **1860**, 792–800.

45 A. C. Alves, A. Magarkar, M. Horta, J. L. F. C. Lima, A. Bunker, C. Nunes and S. Reis, *Sci. Rep.*, 2017, **7**, 6343.

46 I. Kyrikou, S. K. Hadjikakou, D. Kovala-Demertzi, K. Viras and T. Mavromoustakos, *Chem. Phys. Lipids*, 2004, **132**, 157–169.

47 R. J. DeBerardinis and N. S. Chandel, *Sci. Adv.*, 2016, **2**, e1600200.

48 P. P. Deshpande, S. Biswas and V. P. Torchilin, *Nanomedicine (Lond).*, 2013, **8**, 1509–28.

49 S. D. Steichen, M. Caldorera-Moore and N. A. Peppas, *Eur. J. Pharm. Sci.*, 2013, **48**, 416–27.

50 S. Kumar, P. Singh, R. Srivastava, R. R. Koner, A. Pramanik, J. Mathew, S. Sinha, M. Rawat, R. S. Anand and S. Ghosh, *J. Mater. Chem. C*, 2014, **2**, 6637.

51 † Efrén V. García-Báez, † Francisco J. Martínez-Martínez, ‡ and Herbert Höpfl and † Itzia I. Padilla-Martínez*, , DOI:10.1021/CG0255826.

52 K. Cho, X. Wang, S. Nie, Z. Chen and D. M. Shin, , DOI:10.1158/1078-0432.CCR-07-1441.

53 R. Singh and J. W. Lillard, *Exp. Mol. Pathol.*, 2009, **86**, 215–223.

54 A. C. Anselmo, *J. Control. Release*, 2014, **190**, 531–541.

55 M. E. Grigore, *J. Med. Res. Heal. Educ.*

56 P. Ma, H. Xiao, C. Li, Y. Dai, Z. Cheng, Z. Hou and J. Lin, *Mater. Today*, 2015, **18**, 554–564.

57 V. López-Dávila, A. M. Seifalian and M. Loizidou, *Curr. Opin. Pharmacol.*, 2012, **12**, 414–419.

58 S. K. Murthy, *Int. J. Nanomedicine*, 2007, **2**, 129–41.

59 S. J. Soenen, P. Rivera-Gil, J.-M. Montenegro, W. J. Parak, S. C. De Smedt and K. Braeckmans, *Nano Today*, 2011, **6**, 446–465.

60 A. Tan, Z. Wang, R. Lust, S. Hua, L. Sercombe, T. Veerati, F. Moheimani, S. Y. Wu and A. K. Sood, *Front. Pharmacol. | www.frontiersin.org*, 2015, **6**, 286.

61 C. Matos, C. Moutinho and P. Lobão, *J. Membr. Biol.*, 2012, **245**, 69–75.

62 M. Alavi, N. Karimi and M. Safaei, *Adv. Pharm. Bull.*, 2017, 7, 3–9.

63 R. A. Schwendener, *Ther. Adv. Vaccines*, 2014, 2, 159–182.

64 A. Akbarzadeh, R. Rezaei-Sadabady, S. Davaran, S. W. Joo, N. Zarghami, Y. Hanifehpour, M. Samiei, M. Kouhi and K. Nejati-Koshki, *Nanoscale Res. Lett.*, 2013, **8**, 102.

65 B. Maherani, E. Arab-Tehrany, M. R. Mozafari, C. Gaiani and M. Linder, *Curr. Nanosci.*, 2011, **7**, 436–452.

66 L. Sercombe, T. Veerati, F. Moheimani, S. Y. Wu, A. K. Sood and S. Hua, *Front. Pharmacol.*, 2015, 6.

67 S. M. Moghimi and A. C. Hunter, *Pharm. Res.*, 2001, 18, 1–8.

68 X. Yan, G. L. Scherphof and J. A. A. M. Kamps, *J. Liposome Res.*, 2005, 15, 109–139.

69 D. Pozzi, V. Colapicchioni, G. Caracciolo, S. Piovesana, A. L. Capriotti, S. Palchetti, S. De Grossi, A. Riccioli, H. Amenitsch and A. Laganà, *Nanoscale*, 2014, **6**, 2782–2792.

70 A. Vonarbourg, C. Passirani, P. Saulnier and J. P. Benoit, *Biomaterials*, 2006, **27**, 4356–4373.

71 D. E. Owens and N. A. Peppas, *Int. J. Pharm.*, 2006, 307, 93–102.

72 P. Marqués-Gallego and A. I. P. M. de Kroon, *Biomed Res. Int.*, , DOI:10.1155/2014/129458.

73 P. P. Deshpande, S. Biswas and V. P. Torchilin, *Nanomedicine*, 2013, **8**, 1509–1528.

74 D. Marsh, R. Bartucci and L. Sportelli, *Biochim. Biophys. Acta - Biomembr.*, 2003, 1615, 33–59.

75 S. Galindo-rodriguez, E. Alle, H. Fessi and E. Doelker, *Pharm. Res.*, 2004, **21**, 1428–1439.

76 C. Lemarchand, R. Gref and P. Couvreur, *Eur. J. Pharm. Biopharm.*, 2004, 58, 327–341.

77 R. Gref, A. Domb, P. Quellec, T. B.-… drug delivery reviews and undefined 1995, *ncbi.nlm.nih.gov*.

78 A. Vonarbourg, C. Passirani, P. Saulnier and J. P. Benoit, *Biomaterials*, 2006, 27, 4356–4373.

79 M. Vittaz, D. Bazile, G. Spenlehauer, T. Verrecchia, M. Veillard, F. Puisieux and D. Labarre, *Biomaterials*, 1996, **17**, 1575–1581.

80 B. Montdargent, F. Maillet, M. Paule Carreno, M. Jozefowicz, M. Kazatchkinet and D. Labarre, *Biomaterials*, 1993, **14**, 203–208.

81 S. E. Dunn, A. Brindley, S. S. Davis, M. C. Davies and L. Illum, *Pharm. Res. An Off. J. Am. Assoc. Pharm. Sci.*, 1994, **11**, 1016–1022.

82 C. Passirani, … J. B. delivery and targeting of proteins and undefined 2005, *CRC Press New York*.

83 C. Wilhelm, C. Billotey, J. Roger, J. N. Pons, J. C. Bacri and F. Gazeau, *Biomaterials*, 2003, **24**, 1001–1011.

84 K. D. Lee, K. Hong and D. Papahadjopoulos, *BBA - Biomembr.*, 1992, **1103**, 185–197.

85 M. Roser, D. Fischer and T. Kissel, *Eur. J. Pharm. Biopharm.*, 1998, **46**, 255–263.

86 J. K. Gbadamosi, A. C. Hunter and S. M. Moghimi, *FEBS Lett.*, 2002, **532**, 338–344.

87 V. C. F. Mosqueira, P. Legrand, R. Gref, B. Heurtault, M. Appel and G. Barratt, *J. Drug Target.*, 1999, **7**, 65–78.

88 B. Montdargent, F. Maillet, M. Carreno, M. J.- Biomaterials and undefined 1993, *Elsevier*, , DOI:10.1016/0142-9612(93)90024-V.

89 M. El-Gewely, *Biotechnology annual review*, 1996.

90 S. Stolnik, L. Illum and S. S. Davis, *Adv. Drug Deliv. Rev.*, 1995, 16, 195–214.

91 K. Maruyama, T. Yuda, A. Okamoto, … S. K.-… et B. A. (BBA and undefined 1992,

Elsevier.

92 L. Illum, L. Jacobsen, R. Müller, E. Mak, S. D.- Biomaterials and undefined 1987, *Elsevier*.

93 E. Österberg, K. Bergström, K. Holmberg, T. P. Schuman, J. A. Riggs, N. L. Burns, J. M. Van Alstine and J. M. Harris, *J. Biomed. Mater. Res.*, 1995, **29**, 741–747.

94 C. K. Anders, B. Adamo, O. Karginova, A. M. Deal, S. Rawal, D. Darr, A. Schorzman, C. Santos, R. Bash, T. Kafri, L. Carey, C. R. Miller, C. M. Perou, N. Sharpless and W. C. Zamboni, *PLoS One*, 2013, **8**, e61359.

95 A. Gabizon, H. Shmeeda and Y. Barenholz, *Clin. Pharmacokinet.*, 2003, 42, 419–436.

96 L. E. Van Vlerken, T. K. Vyas and M. M. Amiji, *Pharm. Res.*, 2007, **24**, 1405–1414.

97 F. Veronese, G. P.-D. discovery today and undefined 2005, *Elsevier*.

98 K. Knop, R. Hoogenboom, D. Fischer and U. S. Schubert, *Angew. Chemie - Int. Ed.*, 2010, 49, 6288–6308.

99 J. S. Suk, Q. Xu, N. Kim, J. Hanes and L. M. Ensign, *Adv. Drug Deliv. Rev.*, 2016, 99, 28–51.

100 M. N. Khalid, P. Simard, D. Hoarau, A. Dragomir and J. C. Leroux, *Pharm. Res.*, 2006, **23**, 752–758.

101 G. P. Zara, R. Cavalli, A. Bargoni, A. Fundaro, D. Vighetto and M. R. Gasco, *J. Drug Target.*, 2002, **10**, 327–335.

102 P. Zarrintaj, M. R. Saeb, S. H. Jafari and M. Mozafari, in *Compatibilization of Polymer Blends: Micro and Nano Scale Phase Morphologies, Interphase Characterization, and Properties*, Elsevier, 2019, pp. 511–537.

103 M. P. Sikka and V. K. Midha, in *Advanced Textiles for Wound Care*, Elsevier, 2019, pp. 463–488.

104 O. K. Nag and V. Awasthi, *Pharmaceutics*, 2013, 5, 542–569.

105 K. Rahme and N. Dagher, *Pharmaceutics*, 2019, 11.

106 K. Ulbrich, K. Holá, V. Šubr, A. Bakandritsos, J. Tuček and R. Zbořil, *Chem. Rev.*, 2016, **116**, 5338–5431.

107 M. K. Riaz, M. A. Riaz, X. Zhang, C. Lin, K. H. Wong, X. Chen, G. Zhang, A. Lu and Z. Yang, *Int. J. Mol. Sci.*, 2018, 19, 195.

108 O. Garbuzenko, Y. Barenholz and A. Priev, *Chem. Phys. Lipids*, 2005, **135**, 117–129.

109 R. Bartucci, M. Pantusa, D. Marsh and L. Sportelli, *Biochim. Biophys. Acta - Biomembr.*, 2002, **1564**, 237–242.

110 J. S. Suk, Q. Xu, N. Kim, J. Hanes and L. M. Ensign, *Adv. Drug Deliv. Rev.*, 2016, 99, 28–51.

111 A. K. Kenworthy, K. Hristova, D. Needham and T. J. McIntosh, *Biophys. J.*, 1995, **68**, 1921–1936.

112 O. K. Nag, V. R. Yadav, A. Hedrick and V. Awasthi, *Int. J. Pharm.*, 2013, **446**, 119–129.

113 E. Karathanasis, A. L. Ayyagari, R. Bhavane, R. V. Bellamkonda and A. V. Annapragada, *J. Control. Release*, 2005, **103**, 159–175.

114 J. Heyes, K. Hall, V. Tailor, R. Lenz and I. MacLachlan, *J. Control. Release*, 2006, **112**, 280–290.

115 E. Ambegia, S. Ansell, P. Cullis, J. Heyes, L. Palmer and I. MacLachlan, *Biochim.*

Biophys. Acta - Biomembr., 2005, **1669**, 155–163.

116 R. Wang, R. Xiao, Z. Zeng, L. Xu and J. Wang, *Int. J. Nanomedicine*, 2012, 7, 4185–4198.

117 S. Belsito, R. Bartucci and L. Sportelli, *Biophys. Chem.*, 2001, **93**, 11–22.

118 Q. Hu, C. R. Shew, M. B. Bally and T. D. Madden, *Biochim. Biophys. Acta - Biomembr.*, 2001, **1514**, 1–13.

119 K. Shimada, S. Matsuo, Y. Sadzuka, A. Miyagishima, Y. Nozawa, S. Hirota and T. Sonobe, *Int. J. Pharm.*, 2000, **203**, 255–263.

120 R. Zeisig, K. Shimada, S. Hirota and D. Arndt, *Biochim. Biophys. Acta - Biomembr.*, 1996, **1285**, 237–245.

121 Y. Sadzuka, A. Nakade, T. Tsuruda and T. Sonobe, *J. Control. Release*, 2003, **91**, 271–280.

122 Y. Sadzuka, A. Nakade, R. Hirama, A. Miyagishima, Y. Nozawa, S. Hirota and T. Sonobe, *Int. J. Pharm.*, 2002, **238**, 171–180.

123 I. Sugiyama and Y. Sadzuka, *Biol. Pharm. Bull.*, 2013, **36**, 900–906.

124 I. Sugiyama and Y. Sadzuka, *Curr. Drug Discov. Technol.*, 2011, **8**, 357–366.

125 T. M. Allen, C. Hansen, F. Martin, C. Redemann and A. Yau-Young, *BBA - Biomembr.*, 1991, **1066**, 29–36.

126 Y. Er, T. J. Barnes, D. Fornasiero and C. A. Prestidge, *J. Liposome Res.*, 2009, **19**, 29–36.

127 R. E. Gibson, *Mol. Imaging Biol.*, 2011, **13**, 594–598.

128 G. Bastiat, P. Oligere, G. Karlsson, K. Edwards and M. Lafleur, *Langmuir*, 2007, **23**,

7695–7699.

129 P. A. Carlson, M. H. Gelb and P. Yager, *Biophys. J.*, 1997, **73**, 230–238.

130 N. Yoshikawa, S. Fumoto, K. Yoshikawa, D. Hu, K. Okami, R. Kato, M. Nakashima, H. Miyamoto and K. Nishida, *Pharmaceutics*, 2020, **12**, 341.

131 F. Bonté and R. L. Juliano, *Chem. Phys. Lipids*, 1986, **40**, 359–372.

132 S. Moein Moghimi, I. Hamad, T. L. Andresen, K. Jørgensen, J. Szebeni, S. Moein Moghimi, I. Hamad, T. L. Andresen, K. Jørgensen and J. Szebeni, *FASEB J.*, 2006, **20**, 2591–2593.

133 K. Shimada, S. Matsuo, Y. Sadzuka, A. Miyagishima, Y. Nozawa, S. Hirota and T. Sonobe, *Int. J. Pharm.*, 2000, **203**, 255–263.

134 M. S. Webb, D. Saxon, F. M. P. Wong, H. J. Lim, Z. Wang, M. B. Bally, L. S. L. Choi, P. R. Cullis and L. D. Mayer, *Biochim. Biophys. Acta - Biomembr.*, 1998, **1372**, 272–282.

135 S. Beugin, K. Edwards, G. Karlsson, M. Ollivon and S. Lesieur, *Biophys. J.*, 1998, **74**, 3198–3210.

136 P. Kalyanram, A. Gupta and I. Stadler, *J. Nanotoxicology Nanomedicine*, 2019, **3**, 49–59.

137 Y. Kuang, J. Liu, Z. Liu and R. Zhuo, *Biomaterials*, 2012, **33**, 1596–1606.

138 R. Addeo, V. Faiola, R. Guarrasi, L. Montella, B. Vincenzi, E. Capasso, G. Cennamo, M. S. Rotundo, P. Tagliaferri, M. Caraglia and S. Del Prete, *Cancer Chemother. Pharmacol.*, 2008, **62**, 285–292.

139 A. Deniz, A. Sade, F. Severcan, D. Keskin, A. Tezcaner and S. Banerjee, *Biosci. Rep.*,

2010, **30**, 365–373.

140 J. A. Boomer, M. M. Quails, H. D. Inerowicz, R. H. Haynes, V. S. Patri, J. M. Kim and D. H. Thompson, *Bioconjug. Chem.*, 2009, **20**, 47–59.

141 C. Komeda, A. Ikeda, J. Kikuchi, N. Ishida-Kitagawa, H. Tatebe, K. Shiozaki and M. Akiyama, *Org. Biomol. Chem.*, 2013, **11**, 2567.

142 H. Xu, K. Q. Wang, Y. H. Deng and D. W. Chen, *Biomaterials*, 2010, **31**, 4757–4763.

143 X. Cai, C. Dong, H. Dong, G. Wang, G. M. Pauletti, X. Pan, H. Wen, I. Mehl, Y. Li and D. Shi, *Biomacromolecules*, 2012, **13**, 1024–1034.

144 R. M. Sawant, J. P. Hurley, S. Salmaso, A. Kale, E. Tolcheva, T. S. Levchenko and V. P. Torchilin, *Bioconjug. Chem.*, 2006, **17**, 943–949.

145 Y. Fang, J. Xue, S. Gao, A. Lu, D. Yang, H. Jiang, Y. He and K. Shi, *Drug Deliv.*, 2017, **24**, 22–32.

146 J. Shin, P. Shum and D. H. Thompson, in *Journal of Controlled Release*, Elsevier, 2003, vol. 91, pp. 187–200.

147 H. Hatakeyama, H. Akita, E. Ito, Y. Hayashi, M. Oishi, Y. Nagasaki, R. Danev, K. Nagayama, N. Kaji, H. Kikuchi, Y. Baba and H. Harashima, *Biomaterials*, 2011, **32**, 4306–4316.

148 H. Hatakeyama, E. Ito, H. Akita, M. Oishi, Y. Nagasaki, S. Futaki and H. Harashima, *J. Control. Release*, 2009, **139**, 127–132.

149 H. Hatakeyama, H. Akita, K. Kogure, M. Oishi, Y. Nagasaki, Y. Kihira, M. Ueno, H. Kobayashi, H. Kikuchi and H. Harashima, *Gene Ther.*, 2007, **14**, 68–77.

150 W. J. Wedemeyer, E. Welker, M. Narayan and H. A. Scheraga, *Biochemistry*, 2000, **39**,

4207–4216.

151 S. Shaunak, A. Godwin, J. W. Choi, S. Balan, E. Pedone, D. Vijayarangam, S. Heidelberger, I. Teo, M. Zloh and S. Brocchini, *Nat. Chem. Biol.*, 2006, **2**, 312–313.

152 Z. Y. Guo, X. Y. Jia and Y. M. Feng, *Biol. Chem.*, 2004, **385**, 1171–1175.

153 Y. Wu, W. Chen, F. Meng, Z. Wang, R. Cheng, C. Deng, H. Liu and Z. Zhong, in *Journal of Controlled Release*, Elsevier, 2012, vol. 164, pp. 338–345.

154 H. Dong, M. Tang, Y. Li, Y. Li, D. Qian and D. Shi, *Nanomedicine*, 2015, 10, 1941–1958.

155 G. Batist, in *Cardiovascular Toxicology*, Cardiovasc Toxicol, 2007, vol. 7, pp. 72–74.

156 A. Gabizon, R. Catane, B. Uziely, B. Kaufman, T. Safra, R. Cohen, F. Martin, A. Huang and Y. Barenholz, *Prolonged Circulation Time and Enhanced Accumulation in Malignant Exudates of Doxorubicin Encapsulated in Polyethylene-glycol Coated Liposomes 1*, 1994, vol. 154.

157 A. Gabizon, H. Shmeeda and Y. Barenholz, *Clin. Pharmacokinet.*, 2003, **42**, 419–436.

158

159 D. C. Drummond, C. O. Noble, Z. Guo, K. Hong, J. W. Park and D. B. Kirpotin, *Cancer Res.*, 2006, **66**, 3271–3277.

160 U. Bulbake, S. Doppalapudi, N. Kommineni and W. Khan, *Pharmaceutics*, 2017, **9**, 12.

161 M. Viard, H. Reichard, B. A. Shapiro, F. A. Durrani, A. J. Marko, R. M. Watson, R. K. Pandey and A. Puri, *Nanomedicine Nanotechnology, Biol. Med.*, 2018, **14**, 2295–2305.

162 U.S. Patent and Trademark Office., 10,117,942., 2018.

163 NanoRED | Revolutionizing Cancer Care, http://www.nanoredbiotech.com/, (accessed

17 July 2020).

164 P. J. Gaillard, C. C. M. Appeldoorn, R. Dorland, J. Van Kregten, F. Manca, D. J. Vugts, B. Windhorst, G. A. M. S. Van Dongen, H. E. De Vries, D. Maussang and O. Van Tellingen, *PLoS One*, , DOI:10.1371/journal.pone.0082331.

165 J. Chen, C. Q. He, A. H. Lin, W. Gu, Z. P. Chen, W. Li and B. C. Cai, *Int. J. Pharm.*, 2014, **475**, 408–415.

166 J. M. Meerum Terwogt, G. Groenewegen, D. Pluim, M. Maliepaard, M. M. Tibben, A. Huisman, W. W. Ten Bokkel Huinink, M. Schot, H. Welbank, E. E. Voest, J. H. Beijnen and J. H. Schellens, *Cancer Chemother. Pharmacol.*, 2002, **49**, 201–210.

167 T. Boulikas, *Expert Opin. Investig. Drugs*, 2009, 18, 1197–1218.

168 W. C. Zamboni, J. L. Eiseman, S. Strychor, P. M. Rice, E. Joseph, B. A. Zamboni, M. K. Donnelly, J. Shurer, R. A. Parise, M. E. Tonda, N. Y. Yu and P. H. Basse, *J. Liposome Res.*, 2011, **21**, 70–80.

169 W. C. Zamboni, L. J. Maruca, S. Strychor, B. A. Zamboni, S. Ramalingam, R. P. Edwards, J. Kim, Y. Bang, H. Lee, D. M. Friedland, R. G. Stoller, C. P. Belani and R. K. Ramanathan, *J. Liposome Res.*, 2011, **21**, 158–165.

170 F. Danhier, *J. Control. Release*, 2016, 244, 108–121.

171 D. Lombardo, M. A. Kiselev, S. Magazù and P. Calandra, *Adv. Condens. Matter Phys.*, 2015, **2015**, 1–22.

172 R. Gunawidjaja, F. Huang, M. Gumenna, N. Klimenko, G. A. Nunnery, V. Shevchenko, R. Tannenbaum and V. V. Tsukruk, *Langmuir*, 2009, **25**, 1196–1209.

173 B. Lindman and P. Alexandridis, *Amphiphilic molecules: small and large*, 2000.

174 K. Ataka, S. T. Stripp and J. Heberle, *Biochim. Biophys. Acta - Biomembr.*, 2013, **1828**, 2283–2293.

175 G. Devatha, S. Roy, A. Rao, A. Mallick, S. Basu and P. P. Pillai, *Chem. Sci.*, 2017, **8**, 3879–3884.

176 M. F. Ross, T. A. Prime, I. Abakumova, A. M. James, C. M. Porteous, R. A. J. Smith and M. P. Murphy, *Biochem. J.*, 2008, **411**, 633–45.

177 B. L. Naylor, M. Picardo, R. Homan and H. J. Pownall, *Chem. Phys. Lipids*, 1991, **58**, 111–9.

178 J. U. Bowie, *Curr. Opin. Struct. Biol.*, 2011, **21**, 42–9.

179 G. D. Rose and R. Wolfenden, *Annu. Rev. Biophys. Biomol. Struct.*, 1993, **22**, 381–415.

180 T. Utsugi, A. J. Schroit, J. Connor, C. D. Bucana and I. J. Fidler, *Cancer Res.*, 1991, **51**, 3062–6.

181 N. B. Leite, A. Aufderhorst-Roberts, M. S. Palma, S. D. Connell, J. Ruggiero Neto and P. A. Beales, *Biophys. J.*, 2015, **109**, 936–47.

182 A. Kenworthy, *Trends Biochem. Sci.*, 2002, **27**, 435–438.

183 H. Khandelia, J. H. Ipsen and O. G. Mouritsen, *Biochim. Biophys. Acta - Biomembr.*, 2008, **1778**, 1528–1536.

184 S. Galdiero, A. Falanga, M. Cantisani, M. Vitiello, G. Morelli, M. Galdiero, S. Galdiero, A. Falanga, M. Cantisani, M. Vitiello, G. Morelli and M. Galdiero, *Int. J. Mol. Sci.*, 2013, **14**, 18758–18789.

185 A. C. Alves, D. Ribeiro, C. Nunes and S. Reis, *Biochim. Biophys. Acta - Biomembr.*, 2016, **1858**, 2231–2244.

186 A. Szyk, Z. Wu, K. Tucker, D. Yang, W. Lu and J. Lubkowski, *Protein Sci.*, 2006, **15**, 2749–60.

187 I. L. Karle, M. A. Perozzo, V. K. Mishra and P. Balaram, *Proc. Natl. Acad. Sci. U. S. A.*, 1998, **95**, 5501–4.

188 A. Merlino, G. Vitiello, M. Grimaldi, F. Sica, E. Busi, R. Basosi, A. M. D'Ursi, G. Fragneto, L. Paduano and G. D'Errico, *J. Phys. Chem. B*, 2012, **116**, 401–412.

189 G. Vitiello, G. Fragneto, A. A. Petruk, A. Falanga, S. Galdiero, A. M. D'Ursi, A. Merlino and G. D'Errico, *Soft Matter*, 2013, **9**, 6442.

190 D. E. Warschawski, A. A. Arnold, M. Beaugrand, A. Gravel, É. Chartrand and I. Marcotte, *Biochim. Biophys. Acta - Biomembr.*, 2011, **1808**, 1957–1974.

191 E. Strandberg, J. Zerweck, P. Wadhwani and A. S. Ulrich, *Biophys. J.*, 2013, **104**, L9–L11.

192 S. H. Park, A. A. De Angelis, A. A. Nevzorov, C. H. Wu and S. J. Opella, *Biophys. J.*, 2006, **91**, 3032–3042.

193 G. Vitiello, A. Falanga, M. Galdiero, D. Marsh, S. Galdiero and G. D'Errico, *Biochim. Biophys. Acta - Biomembr.*, 2011, **1808**, 2517–2526.

194 D. Marsh, *Biochemistry*, 2009, **48**, 729–737.

195 J. Oreopoulos, R. F. Epand, R. M. Epand and C. M. Yip, *Biophys. J.*, 2010, **98**, 815–23.

196 K. El Kirat, S. Morandat and Y. F. Dufrêne, *Biochim. Biophys. Acta - Biomembr.*, 2010, **1798**, 750–765.

197 P. Joanne, C. Galanth, N. Goasdoué, P. Nicolas, S. Sagan, S. Lavielle, G. Chassaing, C. El Amri and I. D. Alves, *Biochim. Biophys. Acta - Biomembr.*, 2009, **1788**, 1772–1781.

198 M. Kiricsi, E. J. Prenner, M. Jelokhani-Niaraki, R. N. A. H. Lewis, R. S. Hodges and R. N. McElhaney, *Eur. J. Biochem.*, 2002, **269**, 5911–5920.

199 R. W. Woody, *Methods Enzymol.*, 1995, **246**, 34–71.

200 S. Gupta A, Gupta R, Kurwadkar, *Liposome encapsulated antimicrobial peptides: potential infectious diseases therapy: Handbook of Research on Diverse Applications of Nanotechnology in Biomedicine, Chemistry and Engineering.*, IGI Global Publisher, 2014.

201 A. Gupta, University of Rhode Island, 2011.

202 P. Kalyanram, H. Ma, S. Marshall, C. Goudreau, A. Cartaya, T. Zimmerman, I. Stadler, S. Nangia and A. Gupta, *Phys. Chem. Chem. Phys.*, , DOI:10.1039/D0CP00696C.

203 J. Stetefeld, S. A. McKenna and T. R. Patel, *Biophys. Rev.*, 2016, **8**, 409–427.

204 S. Bhattacharjee, *J. Control. Release*, 2016, **235**, 337–351.

205 B. Kronberg, A. Dahlman, J. Carlfors, J. Karlsson and P. Artursson, *J. Pharm. Sci.*, 1990, **79**, 667–671.

206 D. Papahadjopoulos, T. M. Allen, A. Gabizon, E. Mayhew, K. Matthay, S. K. Huang, K. D. Lee, M. C. Woodle, D. D. Lasic, C. Redemann and F. J. Martin, *Proc. Natl. Acad. Sci. U. S. A.*, 1991, **88**, 11460–11464.

207 R. Zeisig, K. Shimada, S. Hirota and D. Arndt, *Biochim. Biophys. Acta - Biomembr.*, 1996, **1285**, 237–245.

208 G. Ye, A. Gupta, R. DeLuca, K. Parang and G. D. Bothun, *Colloids Surfaces B Biointerfaces*, 2010, **76**, 76–81.

209 A. Gupta, R. Gupta and S. Kurwardkar, in *Handbook of Research on Diverse*

Applications of Nanotechnology in Biomedicine, Chemistry, and Engineering, IGI Global, 2014, pp. 301–332.

210 Preiss;Matthew Ryan, Gupta;Anju and G. D. Bothun, *Bionanotechnol. self Assem. its Appl.*, 2013.

211 D. Z. Liu, W. Y. Chen, L. M. Tasi and S. P. Yang, *Colloids Surfaces A Physicochem. Eng. Asp.*, 2000, **172**, 57–67.

212 E. Sikorska, E. Iłowska, D. Wyrzykowski and A. Kwiatkowska, *Biochim. Biophys. Acta - Biomembr.*, 2012, **1818**, 2982–2993.

213 Isothermal titration calorimetry, http://www.cureffi.org/2016/09/12/isothermal-titration-calorimetry/, (accessed 23 July 2020).

214 A. Saponaro, *BIO-PROTOCOL*, , DOI:10.21769/bioprotoc.2957.

215 Isothermal Titration Calorimetry: A Biophysical Method to ..., https://bio-protocol.org/e2957, (accessed 23 July 2020).

216 Jacquie, *Chapter 1: UV-Visible & Fluorescence Spectroscopy*, .

217 H. M. Kieler-Ferguson, D. Chan, J. Sockolosky, L. Finney, E. Maxey, S. Vogt and F. C. Szoka, *Eur. J. Pharm. Sci.*, 2017, **103**, 85–93.

218 S. Kruszewski and D. M. Kruszewska, .

219 A. Kunwar, A. Barik, R. Pandey and K. I. Priyadarsini, *Biochim. Biophys. Acta*, 2006, **1760**, 1513–20.

220 Fluorescence Anisotropy - What is it?, https://www.azom.com/article.aspx?ArticleID=16080, (accessed 24 July 2020).

221 A. Gijsbers, T. Nishigaki and N. Sánchez-Puig, *J. Vis. Exp.*, 2016, **2016**, 54640.

222 X. Zhang and H. Hu, *Chem. Cent. J.*, , DOI:10.1186/s13065-017-0360-7.

223 J. Eastoe, G. Fragneto, B. H. Robinson, T. F. Towey, R. K. Heenan and F. J. Leng, *J. Chem. Soc. Faraday Trans*, 1992, **88**, 461–471.

224 V. Selvamani, in *Characterization and Biology of Nanomaterials for Drug Delivery: Nanoscience and Nanotechnology in Drug Delivery*, Elsevier, 2018, pp. 425–444.

225 A. Yavlovich, A. Singh, R. Blumenthal and A. Puri, *Biochim. Biophys. Acta - Biomembr.*, 2011, **1808**, 117–126.

226 E. Sezgin and P. Schwille, *Cold Spring Harb. Perspect. Biol.*, 2011, **3**, a009803.

227 NMR Spectroscopy, https://www2.chemistry.msu.edu/faculty/reusch/VirtTxtJml/Spectrpy/nmr/nmr1.htm, (accessed 23 July 2020).

228 J. D. Roberts, *J. Chem. Educ.*, 1961, **38**, 581.

229 H. Friebolin, *Basic One-and-Two DImensional NMR Spctroscopy*, WILEY-VCH Verlag, 2011.

230 O. Zerbe and S. Jurt, *Applied NMR Spectroscopy for Chemist and Life Scientists*, Wiley-VCH, 2014.

231 W. Li, G. Kagan, R. Hopson and P. G. Williard, *J. Chem. Educ.*, 2011, **88**, 1331–1335.

232 K. Morris and Johnson Charles Jr., *J. Am. Chem. SOC*, 1992, **114**, 3139–3141.

233 P. Kar and M. Feig, in *Advances in Protein Chemistry and Structural Biology*, Academic Press Inc., 2014, vol. 96, pp. 143–180.

234 L. Zheng, A. A. Alhossary, C. K. Kwoh and Y. Mu, in *Encyclopedia of Bioinformatics and Computational Biology: ABC of Bioinformatics*, Elsevier, 2018, vol. 1–3, pp. 550–

566.

235 X. Han, W. H. Shin, C. W. Christoffer, G. Terashi, L. Monroe and D. Kihara, in *Encyclopedia of Bioinformatics and Computational Biology: ABC of Bioinformatics*, Elsevier, 2018, vol. 1–3, pp. 606–619.

236 T. Mavromoustakos, P. Chatzigeorgiou, C. Koukoulitsa and S. Durdagi, *Int. J. Quantum Chem.*, 2011, **111**, 1172–1183.

237 D. Provasi and M. Filizola, in *Comprehensive Biophysics*, Elsevier Inc., 2012, vol. 9, pp. 123–148.

238 I. Stadler, R. Evans, B. Kolb, J. O. Naim, V. Narayan, N. Buehner and R. J. Lanzafame, *Lasers Surg. Med.*, 2000, **27**, 255–61.

239 P. Brondon, I. Stadler and R. J. Lanzafame, *Lasers Surg. Med.*, 2005, **36**, 409–413.

240 P. Brondon, I. Stadler and R. J. Lanzafame, *Lasers Surg. Med.*, 2009, **41**, 222–226.

241 P. Jain and H. Joshi, *J. Appl. Pharm. Sci.*, 2012, **2**, 236–240.

242 M. E. Marshall, J. L. Mohler, K. Edmonds, B. Williams, K. Butler, M. Ryles, L. Weiss, D. Urban, A. Bueschen, M. Markiewicz and G. Cloud, *J. Cancer Res. Clin. Oncol.*, 1994, **120**, S39–S42.

243 M. E. Riveiro, A. Moglioni, R. Vazquez, N. Gomez, G. Facorro, L. Piehl, E. R. de Celis, C. Shayo and C. Davio, *Bioorg. Med. Chem.*, 2008, **16**, 2665–2675.

244 K. Fylaktakidou, D. Hadjipavlou-Litina, K. Litinas and D. Nicolaides, *Curr. Pharm. Des.*, 2004, **10**, 3813–3833.

245 M. H. Lee, A. Sharma, M. J. Chang, J. Lee, S. Son, J. L. Sessler, C. Kang and J. S. Kim, *Chem. Soc. Rev.*, 2018, **47**, 28–52.

246 X. Chen, F. Wang, J. Y. Hyun, T. Wei, J. Qiang, X. Ren, I. Shin and J. Yoon, *Chem. Soc. Rev.*, 2016, **45**, 2976–3016.

247 Y. Jung, J. Jung, Y. Huh and D. Kim, *J. Anal. Methods Chem.*, 2018, **2018**, 1–11.

248 C. Murata, T. Masuda, Y. Kamochi, K. Todoroki, H. Yoshida, H. Nohta, M. Yamaguchi and A. Takadate, *Chem. Pharm. Bull.*, 2005, **53**, 750–758.

249 L. Skowronski, O. Krupka, V. Smokal, A. Grabowski, M. Naparty and B. Derkowska-Zielinska, *Opt. Mater. (Amst).*, 2015, **47**, 18–23.

250 R. M. Christie, *Rev. Prog. Color. Relat. Top.*, 2008, **23**, 1–18.

251 R. M. Christie and C.-H. Lui, *Dye. Pigment.*, 1999, **42**, 85–93.

252 A. Rabahi, M. Makhloufi-Chebli, S. M. Hamdi, A. M. S. Silva, D. Kheffache, B. Boutemeur-Kheddis and M. Hamdi, *J. Mol. Liq.*, 2014, **195**, 240–247.

253 K. R. Naqvi and M. Clark, *Color. Technol.*, 2011, **127**, 62–68.

254 W. R. Sherman and E. Robins, *Anal. Chem.*, 1968, **40**, 803–805.

255 M. A. Musa, J. S. Cooperwood and M. O. F. Khan, *Curr. Med. Chem.*, 2008, **15**, 2664–79.

256 S. Maiti, N. Park, J. H. Han, H. M. Jeon, J. H. Lee, S. Bhuniya, C. Kang and J. S. Kim, *J. Am. Chem. Soc.*, 2013, **135**, 4567–4572.

257 R. Kumar, W. S. Shin, K. Sunwoo, W. Y. Kim, S. Koo, S. Bhuniya and J. S. Kim, *Chem. Soc. Rev.*, 2015, **44**, 6670–6683.

258 J. Donovalová, M. Cigáň, H. Stankovičová, J. Gašpar, M. Danko, A. Gáplovský and P. Hrdlovič, *Molecules*, 2005, **17**, 3259–3276.

259 K. Rohatgi-Mukherjee, *Fundamentals of photochemistry*, New Age International, 1978.

260 N. Nagahora, S. Yahata, S. Goto, K. Shioji and K. Okuma, *J. Org. Chem.*, 2018, **83**, 1969–1975.

261 G. Ye, N.-H. Nam, A. Kumar, A. Saleh, D. B. Shenoy, M. M. Amiji, X. Lin, G. Sun and K. Parang, *J. Med. Chem.*, 2007, **50**, 3604–3617.

262 G.-B. Jiang, D. Quan, K. Liao and H. Wang, *Mol. Pharm.*, 2006, **3**, 152–160.

263 T. Curstedt, J. Johansson, P. Persson, A. Eklund, B. Robertson, B. Löwenadler and H. Jörnvall, *Proc. Natl. Acad. Sci. U. S. A.*, 1990, **87**, 2985–9.

264 F. Ghomashchi, X. Zhang, L. Liu and M. H. Gelb, *Biochemistry*, 1995, **34**, 11910–11918.

265 O. Kisselev, M. Ermolaeva and N. Gautam, *J. Biol. Chem.*, 1995, **270**, 25356–8.

266 M. Seabra, M. Brown and J. Goldstein, *Science (80-.).*, 1993, **259**, 377–381.

267 G. Ye, A. Gupta, R. DeLuca, K. Parang and G. D. Bothun, *Colloids Surfaces B Biointerfaces*, 2010, **76**, 76–81.

268 P. Kurtzhals, S. Havelund, I. Jonassen, B. Kiehr, U. D. Larsen, U. Ribel and J. Markussen, *Biochem. J.*, 1995, **312 (Pt 3**, 725–31.

269 L. Thøgersen, B. Schiøtt, T. Vosegaard, N. C. Nielsen and E. Tajkhorshid, *Biophys. J.*, 2008, **95**, 4337–4347.

270 D. Shental-Bechor, T. Haliloglu and N. Ben-Tal, *Biophys. J.*, 2007, **93**, 1858–71.

271 A. S. Baghel, R. Tandon, G. Gupta, A. Kumar, R. K. Sharma, N. Aggarwal, A. Kathuria, N. K. Saini, M. Bose, A. K. Prasad, S. K. Sharma, M. Nath, V. S. Parmar and H. G. Raj, *Microbiol. Res.*, 2011, **166**, 662–72.

272 S. J. Marrink, H. J. Risselada, S. Yefimov, D. P. Tieleman and A. H. de Vries, *J. Phys.*

Chem. B, 2007, **111**, 7812–7824.

273 J. A. Graham, J. W. Essex and S. Khalid, *J. Chem. Inf. Model.*, 2017, **57**, 650–656.

274 H. J. C. Berendsen, D. van der Spoel and R. van Drunen, *Comput. Phys. Commun.*, 1995, **91**, 43–56.

275 M. J. Abraham, D. van der Spoel, E. Lindahl, B. Hess and and the G. development Team, .

276 T. A. Wassenaar, H. I. Ingólfsson, R. A. Böckmann, D. P. Tieleman and S. J. Marrink, *J. Chem. Theory Comput.*, 2015, **11**, 2144–2155.

277 W. Humphrey, A. Dalke and K. Schulten, *J. Mol. Graph.*, 1996, **14**, 33–38.

278 J. Coates, in *Encyclopedia of Analytical Chemistry*, John Wiley & Sons, Ltd, 2006.

279 S. M. Hasan, M. M. Alam, A. Husain, S. Khanna, M. Akhtar and M. S. Zaman, *Eur. J. Med. Chem.*, 2009, **44**, 4896–4903.

280 K. Makino, T. Yamada, M. Kimura, T. Oka, H. Ohshima and T. Kondo, *Biophys. Chem.*, 1991, **41**, 175–183.

281 S. Garcia-Manyes, G. Oncins and F. Sanz, *Biophys. J.*, 2005, **89**, 4261–4274.

282 M. A. Morini, M. B. Sierra, V. I. Pedroni, L. M. Alarcon, G. A. Appignanesi and E. A. Disalvo, *Colloids Surfaces B Biointerfaces*, 2015, **131**, 54–58.

283 D. H. Ripin and D. A. Evans, pKa's of Inorganic and Oxo-Acids, http://www.chem.wisc.edu/areas/reich/pkatable/index.htm, (accessed 8 November 2018).

284 G. Singh, I. Brovchenko, A. Oleinikova and R. Winter, *Biophys. J.*, 2008, **95**, 3208–21.

285 M. Novo, S. Freire and W. Al-Soufi, *Sci. Rep.*, 2018, **8**, 1783.

286 M. L. Waters, *Curr. Opin. Chem. Biol.*, 2002, **6**, 736–741.

287 S. R. Amrutha and M. Jayakannan, *J. Phys. Chem. B*, 2008, **112**, 1119–1129.

288 T. Lei, in *Design, Synthesis, and Structure-Property Relationship Study of Polymer Field-Effect Transistors.* , Berlin, Heidelberg, Springer., 2015, pp. 23–57.

289 K. Nagarajan, G. Gopan, R. T. Cheriya and M. Hariharan, *Chem. Commun.*, 2017, **53**, 7409–7411.

290 W. H. Binder, V. Barragan and F. M. Menger, *Angew. Chemie Int. Ed.*, 2003, **42**, 5802–5827.

291 Y. Hong, J. W. Y. Lam and B. Z. Tang, *Chem. Soc. Rev.*, 2011, **40**, 5361.

292 Y. Shen, H. Liu, S. Zhang, Y. Gao, B. Li, Y. Yan, Y. Hu, L. Zhao and B. Yang, *J. Mater. Chem. C*, 2017, **5**, 10061–10067.

293 N. G. Zhegalova, S. He, H. Zhou, D. M. Kim and M. Y. Berezin, *Contrast Media Mol. Imaging*, 2014, **9**, 355–62.

294 J. R. Lakowicz, in *Principles of Fluorescence Spectroscopy*, Springer US, Boston, MA, 2006, pp. 277–330.

295 V. I. Gordeliy, M. A. Kiselev, P. Lesieur, A. V. Pole and J. Teixeira, *Biophys. J.*, 1998, **75**, 2343–2351.

296 M.-A. de Ménorval, L. M. Mir, M. L. Fernández and R. Reigada, *PLoS One*, 2012, **7**, e41733.

297 O. Cañadas and C. Casals, Humana Press, Totowa, NJ, 2013, pp. 55–71.

298 A. Mecke, D.-K. Lee, A. Ramamoorthy, B. G. Orr and M. M. Banaszak Holl, *Biophys. J.*, 2005, **89**, 4043–50.

299 E. J. M. Van Kan, D. N. Ganchev, M. M. E. Snel, V. Chupin, A. Van Der Bent and B. De Kruijff, *Biochemistry*, 2003, **42**, 11366–11372.

300 M. C. Sainz, J. R. Chantres, B. Elorza and M. A. Elorza, *Int. J. Pharm.*, 1993, **91**, 1–8.

301 M. S. C. Abreu, M. J. Moreno and W. L. C. Vaz, *Biophys. J.*, 2004, **87**, 353–65.

302 S. Jo, H. Rui, J. B. Lim, J. B. Klauda and W. Im, *J. Phys. Chem. B*, 2010, **114**, 13342–13348.

303 W. F. D. Bennett, J. L. MacCallum, M. J. Hinner, S. J. Marrink and D. P. Tieleman, *J. Am. Chem. Soc.*, 2009, **131**, 12714–12720.

304 A. Choubey, R. K. Kalia, N. Malmstadt, A. Nakano and P. Vashishta, *Biophys. J.*, 2013, **104**, 2429–2436.

305 S. J. Marrink, A. H. De Vries, T. A. Harroun, J. Katsaras and S. R. Wassall, *J. Am. Chem. Soc.*, 2008, **130**, 10–11.

306 D. Lichtenberg, H. Ahyayauch and F. M. Goñi, *Biophys. J.*, 2013, 105, 289–299.

307 H. Heerklotz, *Q. Rev. Biophys.*, 2008, 41, 205–264.

308 F.-X. Contreras, L. Sánchez-Magraner, A. Alonso and F. M. Goñi, *FEBS Lett.*, 2010, **584**, 1779–1786.

309 C. A. Brautigam, *Methods*, 2015, **76**, 124–136.

310 Q. Yang, X. Y. Liu, K. Umetani, T. Ikehara, S. Miyauchi, N. Kamo, T. Jin and J. Miyake, *J. Phys. Chem. B*, 2000, **104**, 7528–7534.

311 H. Osanai, T. Ikehara, S. Miyauchi, K. Shimono, J. Tamogami, T. Nara and N. Kamo, *J. Biophys. Chem.*, 2013, **4**, 11–21.

312 O. Mertins and R. Dimova, *Langmuir*, 2013, **29**, 14545–14551.

313 J. Seelig and P. Ganz, *Biochemistry*, 1991, **30**, 9354–9359.

314 M. Fernández-Vidal, S. H. White and A. S. Ladokhin, *J. Membr. Biol.*, 2011, **239**, 5–14.

315 P. W. Snyder, J. Mecinović, D. T. Moustakas, S. W. Thomas, M. Harder, E. T. Mack, M. R. Lockett, A. Héroux, W. Sherman and G. M. Whitesides, *Proc. Natl. Acad. Sci. U. S. A.*, 2011, **108**, 17889–17894.

316 N. T. Southall, K. A. Dill and A. D. J. Haymet, *J. Phys. Chem. B*, 2002, 106, 521–533.

317 Y. Ma, J. Huang, S. Song, H. Chen and Z. Zhang, *Small*, 2016, **12**, 4936–4954.

318 Y. N. Konan, R. Gurny and E. Allemann, *J. Photochem. Photobiol. B Biol.*, 2002, **66**, 89–106.

319 M. Ashoori and A. Saedisomeolia, *Br. J. Nutr.*, 2017, **111**, 1985–1991.

320 N. Kandzija and V. V. Khutoryanskiy, *J. Pharm. Sci.*, 2017, **106**, 3041–3049.

321 E. V. Khaydukov, K. E. Mironova, V. A. Semchishen, A. N. Generalova, A. V. Nechaev, D. A. Khochenkov, E. V. Stepanova, O. I. Lebedev, A. V. Zvyagin, S. M. Deyev and V. Y. Panchenko, *Sci. Rep.*, 2016, **6**, 35103.

322 A. Arboleda, D. Miller, F. Cabot, M. Taneja, M. C. Aguilar, K. Alawa, E. Perez, G. Amescua, S. H. Yoo and J.-M. A. Parel, *Rose Bengal- and Riboflavin-mediated Photodynamic Therapy of Fungal Keratitis Isolates*, [Association for Research in Vision and Ophthalmology, etc.], 2014, vol. 55.

323 R.-M. Ion, *Rev. Roum. Chim.*, 2007, **52**, 1093–1102.

324 A. M. Edwards, F. Barredo, E. Silva, A. E. De Ioannes and M. I. Becker, *Photochem. Photobiol.*, 1999, **70**, 645–9.

325 K. Sato, N. Sakakibara, K. Hasegawa, H. Minami and T. Tsuji, *J. Dermatol. Sci.*, 2000, **23**, 22–26.

326 R. T. Kashiwabuchi, Y. Khan, F. R. de S. Carvalho, F. Hirai, M. S. Campos and P. J. McDonnell, *Arq. Bras. Oftalmol.*, 2012, **75**, 423–426.

327 J. Shen, Q. Liang, G. Su, Y. Zhang, Z. Wang, H. Liang, C. Baudouin and A. Labbé, *J. Biophys.*, 2017, **2017**, 1–7.

328 J. O. Eloy, M. Claro de Souza, R. Petrilli, J. P. A. Barcellos, R. J. Lee and J. M. Marchetti, *Colloids Surfaces B Biointerfaces*, 2014, **123**, 345–363.

329 X. Xu, M. A. Khan and D. J. Burgess, *Int. J. Pharm.*, 2012, **423**, 410–418.

330 G. Pabst, N. Kučerka, M.-P. Nieh and J. (John) Katsaras, *Liposomes, lipid bilayers and model membranes : from basic research to application*, .

331 V. P. Torchilin, *Nat. Rev. Drug Discov.*, 2005, **4**, 145–160.

332 I. Ahmad, A. Arsalan, S. A. Ali, M. A. Sheraz, S. Ahmed, Z. Anwar, I. Munir and M. R. Shah, *J. Photochem. Photobiol. B Biol.*, 2015, **153**, 358–366.

333 M. A. Ioniţă, R. M. Ion and B. Cârstocea, *Oftalmologia*, 2003, **58**, 29–34.

334 K. Jacobson and D. Papahadjopoulos, *Biochemistry*, 1975, **14**, 152–161.

335 S. Mitaku, T. Jippo and R. Kataoka, *Biophys. J.*, 1983, **42**, 137–144.

336 M. H. Chiu and E. J. Prenner, *J. Pharm. Bioallied Sci.*, 2011, **3**, 39–59.

337 A. Genz, J. F. Holzwarth and T. Y. Tsong, *Biophys. J.*, 1986, **50**, 1043–1051.

338 C. Matsingou and C. Demetzos, *Chem. Phys. Lipids*, 2007, **145**, 45–62.

339 E. Austin, E. Koo and J. Jagdeo, *Sci. Rep.*, 2018, **8**, 12599.

340 A. Blume and P. Garidel, *Lipid Model Membranes and Biomembranes*, Elsevier Science B.V., 1999, vol. 4.

341 C. Demetzos, *J. Liposome Res.*, 2008, **18**, 159–173.

342 F. Korkmaz and F. Severcan, *Arch. Biochem. Biophys.*, 2005, **440**, 141–147.

343 S. M. Ohline, M. L. Campbell, M. T. Turnbull and S. J. Kohler, *J. Chem. Educ.*, 2001, **78**, 1251.

344 G. M. M. El Maghraby, A. C. Williams and B. W. Barry, *Int. J. Pharm.*, 2005, **292**, 179–185.

345 V. P. Torchilin and V. Weissig, *Liposomes: a practical approach*, Oxford University Press Oxford, 2003, vol. 264.

346 M. Çağdaş, A. D. Sezer and S. Bucak, in *Application of Nanotechnology in Drug Delivery*, InTech, 2014.

347 P. Vabbilisetty and X. L. Sun, *Org. Biomol. Chem.*, 2014, **12**, 1237–1244.

348 M. K. Riaz, M. A. Riaz, X. Zhang, C. Lin, K. H. Wong, X. Chen, G. Zhang, A. Lu and Z. Yang, *Int. J. Mol. Sci.*, 2018, 19, 195.

349 C. Sun, J. Wang, J. Liu, L. Qiu, W. Zhang and L. Zhang, *AAPS PharmSciTech*, 2013, **14**, 332–338.

350 B. S. Pattni, V. V. Chupin and V. P. Torchilin, *Chem. Rev.*, 2015, 115, 10938–10966.

351 S. Kumar Pramanik, P. Losada-Pérez, G. Reekmans, R. Carleer, M. D'Olieslaeger, D. Vanderzande, P. Adriaensens and A. Ethirajan, *Sci. Rep.*, 2017, **7**, 46257.

352 S. M. S Barua, *Nano Today*, 2014, **9**, 223–243.

353 T. S. RK Jain, *Nat. Rev. Clin. Oncol.*, 2010, **7**, 653–664.

354 T. L. Andresen, S. S. Jensen and K. Jørgensen, *Prog. Lipid Res.*, 2005, 44, 68–97.

355 K. Raemdonck, K. Braeckmans, J. Demeester and S. C. De Smedt, *Chem. Soc. Rev.*, 2014, **43**, 444–472.

356 A. Yavlovich, B. Smith, K. Gupta, R. Blumenthal and A. Puri, *Mol. Membr. Biol.*, 2010, **27**, 364–381.

357 A. Puri, *Pharmaceutics*, 2013, **6**, 1–25.

358 N. T. Thet, W. D. Jamieson, M. Laabei, J. D. Mercer-Chalmers and A. T. A. Jenkins, *J. Phys. Chem. B*, 2014, **118**, 5418–5427.

359 J. Moon, H. Suh, A. Bershteyn, M. Stephan, H. L.-N. materials and undefined 2011, *nature.com*.

360 R. Jelinek, S. K.-C. C. S. Systems and undefined 2007, *Springer*, 2007, **277**, 155–180.

361 D. D. Lasic and D. Needham, *Chem. Rev.*, 1995, **95**, 2601–2628.

362 D. H. Napper, *J. Colloid Interface Sci.*, 1977, **58**, 390–407.

363 V. S. Stenkamp and J. C. Berg, *Langmuir*, 1997, **13**, 3827–3832.

364 J. W. Virden and J. C. Berg, *Langmuir*, 1992, **8**, 1532–1537.

365 R. Demel, B. D. K.-B. et B. A. (BBA)-R. on and undefined 1976, *Elsevier*.

366 A. R. Mohammed, N. Weston, A. G. A. Coombes, M. Fitzgerald and Y. Perrie, *Int. J. Pharm.*, 2004, **285**, 23–34.

367 D. G. Rhodes, S. L. Blechner, P. Yager and P. E. Schoen, *Chem. Phys. Lipids*, 1988, **49**, 39–47.

368 E. Schnitzer, I. Pinchuk, A. Bor, A. Leikin-Frenkel and D. Lichtenberg, *Chem. Phys.*

Lipids, 2007, **146**, 43–53.

369 E. Rudolphi-Skórska, M. Filek and M. Zembala, *J. Membr. Biol.*, 2017, **250**, 493–505.

370 E. Touitou and B. Barry, *Enhancement in drug delivery*, 2006.

371 A. Vejux, L. Malvitte and G. Lizard, *Brazilian J. Med. Biol. Res.*, 2008, 41, 545–556.

372 R. Domínguez, M. Pateiro, M. Gagaoua, F. J. Barba, W. Zhang and J. M. Lorenzo, *Antioxidants*, 2019, 8.

373 V. Bharadwaz and V. Maulick, , DOI:10.1007/s13204-015-0421-y.

374 M.-Y. Yang, C.-J. Chang and L.-Y. Chen, *J. Photochem. Photobiol. B Biol.*, 2017, **173**, 325–332.

375 M. Chiu and E. Prenner, in *Journal of Pharmacy and Bioallied Sciences*, Wolters Kluwer -- Medknow Publications, 2011, vol. 3, pp. 39–59.

376 Z. Cao, L. Zhang and S. Jiang, *Langmuir*, 2012, **28**, 11625–11632.

377 J. M. (Joseph M. Smith, H. C. (Hendrick C. . Van Ness, M. M. Abbott and M. T. (Mark T. Swihart, *Introduction to chemical engineering thermodynamics*, .

378 J. M. A. Abdulla, Y. T. F. Tan and Y. Darwis, *AAPS PharmSciTech*, 2010, **11**, 663–671.

379 S. A. Rahman, N. S. Abdelmalak, A. Badawi, T. Elbayoumy, N. Sabry and A. El Ramly, *Drug Deliv.*, 2015, **22**, 731–739.

380 D. Machado, S. M. Shishido, K. C. S. Queiroz, D. N. Oliveira, A. L. C. Faria, R. R. Catharino, C. A. Spek and C. V. Ferreira, *PLoS One*, 2013, **8**, e54269.

381 L. Bartmann, D. Schumacher, S. Von Stillfried, M. Sternkopf, S. Alampour-Rajabi, M. A. M. J. Van Zandvoort, F. Kiessling and Z. Wu, *Front. Pharmacol.*, 2019, **10**, 79.

382 B. Ozsvari, G. Bonuccelli, R. Sanchez-Alvarez, R. Foster, F. Sotgia and M. P. Lisanti, *Aging (Albany. NY).*, 2017, **9**, 2610–2628.

383 H. Amawi, C. Karthikeyan, R. Pathak, N. Hussein, R. Christman, R. Robey, C. R. Ashby, P. Trivedi, A. Malhotra and A. K. Tiwari, *Eur. J. Med. Chem.*, 2017, **138**, 1053–1065.

384 K. Mikkelsen, M. D. Prakash, N. Kuol, K. Nurgali, L. Stojanovska and V. Apostolopoulos, *Int. J. Mol. Sci.*, , DOI:10.3390/ijms20153763.

385 A. R. Mohammed, N. Weston, A. G. A. Coombes, M. Fitzgerald and Y. Perrie, *Int. J. Pharm.*, 2004, **285**, 23–34.

386 M. L. Briuglia, C. Rotella, A. McFarlane and D. A. Lamprou, *Drug Deliv. Transl. Res.*, 2015, **5**, 231–242.

387 S. Li, L. H.-J. of controlled release: official journal of the and undefined 2010, *ncbi.nlm.nih.gov*.

388 Q. Yang, S. W. Jones, C. L. Parker, W. C. Zamboni, J. E. Bear and S. K. Lai, *Mol. Pharm.*, 2014, **11**, 1250–1258.

389 S. Salmaso and P. Caliceti, *J. Drug Deliv.*, , DOI:10.1155/2013/374252.

390 Z. Shen, H. Ye, M. Kröger and Y. Li, *Nanoscale*, 2018, **10**, 4545–4560.

391 M. Johnsson, *Comprehensive Summaries of Uppsala Dissertations from the Faculty of Science and Technology 629 Sterically Stabilised Liposomes and Related Lipid Aggregates Fundamental Studies on Aggragate Structure and Stability*, 2001.

392 S. C. Lee, K. E. Lee, J. J. Kim and S. H. Lim, *J. Liposome Res.*, 2005, **15**, 157–166.

393 F. K. Bedu-Addo, P. Tang, Y. Xu and L. Huang, *Pharm. Res.*, 1996, **13**, 710–7.

394 K. Hashizaki, H. Taguchi, C. Itoh, H. Sakai, M. Abe, Y. Saito and N. Ogawa, *Chem. Pharm. Bull.*, 2003, **51**, 815–820.

395 T. M. Allen and P. R. Cullis, *Adv. Drug Deliv. Rev.*, 2013, 65, 36–48.

396 A. Miquel-Clopés, E. G. Bentley, J. P. Stewart and S. R. Carding, *Clin. Exp. Immunol.*, 2019, 196, 205–214.

397 M. Henriksen-Lacey, K. S. Korsholm, P. Andersen, Y. Perrie and D. Christensen, *Expert Opin. Drug Deliv.*, 2011, 8, 505–519.

398 D. D. Lasic, *J. Colloid Interface Sci.*, 1990, 140, 302–304.

399 M. Grit and D. J. A. Crommelin, *Chem. Phys. Lipids*, 1993, **64**, 3–18.

400 S. J. Leung and M. Romanowski, *Theranostics*, 2012, **2**, 1020–1036.

401 G. Qin, Z. Li, R. Xia, F. Li, B. O'Neill, … J. G.- and U. 2011, *iopscience.iop.org*.

402 H. Takeuchi, H. Kojima, H. Yamamoto and Y. Kawashima, *J. Control. Release*, 2000, **68**, 195–205.

403 X. Mu and Z. Zhong, *Int. J. Pharm.*, 2006, **318**, 55–61.

404 J. Liu, B. Boonkaew, J. Arora, S. H. Mandava, M. M. Maddox, S. Chava, C. Callaghan, J. He, S. Dash, V. T. John and B. R. Lee, *J. Pharm. Sci.*, 2015, **104**, 1187–1196.

405 T. Verrecchia, G. Spenlehauer, D. V. Bazile, A. Murry-Brelier, Y. Archimbaud and M. Veillard, *J. Control. Release*, 1995, **36**, 49–61.

406 F. Martin, M. Woodle, 213,804 C Redemann - … Patent 5 and undefined 1993, *Solid tumor treatment method and composition*, .

407 M. C. Woodle, *Adv. Drug Deliv. Rev.*, 1995, 16, 249–265.

408 K. Kostarelos, T. F. Tadros and P. F. Luckham, *Langmuir*, 1999, **15**, 369–376.

409 M. Silvander, *Prog. Colloid Polym. Sci.*, 2002, 120, 35–40.

410 R. Treanor and M. D. Pace, *Biochim. Biophys. Acta (BBA)/Lipids Lipid Metab.*, 1990, **1046**, 1–11.

411 S. Colantonio, J. T. Simpson, R. J. Fisher, A. Yavlovich, J. M. Belanger, A. Puri and R. Blumenthal, *Lipids*, 2011, **46**, 469–477.

412 A. Puri, *Pharmaceutics*, 2014, 6, 1–25.

413 A. Puri, H. Jang, A. Yavlovich, M. A. Masood, T. D. Veenstra, C. Luna, H. Aranda-Espinoza, R. Nussinov and R. Blumenthal, *Langmuir*, 2011, **27**, 15120–15128.

414 A. Yavlovich, A. Singh, S. Tarasov, J. Capala, R. Blumenthal and A. Puri, *J. Therm. Anal. Calorim.*, 2009, **98**, 97–104.

415 G. Sun, M. A. Anderson, E. C. Gorospe, C. L. Leggett, L. S. Lutzke, L. M. Wong Kee Song, M. Levy and K. K. Wang, *Lasers Surg. Med.*, 2012, **44**, 755–761.

416 D. A. Bellnier, W. R. Greco, G. M. Loewen, H. Nava, A. R. Oseroff and T. J. Dougherty, *Lasers Surg. Med.*, 2006, **38**, 439–444.

417 D. A. Bellnier, W. R. Greco, G. M. Loewen, H. Nava, A. R. Oseroff, R. K. Pandey, T. Tsuchida and T. J. Dougherty, *Cancer Res.*

418 A. Puri, *Pharmaceutics*, 2014, 6, 1–25.

419 J. V. Jokerst, T. Lobovkina, R. N. Zare and S. S. Gambhir, *Nanomedicine*, 2011, 6, 715–728.

420 S. M. Moghimi and J. Szebeni, *Prog. Lipid Res.*, 2003, 42, 463–478.

421 M. L. Immordino, F. Dosio and L. Cattel, *Int. J. Nanomedicine*, 2006, **1**, 297–315.

422 M. Silvander, P. Hansson and K. Edwards, , DOI:10.1021/la9912646.

423 M. Kepczyński, K. Nawalany, M. Kumorek, A. Kobierska, B. Jachimska and M. Nowakowska, *Chem. Phys. Lipids*, 2008, **155**, 7–15.

424 M. Stepniewski, M. Pasenkiewicz-Gierula, T. Rog, R. Danne, A. Orlowski, M. Karttunen, A. Urtti, M. Yliperttula, E. Vuorimaa and A. Bunker, *Langmuir*, 2011, **27**, 7788–7798.

425 S. Tsuda, T. Sakakura, S. Fujii, H. Suzuki and T. Yomo, *PLoS One*, 2015, **10**, e0132963.

426 S. R. Sheth and D. Leckband, *Proc. Natl. Acad. Sci. U. S. A.*, 1997, **94**, 8399–8404.

427 T. Drobek, N. D. Spencer and M. Heuberger, *Macromolecules*, 2005, **38**, 5254–5259.

428 C. Feng and X. Huang, *Acc. Chem. Res.*, 2018, **51**, 2314–2323.

429 R. L. Biltonen and D. Lichtenberg, *Chem. Phys. Lipids*, 1993, **64**, 129–142.

430 J. Welti-Chanes, .

431 A. Khajeh and H. Modarress, *Biochim. Biophys. Acta - Biomembr.*, 2014, **1838**, 2431–2438.

432 D. Lombardo, P. Calandra, D. Barreca, S. Magazù and M. A. Kiselev, *Nanomaterials*, 2016, 6.

433 L. Viitala, S. Pajari, L. Gentile, J. Määttä, M. Gubitosi, J. Deska, M. Sammalkorpi, U. Olsson and L. Murtomäki, *Langmuir*, 2019, **35**, 3999–4010.

434 N. Kamaly, Z. Xiao, P. M. Valencia, A. F. Radovic-Moreno and O. C. Farokhzad, *Chem. Soc. Rev.*, 2012, 41, 2971–3010.

435 F. S. Majedi, M. M. Hasani-Sadrabadi, S. Hojjati Emami, M. A. Shokrgozar, J. J. Vandersarl, E. Dashtimoghadam, A. Bertsch and P. Renaud, *Lab Chip*, 2013, **13**, 204–

207.

436 K. A. Carter, S. Shao, M. I. Hoopes, D. Luo, B. Ahsan, V. M. Grigoryants, W. Song, H. Huang, G. Zhang, R. K. Pandey, J. Geng, B. A. Pfeifer, C. P. Scholes, J. Ortega, M. Karttunen and J. F. Lovell, *Nat. Commun.*, 2014, **5**, 3546.

437 M. Dzieciuch, S. Rissanen, N. Szydłowska, A. Bunker, M. Kumorek, D. Jamróz, I. Vattulainen, M. Nowakowska, T. Róg and M. Kepczynski, *J. Phys. Chem. B*, 2015, **119**, 6646–6657.

438 M. N. Sahib, S. Abdalwahed, S. A. Abdulameer, Y. Darwis, K. K. Peh and Y. T. F. Tan, *Drug Des. Devel. Ther.*, 2012, **6**, 29–42.

439 U. Sah, K. Sharma, N. Chaudhri, M. Sankar and P. Gopinath, *Colloids Surfaces B Biointerfaces*, 2018, **162**, 108–117.

440 J. H. Georger, A. Singh, R. R. Price, J. M. Schnur, P. Yager and P. E. Schoen, *J. Am. Chem. Soc.*, 1987, **109**, 6169–6175.

441 A. Priev, A. M. Samuni, O. Tirosh and Y. Barenholz, in *Targeting of Drugs 6*, Springer US, Boston, MA, 1998, pp. 147–167.

442 M. I. Morandi, M. Sommer, M. Kluzek, F. Thalmann, A. P. Schroder and C. M. Marques, *Biophys. J.*, 2018, **114**, 2165–2173.

443 K. Hashizaki, C. Itoh, H. Sakai, S. Yokoyama, H. Taguchi, Y. Saito, N. Ogawa and M. Abe, *Colloids Surfaces B Biointerfaces*, 2000, **17**, 275–282.

444 D. L. Melchior and J. M. Steim, *Annu. Rev. Biophys. Bioeng.*, 1976, 5, 205–238.

445 M. O. Eze, *Biochem. Educ.*, 1991, **19**, 204–208.

446 M. Kastantin, B. Ananthanarayanan, P. Karmali, E. Ruoslahti and M. Tirrell, *Langmuir*,

2009, **25**, 7279–7286.

447 W. R. Perkins, X. Li, J. L. Slater, P. A. Harmon, P. L. Ahl, S. R. Minchey, S. M. Gruner and A. S. Janoff, *Biochim. Biophys. Acta - Biomembr.*, 1997, **1327**, 41–51.

448 C. Naumann, T. Brumm and T. M. Bayerl, *Biophys. J.*, 1992, **63**, 1314–1319.

449 N. Monteiro, A. Martins, R. L. Reis and N. M. Neves, *J. R. Soc. Interface*, 2014, **11**, 20140459.

450 B. Gruenewald, S. Stankowski and A. Blume, *FEBS Lett.*, 1979, **102**, 227–229.

451 I. G. Denisov, M. A. McLean, A. W. Shaw, Y. V. Grinkova and S. G. Sligar, *J. Phys. Chem. B*, 2005, **109**, 15580–15588.

452 N. Beztsinna, Y. Tsvetkova, M. Bartneck, T. Lammers, F. Kiessling and I. Bestel, *Bioconjug. Chem.*, 2016, **27**, 2048–2061.

453 Y.-C. Tseng and L. Huang, *J. Biomed. Nanotechnol.*, 2009, **5**, 351–63.

454 R. L. G. Lecaros, L. Huang, T. C. Lee and Y. C. Hsu, *Mol. Ther.*, 2016, **24**, 106–116.

455 A. Puri, M. Viard, P. Zakrevsky, L. Parlea, K. P. Singh, B. A. Shapiro, M. Viard, P. Zakrevsky, L. Parlea, K. P. Singh and B. A. Shapiro, 2018, 419–448.

456 Y. Jin, L. Song, Y. Su, L. Zhu, Y. Pang, F. Qiu, G. Tong, D. Yan, B. Zhu and X. Zhu, *Biomacromolecules*, 2011, **12**, 3460–3468.

457 K. Gupta, S. J. Mattingly, R. J. Knipp, K. A. Afonin, M. Viard, J. T. Bergman, M. Stepler, M. H. Nantz, A. Puri and B. A. Shapiro, *Nanomedicine*, 2015, **10**, 2805–2818.

458 D. Reddy, M. Kongot, S. Netalkar, … M. K.-E. journal of and U. 2018, *Eur. J. Med. Chem.*, 2018, **150**, 864–875.